Structural Dynamics of Photochemical Reactions, Studied with Ultrafast X-ray Methods

Vester, Peter

Publication date:
2018

Document Version
Publisher's PDF, also known as Version of record

TECHNICAL UNIVERSITY OF DENMARK

DOCTORAL THESIS

Structural Dynamics of Photochemical Reactions, Studied with Ultrafast X-ray Methods

Author:
Peter VESTER

Supervisor:
Martin MEEDOM NIELSEN
Kristoffer HALDRUP

A thesis submitted in fulfillment of the requirements for the degree of Doctor of Philosophy

in the

NEXMAP Group
DTU Physics

November 17, 2018

Declaration of Authorship

I, Peter VESTER, declare that this thesis titled, "Structural Dynamics of Photochemical Reactions, Studied with Ultrafast X-ray Methods" and the work presented in it are my own. I confirm that:

- This work was done wholly or mainly while in candidature for a research degree at this University.
- Where any part of this thesis has previously been submitted for a degree or any other qualification at this University or any other institution, this has been clearly stated.
- Where I have consulted the published work of others, this is always clearly attributed.
- Where I have quoted from the work of others, the source is always given. With the exception of such quotations, this thesis is entirely my own work.
- I have acknowledged all main sources of help.
- Where the thesis is based on work done by myself jointly with others, I have made clear exactly what was done by others and what I have contributed myself.

Signed:

Date:

Abstract

The overarching scientific theme of the thesis regards energy transfer processes within the field of chemistry and biology with technical applications such as e.g. solar cells and photo catalysts. By developing existing methods and executing X-ray experiments aimed at investigating structural and electronic dynamics in photoactive molecules, the thesis aims to provide detailed understanding of such processes by imaging how atoms move as energy flows through a complex chemical system.

First, a systematic review will be given of the data analysis process of femtosecond Time-Resolved Wide Angle X-ray Scattering (TR-WAXS) solution data from modern X-ray Free Electron Laser (XFEL) facilities. In combination with structural modelling of complex dynamic photochemical systems, the experimental results allow for the creation of "Molecular Movies" and direct probing of the real-time atomic movements in such processes.

The first study presented in the thesis, focuses on developing a method to directly probe the sub-picosecond ground and excited state structural dynamics on the potential energy surfaces of photo excited PtPOP/AgPtPOP molecules. These are model systems for a group of transition metal complexes of relevance to catalysis and light-harvesting purposes. A successful comparison with high-level quantum simulations allowed for an experimentally supported visualization of the structural dynamics.

The second study investigates the sub-picosecond structural changes in the solvation shell following an aqueous $I^- \rightarrow I^0$ photoreaction. It represents a simple system for studying solvent reorganization upon a solute charge change as a model system for a variety of chemical and biological systems. Simultaneous measurements of the X-ray absorption enabled direct coupling of the structural changes to changes in the electronic configuration to support the theory of increased electron back donation to I^0 as a result of the structural changes in the solvent shell.

The final part of the thesis, introduces X-ray Cross Correlation Analysis (XCCA) as an additional and powerful tool to analyze the scattering signals from XFEL experiments. This method reveals additional information about the sample, as it takes advantage of the angular intensity correlations in the full 2-dimensional detector space, instead of reducing the data by azimuthal averaging. This approach revealed additional structural information about the PtPOP sample and a hidden timescale (~ 50 ps) related to the rotational dephasing of the molecules.

Resumé

Det overordnede videnskabelige tema i denne afhandling omhandler energioverførselsprocesser inden for kemi og biologi med tekniske applikationer som f.eks. solceller og fotokatalysatorer. Ved at udvikle eksisterende metoder og udføre røntgenforsøg med henblik på at undersøge strukturel og elektronisk dynamik i fotoaktive molekyler, sigter afhandlingen imod at give en detaljeret forståelse for sådanne processer ved at måle hvordan atomer bevæger sig, når energi strømmer igennem et komplekst kemisk system.

Afhandlingen giver en systematisk gennemgang af datanalyseprocessen for femtosekund Time-Resolved Wide-Angle Scattering (TR-WAXS) opløsningsdata fra moderne X-ray Free Electron Laser (XFEL) faciliteter. I kombination med strukturelle modelleringer af komplekse dynamiske fotokemiske systemer muliggør de eksperimentale resultater skabelsen af "Molekylære Film" og direkte sondering af realtids atombevægelser i sådanne processer.

Den første undersøgelse præsenteret i afhandlingen, fokuserer på at udvikle en metode til direkte at undersøge sub-picosekund grund- og exciteret tilstandes strukturelle dynamik på de potentielle energioverflader af foto exciteret PtPOP / AgPtPOP molekyler. Disse er modelsystemer for en gruppe af overgangsmetalkomplekser af relevans for katalyse og solenergi. En vellykket sammenligning med høj-niveau kvantesimuleringer skabte en eksperimentelt understøttet visualisering af strukturdynamikken.

Den anden undersøgelse omhandler strukturændringer i opløsningsskallen omkring opløste atomer efter en vandig $I^- \rightarrow I^0$ fotoreaktion. Det repræsenterer et simpelt system til at studerer opløsningsreorganisation efter en ladningsændring af det opløste materiale som et modelsystem til en række kemiske og biologiske systemer. Yderligere målinger af røntgenabsorptionen muliggjorde direkte kobling af strukturændringerne til ændringer i den elektroniske konfiguration for at understøtte teorien om en øget elektron tilbagegivning til I^0 som et resultat af strukturændringerne i opløsningsskallen.

Den sidste del af afhandlingen, introducerer X-ray Cross Correlation Analysis (XCCA) som et ekstra og kraftfuldt værktøj til at analysere spredningssignalerne fra XFEL eksperimenter. Dette værktøj afslører yderligere oplysninger om prøven, da den udnytter vinkelfrekvenskorrelationerne i det fulde 2-dimensionelle detektorrum, i stedet for at reducere dataene ved en azimutal-middelværdi. Denne fremgangsmåde afslørede yderligere strukturelle oplysninger om PtPOP-prøven og en skjult tidsskala (~ 50 ps), der er relateret til molekylernes rotationsaffasning.

Acknowledgements

I have been working on my PhD for the last three years and I feel a need to thank some of the people who made it all possible, for supporting me and for giving me a great experience.

First, I would like to express my sincere gratitude to my supervisors Martin Meedom Nielsen and Kristoffer Haldrup for their continuous support of my Ph.D. study and related research, for their patience, motivation, and immense knowledge. Their guidance helped me in all the time of research and writing of this thesis. I could not have imagined having better advisors and mentors for my Ph.D. study. Also thanks, for introducing me to the very fascinating field of X-ray Time-Resolved X-ray Scattering and for giving me the opportunity to participate in experiments at world class X-ray facilities in San Francisco (LCLS) and Hamburg (European XFEL).

A big thank you also goes to Ivan Vartaniants for welcoming me into his research group at DESY for my external research stay. I had a wonderful time in Hamburg and I am thankful for our continued collaboration on applying X-ray Cross Correlation Analysis on experimental data from X-ray facilities and the article we have worked on together.

Mads Laursen, Diana Zederkof and Frederik Beyer Hansen, It has been amazing to do my PhD at the same time as you, and share an office with you during the last three years. Your support and discussions have been valuable and you are without doubt very talented scientists. Furthermore, I would like to thank the rest of the people in the NEXMAP group for day-to-day discussions, encouragement, and for helping with the beamtimes.

I would also like to express my gratitude for the people working at the beamlines at LCLS and XFEL - without their expertise and hard work, this project and many others would not have been possible.

Finally, I would like to thank my friends and family for always being there for me and supporting me through all the good and difficult times of my PhD.

Publications Included in This Work

This thesis is based on the following publications. All publications have been attached in their current state by the end of the thesis.

Paper I

Ultrafast Structural Dynamics of Photo-Reactions Revealed by Model-Independent X-ray Cross-Correlation Analysis
Peter Vester, Ivan A. Zaluzhnyy, Ruslan P. Kurta, Klaus B. Møller, Elisa Biasin, Kristoffer Haldrup, Martin Meedom Nielsen and Ivan A. Vartanyants
Submitted to: *Structural Dynamics*

Paper II

Ultrafast X-ray Scattering Measurements of Coherent Structural Dynamics on the Ground-State Potential Energy Surface of a Diplatinum Molecule
Kristoffer Haldrup, Gianluca Levi, Elisa Biasin, Peter Vester, Mads Laursen, Frederik Beyer, Kasper Skov Kjaer, Tim Brandt van Driel, Tobias Harlang, Asmus O. Dohn, Robert Hartsock, Silke Nelson, James Glownia, Henrik Lemke, Morten Christensen, Kelly Gaffney, Niels Henriksen, Klaus Møller and Martin M. Nielsen
Submitted to: *Physical Review Letters*

Paper III

Anisotropy Enhanced X-ray Scattering from Solvated Transition Metal Complexes
Elisa Biasin, Tim B. van Driel, Mads Laursen, Gianluca Levi, Asmus O. Dohn, Asbjørn Moltke, Peter Vester, Frederik B. K. Hansen, Kasper S. Kjaer, Tobias Harlang, Robert Hartsock, Morten Christensen, Kelly J. Gaffney, Niels E. Henriksen, Klaus B. Møller, Kristoffer Haldrup and Martin M. Nielsen
Journal of Synchrotron Radiation (2018)

Paper IV

Solvent Control of Charge Transfer Excited State Relaxation Pathways in [Fe(2,2-bipyridine)(CN)4]2-
Kasper S. Kjær, Kristjan Kunnus, Tobias C. B. Harlang, Tim B. Van Driel, Kathryn Ledbetter, Robert W. Hartsock, Marco E. Reinhart, Sergey Koroidov, Lin Li, Mads Laursen, Elisa Biasin, Frederik B. Hansen, Peter Vester, Morten Christensen, Kristoffer Haldrup, Martin M. Nielsen, Pavel Chabera, Yizhu Lui, Hideyuki Tatsuno, Cornelia Timm, Jens Uhlig, Villy Sundstöm, Zoltan Nemeth, Dorottya Szemes, Eva Bajnoczi, Gyorgy Vanko, Roberto Alonso Mori, James M. Glownia, Silke Nelson, Marcin Sikorski, Dimosthenis Sokaras, Henrik T. Lemke, Sophie Canton, Kenneth Wärnmark, Petter Persson, Amy A. Cordones and Kelly J. Gaffney
Physical Chemistry Chemical Physics (2018)

Other Publications

The following publications are not included in the work of this thesis.

Paper V

Laser Driven Acoustic Vibrations in Nanowires Studied by Time-Resolved GIXD
Dmitry Khakhulin, Tomas Stankevic, Peter Vester, Simon O. Mariager, Peter Krogstrup, Michael Wulff and Robert Feidenhans'l
Acta Crystallographica Section A (2016)

XFEL Beamtime Proposals as Main Proposer

Proposal I

Revealing the Ultrafast Dynamics and Hidden Symmetries During Ion-Release from a Transition-Metal Complex
Peter Vester, Kristoffer Haldrup, Mads Laursen, Diana Zederkof, Kasper Skov Kjaer, Ruslan Kurta, Ivan Zaluzhnyy, Ivan Vartaniants and Martin Meedom Nielsen
European XFEL (2018), Accepted ($\sim 10\%$ acceptance rate).

A slightly modified proposal was also accepted for beamtime at *LCLS* in 2018.

Contributions to Publications

Paper I Main author. Participation in experiment, development of the XCCA method, XCCA simulations and data analysis.

Paper II Participation in the experiment, scientific discussions, commenting on the paper, validation of the results. Development of the structural modelling method and analysis of the isotropic X-ray scattering data.

Paper III Participation in the experiment, scientific discussions, commenting on the paper and validation of the results.

Paper IV Participation in the experiment, scientific discussions, commenting on the paper.

Paper V Participation in the experiment, scientific discussions. Analysis of TR-GIXD data (Time-Resolved Grazing Incidence X-ray Diffraction).

Contents

Declaration of Authorship iii

Acknowledgements vii

Publications Included in This Work ix

Contributions to Publications xi

1 Introduction 1
1.1 Outline of the Thesis . . . 5

2 An Introduction to X-ray Scattering and Molecular Dynamics 7
2.1 Introduction . . . 7
2.2 Coherent X-ray Scattering . . . 7
2.2.1 Scattering from an Electron . . . 7
2.2.2 Scattering from an Atom . . . 8
2.2.3 The Debye Equation - The Orientational Average . . . 9
Molecular Structure . . . 10
Small and Large-Angle Limits . . . 10
Liquid Scattering . . . 11
2.3 Incoherent X-ray Scattering . . . 11
2.4 Molecular Dynamics . . . 12
2.4.1 DFT Calculation Methods . . . 12
2.4.2 Comparison with Experimental Results . . . 13
2.5 Time-Resolved X-ray Scattering . . . 14
2.6 Summary . . . 15

3 Data Reduction from X-ray Free-Electron Laser Facilities 17
3.1 Free-Electron Lasers - A Revolution in X-ray Science . . . 17
3.2 A Typical Experimental Setup for Time-Resolved X-ray Scattering . . . 19
3.3 Data Reduction - How to Handle the Data? . . . 20
3.3.1 Sorting, Masking and Dark Image Substraction . . . 20
3.3.2 Non-Linear SVD Corrections . . . 22
3.3.3 Scaling Corrections . . . 22
3.3.4 Difference Images and Time Binning . . . 23
3.3.5 S_0 and S_2 Separation . . . 23
3.4 Model Framework and Uncertainties . . . 24
3.4.1 Outlook: Correlation Maps . . . 26
3.5 Summary . . . 27

4 Potential Energy Landscapes in Transition Metal Complexes 29
4.1 Introduction . . . 29
4.2 The PtPOP XFEL Analysis . . . 31
4.2.1 Pre-Analysis . . . 31

4.2.2 QM/MM BOMD Simulations . . . 33
4.2.3 The Structural Model . . . 34
The Solvent . . . 34
The Solute . . . 35
The Cage . . . 36
4.2.4 Data Analysis . . . 37
Scaling to a Unit Liquid Cell . . . 37
The Excitation Fraction . . . 37
Fitting the Model to Data . . . 38
Best-Fit Parameters . . . 38
4.2.5 Discussion . . . 42
4.3 The AgPtPOP XFEL Analysis . . . 43
4.3.1 Structural Optimization of the Ground/Excited State . . . 43
4.3.2 Pt-Pt-Ag Bond Dynamics . . . 45
4.3.3 Discussion . . . 46
4.4 Summary . . . 48

5 The Solvation Response to a Photo-Induced Solute Charge Change 49
5.1 Introduction . . . 49
5.2 Classical MD Simulations . . . 51
5.3 Experimental Results . . . 52
5.3.1 L1-Edge Absorption Spectra . . . 52
5.3.2 X-ray Scattering Experiments . . . 52
5.3.3 Kinetics . . . 54
5.4 Discussion . . . 57
5.5 Outlook - The Hydrated Electron . . . 58
5.6 Summary . . . 59

6 Revealing Structural Information with Cross Correlation Analysis 61
6.1 Introduction . . . 61
6.2 Theory . . . 62
6.3 Simulations: Scattering from a Solution of Molecules . . . 64
6.4 X-ray Cross-Correlation Analysis . . . 67
6.5 Analysis of PtPOP XFEL Data . . . 70
6.5.1 The CCF Fourier Components . . . 71
6.5.2 The "Linear Molecule" Model . . . 72
6.5.3 Time Dynamics . . . 73
6.5.4 Correlated Parameters . . . 75
6.5.5 The Random Phasor Sum vs. Internal Contributions . . . 77
6.5.6 Investigating the Internal Contributions . . . 79
6.6 Discussion and Outlook . . . 80
6.7 Summary . . . 83

7 Conclusions 85
7.1 Outlook . . . 86

Paper I **93**

Paper II **114**

Paper III **146**

Paper IV **163**

Proposal I **185**

Chapter 1

Introduction

The field of photochemistry deals with studies of chemical reactions caused by absorption of photons. These reaction paths are processes of transformations from one chemical substance to another by accessing high-energy intermediates that are otherwise inaccessible by thermal reactions. Photochemistry is of great importance in nature and can be seen in e.g. photosynthesis, vision and the formation of vitamin D [1]. A detailed understanding of these reactions is not only interesting to understand these chemical reactions but the knowledge can be directly applied in e.g. the conversion of sun light to energy in the solar cell industry. This industry shows a lot of potential as a green energy source to replace fossil fuels especially if they can be designed with a high efficiency at a lower cost. One of the main problems in the research of photochemical reactions is to understand the intermediate steps that are hard to probe due to their short lifetimes often at a sub-picosecond timescale. The dream is to develop "molecular movies" of the structure and chemical properties *during* ($\rightarrow$) the photochemical reaction and not only to investigate the reactions *before* (A) and *after* (B) the absorption of photons and making qualified guesses of what happens in the *during*-steps ($\rightarrow$):

$$A + Photon \rightarrow B \tag{1.1}$$

This thesis will focus on how to directly investigate time-resolved structural dynamics and couple them to electronic properties to understand the *during*-steps ($\rightarrow$) of the reactions, by using advanced X-ray techniques to create "molecular movies".

The idea of producing moving pictures or movies to directly probe the dynamics of physical processes has long been a fascinating field of research. The field of time-resolved studies of structural dynamics have developed immensely during the last 150 years, and is widely believed to have started with a simple question about horses in 1872: "will all four feet of a horse be off the ground at the same time while trotting and during gallop?". Leland Stanford, the governor of California and later founder of Stanford University, entered the debate of this popular question and decided to have it proven scientifically by hiring Eadweard Muybridge. He planned a famous experimental setup known as "Sallie Gardner at a Gallop"/"Horse in Motion" (Figure 1.1), published in e.g. *Scientific American* [2], at what is now the campus of Stanford University. Muybridge placed 24 glass-plate cameras equally spaced along the edge of the track and used thread across the track to trigger each of the cameras as the horse passed. This created 24 snapshots of the running horse around 0.04 seconds apart from which the question could be answered. The horse did indeed have all four feet off ground at the same time while its legs were collected beneath its body and not extended to the front and back as imagined by most artists at that time. These images could then be copied to a circular disk and viewed in a machine by

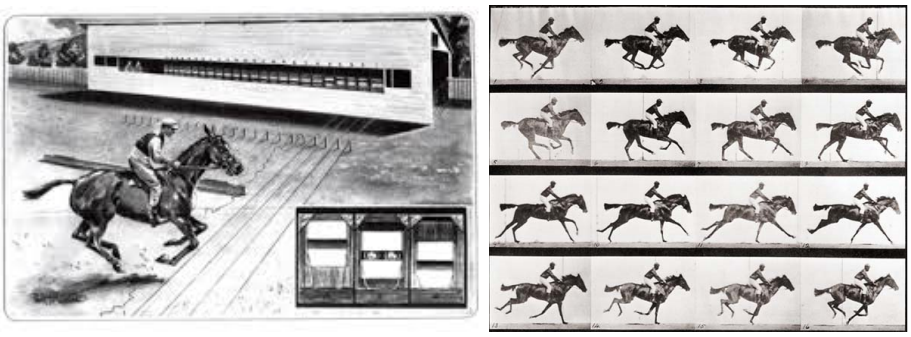

FIGURE 1.1: **Left:** Artist's impression of Muybridge's multi-camera arrangement (Illustrated London News, 18 July 1931). **Right:** The Horse in Motion, Eadweard Muybridge (1878).

rotating the disk to create a movie.

Nowadays the scientific community still ask similar questions about physical movements that cannot be seen by the naked eyes, but instead of asking "will all four feet of a horse be off ground at the same time?" a question might instead be "does the Pt-Pt bond of the PtPOP molecule contract upon absorption of light?". To answer such questions and create "molecular movies" much smaller dimensions have to be investigated at an even faster time scale.

The speed of light of $c = 10^8$ m/s gives an unique possibility to measure ultrafast photochemical reactions in a pump-probe scheme. Imagine an experiment with a photochemical reaction started by a short pulse of light (pump) and measured by another pulse of light (probe). The time delay of the second probe pulse can then be varied simply by moving mirrors and changing the length of the travelling path of the probe light pulse. This means that e.g. a change of one millimetre will corresponds to a controlled time delay of 10^{-11} s which can be used to create images divided by very small time intervals. This technique is called a pump-probe scheme and was pioneered by Ahmed Zewail who was awarded the Nobel prize in 1999 [3]. It is in principle very similar to the "Horse in Motion" example with the breaking of the threads (pump) to initiate cameras (probe) at certain time delays to create a sequence of snapshots as in a movie.

The possibility of following a "movie" of molecular structural changes is possible by using the ultrashort-pulsed nature of X-rays produced in modern synchrotrons and Free-Electron Laser (XFEL) facilities as probe pulses and the ability of X-rays to directly probe internal atomic structures by analyzing scattering images (Figure 1.2). A similar feature cannot be achieved by e.g. neutrons and electrons diffraction is severely limited to gas phase experiments due to their too strong interaction with matter [4, 5]. X-rays has the ability to probe solution experiments where most chemical reactions take place. In this way, X-rays represent an unique tool which will be further discussed in *Chapter 2*. Ironically, Stanford University is now home to LCLS (not long from the horse track of "Horse in Motion" 150 years ago) which is one of the most advanced XFEL facilities in the world.

During the last decades, remarkable improvements have been obtained in X-ray sources for performing time-resolved solution experiments [6]. The construction of third generation synchrotrons and XFELs has produced sources of extreme brilliance

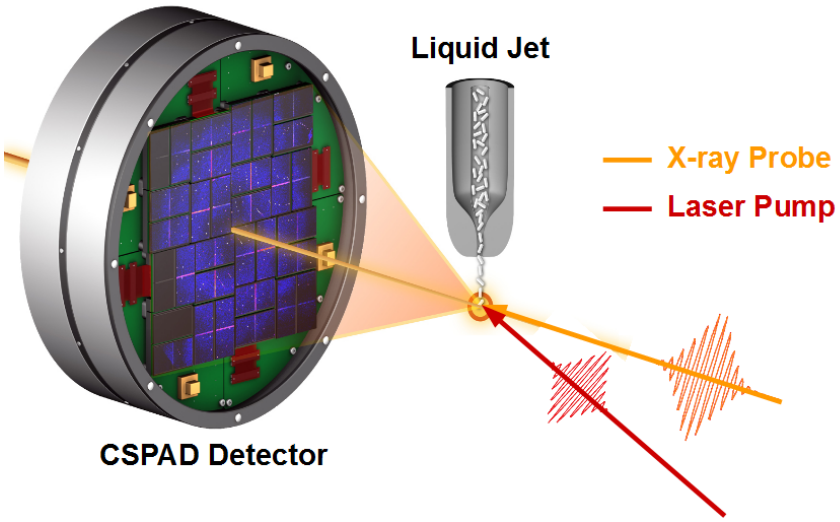

FIGURE 1.2: Setup for a typical time-resolved X-ray scattering experiment on a liquid sample at LCLS. Every X-ray pulse yields a scattering image at a predefined time delay after the excitation by the laser pulse. Adapted from [7].

.

that have greatly expanded the capabilities of studies within structural chemistry and materials science. The development is a continuous progress, a new XFEL (European XFEL, Hamburg) have just opened up for experiments with a time-resolution in the femtosecond regime and LCLS is currently being upgraded. Unfortunately, the data analysis is not so straightforward due to several reasons. First, the X-rays are not an element selective probe and all the changes in structure and shape induced by the laser pump are recorded in the scattering pattern that have to be simulated from specific atomic structures. Secondly, the tera-byte sized data of 2D detector images has to be sorted, cleaned, normalized and analyzed before they can be compared to multivariable simulations of the structural dynamics. *Chapter 3* is dedicated to introducing a systematic approach to deal with those challenges.

The focus of this thesis will be the analysis of XFEL experiments with a sub-picosecond time resolution. The X-ray scattering signal from an XFEL solution experiment can be divided into individual contributions from the solute, the solvent and the solvent-solute interactions (cage). This thesis will mainly focus on the analysis of two XFEL experiments; System I will be an example where focus is on the *solute* contribution and the internal structural changes of the molecule; System II will be an example of an experiment where the main focus will be on the *cage* contribution and solvation effects.

System I (*Chapter 4*) consist of solutions of PtPOP/AgPtPOP/TlPtPOP (PtPOP = $Pt_2(H_2P_2O_5)_4]^{4-}$) which belong to a class of very well studied transition-metal complexes [8, 9, 10, 11] with the metal atoms connected by bridging ligands. These compounds are generally characterized by large structural changes upon photo-excitation due to photo-induced bond formation between the metal atoms. Many of these transition metal complexes show great catalytic promises in e.g. hydrogen generation. They also have important roles in solar energy conversion due to their capability of transferring electrons and energy through the metal-to-ligand charge transfer (MLCT) states, but

their ability to absorb light and efficiently transfer it is still far from optimal and lacks a better understanding of the fundamental photochemistry [12, 13, 14, 15]. Therefore, the ground and photo-excited states of transition-metal complexes are of great interest from a photochemical point of view with photo conversion of solar energy being of particular interest. With the arrival of X-ray sources with pulse lengths in the femtosecond regime, the structural dynamics of the photo excited molecules can be measured, as they traverse the potential landscape of the electronic *excited states* [16]. This chapter presents an additional method based on off-resonance optical excitations of electrons to directly measure structural *ground state* "hole" dynamics of PtPOP molecules (**Paper II-III**) which gives valuable information of the *ground state* potential energy landscape. The change in the potential energy surfaces and the structural dynamics by the asymmetric end-on coordination of silver in AgPtPOP molecules will also be investigated.

Transition metal complexes based on earth-abundant iron, instead of rare-earth metals, are of great interest in photocatalytic reaction due to the much cheaper cost of a large scale production. However, one of the main problems is to control the lifetime of the important metal-to-ligand charge transfer (MLCT) state. It typically has a much shorter lifetime in iron complexes and limits the applicability for collection of solar energy. It is therefore of great importance to optimize the lifetime of the MLCT states by e.g. varying the solvent or the ligand groups. Additional experiments at XFEL have investigated how the bulkiness of the ligand groups influence the structural dynamics and MLCT state lifetimes of Iron-Carbene systems and **Paper IV** focuses on the direct control of MLCT state relaxation pathways and lifetimes in $[Fe(bpy)(CN)_4]^{2-}$ by changing the solvent properties. The paper aims to measure the electronic and geometric structure dynamics for iron-centered complexes as they traverse potential landscapes that change dramatically as a function of the ligand groups and the solvent environment. This will have a profound impact on our ability to design photo-sensitizers based on iron.

System II (*Chapter 5*) consist of aqueous Iodine and the goal is to investigate the $I^- \rightarrow I^0$ photoreaction in water (photo-induced detachment of an electron). The solvation shell changes during such a reaction represents a simple model system of solvent reorganizing upon a solute charge change in a chemical reaction. Further, it is an excellent example of the possibilities of measuring solvent shell changes in XFEL experiments. Simultaneous measurements of the X-ray absorption allow for a direct comparison of structural dynamics and electronic changes following the photoreaction and makes it possible to measure an increased electron back donation to I^0 as a result of the structural changes in the solvent shell. Solvation dynamics, the process of solvent shell reorganization upon electronic structure changes in a solute, is one of the most studied phenomena in chemical physics [17, 18, 19], due to its importance in liquid phase chemistry and in biology, where the solvent shell has an active role in assisting, hindering, or triggering chemical reactions.

Tools to study disordered systems with local structural order, such as molecules or proteins in solution, remain limited. In conventional Small/Wide Angle X-ray Scattering (SAXS/WAXS) experiments the scattering images are azimuthally averaged, which reduces the information content available for a structural analysis. A general problem within the structural analysis framework of scattering experiments from molecules in solution is to deduce a large number of parameters (three-dimensional structural model of the molecules and their interactions with the surrounding solvent

molecules) just from a single azimuthally averaged one-dimensional scattering curve. Moreover, the key structural parameters deduced from conventional analysis are known to be strongly correlated [14]. One way to enhance the structural information content is by aligning the molecules and using the anisotropic information from the full angular space of the 2D detector images to better benchmark the structural models. The method of angular intensity correlations in X-ray diffraction goes back to a pioneering work of Kam [20]. He showed that correlated X-ray scattering from randomly oriented particles could, in principle, reveal information about the internal structure of individual particle not obtainable from azimuthally integrated scattering measurements. This is of great interest in biology and chemistry to determine molecular structures with a high precision.

The aim of *Chapter 6* is to develop X-ray Cross-Corelation Analysis (XCCA) as a tool in XFEL scattering studies to obtain additional structural information from a sample, going beyond traditional analysis of the azimuthally averaged intensities, where mainly average pair distribution functions can be accessed. The angular integration effectively throws away information in the diffraction patterns that can help solving structures of molecules in solution to an even higher resolution, reveal otherwise hidden n-fold symmetries and potentially lead to a direct reconstruction of the molecular structure, directly from correlation functions determined by XCCA [21, 22]. The ultrabright femtosecond X-ray pulses from XFELs provide an opportunity to measure scattering signals in short exposure time compared to rotational relaxation times [21, 23, 24], meaning that the instantaneous positions and orientations of the molecules can be measured. In this case, XCCA offers a method for investigations of the anisotropic scattering from solution systems with a photo-aligned sub-population of molecules, that can be applied to various kinds of molecules, proteins and particles. While XCCA methods are normally working best in very dilute systems [25, 26] our studies (**Paper I**) of the solvated PtPOP transition metal complexes demonstrates that similar methods may let us significantly enhance the information content of scattering images, even in denser systems, such as solvated molecules in case of a predominant orientation of the molecules. The development of this technique is the foundation for two recent beam time proposals at European XFEL (**Proposal I**) and LCLS.

To summarize this section, there were four main goals; i) Describe how scattering data from modern XFEL facilities can be analyzed to generate new knowledge of photochemical reactions; ii) Investigate the structural dynamics on the ground and excited state potential surfaces of transition metal complexes (PtPOP/AgPtPOP); iii) Investigate the structural and electronic dynamics in the aqueous $I^- \rightarrow I^0$ photoreaction as a simple model system of the solvation response to a solute charge change; iv) To further advance the field of XFEL solution experiments by introducing and developing the XCCA method.

1.1 Outline of the Thesis

Chapter 2 *An Introduction to X-ray Scattering and Molecular Dynamics* will provide the necessary theoretical background in X-ray Science and Molecular Dynamics in order to understand the experiments described in the thesis. The section will focus on X-ray scattering and the Debye equation which provides a direct link between X-ray scattering data from solution experiments and the molecular structural dynamics

that can be estimated from quantum simulations.

Chapter 3 *Data Reduction from X-ray Free-Electron Laser Facilities* introduces X-ray Free Electron Laser (XFEL) facilities and their ability to perform time-resolved high-brilliance X-ray experiments with a femtosecond time-resolution. The chapter continues to give an overview of the relevant steps in the acquisition, sorting, correction, binning and azimuthal averaging of the terabyte-sized datasets of 2D scattering patterns. The reduced 1D difference scattering curves can then be compared to simulated curves from structural dynamic models.

Chapter 4 *Potential Energy Landscapes in Transition Metal Complexes* presents a method based on high-level quantum simulations and femtosecond Time-Resolved X-ray Scattering to directly measure the structural ground and photo-excited state dynamics on the potential energy surfaces of aqueous PtPOP/AgPtPOP transition metal complexes. Ground and photo-excited states of transition metal complexes are of interest in studies of e.g. photo conversion of solar energy.

Chapter 5 *The Solvation Response to a Photo-Induced Solute Charge Change* describes the analysis of the Time-Resolved X-ray Scattering/Absorption data following the aqueous $I^- \rightarrow I^0$ photoreaction and a direct comparison of the experimental results to classical MD simulations. The solvation shell changes represents a simple case of solvent reorganizing upon a solute charge change in a chemical reaction and can be used as a model system for a variety of chemical and biological systems. The structural dynamics deduced from the scattering data was complemented by electronic charge information from the absorption data, to verify an increased electron back donation to I^0 as a result of the structural changes of the solvent shell.

Chapter 6 *Revealing Structural Information with Cross Correlation Analysis* shows how X-ray Cross Correlation Analysis (XCCA) can be directly used on X-ray scattering data obtained at X-ray Free Electron Laser (XFEL) facilities. This method was used on the data from the PtPOP experiment to reveal additional structural information and time constants related to the rotational dephasing of the molecules. The chapter seeks to establish this powerful tool in the field of XFEL solution experiments in order to use the full angular space of the 2D detectors instead of azimuthal averaging.

Chapter 7 *Conclusions* shortly draws main conclusions from the thesis and provides a brief outlook of the field.

Chapter 2

An Introduction to X-ray Scattering and Molecular Dynamics

This chapter provides a description of the X-ray scattering theory necessary to understand and interpret the results acquired in a Time-Resolved X-ray Scattering (TRXS) experiment. Particular focus will be on the Debye equation, its importance for experiments with scattering from dissolved species and how it can be directly linked to measuring molecular structure dynamics.

2.1 Introduction

X-rays are electromagnetic waves with a wavelength of the order of one Ångstrøm (Å$= 10^{-10}$ m), that are scattered by electrons. Especially important for the X-ray scattering experiments are X-ray beams with high intensity and collimation, which can be produced at synchrotron radiation facilities or X-ray Free Electron Laser (XFEL) facilities. Since the wavelength is close to interatomic distances, X-rays can be used to investigate the structure of crystals or molecules. This can be done by analyzing the diffraction pattern, which is a result of destructive and constructive interference of the scattered waves.

The periodicity of a crystal gives rise to constructive interference of all scattered waves in specific directions, which are called Bragg reflections and are given by Bragg's law and the orientation of the crystal planes. It turns out, that the measured sample does not have to be a crystal to see sharp characteristic diffractions, as long as there are some characteristic distances in the sample. If there is no special direction in the sample, e.g. it is dissolved or in a gas phase, the Bragg peaks will be broadened to rings. This will be shown in the Debye Equation, which predicts the scattering pattern from disordered samples as a function of all the interatomic distances. The analysis of these scattering rings makes it possible to get snapshots of molecular structures which can be directly compared to structural calculations and simulations. Equation (2.1-8) in this chapter are taken from [27].

2.2 Coherent X-ray Scattering

2.2.1 Scattering from an Electron

As known from optics, a simple description of an X-ray beam is as a linearly polarized electromagnetic plane wave. This can be represented by a wave vector along the direction of propagation $\hat{\boldsymbol{n}}$, with a length dependent on the wavelength λ of the

X-rays:

$$\boldsymbol{k} = \hat{\boldsymbol{n}} \cdot \frac{2\pi}{\lambda} \tag{2.1}$$

A scattering event of a photon on an electron can happen in two different ways; an elastic or an inelastic process. In this section, we will consider the coherent elastic process called Thomson scattering where the photon is scattered without change of phase or kinetic energy. It is the main process by which structural investigations can be made due to interference between coherent scattered waves (Incoherent scattering is covered in *Section 2.3*). The classical description of an scattering event is that an electron in the electric field of a propagating X-ray beam will be forced to vibrate in the field and thus acts as a radiation source of a new propagating spherical electric field with the same phase (and thus frequency) as the incident radiation field. The scattering from an ensemble of electron can then be visualized as expanding spherical waves from all the electrons in the pathway of the X-rays, oscillating in phase with the electrons they are scattered from. These waves will interfere constructively and destructively with each other on their way to a detector and thus carry information about the spatial distribution density of the electrons in the sample.

In Thomson scattering the modulus squared of the radiated electric field $|E_{rad}|^2$ at a distance R from a single electron source, and at an angle Θ with respect to the direction of propagation of the incident beam is related to the incident radiation field E_0 by:

$$|E_{rad}|^2 = \frac{r_0^2}{R^2}|E_0|^2 P(\Theta) \tag{2.2}$$

Where the squared Thomson scattering length r_0^2 defines the scattering strength from a single electron (defininf the proportion of electrons getting scattered) and $P(\Theta)$ is a polarization factor which can be derived from the dot product of the polarization of the electric fields of the incoming and radiated beams respectively. The equation can be derived from Maxwells equation and the detailts can be found in standard X-ray scattering textbooks [27].

For e.g. horizontally polarized light at a fixed distance R, it can be shown that the scattered intensity from a single electron is angle-dependent and given by the product of a polarization factor $P(\Theta)$ and the squared Thomson scattering length r_0^2. The polarization factor is 1 for scattering in the vertical plane perpendicular to the polarization, and equal to $\cos^2(\Theta)$ for scattering in the horizontal plane where Θ is the scattering angle. The polarization is compensated for in the data reduction as discussed in *Chapter 3*.

2.2.2 Scattering from an Atom

Let us start by considering the scattering by a monochromatic X-ray beam (with a wave vector $\boldsymbol{k}$) from just two electrons separated by a distance $\boldsymbol{r}$. The far-field assumption is used where it is assumed that the detector is sufficiently far away for the scattered waves to be regarded as plane waves. As the two electrons are separated in space, the incident X-ray beam hits the two electrons with a phase difference of $\phi_{in} = \boldsymbol{k} \cdot \boldsymbol{r}$. On the other hand, the scattered X-rays ($\boldsymbol{k'}$) from the electrons will have a phase difference of $\phi_{out} = \boldsymbol{k'} \cdot \boldsymbol{r}$ when they hit the detector. The two phase differences will be in the opposite directions as illustrated in figure 2.1, and thus the total resulting phase difference is $\phi = (\boldsymbol{k} - \boldsymbol{k'}) \cdot \boldsymbol{r} = \boldsymbol{Q} \cdot \boldsymbol{r}$. This defines the $\boldsymbol{Q}$-vector. The electrons in an atom can be approximated as a cloud of charge

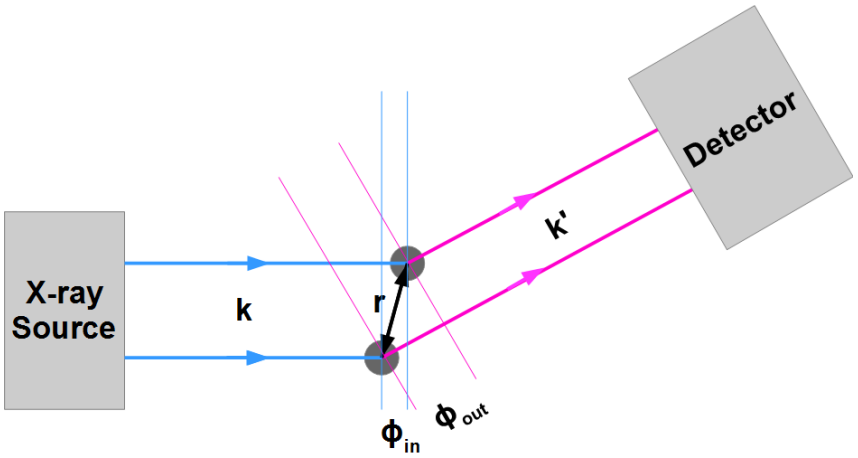

FIGURE 2.1: Illustration of the measured coherent X-ray scattering from two separated electrons, as discussed in *Section 2.2.2*.

surrounding the centre with a radius-dependent density $\rho(\boldsymbol{r})$. For this reason, the scattering amplitude from an atom can be calculated by weighting with the phase differences compared to waves scattered from the origin of the atom, as:

$$f(\boldsymbol{Q}) = \int \rho(\boldsymbol{r}) e^{i\boldsymbol{Q}\cdot\boldsymbol{r}} d\boldsymbol{r} \tag{2.3}$$

This is called the atomic form factor and the total scattering intensity is given by $r_0^2|f(\boldsymbol{Q})|^2$, where r_0 is the Thomson scattering length of a single free electron as discussed in the previous section. For elastic scattering where the length of the wave vector is conserved, it can be shown directly from the definition that:

$$|\boldsymbol{Q}| = \frac{4\pi}{\lambda}\sin(\theta) \tag{2.4}$$

Where 2θ is the scattering angle.

2.2.3 The Debye Equation - The Orientational Average

From the previous section, the scattering from a single atom is known. By following the same procedure, an equation for the scattering intensity from a collection of N atoms (denoted $n = 1, 2, 3, ...N$) in a molecule can be derived by simply keeping track of the phase differences and the atomic form factors:

$$I(\boldsymbol{Q}) = r_0^2 \left| \sum_{n=1}^{N} f_n(\boldsymbol{Q}) e^{i\boldsymbol{Q}\cdot\boldsymbol{r_n}} \right|^2 \tag{2.5}$$

By the same procedure the scattering from a ensemble of molecules can be calculated by keeping track of the individual orientations of the molecules in the ensemble. In the special case where the molecules e.g. are in a gas phase or dissolved in a liquid where there are no preferred orientations and each molecule behave as individual scattering objects (separated by longer distance than the X-ray coherence length), then an orientational average can be made. This greatly simplifies the calculations of the scattering from many molecules, and was first derived in 1915 by Debye [28].

He found that:

$$\frac{\langle I(\boldsymbol{Q})\rangle_{orient.av.}}{r_0^2} = \langle \left| \sum_n f_n e^{i\boldsymbol{Q}\cdot\boldsymbol{r_n}} \right|^2 \rangle_{orient.av.} = \sum_n |f_n|^2 + \sum_{n\neq m} f_n f_m \frac{\sin(Qr_{nm})}{Qr_{nm}} \quad (2.6)$$

Where Q is the length of the scattering vector and r_{nm} denotes the distance between atom n and m. This is a very central equation in this thesis as it provides a direct link between the scattering images from an X-ray experiment and the molecular structures of the individual molecules in a solution. Some space will thus be used to discuss it in this section.

Molecular Structure

By looking at the Debye equation, two terms can be clearly identified. The first term is solely dependent on the atomic composition of the sample through the atomic form factors. The second term is dependent on the molecular structure through the interatomic couplings and the distance dependent $\frac{\sin(Qr_{nm})}{Qr_{nm}}$ term. This structural term will appear as a sum of oscillating modulations around the "equilibrium curve", given by the first composition dependent term in equation (2.6), and the modulations will decrease with larger scattering angles. If no recombination or dissociation is induced in the experiment the atomic composition does not change, and structural changes will appear only as a shift of these oscillations.

The Debye equation gives a simple way of accurately calculating the scattering pattern from many different systems, only using their distribution of interatomic distances and the atomic form factors. This greatly simplifies the interpretation of obtained scattering data. As many systems can be dissolved in water or other solvents, which allows for using the orientational averaging, it opens up for the study of a wealth of processes in disordered environments with high chemical, physical, biological and industrial relevance. The capability of calculating X-ray scattering profiles from interatomic distances is what provides the key to the determination of molecular or particle structures. However, the orientational averaging comes at a price compared to ordered crystals as the sharp Bragg peaks characteristic of a ordered crystal lattice are lost. They become broadened to rings, and this loss of order implies that the observed scattering signals in a liquid state experiment only provides information about the orientational averaged changes in the sample. Another problem is the often small solute-to-solvent ratio and contributions from the solvent and its interaction with the solute, which often complicates the analysis. In addition, the Debye equation does not distinguish between bonded and non-bonded atoms due to the assumption that only the scattering contribution from core-electrons are considered and not the valence bonded electrons.

Small and Large-Angle Limits

Another important feature of the coherent scattering intensity can be seen directly from equation (2.3) and (2.6). For the large-angle limit ($Q \to \infty$) you have a random phase situation in the integral in equation (2.3), which means it averages to zero, thus all the atomic form factors are zero. In the small-angle limit ($Q = 0$) all the phases in equation (2.3) are instead zero, why the atomic form factors just gives the number of electrons Z in the atoms. By looking at equation (2.5) in the ($Q = 0$) limit and using that the atomic form factors are given by Z, it can be seen that the intensity

of the elastically scattered X-rays goes towards a value of Z_{tot}^2, where Z_{tot} is the total number of electrons in the system. These two results can be summarized, as:

$$I_{coh}(Q) \rightarrow Z_{tot}^2 \;\; for \;\; Q \rightarrow 0 \quad and \quad I_{coh}(Q) \rightarrow 0 \;\; for \;\; Q \rightarrow \infty \tag{2.7}$$

In the small-angle region, recombination or dissociative reactions thus significantly affect the scattering intensity.

Liquid Scattering

In an ordered crystal, atoms sit on a regular array called a lattice meaning that the location of all the atoms relative to the origo atom can be located exactly (neglecting lattice vibrations). In non-crystalline materials, such as liquids, it is not the case as there is a degree of randomness in the positions. Any structural order, can only be described in a statistical sense that can be done with the introduction of the radial distribution function $g(r)$. It is constructed by first choosing one atom at the origin and then finding the average numbers of atoms in a shell of radius r and thickness dr around this atom. For crystals this function will have very sharp peaks. For a liquid it will also have peaks, although broadened and less sharp. This arises from the fact that mobile atoms or molecules cannot occupy the same volume in space, basically as a consequence of quantum mechanics. This means, that even in liquids there are some characteristics lengths. As we fulfil the condition of orientational averaging, the Debye equation can be calculated directly from the radial distribution function. These distribution functions can be measured or calculated to predict the liquid scattering [27, 29]. As will be illustrated in *Chapter 4* and *Chapter 5* it is also possible to simulate solvation (cage) effects in a solution of molecules through simulations and calculations of the radial distribution function $g(r)$.

2.3 Incoherent X-ray Scattering

The scattering from an electron can also be inelastic, the so-called Compton scattering, in which the scattering can be treated like a relativistic collision between the photon and the electron. The incoming photon collides with a stationary electron, transferring energy, and leaves at an angle to the incoming path with less momentum. The most important difference from the Thomson scattering is that it is incoherent, meaning no interference between the photons scattered from different parts of the sample. It can be shown that the incoherent scattering from an atom with atomic number Z, follows [27]:

$$I_{Incoh}(Q) \rightarrow 0 \;\; for \;\; Q \rightarrow 0 \quad and \quad I_{Incoh}(Q) \rightarrow Z \;\; for \;\; Q \rightarrow \infty \tag{2.8}$$

The incoherent scattering is not dependent on structural changes in the sample but only on the atomic composition. The structural analytical consequence of this is that the scattering signal at lower scattering angles mainly provides information on the structure through the coherent scattering, while the high angle scattering part of the signal mainly provides information on the atomic composition of the sample. As the coherent scattering signal is trending towards zero at large scattering angles (*Section 2.2.3*), this high-Q part of the signal can be used for normalization of the obtained data as the atomic composition is typically not changing during these kinds of experiments. This normalization procedure will later be used, for analyzing the obtained experimental data.

2.4 Molecular Dynamics

X-ray scattering experiments at X-ray Free Electron Laser (XFEL) facilities gives the possibility to measure photo-excited structural changes with a femtosecond time-resolution as discussed in *Chapter 3*. The time-resolved scattering signal is directly related to the structure of the molecules through the Debye equation, as discussed in *Section 2.2.3*:

$$I(Q) \propto \sum_n |f_n|^2 + \sum_{n \neq m} f_n f_m \frac{\sin(Q r_{nm})}{Q r_{nm}} \tag{2.9}$$

To analyze the obtained scattering signals from an XFEL experiment, quantum mechanical calculations of the molecular structures are often needed to compare to the experimental data to identify time-dependent structural behavior. Simulating such scattering signals is an essential part of this thesis. This section tries to introduce the underlying Density-Functional Theory (DFT) calculation methods needed to predict molecular structures.

A simple way of simulating time-dependent trajectories of the atoms in a system is to make a MD (Molecular Dynamics) simulation [30]. It is simply done by defining time steps and calculating the force on all the atoms for every time step from which their change in velocity can be calculated through Newton's equation of motion. The forces between the particles and their potential energies are normally calculated using interatomic potentials or molecular mechanics force fields.

2.4.1 DFT Calculation Methods

GPAW has been used for the simulations performed in this thesis. GPAW [31, 32] is a DFT Python code based on the projector-augmented wave (PAW) method [33] and the atomic simulation environment (ASE) [34, 35, 36].

GPAW calculates the electronic structure of systems using a soft valence pseudo-wave function-description while keeping the rapidly varying features of electrons in the core (augmentation) region. In the FD mode the pseudo-wave functions are evaluated directly, by discretizing the Kohn-Sham equations [33] and solving them numerically using the Finite Difference (FD) method [37, 38]. FD is a numerical method where differential equations are solved by approximating them with difference equations (discretization) which also makes the calculations parallelizable. Due to the smoothness of the pseudo-wave function outside the core region the uniform, real-space grids can be surprisingly coarse. The all-electron core states within the core region are described on a much finer, radial grid and are evaluated independently of the neighbouring environment, which means they can be calculated before the actual DFT calculations and saved in a GPAW setup. The two regions are smoothly connected by a PAW transformation [39, 40].

GPAW also has a calculation method called LCAO (Linear Combination of Atomic Orbitals) [33], which speeds up calculation although the accuracy is limited by the chosen basis. In the LCAO mode, a basis set of atomic orbital-like functions is used rather than grid-based wave functions. The grid-based methods are however still used for the density and the potential. A minimal basis set consists of one atomic orbital-like function for each valence state of the atom. Radial functions can be added to improve the basis set and the basis set is called single-zeta (sz), double-zeta (dz) etc., depending on the number of such radial functions per valence state.

Often a basis function corresponding to the lowest unoccupied angular momentum quantum number is added. This is called a polarization function and change the basis set name to e.g. szp and dzp.

The main idea of DFT is that the Hamiltonian is a function of the number of electrons and the potential created by the nuclei in the system, all of which is included in the electron density $\rho(\mathbf{r})$. The energy of the system can then be described as a functional [33]:

$$E[\rho(\mathbf{r})] = \int p(\mathbf{r}) \frac{\partial E[p(\mathbf{r})]}{\partial p(\mathbf{r})} d\mathbf{r} \tag{2.10}$$

Reducing the complexity as a wave function for N electrons contains $4N$ variables (three dimensions and spin) whereas the electron density only depends on $\mathbf{r}$. It has further been proven that the total energy is an unique functional of the electron density and that the variational principle also applies for the energy functionals. This means that if the exact functional is known the complexity of obtaining the energy is greatly reduced [41].

The exact functional ($E[\rho(\mathbf{r})]$) is however not known. Basis sets as e.g. Hartree-Fock are used in the DFT method so the Kohn-Sham orbitals are represented by linear combinations of atomic orbitals [33]. The total DFT energy of a non-interacting system is given as the sum of the kinetic (calculated by solving the one-electron Schrödinger equation) and potential energies:

$$E_{nonint}[\rho(\mathbf{r})] = T_{nonint}[\rho(\mathbf{r})] + \int \rho(\mathbf{r}) V_{ext}(\mathbf{r}) d\mathbf{r} \tag{2.11}$$

To include interactions in the system, the coulomb repulsion and the exchange-correlation term is included in the functional. The BLYP exchange-correlation functional [42] used in this work is partly fitted to experimental molecular data. It is within the Generalized Gradient Approximation (GCA) group where the exchange and correlation energies depend on the electron density and derivatives of it [33].

2.4.2 Comparison with Experimental Results

Unfortunately the calculated structures are not always precise and can normally only be used as a first approximation to the real molecular structures. The calculated structure can then often be optimized by directly comparing the simulated scattering pattern to the experimental results, for different variations of the atomic positions in the simulation. This is essentially a $3N$ multivariable optimization problem (N is the number of atoms in the structure). Often it is faster and easier to simplify the problem by looking at key variables in the system. As an example we can take the PtPOP molecule discussed in *Chapter 4* where the symmetric Pt-Pt bond length is considered the most essential variable, reducing the problem to just one variable in the simplest case. The idea is then to create a set of simulated scattering signals for different Pt-Pt bond lengths and find the best match to the experimental scattering patterns. These best-fit values can further be optimized and compared to to the time-resolved X-ray scattering experiments at different time delays to e.g. identify dynamics and time-dependent oscillations in this bond length.

The set of simulated scattering signals are easily calculated through the Debye equation when the position of all the atoms are known using equation (2.9). There are two

simple ways of estimating such signals: The first one is to take the DFT relaxed structure and varying the bond lengths by hand without relaxing the structure afterwards. The second method is to fix the bond lengths at different values and relax all the other atoms in the structure. None of these methods are completely correct as the structures are expected to be in between a non-relaxed and fully relaxed configuration during a fast vibration with a period on e.g. a femtosecond timescale.

2.5 Time-Resolved X-ray Scattering

In *Chapter 3* it will be described how the generation of pulsed X-rays at an XFEL facility, naturally brings the possibility of doing time-resolved experiments in the same sense as an optical pump and probe experiment. In the experiments in this work, the pulsed X-rays were used as the probe and the pump was a laser pulse. Therefore the precise control of the timing of the laser pulses, gives us the possibility of varying the time difference between the pump and probe, giving us the time resolution as a sequence of snapshots (as in a movie).

These types of scattering experiments are denoted Time-Resolved Wide-Angle X-ray Scattering (TR-WAXS). As the probe gives us structural information about the system, it can be used to make structural movies of e.g. molecular dynamics during a photochemical reaction. These experiments, however, mainly gives result if the desired structural change can be induced by short laser pulses (E-fields) and reliably detected at the experimental setup. In e.g. a solution experiment the laser induced changes must normally be traceable in the azimuthally averaged scattering patterns as discussed in *Section 2.2.3* (exceptions are discussed in *Chapter 6*).

X-ray scattering is a technique, where the measured signal arises from all the atoms within the X-ray beam path. As seen earlier in this chapter, the Debye equation used on a assembly of randomly oriented molecules, will give a very long expression summing terms for every interatomic distance. For a liquid-sheet solution experiment, these interatomic distances can be sorted into three distinct categories of contributions arising from interactions within the solute, within the bulk solvent, and the solute-solvent cross interactions (the solvent cage). The solute-solute cross interactions are neglected by assuming their distances are longer than the X-ray coherence length (dilute limit), giving:

$$S(Q)_{solution} = S(Q)_{solute} + S(Q)_{solvent} + S(Q)_{cage} \tag{2.12}$$

If the solute structure, solvent cage and radial distribution function of the solvent are known, the total scattering intensity can be calculated as the linear combination of these three terms and directly be compared to the experimental data.

Often there is only one solute molecule for every thousands of solvent molecule making it necessary to reduce temporal noise in the experiments. In order to ensure general homogeneity of recording conditions, laser-on ($S_{LaserOn}$ - where the sample have been irradiated by a laser pulse) and laser-off images ($S_{LaserOff}$ - without laser) are collected in an alternating fashion. This ensures that any long-term effects (on a time scale longer than the time difference between the recorded $S_{LaserOn}$ and $S_{LaserOff}$ signals) will be included in both images such as e.g. beam divergence, equipment drift, fluctuations in the liquid sample and slow variations in the XFEL X-ray intensity. These effects can then be removed by subtracting the scattering signal

of the non-excited sample from the scattering signal of the laser-excited sample, obtained only a short time before:

$$\Delta S(Q)_{solution} = S(Q)_{LaserOn} - S(Q)_{LaserOff} \tag{2.13}$$

Any structural changes in the probed volume will then cause a change in the difference scattering pattern. From an analytical point of view, the difference scattering signal can be decomposed into the three terms mentioned in equation (2.12):

$$\Delta S(Q)_{solution} = \Delta S(Q)_{solute} + \Delta S(Q)_{solvent} + \Delta S(Q)_{cage} \tag{2.14}$$

The outline of the data analysis is to calculate difference scattering signals as linear combinations of the three terms arising from hypothesized structural changes within the solute, the bulk solvent and the solvent cage and compare to the obtained data. Here the main interest is typically (but not always) the term addressing the difference signal of the solute, which gives information of the molecular dynamics during e.g. a photochemical reaction.

The change in the solvent scattering signal arises from changes in the three hydrodynamic parameters which are density (ρ), temperature (T) and pressure (P). As demonstrated in the work by Cammarata [44], only two of these parameters are necessary in order to describe the solvent difference signal in the linear regime (small temperature increase/low laser power). This can e.g. be written up as:

$$\Delta S(Q)_{solvent} = \Delta T \frac{\partial S}{\partial T}\bigg|_{\rho} + \Delta \rho \frac{\partial S}{\partial \rho}\bigg|_{T} \tag{2.15}$$

The two components can be estimated from Molecular Dynamics (MD) simulations or measured in separate experiments. The later often shows the best performance as discussed in the work of Kjær et al. [43] and Cammarata et al. [44]. In a pump-probe experiment the absorption of the laser pulse results in a fast release of energy and a rise in solvent temperature, followed by a slower decrease in solvent density (thermal expansion). It can be shown that the thermal expansion for a solvent heated by a Gaussian laser pulse, sets in at times of around $t = L/v$ [45], where L is the radius of the laser spot and v the speed of sound in the solvent which is typically on a nanosecond timescale. For XFEL experiments on the femto- to picosecond timescale the thermal expansion term can normally be neglected:

$$\Delta S(Q)_{solvent} \approx \Delta T \frac{\partial S}{\partial T}\bigg|_{\rho} \tag{2.16}$$

Regarding the cage signal, MD-based fitting of changes in the solute and solvent cage (rearrangements of atoms near the surface) can be done. In e.g. *Chapter 5* the cage term was calculated in a classical MD framework and in *Chapter 4* with a DFT description of the solute and a classical force field description of the solvent.

2.6 Summary

This chapter started out by calculating the coherent scattering signal from two electrons and generalized the procedure to calculating the signal from single atoms, the atomic form factor, by assuming a localized distribution of electrons around the core. This was further generalized to an assembly of atoms. In the specific case of randomly

orientated molecules the scattering signal can be calculated by a simple equation called the Debye equation, by using all the interatomic distances in the system. As many systems can be dissolved in a liquid, with random orientations, it provides a simple approach towards the analysis of structural changes. However, it only gives information about the orientational averaged structural changes in the sample.

Lastly, it was discussed how the difference scattering signal from a Time-Resolved Wide-Angle X-ray Scattering (TR-WAXS) experiment of solution state systems, can be split up into contributions arising from interactions within the solute, within the bulk solvent, and the solute-solvent cross interactions (the solvent cage). These scattering results at different time delays can be directly compared to simulations to give direct information of structural dynamics during e.g. a photochemical reaction.

Chapter 3

Data Reduction from X-ray Free-Electron Laser Facilities

This chapter will introduce the concept behind X-ray Free Electron Laser (XFEL) facilities and the possibility of performing time-resolved femtosecond scattering experiments with a high brilliance and coherence. It continues to give an overview of the relevant steps in the acquisition, sorting, correction and binning of the terabyte-sized datasets of 2D scattering patterns. It it not meant as a complete description of all the steps involved but more as a general guideline to understand the experiments. These reduced data sets can then be compared to structural models in a multivariable framework. All examples in this chapter are from the XPP beamline at the LCLS facility, but can be generalized to similar data at other XFELs. The importance of the S_0 and S_2 separation are discussed in greater detail in **Paper III**.

3.1 Free-Electron Lasers - A Revolution in X-ray Science

The progress in our theoretical understanding and ability to exploit X-rays scientifically have been steady since the discovery of X-rays in 1895 by Wilhelm Röntgen. The main limitation has been the source, but in the 1970s, it was discovered that radiation emitted from charged particles in storage rings designed for high energy nuclear physics could be used as a much better source of X-rays. This culminated with so-called third-generation synchrotron sources with a brilliance of around 10^{12} better than early lab-based sources. Today the progress shows no sign of slowing down with the opening of X-ray Free Electron Laser (XFEL) facilities during the last 10 years, which creates a world of new possibilities for X-ray science.

The peak brilliance of these facilities is several orders of magnitude higher than the typical brilliance of undulator radiation from a third-generation synchrotron. More importantly for the experiments presented in this thesis, the X-rays are pulsed with a typical pulse length on the tens to hundreds of femtoseconds [6], allowing for much better time-resolution than possible at synchrotrons with typically pulses of hundreds of picoseconds. However, these few facilities are much more expensive and harder to get access to than third-generation synchrotrons, as only few experiments can be performed at the same time. Further, the datasets are often on the tens of terabyte level which complicates the data handling.

In a traditional undulator in a synchrotron, the electron bunches in the storage ring are forced to oscillate in such a way, that the radiation from one oscillation is in phase with that from subsequent ones. However the radiation from the individual electrons in a single bunch is still incoherent, because the scattering from the randomly

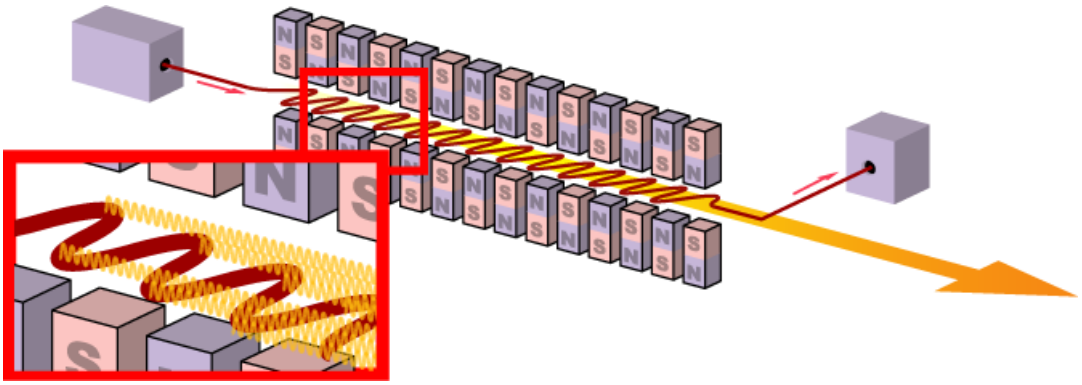

FIGURE 3.1: Schematic representation of an undulator, at the core of a X-ray Free-Electron Laser. From [46].

distributed electrons in a bunch interfers constructively and destructively in time.

In an X-ray Free-Electron Laser, a beam of electron bunches is created and accelerated linearly to almost the speed of light. The beam then passes through a long undulator as illustrated in figure 3.1, where the radiation field increases from zero to its full value at the end. As the radiation field increases as the electrons move along the undulator, the electrons begin to respond to the force from the other electrons in the bunch. The interaction with the radiation is modulated with the wavelength of the X-rays; creating micro bunches where the electrons are spatially confined within a distance shorter than the emitted wavelength (can be considered point like). For this reason the radiation emitted from the micro bunches are in phase, and the fields add together coherently. Due to the large amount of electrons in the micro bunches, the radiation reaches a saturated power of several orders of magnitude higher than that of undulator radiation in synchrotrons with a much shorter wavelength.

This mechanism requires that the radiation field is strong enough to produce the micro bunches, which is only possible for a high electron density. In synchrotrons, the electron density is not sufficiently high, but it can be obtained in linear accelerators which is why X-ray Free-Electron Lasers are linear.

With recently developed electron guns and LINAC bunch compression devices, a bunch length of tens of micrometers can be obtained corresponding to tens of femtoseconds X-ray pulses. However, due to the inherent stochastic nature of FELs the energy and intensity of each pulse vary, which is a complication that will be addressed in this chapter.

The Linac Coherent Light Source (LCLS, California, USA) was the world's first operational hard X-ray Free-Electron Laser, which lased for the first time in 2009 and another one named SACLA (Hyogo Prefecture, Japan) lased for the first time in 2011. Further, a new European X-ray Free Electron Laser (XFEL, Hamburg, Germany) has just started user operation in 2017, and LCLS is currently being upgraded and more XFELs are being built around the world to meet the scientific demands. This will allow for even better XFEL experiments in the future and much higher requirements to the data handling.

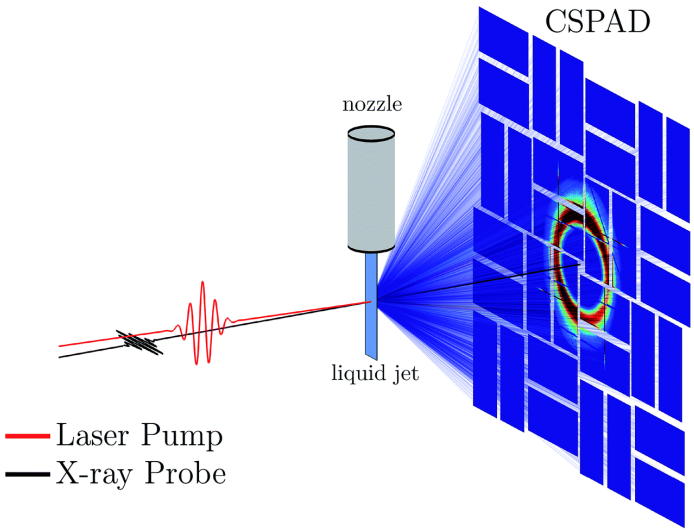

FIGURE 3.2: Setup for a typical time-resolved X-ray scattering experiment on a liquid sample at LCLS. Every X-ray pulse yields a scattering image at a predefined time delay after the excitation by the laser pulse. From [47].

.

3.2 A Typical Experimental Setup for Time-Resolved X-ray Scattering

As discussed in *Chapter 2.5* the experiments are performed in a pump-probe setup (figure 3.2), where the solution is being circulated in a liquid jet system. The idea is to have a sufficient flow of solution to renew the measured volume between each pump-probe event. The renewal is necessary since the energy deposition in the sample will inflict damage in the system.

A fraction of the molecules are pumped to their excited state with an optical pulse at a time t_0, prior to probing the sample with a short X-ray pulse at a later time t^*. Such a pump-probe event yields a single 2D scattering image in the stack at a time delay of $t = t^* - t_0$. At short intervals (e.g. every 10 shots of $t^* > t_0$) the sample will be probed once with the pump-laser turned off to later construct the scattering difference signals. At regular intervals (e.g. every 500 shots) both the laser pulse and X-ray pulse are switched off to measure the background noise in so-called dark images.

The time-resolved scattering signal in these types of experiments is normally weak, so it is crucial for the detector to have a large angular acceptance over which the signal can be radially integrated to increase statistics. Further, it is important to measure over a large Q-range to better compare the obtained data with models. Big 2D detectors with small pixel sizes can achieve this. In principle, time-resolved X-ray scattering experiments could be achieved by fast detectors that could record the time-dependency of the signal directly, without using isolated X-ray pulses. However, big 2D detectors are not available faster than on a microsecond timescale, which is not sufficient for these experiments. Instead, the Pump-Probe technique discussed in this section has been used. Here the detector can simply integrate over many pulses, without any temporal information, always looking at the system state at a definite time-delay after the laser pulse event. For this to work, it is crucial that

each X-ray pulse probe an excited sample as the detector itself cannot distinguish them.

Considerable pulse-to-pulse variations and drifting in experimental parameters are expected due to the stochastic nature of the SASE process in the XFEL sources [48]. Therefore, the relevant experimental parameter has to be saved on a shot-to-shot basis, some of which are:

Parameter	Format	Description
Status	Boolean	Used to classify the shot into On (11), Off (10) and Dark Images (00).
X-ray Intensity	Numerical	Monitored at several diodes along the X-ray beam path.
X-ray Energy	Numerical	Calculated from the energy of the electron beam.
Timing Tool	Numerical	The actual time-delay of the X-ray pulse measured by a timing-tool.
Detector Image	Array	Monitored by e.g. a 2.3M pixel CSPAD detector.
etc.		

The experimental values are saved from each shot in a HDF5 format. Usually the preset time delays are moved in discrete steps with thousands of images at each step producing the large terabyte-sized data sets.

3.3 Data Reduction - How to Handle the Data?

This section gives an overview of the necessary steps in a data reduction process of raw 2D scattering images from an XFEL experiment. First, the images are cleaned, corrected and scaled before they are azimuthally averaged and outliers are removed. The overall process is illustrated in figure 3.3.

3.3.1 Sorting, Masking and Dark Image Substraction

In these kinds of measurements, it is crucial to use a robust method for rejecting outlier images due to various effects such as unstable jet conditions, formed precipitates, rapid fluctuations in air background or variations in the pump/probe pulses. The goal of the outlier rejection is to identify ideal experimental conditions for which the experimental results are stable. The experimental conditions are measured on a shot-to-shot basis from the X-ray diagnostics (intensity, energy, pulse duration etc.) and timing tool at the beamline. The shots can then be sorted into "good" images by defining cutoffs for important parameters to ensure stable experimental conditions and to e.g. ensure that the X-ray intensity from the beam diagnostics are proportional to the total detector intensity.

Several dark images (without laser and X-rays) can be averaged ($\mathbf{I}_{Dark}$) and subtracted from the raw images ($\mathbf{I}_{Raw}$) in order to compensate for the detector background. The next step is to identify and mask out unwanted pixels in the analysis by constructing an image of binary values ($\mathbf{M}$) where zero represents the pixels to be excluded. This can e.g. be pixels at the beam center, along the edge of the detector tiles,

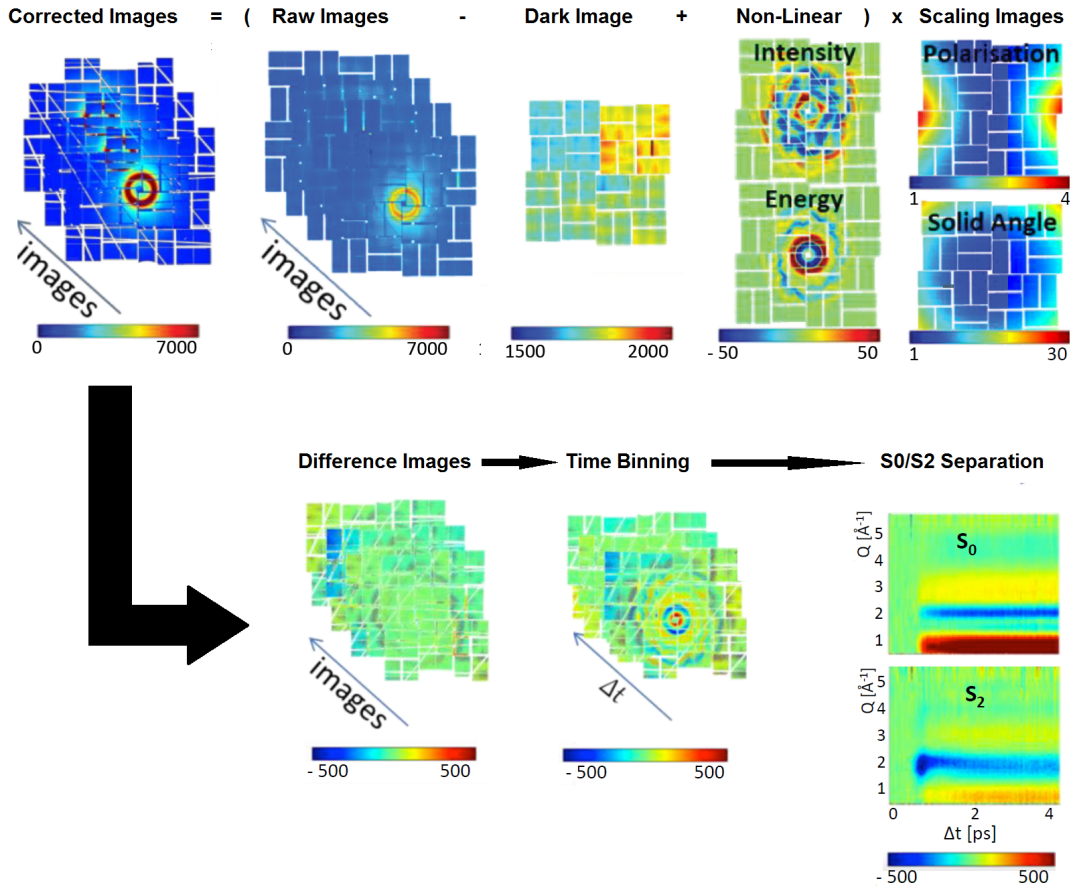

FIGURE 3.3: Schematic illustration of the 2-dimensional data reduction process in an XFEL scattering experiment. First, the background is subtracted and corrections are made for non-linear intensity and energy correlations. Then contributions from e.g. X-ray polarization and solid angle effects are removed. Finally, the difference signals can be constructed from the corrected images and time binned. The data can then be reduced to an isotropic (S_0) and an anisotropic (S_2) part. Figure modified from [47].

shadowed due to the experimental setup or simply broken pixels. These steps can be summarized as:

$$\mathbf{I}_{Mask,Dark} = \mathbf{M} \times (\mathbf{I}_{Raw} - \mathbf{I}_{Dark}) \tag{3.1}$$

3.3.2 Non-Linear SVD Corrections

Due to the SASE nature of the source, the experimental parameters such as X-ray energy and intensity fluctuates on a shot-to-shot basis. The signal strength is proportional to the intensity of the X-rays and the energy of the individual X-ray pulse will influence the translation from the pixels position on the detector to the scattering vector Q. Typically, these effects are of the same order of magnitude as the difference scattering signals. The goal of this section is to establish a method to identify components in the images that correlates with the fluctuations in the X-ray source so they can be corrected for and be removed in the data reduction. The procedure is based on a smaller r-rank SVD analysis on all the off-images (total number of h), represented in a matrix $\mathbf{A}$ with a stack of h row vectors consisting of all l pixel values in the individual off-images. The off-images are chosen in the analysis to ensure that no signal is removed arising from the photo induced dynamics in the sample. A low rank SVD analysis (typically a r=6 rank) is applied partly because it is able to describe all necessary components and partly due to the enormous size of the matrices in a full analysis and computer memory reasons. The SVD analysis can be written as:

$$\mathbf{A} = \mathbf{I}^{SVD}\mathbf{S}\mathbf{V}^{\mathbf{T}} \tag{3.2}$$

Where $\mathbf{I}^{SVD}$ is an orthonormal $l \times r$ matrix defining the SVD components. $\mathbf{S}$ is a $r \times r$ diagonal matrix giving the singular values. $\mathbf{V}^{\mathbf{T}}$ is an $h \times r$ orthonormal transposed matrix carrying the column-to-column variations of $\mathbf{A}$.

The physical interpretation of some of the SVD components (e/i =1,2,3,...r) can be identified by looking at their dependency of X-ray energy $f_e(E)$ and intensity $f_i(I)$ through e.g. a 9th order polynomial fit. These contributions can then be subtracted from all the detector images as an additional term to the correction introduced in the previous section:

$$\mathbf{I}_{Mask,Dark,NonLinear} = \underbrace{\mathbf{M}}_{\text{Mask}} \times (\underbrace{\mathbf{I}_{Raw} - \mathbf{I}_{Dark}}_{\text{Background Substraction}} - \underbrace{[\sum_i f_i(I)\mathbf{I}_i^{SVD} + \sum_e f_e(E)\mathbf{I}_e^{SVD}]}_{\text{Non-Linear}}) \tag{3.3}$$

3.3.3 Scaling Corrections

The images have to be corrected and scaled due to several different geometrical effects in the experiment. This can be included using a term described by a set (f=1,2,3... etc.) of scaling images $\mathbf{S}_f$:

$$\mathbf{I}_{Corrected} = \underbrace{\mathbf{M}}_{\text{Mask}} \times (\underbrace{\mathbf{I}_{Raw} - \mathbf{I}_{Dark}}_{\text{Background Substraction}} - \underbrace{[\sum_i f_i(I)\mathbf{I}_i^{SVD} + \sum_e f_e(E)\mathbf{I}_e^{SVD}]}_{\text{Non-Linear}}) \times \underbrace{\prod_f \mathbf{S}_f}_{\text{Scaling}} \tag{3.4}$$

First, there is the polarization effect that arises because of the (normally) horizontally polarized X-rays created by the horizontal motion of the electrons in the undulator. This gives an angle dependent correction factor, which has been implemented in the data reduction following the work of Hura [49].

Secondly, a correction can be done to correct for the decreasing space angle covered by each pixel with increasing angle of scattering. This is a result of all the pixels having the same size, independent of where they are placed on the 2D detector. This correction based on the work of Boesecke and Diat [50], however, also increases the level of noise in the high-Q signal compared to the low-Q signal.

Additional effects can be considered if necessary. If e.g. the X-rays are not completely absorbed in the detector, the amount of absorption depends on the X-ray path length through the detector and therefore the scattering angle. This can be accounted for using the dimensions of the detector and the absorption coefficient [50]. Further, there is an angle-dependent absorption of the X-rays in the liquid sheet especially if the energy of the X-rays are near an absorption edge, which can also be corrected for by geometrical considerations.

3.3.4 Difference Images and Time Binning

The scattering difference images at time-delays t are constructed by subtracting from each corrected on-image, the mean of the two corrected off-images taken immediately before and after the on-image:

$$\Delta\mathbf{I}(t) = \mathbf{I}^{On}_{Corrected}(t) - \frac{(\mathbf{I}^{Off,After}_{Corrected} + \mathbf{I}^{Off,Before}_{Corrected})}{2} \tag{3.5}$$

Typically, the intensity is 0.1 % of the total scattering images. Therefore, it is important to ensure that the total images are scaled correctly by e.g. self-normalizing them in an interval where the expected difference scattering signal integrates to zero. All the scattering difference patterns are then grouped into specific time bins of δt, using the timing tool values (if available). The binned images can then be used to 1); identify outliers e.g. through an application of the unbiased Chauvenent criterion [51], 2); be averaged to increase counting statistics. Figure 3.4 illustrates how the difference scattering signal becomes more clearly visible as more images are averaged and might even reveal possible anisotropic contributions.

3.3.5 S_0 and S_2 Separation

The details and advantages of separating the difference images into S_0 and S_2 contributions are the focus of **Paper III**, but will not be discussed in greater detail in this thesis. Similar information can also be obtained from an XCCA analysis as discussed in *Chapter 6*.

The main idea is that if a population of excited molecules have a cosine-squared distribution of orientations around the laser polarization axis (as expected for the PtPOP molecules in *Chapter 4* and *Chapter 6*), the difference scattering images can be split up in two contributions:

$$\Delta I(Q, \cos\theta_Q) \propto \Delta S_0(Q) - P_2(\cos\theta_Q)\Delta S_2(Q) \tag{3.6}$$

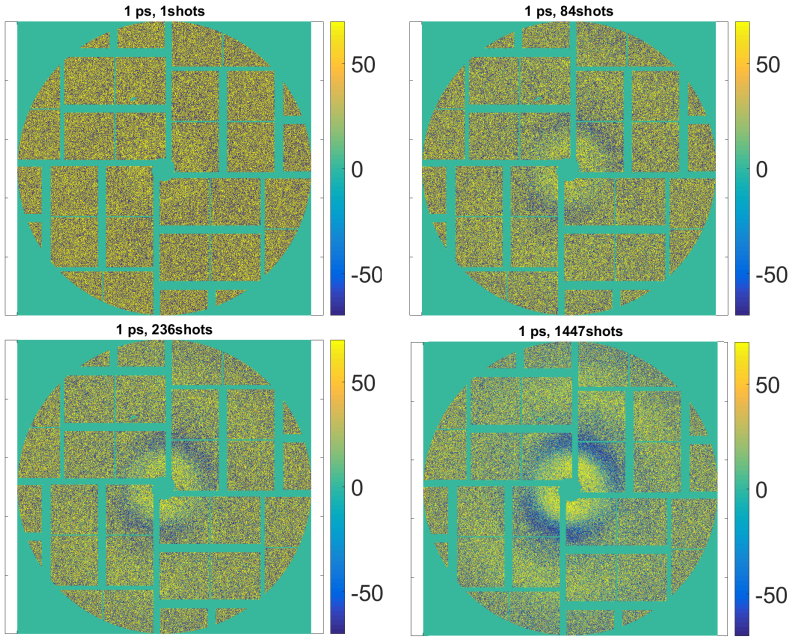

FIGURE 3.4: Illustrates how the difference scattering signal becomes gradually more visible as more difference images are averaged, until the anisotropic part of the signal is clearly visible. The detector images are from the PtPOP experiment discussed in *Chapter 4* and *Chapter 6*.

Where S_0 and S_2 represents the isotropic and anisotropic scattering. P_2 is a second order Legendre polynomial dependent on the angle θ_Q between the laser polarization axis and the scattering vector Q:

$$P_2(\cos\theta_Q) = \frac{1}{2}(\cos^2\theta_Q - 1) \tag{3.7}$$

For each value of Q a linear relationship can be established between ΔI and P_2 using equation (3.6), from which the ΔS_0 and ΔS_2 contributions can be extracted through a straight line fit [52]. For isotropic systems ΔS_0 can found by direct azimuthal averaging of the detector pixels binned in Q-values.

3.4 Model Framework and Uncertainties

The corrected data is now given as time series of one-dimensional difference scattering curves that can be analyzed for each individual time delay. According to the theory discussed in *Chapter 2* these signals include three contributions from; 1) the solvent response; 2) structural changes in the solute molecules; 3) the cross-terms describing the solvent-solute interactions. These data can then be modelled by a linear combination (solute, solvent and cage) of functions of Q:

$$\Delta S(Q,t) = \Delta S(Q,t)_{solute} + \Delta S(Q,t)_{solvent} + \Delta S(Q,t)_{cage} \tag{3.8}$$

As discussed in *Chapter 2* the structural solute part of the difference scattering signal ΔS_{Solute} can be calculated starting from DFT structures of the ground and excited state of the solute and the Debye equation. The structural refinement of the structures (or structural dynamics) can be done by a geometrical optimization of the solute for each time delay and selecting the best-fit structures to the measured scattering. A refinement of each interatomic distance in the solute quickly becomes a very demanding task as the number of necessary free parameters scales with the number of atoms squared. Normally only a few key interatomic distances are picked for the refinement e.g. heavy atoms which contributes the most to the total scattering. The cage signal ΔS_{cage} can be estimated using a similar method or from a combined DFT calculation of solute and cage. The solvent response $\Delta S_{solvent}$ can be described by two parameters, a change in solvent temperature and in density according to literature [43], whereas the density signal typically kicks in on a nanosecond timescale and can be neglected on the femto- to picosecond timescale. The modelling then typically depends on multiple parameters.

As the scattering can be calculated as a linear combination of the three contribution, linear least square fitting is a strong toolbox for the fitting procedures. The linear least square fitting method used in this thesis, is described in literature [53]. It comes down to minimizing the χ^2 value, which is a value indicating how well the model is fitting the data considering the amount of noise in the data. It is calculated from a set of N data points $(Q, \Delta S_{Dat}(Q))$ with a noise given by σ_Q and the results predicted by a model with M parameters $\Delta S_{Mod}(Q)$, as:

$$\chi^2 = \frac{1}{N-M-1} \sum_Q \frac{(\Delta S_{Mod}(Q) - \Delta S_{Data}(Q))^2}{\sigma_Q^2}, \quad L \propto e^{-\chi^2/2} \tag{3.9}$$

This sum of squared difference between the model and the data, yields positive values which should be minimized for finding the best fitting parameters (or L to be maximized). The two fundamental assumptions in this framework are that all data points must be independent and that the *a priori* probability of data is one. The standard deviation, σ_Q, can in principle be estimated from the detector counts on each pixel of the detector. However, in this thesis a more straightforward method introduced by Dent et al. in 1991 [54] will be used. Here the data is fitted with a low-order (3th order) polynomial in a narrow region (20 data points) around each data point - a kind of smoothing - and the noise can then be estimated from the residuals. This is justified as a 3th order polynomial is expected to fit the experimental curve well in a narrow region around each data point (No sharp feature are expected on this Q-range), and the variations from this curve must then arise from the noise.

In principle χ^2 is a weighted measure of the residuals with a significant weight assigned to outliers with respect to the amplitude of the noise/uncertainty. L could loosely be interpreted as the probability that one can reconstruct the data, given the model. However comparing models within a χ^2 framework can be difficult as it may be difficult to asses weather one model is significantly better than the other [14, 55]. It is possible that individual models are equally good, introducing the need for establishing a framework to assess the uncertainties on the optimized parameters.

3.4.1 Outlook: Correlation Maps

This section introduces an alternative method, based on the work of Franke et al. [56], to deal with the problems of model comparison, outlier rejection, estimating uncertainties and separating systematic errors from the true signals. This method is not yet implemented in the analysis.

Using a χ^2 statistical framework for data-model comparison is not without problems, as it requires the explicit estimation of experimental errors for each data point (systematic and/or random). If done incorrectly the statistical comparison might not be valid. Uncertainties are normally estimated assuming Poisson statistics, and especially at XFELs with thousands of collected data sets there is a risk of collecting data with poorly determined or incorrectly propagated errors that will influence the data analysis and model comparison. However, there exist an alternative statistical method based on Correlation Maps (CorMap) that has recently been successfully applied to SAXS measurements [56] (straightforward translation to WAXS data). In this CorMap method, differences between the data curves are found without explicit estimation of the errors, but only by using data point correlations.

The experimental scattering curves can be defined as experimental values I_{exp} for a population of scattering vector values Q_k where $k = 1, 2, 3...n$. If we consider the data points given by $I_{exp}(Q_k)$ they are each collected as a radial integration from a counting detector. They can be regarded as a sample drawn from a normally distributed ensemble with expectation value $I(Q_k)$ and standard variation $\sigma(I(Q_k))$. An entire scattering curve can be considered as a collection of n such data points simultaneously drawn from a n-variate normal distribution. Normally a series of m data curves are collected for each time delay, meaning that the elements in a $n \times n$ variance-covariance matrix can be defined as:

$$\sigma(I_{exp}(Q_k), I_{exp}(Q_l) = \frac{1}{m-1}\sum_{i=1}^{m}(I_{exp}(Q_k)_i - < I_{exp}(Q_k) >)(I_{exp}(Q_l)_i - < I_{exp}(Q_l) >) \tag{3.10}$$

Where:

$$< I_{exp}(Q_k) >= \frac{1}{m}\sum_{i=1}^{m} I_{exp}(Q_k)_i \tag{3.11}$$

And the $n \times n$ correlation map $-1 \leq r_{kl} \leq +1$ is defined by:

$$r_{kl} = \frac{\sigma(I_{exp}(Q_k), I_{exp}(Q_l))}{\sigma(I_{exp}(Q_k))\sigma(I_{exp}(Q_l))} \tag{3.12}$$

If all I_{exp} values are normally distributed and uncorrelated the correlation map will consist of random values. However, e.g. systematic differences will show up as features of contiguous areas of positive or negative correlations in the map. Comparisons of two scattering curves at the same time delay is also possible. Pairwise comparisons make it possible to identify subtle changes between data points e.g. radiation damage, inter-particle or concentration effects. Further, the CorMap method can be used to compare the quality of fits by comparing measured and simulated scattering results, where nonrandom patterns point towards systematic deviations and incorrect model fits.

The probability P of similarity in such comparisons can be quantified by considering

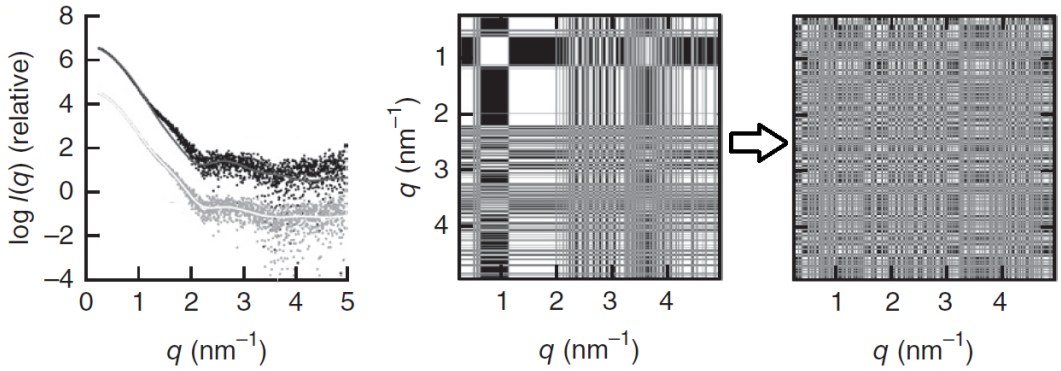

FIGURE 3.5: Example of data model fits using an initial *dark gray* and refined *white* model on the same data set (**left**). Corresponding CorMaps for the initial (**middle**, $P < 10^{-6}$) and refined model (**right**, $P = 0.011$). It can be seen from the CorMaps that the refined model is significantly improved e.g. for q values of 1-2 nm^{-1}. Adopted from [56].

if the largest contiguous area of positive/negative values is likely to be random by e.g. using the Schilling distribution [57] and significance levels [58]. The significance level is a predefined probability cutoff to determine if the differences are statistically significant. An example of CorMaps is shown in figure 3.5, where the maps and P values are calculated for two different models to the same data set.

3.5 Summary

This chapter introduced the concept of X-ray Free Electron Laser (XFEL) facilities and the possibility of performing time-resolved femtosecond experiments with a high brilliance and coherence. It continued to give an overview of the relevant steps in the acquisition, sorting, correction and binning of the terabyte-sized datasets of 2D scattering patterns. These reduced data sets can then be compared to structural models in a multivariable χ^2 framework.

A χ^2 statistical framework for data-model comparison is not without problems, as it requires the explicit estimation of experimental errors. An alternative statistical method based on Correlation Maps (CorMap) was therefore introduced. In this CorMap method, differences between the data curves are found without explicit estimation of the errors, but only by using data point correlations.

Chapter 4

Potential Energy Landscapes in Transition Metal Complexes

This chapter aims at exemplifying the structural analysis of a Time-resolved Wide-Angle X-ray Scattering (TR-WAXS) experiment at an X-ray Free-Electron Laser (XFEL) facility, for a solvated transition metal complex. The system of interest is an aqueous solution of PtPOP ($Pt_2(H_2P_2O_5)_4]^{4-}$) much studied in literature, but the application of the analysis method goes much beyond this model compound. Many of these transition metal complexes show great catalytic promises, but their ability to absorb light and efficiently transfer it is still far from optimal and lacks a better understanding of the fundamental photochemistry. This chapter describes a TR-WAXS based method to directly measure the femtosecond ground and excited state state structural dynamics, which gives valuable information of the potential energy surfaces involved in these chemical photoreactions. The focus will be on the analysis of the isotropic part of the scattering signal but the system will be used as a model system for X-ray Cross-Correlation Analysis (XCCA) in *Chapter 6*. This chapter revisits the content of **Paper II-III**.

4.1 Introduction

Investigating the potential energy surfaces of the ground and excited state of molecules is an interesting field of research, as these surfaces are essential for all the chemical reactions taking place in and between molecules in these states. Steady-state IR and Raman spectroscopy provide information of the vibrational space, and the dynamics have mainly been investigated through time-resolved methods based on preparing vibrationally excited states through Raman processes in methods like e.g. Resonant Impulse Stimulated Raman Scattering (RISRS) and Coherent Anti-Stoke Raman Scattering (CARS) [59, 60, 61, 62, 63, 64]. These methods are excellent in determining the fundamental vibrational eigen frequencies for harmonic modes but does not give direct structural information about the dynamics as it has to be inferred from structure-energy relations or simulations.

This chapter seeks to illustrate how modern X-ray Free-Electron Laser (XFEL) sources makes it possible to directly map the structural dynamics on the ground and excited state surface of molecules in solution with a sub-picosecond time resolution. As an illustration of this approach, the PtPOP molecule is investigated in this chapter which creates the foundation for **Paper II-III**. First synthesized in 1977, it consist of a bi-planar Pt-Pt pair held together by four pyrophosito ligands. Due to a combination of its activity as a photo catalyst, high X-ray scattering power, long lifetime and high symmetry it has become a model compound for Time-resolved X-ray studies

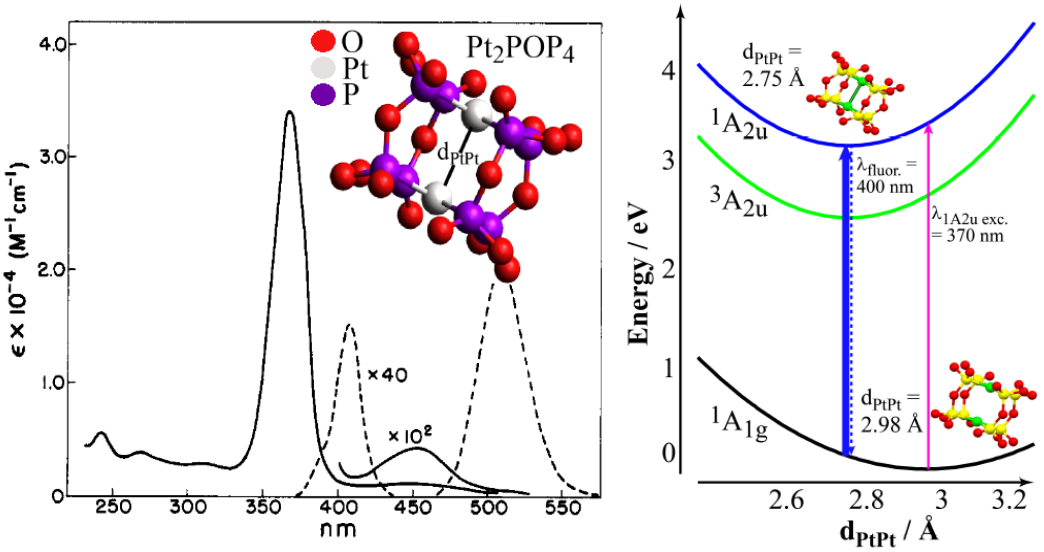

FIGURE 4.1: **Left:** Absorption (full line) and emission (dashed line) of aqueous PtPOP, from [65], **Right:** Sketch of the potential landscape of PtPOP. Vertical lines illustrates photo-excitation at 400/370 nm (full blue/purple lines) and fluorescence from the singlet excited state (dashed line). Adopted from **Paper II**.

and an excellent candidate for mapping the dynamics on the ground and excited state potential surfaces [11]. Transition metal complexes are also known to show promising properties as future sources of clean energy [13, 14, 15]. Due to its long-lived photo induced Metal to Metal Charge Transfer (MMCT) excited state the complex has been found to be an efficient catalyst for molecular hydrogen generation.

During the photo excited structural investigations of the molecule during the last four decades, several interesting phenomena has been found on time-scales of a few picoseconds [8, 9, 10]. It is well established that that the optical absorption centered at 370 nm (figure 4.1, left) corresponds to an excitation where an electron is promoted from an anti-bonding $5d\sigma*$ HOMO orbital to the bonding $6p\sigma$ LUMO orbital. As this orbital is located between the Pt atoms, it leads to an $\approx$ 0.2 Å ($\approx$ 10 %) contraction of the Pt-Pt bond. Further the Pt-Pt potential has been reported to be very harmonic and have characteristic picosecond-coherent vibrations of $\approx$ 280 fs and $\approx$ 220 fs in the ground and excite stated respectively [65, 66, 67]. Figure 4.1 (right) shows the schematic potential surfaces of the ground state and the initially excited singlet state and long-lived ($\approx$ 10 μs) triplet state.

Investigations of the structural dynamics on the excited state potential surface of transition metal complexes have already been done in literature [13, 16]. To investigate the structural dynamics on the ground state potential surface, off-resonance optical excitation at 400 nm is used to create a "hole" in the ground state population of PtPOP molecules. As the energy of these photons only is sufficient to excite the molecules from a contracted Pt-Pt ground state configuration to the bottom of the excited state potential, the excited state dynamics is effectively quenched as the excited state molecules are already near their minimum-energy configuration (figure 4.1, right). However, the "hole" created at the contracted Pt-Pt configuration of the ground state population is not a minimum-energy configuration and "hole" dynamics will be the main observable in the experiment. This makes it possible to

measure dynamics on the ground state potential surface.

Due to in part the long lifetime and high quantum yield the compound has a very high reactivity in the excited state and can e.g. abstract hydrogen from several compounds and generate H_2 in photocatalytic cycles through linear end-on coordination of d^{10} metals (eg. Ag^+) along the Pt-Pt axis [8, 14]. This chapter will also provide a brief structural analysis of photo excited PtPOP with end-coordination of Ag^+ (AgPtPOP), an exciplex-like structure which is dramatically more stable in the excited state.

4.2 The PtPOP XFEL Analysis

The data reduction process from an XFEL experiment to obtain $S_0(Q,t)$ and $S_2(Q,t)$ difference scattering curves, is presented in *Chapter 3*. The analysis presented in this section will focus on $S_0(Q,t)$ but a full analysis of $S_2(Q,t)$ can be found in **Paper III**. Figure 4.3 (top) shows a reduced dataset of $\Delta S_0(Q,t)$ with the pump-probe time delay t along the horizontal axis and the scattering vector Q along the vertical axis. In this section, a model based on DFT simulations will be developed to describe the scattering signals and to understand the underlying structural dynamics.

4.2.1 Pre-Analysis

From the experimental results presented in figure 4.3 (top) characteristic features in the difference scattering curves can be seen at $t > 0$. A powerful tool to disentangle the time information for different components in the $S_0(Q,t)$ data set ($m \times n$ matrix) is to use a Singular Value Decomposition (SVD) of the full dataset, which has the form:

$$\Delta S_0(Q,t) = \mathbf{USV^T} \tag{4.1}$$

Where $\mathbf{U}$ is an $m \times m$ unitary matrix defining the SVD components and $\mathbf{V^T}$ is an $n \times n$ unitary matrix carrying the column-to-column (temporal) variations of $\Delta S_0(Q,t)$. The diagonal elements of the $m \times n$ rectangular diagonal matrix $\mathbf{S}$ are the singular values which weight each column of $\mathbf{U}$ and $\mathbf{V}$, sorted in descending order. The columns of $\mathbf{U}$ then represent distinct signals in Q independent of time, and the rows of $\mathbf{U}$ represent their evolution in time. In this way, a SVD analysis provides an overview of the dominating features in Q and t without any *a priori* knowledge of the underlying structural dynamics.

Figure 4.2 (bottom) shows the five strongest SVD components from the measured data set $\Delta S_0(Q,t)$ and their temporal evolutions. The strongest component describes $\sim$ 90 % of the total signal and exhibit rapidly oscillating temporal behavior. A temporal Fourier transformation of the strongest component (figure 4.2, top) has a clear maximum at 280 fs which is exactly the same period as the expected Pt-Pt stretching mode in the ground state of PtPOP (280 fs) as opposed to the excited state (220 fs) [8, 9, 10]. The fact that the 220 fs component in the analysis is almost non-existing is a clear indication that we do indeed probe the structural dynamics on the ground state potential surface. These results can be understood directly from the structural dynamics following off-resonance absorption of light at 395 nm, where the oscillations in the excited state are effectively quenched. Instead, the

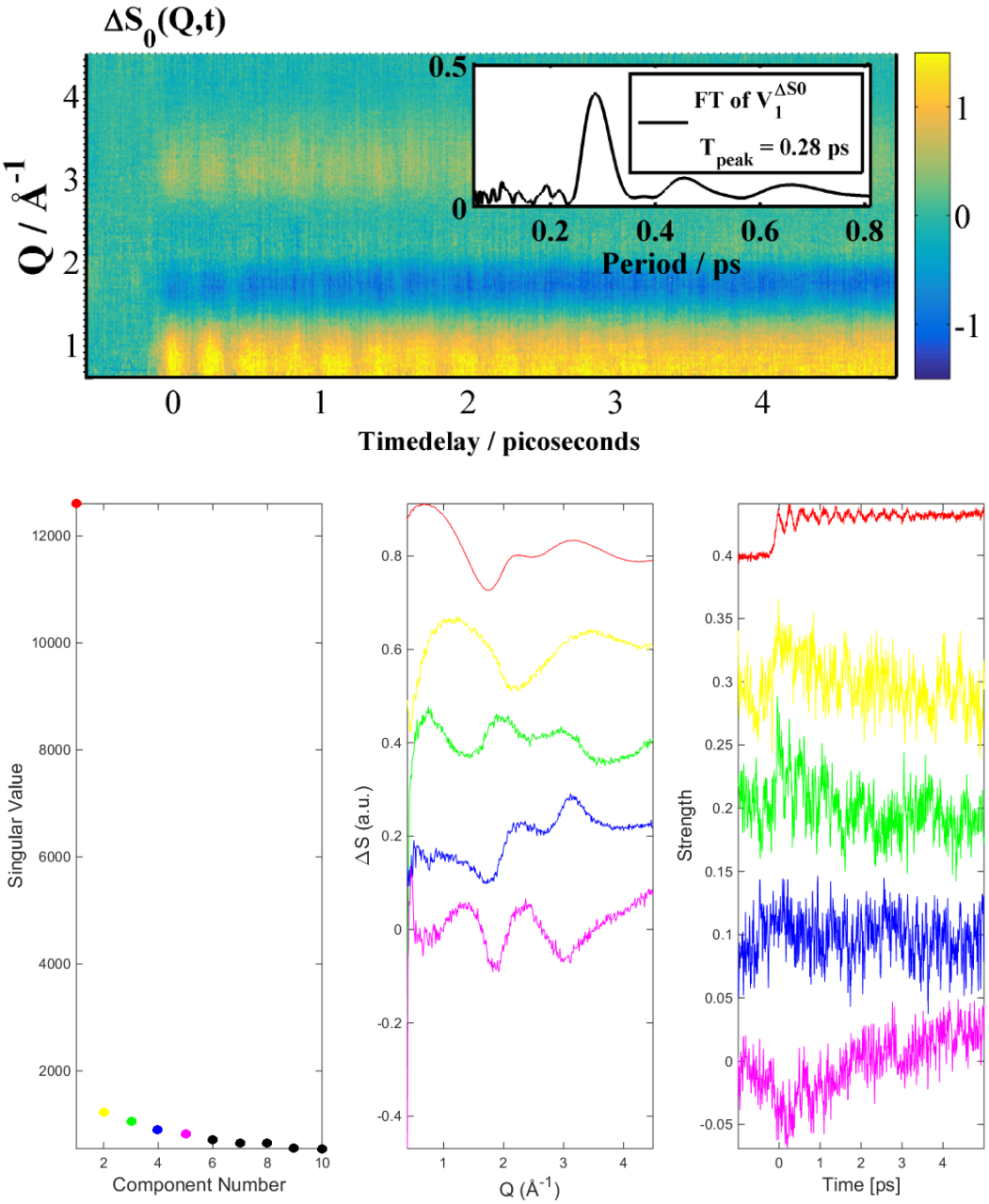

FIGURE 4.2: **Top:** The isotropic part of the measured difference signals $\Delta S_0(Q,t)$. The inset shows the Fourier transformation of the temporal evolution in the strongest SVD component, **Bottom:** A singular value decomposition of the scattering data with the five strongest components highlighted by colors (left). **U** describes the fundamental Q-dependent components in the data (middle) with a time evolution given by **V** (right).

structural dynamics of the "hole" burned into the ground state population is probed, as demonstrated in the simulations in the next section.

4.2.2 QM/MM BOMD Simulations

Simulations based on quantum mechanics can be used to quantify the results from an analysis of the structural dynamics and to give a better understanding of the chemistry governing these processes. The "hole"-burning process in the ground state population due to off-resonance excitation, were simulated using a hybrid Quantum-Mechanical Molecular Dynamics (QM/MM) Born-Oppenheimer Molecular Dynamics (BOMD) method [68] implemented in ASE/GPAW (see *Section 2.4*). These simulations were done by Gianluca Levi from the Technical University of Denmark.

The QM/MM BOMD simulations combine a DFT description of the PtPOP solute molecules with a classical force field (TIP4P) description of the solvent. The PtPOP molecules were modelled at the BLYP level, utilizing a tzp basis set for the Pt atoms and a dzp basis for the rest of the atoms. The first step in simulating the off-resonance excitation process is to prepare the initial population of the unperturbed MD ground state configurations. The photo excitation to the first singlet excited state can be simulated by allowing excitation of the ground state population with contracted Pt-Pt distances (see figure 4.1), taken into account the spectral width of the (3.14 eV / 395 nm) excitation pulse. Fifty independent trajectories of the system were calculated using the ΔSCP method [69, 70] which represent the temporal evolution of the depleted ground state population.

Figure 4.3 (left) shows snapshots of the simulated Pt-Pt bond length distribution d_{PtPt} during the first two periods, for the excited state population and the "hole" burned into the ground state population. Figure 4.3 (right) shows the simulated "hole" dynamics during the first 2 ps including the average Pt-Pt distance for the whole ensemble. By using the same fitting function as introduced later in *Section 4.3*, oscillating behavior with of period of around 270 fs is found, decaying on a time scale of 700 fs.

The inset of Figure 4.3 shows the average Pt-Pt distance for the entire simulated ensemble from which the expected overall decrease in the average Pt-Pt distance is evident. The simulation confirms that the off-resonance excitation burns a "hole" in the ground state population, coherent over several periods of the Pt-Pt bond-stretching mode. The "hole" oscillates with the ground state stretching mode period as it continues to propagate on the ground state potential surface, eventually broadening to reflect the equilibrium ground state distribution. The population of ground state molecules will continuously fill up and move the hole back and forth on the potential surface and because of the very harmonic potentials the "hole" movement will stay coherent over several oscillations. The newly created population of excited state PtPOP molecules will already be close to a minimum energy configuration and the oscillations will be effectively quenched. It can also be seen from the simulations that the "hole" and excited state population develop a Gaussian-like shape during the first half a period.

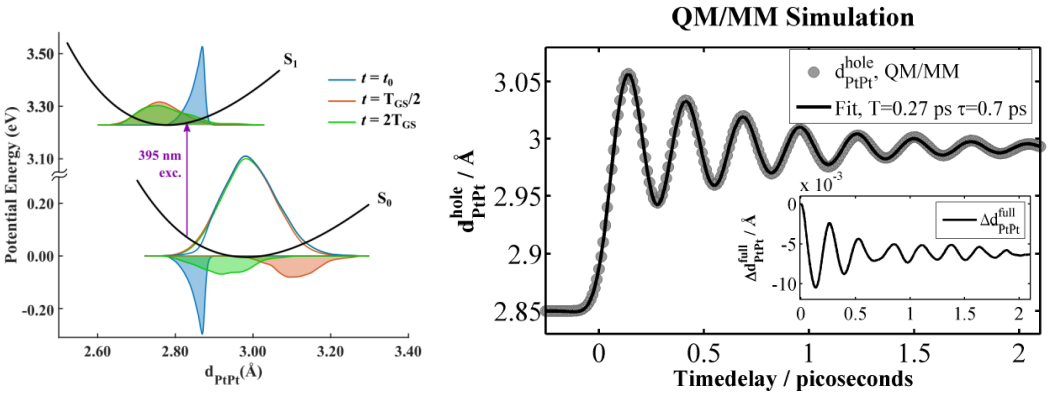

FIGURE 4.3: **Left:** QM/MM BOMD simulation of the structural dynamics in PtPOP following off-resonance excitation at 395 nm. The distribution of Pt-Pt bond lengths (full lines) in the ground and excited state ensembles are given at time steps of $t = 0$, $t = T/2$ and $t = 2T$, where T is the period of the Pt-Pt stretching mode. Shaded areas indicate Pt-Pt bond length distributions in the excited state and ground state "hole" population. **Right:** Temporal evolution of the "hole" in the simulations fitted with the same function as discussed in *Section 4.3*. Inset shows the average Pt-Pt distance for the entire simulated ensemble. Adopted from **Paper II**.

4.2.3 The Structural Model

This section will discuss the structural model used for the analysis of the PtPOP XFEL scattering data. In these experiments Laser-On and Laser-Off scattering curves were obtained to construct difference scattering curves. The full Laser-On/Laser-Off scattering curves can be described by a linear combination of contributions from the solvent, solute and solvent cage (solvent-solute interactions):

$$S_{on}(Q,t) = S_{solv,on}(Q,t) + S_{solu,on}(Q,t) + S_{cage,on}(Q,t) \tag{4.2}$$

$$S_{off}(Q) = S_{solv,off}(Q) + S_{solu,off}(Q) + S_{cage,off}(Q) \tag{4.3}$$

The Laser-Off curves are time-independent as the whole ensemble of molecules will be in an equilibrium configuration prior to photo excitation, even if the molecules will oscillate individually. The difference scattering signal can then be written as a sum of three terms:

$$\Delta S(Q,t) = S_{on}(Q,t) - S_{off}(Q) = \Delta S_{solv}(Q,t) + \Delta S_{solu}(Q,t) + \Delta S_{cage}(Q,t) \tag{4.4}$$

Each of which will be discussed in the following subsections.

The Solvent

The contribution to the difference scattering curves from the solvent is caused by reorganization of the bulk solvent molecules, due to changes in pressure, temperature and density. As discussed in *Section 2.5* two of the hydrodynamic parameters are enough to describe the scattering in the linear regime and the thermal expansion can be neglected on a timescale of a few picoseconds. The solvent term is then a

function of the change in solvent temperature:

$$\Delta S_{solv}(Q,t) \approx \Delta T(t) \left.\frac{\partial S_{solv}(Q)}{\partial T}\right|_{\rho} = \Delta T(t) S_{solv,dT}(Q) \tag{4.5}$$

Where $S_{solv,dT}(Q)$ have been obtained from reference measurements of dye mediated (water) solvent heating [43]. The strength of the solvent term therefore gives direct information of the solvent temperature increase $\Delta T(t)$. This is of great importance in many photochemical reactions as it keeps track of the thermal energy release from the solute molecules.

The Solute

The difference scattering contribution from the solute molecules arises from two different populations of PtPOP molecules. The laser-Off population is in equilibrium in the ground state $S_{GS}(Q)$. The laser-On population consist of some ground state molecules $S_{GS}(Q)$ and some photo excited molecules from an excitation of Pt-Pt contracted molecules $\alpha S_{ES}(Q,t)$ (α is the excitation fraction) with characteristic *excited state* modes. This effectively burns a dynamic "hole" in the ground state population with characteristic *ground state* modes. Both of these populations exhibit structural dynamics on different time scales. The Laser-On solute signal is given by $S_{solu,on}(Q,t) = S_{GS}(Q) + \alpha(S_{ES}(Q,t) - S_{GS,hole}(Q,t))$ and the Laser-Off solute signal by $S_{solu,off}(Q) = S_{GS}(Q)$. The solute difference signal can then be written as:

$$\Delta S_{solu}(Q,t) = S_{solu,on}(Q,t) - S_{solu,off}(Q) \tag{4.6}$$

$$\Delta S_{solu}(Q,t) = S_{GS}(Q) + \alpha S_{ES}(Q,t) - \alpha S_{GS,hole}(Q,t) - S_{GS}(Q) \tag{4.7}$$

$$\Delta S_{solu}(Q,t) = \alpha(S_{ES}(Q,t) - S_{GS,hole}(Q,t)) \tag{4.8}$$

The PtPOP ligand structure has been found to be very rigid and the most dominant mode is expected to be the lowest energy mode, the Pt-Pt bond stretching [8, 10]. DFT simulations confirms this picture and e.g. changes in the P interplane distances only contributes with $\sim 20\%$ of the scattering compared to similar changes in the Pt-Pt bond length. Therefore it is assumed that the solute difference signal only arises from structural changes in the Pt-Pt bond length $d_{PtPt}(t)$ meaning that $S_{GS,hole}$ is only dependent on Q and $d_{PtPt}(t)$. Further, the ground state "hole" is assumed to be reasonable described by an average Pt-Pt bond length of the whole population (see e.g. the QM/MM simulations in *Section 4.2.2*). The experimental measurements presented in *Section 4.2.1* and figure 4.2 shows that only one fundamental oscillation of ≈ 280 fs is clearly visible in the system. This corresponds to a situation where the excited state oscillations are effectively quenched and $S_{ES}(Q,t)$ is time-independent, giving:

$$\Delta S_{solu}(Q,t) = \alpha[S_{ES}(Q) - S_{GS,hole}(Q, d_{PtPt}(t))] \tag{4.9}$$

Giving a direct correlation between the temporal evolution of the difference scattering signal and the Pt-Pt bond dynamics. All time dependence are parametrized through the position of the (delta-function) ground state "hole".

The scattering signals from the ground and excited state structures can be estimated from DFT calculations by using the calculated structures and the Debye equation on all the interatomic distances. The calculations were carried out using the BLYP functional and the method discussed in *Section 2.4*. To avoid wave function cutoff the

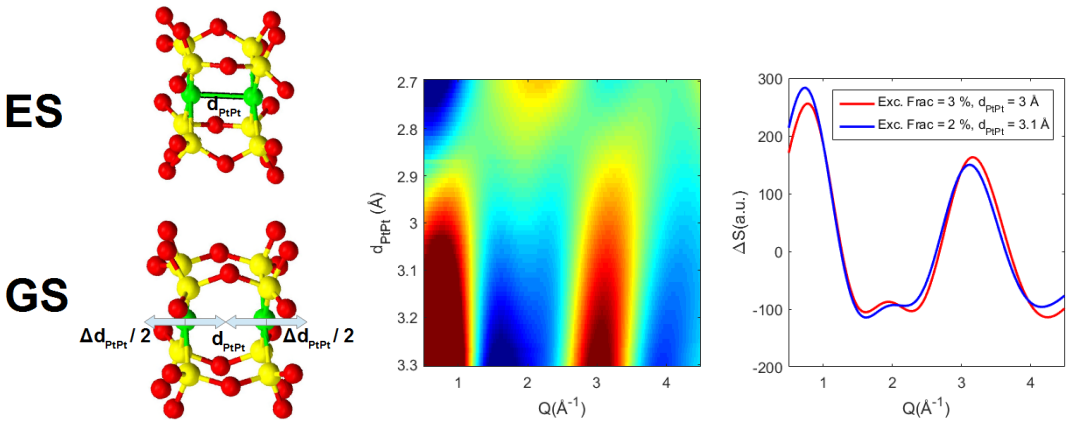

FIGURE 4.4: **Left:** Illustrates how the PtPOP difference scattering signals (**middle**) are calculated from a fixed excited state (ES) structure and a ground state (GS) structure with a set of possible Pt-Pt bond lengths, **Right:** The calculated signals are almost linear in the GS Pt-Pt bond length change.

box size was chosen to $(16\ \text{Å})^3$ (converged) and the QuasiNewton optimizer from ASE was used to minimize the forces to a convergence limit of 0.02 eV/Å. To find the optimal spacing and basis set a convergence test was performed with continuously more accurate calculations. The calculation results converged to within 0.3 % (0.01 Å) and based on these results a tzp basis set and a grid spacing of 0.18 Å were used.

The averaged Pt-Pt bond length of the ground state "hole" will change over time. Therefore a whole set of simulated difference scattering curves at different ground state Pt-Pt bond lengths is necessary in order to find the best-fit value of $d_{PtPt}(t)$ for every single time delay. There are two straightforward ways of creating such a set of curves; 1) Change the Pt-Pt bond length of the DFT relaxed structure; 2) Change the Pt-Pt bond length of the DFT relaxed structure and calculate a new DFT structure by keeping the new Pt-Pt bond length fixed. None of these methods are completely correct as the real structures are expected to be in between a non-relaxed and fully relaxed configuration during a fast vibration of a couple of hundred femtoseconds. In this thesis, the relaxed structures have been used. Figure 4.4 shows the calculated difference scattering signals from a set of ground state Pt-Pt bond lengths. The signal is seen to be almost linear in the change of the bond length.

The Cage

The cage term was estimated from the DFT simulations through calculations of radial distribution functions [29]. The shape of the difference scattering signal is assumed to not change over time, meaning that the calculated signal from one single set of structures can be used and scaled accordingly as a function of time ($\beta(t)$):

$$\Delta S_{cage}(Q,t) \approx \beta(t)\Delta S_{cage}(Q) \tag{4.10}$$

The cage term can have an important influence on condensed phase chemical properties [13, 71, 72, 73]. A more in-depth discussion can be found in e.g. **Paper IV** where the solvent is directly used to control the charge transfer excited state relaxation pathways in a transition metal complex.

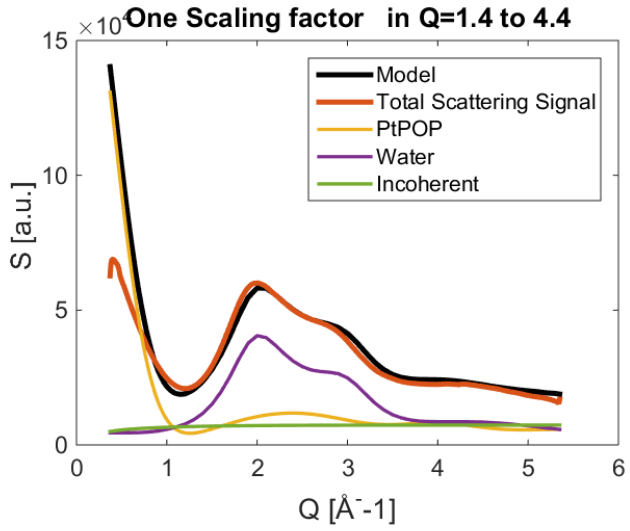

FIGURE 4.5: The scaling value was found by comparing the total measured scattering signal (off images) to the total calculated scattering signal (coherent + incoherent) from a liquid unit cell.

4.2.4 Data Analysis

This section will describe the analysis of the $S_0(Q,t)$ scattering curves from the PtPOP XFEL experiments. The data was first scaled to a liquid unit cell in order to estimate the excitation fraction and then analyzed using the model described in the previous section.

Scaling to a Unit Liquid Cell

In order to compare the measured scattering curves to the simulations, the obtained total scattering curves from the ground state (off images) were scaled to a unit liquid cell. The liquid unit cell consists of the calculated scattering (coherent + incoherent) from 694 water molecules and one ground state PtPOP molecule, corresponding to a 80 mM solution. Figure 4.5 shows how the scaled signal from a liquid cell in an Q interval from 1.4 to 4.4 Å^{-1} fits the measured total scattering signal, by using a scaling value of 37,000. The huge discrepancy at low-Q is assigned to effects such as air scattering in the reference signal.

The Excitation Fraction

The excitation fraction is expected to be constant on a ps-timescale, due to the long-lived ($\sim$ 10 µs) excited state structure of PtPOP. An estimation of the value is found by first defining it as a time-dependent parameter:

$$\Delta S(Q,t) = \Delta T(t) S_{solv,dT}(Q) + \alpha(t)[S_{ES}(Q) - S_{GS,hole}(Q, d_{PtPt}(t))] + \beta(t)\Delta S_{cage}(Q) \tag{4.11}$$

A model with four time-dependent parameters: solvent temperature increase ΔT, excitation fraction α, cage factor β and the Pt-Pt Ground state bond length d_{PtPt}. The best-fit values for the Pt-Pt bond lengths $d_{PtPt}(t)$ (left) and the excitation fraction $\alpha(t)$ (right) are shown in figure 4.6. Surprisingly, the excitation fraction shows an oscillating behavior with a period close to the ground state Pt-Pt stretching mode. Within the structural analysis framework, the excitation fraction and key structural

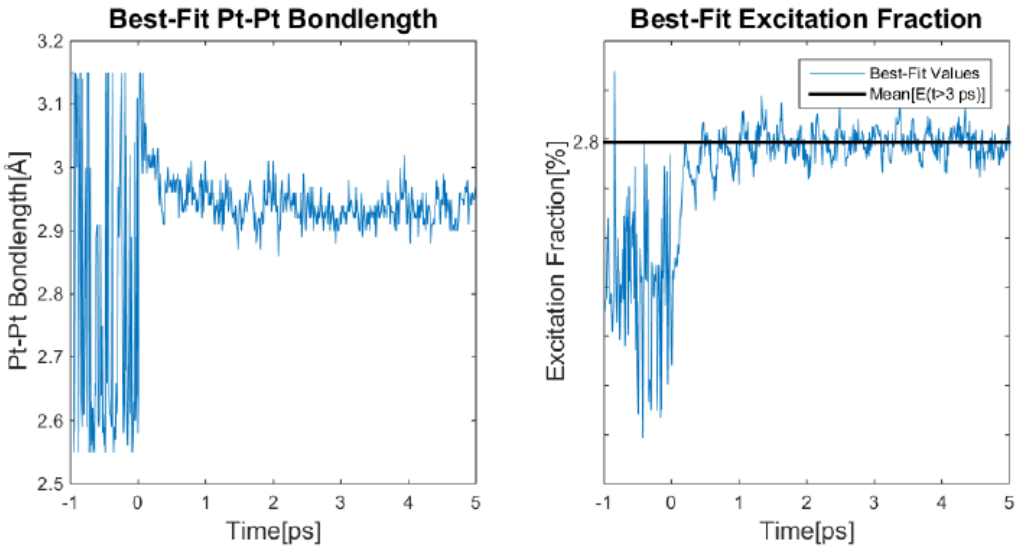

FIGURE 4.6: The best-fit values for the ground state Pt-Pt bond length (**left**) and the excitation fraction (**right**) using the excitation fraction as a time-dependent parameter (see equation (4.11)).

parameters are known to be strongly correlated [14]. Following the discussion in *Section 4.2.3* and figure 4.4 the excitation fraction and the change in the Pt-Pt bond lengths are clearly correlated. As the excitation fraction is known to be constant on the ps-timescale it is kept fixed by using the mean value at $t > 3$ ps, $\alpha = 2.8$ %. The second step is to lock this value in the full analysis of the XFEL data by assuming it a step function.

Fitting the Model to Data

To quantify the structural dynamics underlying the difference scattering curves, the data was analyzed by structural fitting, employing the model incorporating a Pt-Pt distance-dependent depletion of the ground state population. The fitting of the time-binned experimental data was done by fitting every single time slice, using equation (4.11) and a fixed time-independent excitation fraction α:

$$\Delta S(Q,t) = \Delta T(t) S_{solv,dT}(Q) + \alpha[S_{ES}(Q) - S_{GS,hole}(Q, d_{PtPt}(t))] + \beta(t)\Delta S_{cage}(Q) \tag{4.12}$$

Figure 4.7 shows the best-fit difference scattering signals (5 fs bins) obtained using this model (middle) to the measured difference scattering data (left) with residuals (right). Figure 4.8 shows the temporal evolution of the best-fit parameters. The best-fit value for $d_{PtPt}(t)$ as a function of time delay t is observed to move towards longer distances immediately after photo excitation while it oscillates around the ground-state equilibrium distance. This is in agreement with the expectations from *Section 4.2.1*.

Best-Fit Parameters

The three obtained time-dependent best-fit parameters for the analysis are shown in figure 4.8 and discussed in the following subsections.

PtPt Bond Length

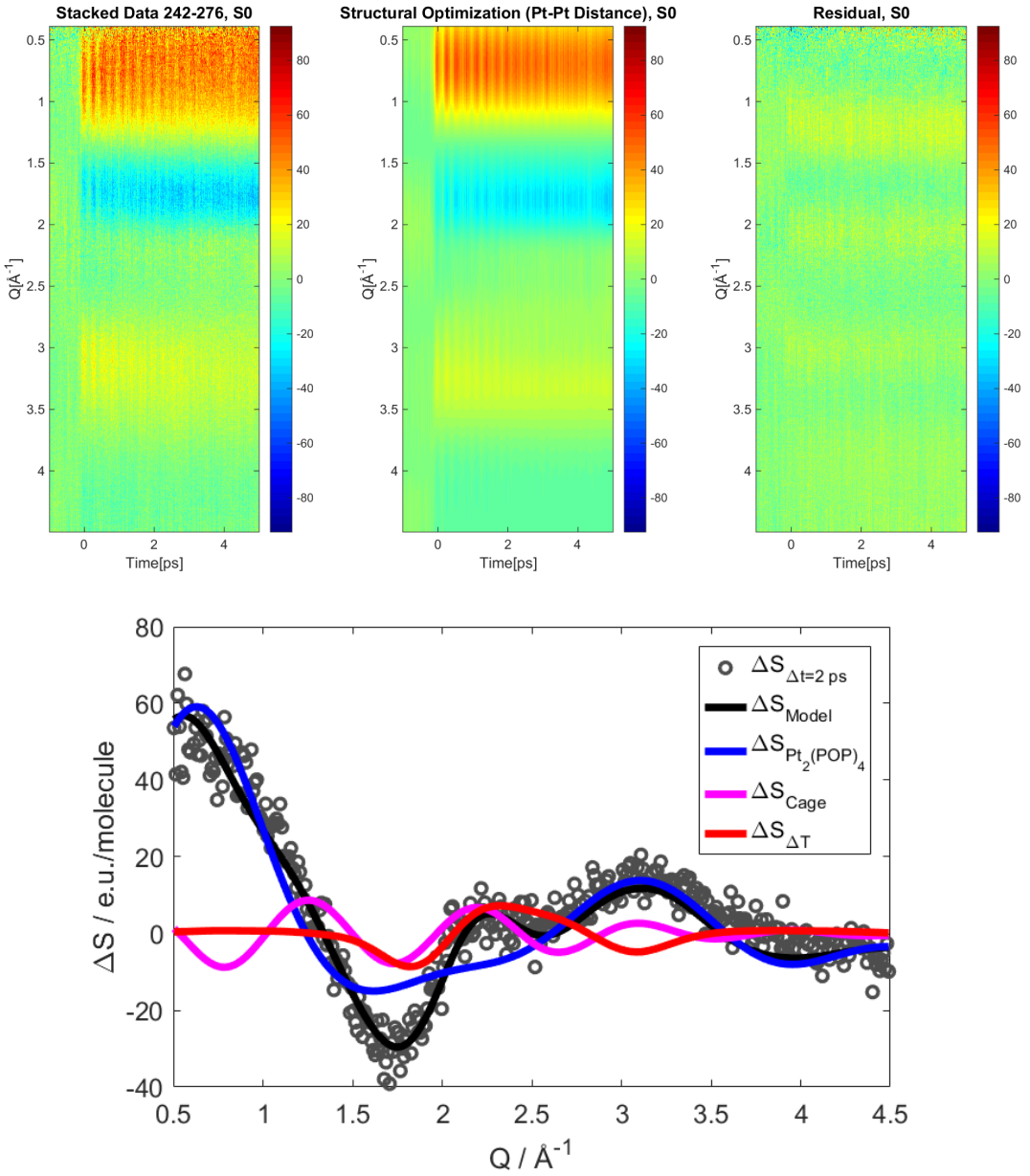

FIGURE 4.7: **Top:** The measured S_0 difference scattering data (left), the best-fit difference scattering signal using equation (4.12) (middle) and their residuals (right). **Bottom:** Example of the fit components at a 2 ps time delays. The three terms are solute $\Delta S_{Pt_2(POP)_4}$, solvent $\Delta S_{\Delta T}$ and cage ΔS_{cage}.

Because the difference scattering signal is calculated as $\Delta S(t) = S_{ES} - S_{GS}(d_{pt-pt}(t))$ in the model, and it can be assumed that $\Delta S(t < 0) = S_{ES} - S_{GS}(d_{pt-pt}(t < 0)) = 0$, then $S_{ES} = S_{GS}(d_{pt-pt}(t < 0))$. This means that the model will try to find the closest ground state configuration to the excited state configuration before time zero, and explains why $d_{pt-pt}(t < 0) = 2.76$ Å in the model as it is equal to the excited state Pt-Pt bond length.

The time evolution of d_{pt-pt} can be fitted by a decaying oscillating function starting at $t = t_0$, shifted according to the new equilibrium Pt-Pt distance (different than the excited state distance of 2.76 Å). To account for the instrument response function

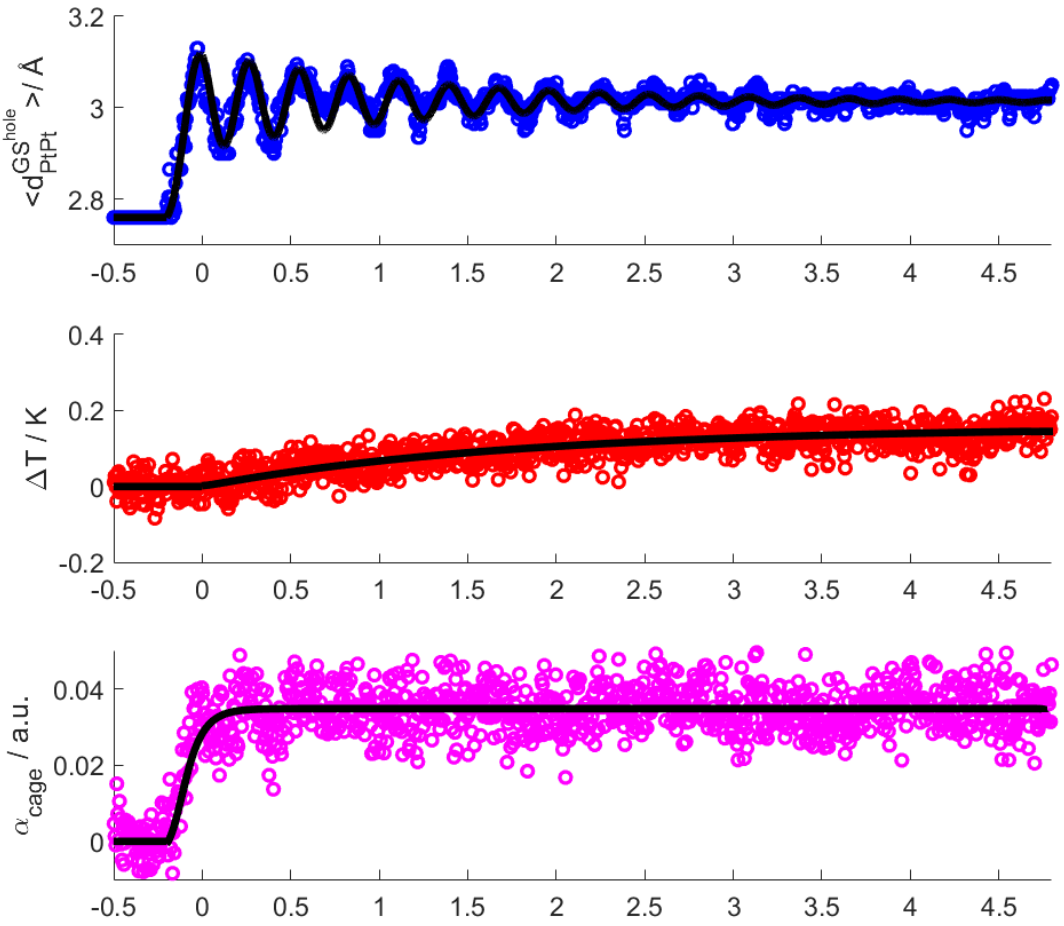

FIGURE 4.8: The temporal evolution of the best-fit parameters by comparison to the measured difference scattering data and the model described in equation (4.11). The Pt-Pt bond length changes d_{PtPt} (**top**), solvent heating ΔT (**middle**) and the cage scaling factor β (**bottom**) were modelled and fitted according to equation 4.(12-14).

(IRF) of the experiment, the whole function was convoluted with a Gaussian of width α:

$$f(t) = 2.76\ \text{Å} + \text{Gauss}(\sigma) \otimes \begin{cases} 0\ \text{Å} \ \text{ if } t < t_0 \\ A + B\cos(C(t-t_0) - \pi) \cdot e^{-\frac{(t-t_0)}{\tau}} \ \text{ if } t > t_0 \end{cases} \tag{4.13}$$

With best-fit values are given by $A = 0.250$ Å, $B = 0.256$ Å, $C = 22.2$ ps^{-1} (284 fs period), $t_0 = 0.11$ ps, $\tau = 1.52$ ps, $\sigma = 72$ fs.

To locate possible changes in the ground state period as the "hole" evolves and potential mixing of other frequencies, a Fourier transformation was done in intervals of 1.5 ps Hann windows (figure 4.9, top) for every (binned) time delay. The Hann window function is a mathematical function ensuring zero-values at the boundaries of the interval, in order to better perform a Fourier transformation of small subsets of a function. Figure 4.9 (bottom) shows the distribution of Fourier period for each time-delay using this method. The strongest component is ≈ 280 fs as expected and no clear periods of ≈ 220 fs corresponding to the excitation state Pt-Pt stretching mode was observed.

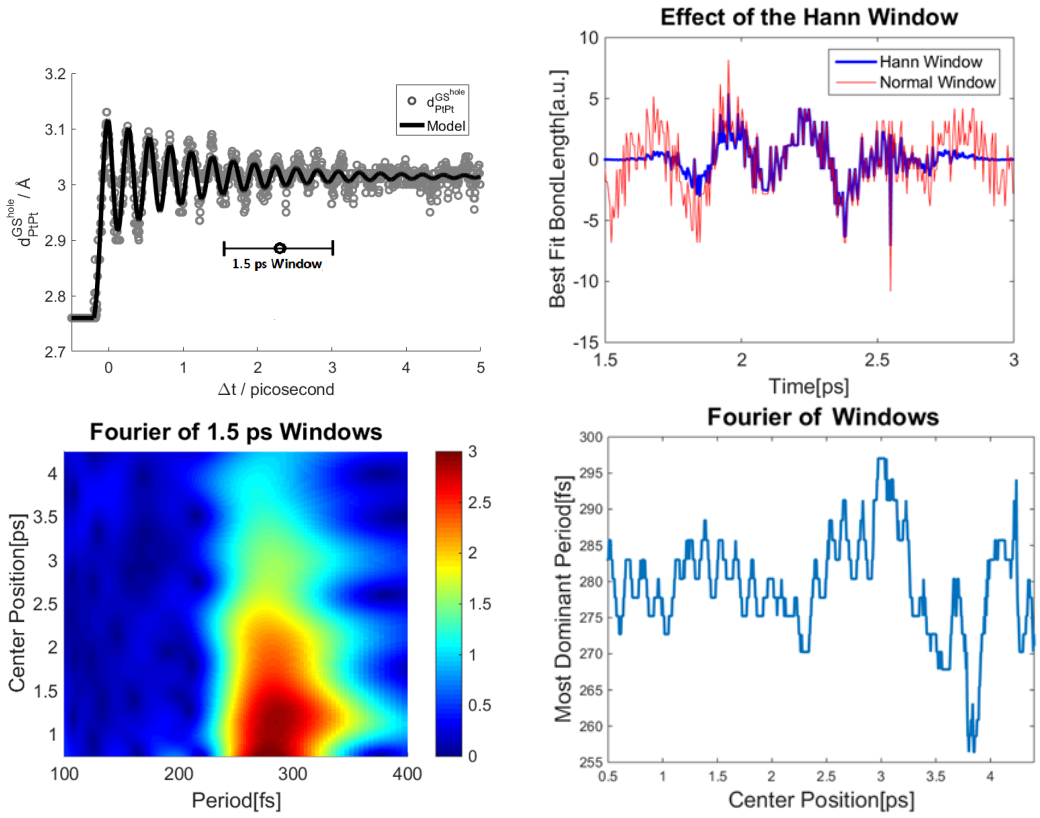

FIGURE 4.9: Illustration of a Fourier transformation of d_{pt-pt} using a 1.5 ps Hann window from 1.5-3.0 ps (**top**). It can be centered at every time bin to investigate the evolution of Fourier periods over time (**bottom-left**). The most dominant $\approx$ 280 fs (**bottom-right**) period corresponds to the ground state stretching mode. No clear period corresponding to the excited state stretching mode of $\approx$ 220 fs was identified.

Temperature and Cage

The time evolution of the best-fit values for the change in solvent temperature $\Delta T(t)$ and the cage term $cage(t)$ can be fitted by a convolution of the IRF and a function starting at t_0 with an exponential growth towards a new equilibrium value:

$$\Delta T(t) = \text{Gauss}(\sigma) \otimes \begin{cases} 0\ \text{K} & \text{if } t < t_0 \\ A \cdot (1 - e^{-\frac{(t-t_0)}{\tau}}) & \text{if } t > t_0 \end{cases} \tag{4.14}$$

With best-fit values given by $A = 0.166$ K, $t_0 = 0.11$ ps, $\tau = 2.15$ ps, $\sigma = 95$ fs.

$$cage(t) = \text{Gauss}(\sigma) \otimes \begin{cases} 0 & \text{if } t < t_0 \\ A \cdot (1 - e^{-\frac{t}{\tau}}) & \text{if } t > t_0 \end{cases} \tag{4.15}$$

With best-fit values given by $A = 0.035$, t_0 = 0.12 ps, $\tau = 0.077$ ps, $\sigma = 44$ fs.

The necessary energy release from every excited PtPOP molecule in order to increase the water temperature by 0.17 K, can be calculated. The amount of water molecules N_{H_2O} in a liter of water is given by Avogadro's constant $N_A = 6.02 \cdot 10^{23}$ mol^{-1} and

the molar mass $M_{H_2O} = 18 \frac{\text{g}}{\text{mol}}$:

$$N_{H_2O} = \frac{N_A}{M_{H_2O}} = \frac{6.02 \cdot 10^{23} \frac{1}{\text{mol}}}{18 \frac{\text{g}}{\text{mol}}} = 3.34 \cdot 10^{25} \text{ L}^{-1} \tag{4.16}$$

The energy ($E_{H_2O,0.17K}$) required to raise the temperature of a single water molecule by $\Delta T = 0.17$ K, is then given by the specific heat capacity of water $C_{H_2O} = 4187 \frac{\text{J}}{\text{L·K}}$:

$$E_{H_2O,0.17K} = \frac{C_{H_2O} \Delta T}{N_{H_2O}} = 0.17 \text{ K} \cdot \frac{4187 \frac{\text{J}}{\text{L·K}}}{3.34 \cdot 10^{25} \text{ L}^{-1}} = 2.1 \cdot 10^{-23} \text{ J} = 0.14 \text{ meV} \tag{4.17}$$

As there are 695 water molecules per one PtPOP molecule and the excitation fraction was estimated to 2.8 %, it means that each excited PtPOP molecules on average releases E_{PtPOP} (ignoring direct photo absorption in the water):

$$E_{PtPOP} = \frac{0.14 \text{ meV} \cdot 695}{2.8 \text{ \%}} = 3.2 \text{ eV} \tag{4.18}$$

4.2.5 Discussion

The 284 fs oscillation period determined by both the direct Fourier transformation (Figure 4.2) of the measured difference scattering data as well as from the fit of the PtPOP ground state Pt-Pt bond length (Figure 4.8) is in very good agreement with the value reported for the ground state stretching mode from optical studies of 281 fs [74]. Further, no clear sign was seen of the ≈ 220 fs stretching mode period in the excited state. This demonstrates the preparation of a vibrationally cold excited state population through off-resonance photo excitation with a measurable time evolution of the ground-state "hole" population. Further, the measured "excitation fraction" of the cage (Figure 4.8) signal was 3.5 % which corresponds reasonable well with the excitation fraction of the PtPOP molecules of 2.8 %. As a proof-of-concept, the experiment successfully shows how to directly follow ultrafast structural (solute and cage) dynamics on a ground state potential surface in an XFEL experiment.

The QM/MM BOMD simulations (Figure 4.3) gives an idea of how the population distributions might evolve on the potential energy surfaces according to quantum mechanics. These simulation have a ground state period of 270 fs which agrees to within 5 % with the experimental data and further validates the concept of off-resonance "hole" burning and dynamics in the ground state population. The decay of the ground-state oscillations in the simulations takes place in 0.7 ps, somewhat faster than the observed τ = 1.52 ps. Further, a stronger component from the excited state dynamics is observed in the simulations. This gives room for further improvements of the simulation method, which might identify the underlying atomistic mechanism for the faster decoherence and optimize the description of the energy surfaces.

The fit of the Pt-Pt bond length oscillations seems to underestimate the observed amplitude of the oscillations during the first picosecond or so. The discrepancies from perfect harmonic oscillations gives insight into the anharmonicity of the ground state potential or possible contributions from excited-state dynamics. Further experiments with better Q-space coverage might resolve the dynamics in more detail, as recently discussed from a theoretical point of view [51].

The estimated energy release from a single excited PtPOP molecule was found to be

3.2 eV that is slightly higher than the photon energy of 3.1 eV. Most of the absorbed energy stays in the excited molecules for the whole excited state life time and only around 1 eV are released from the difference in energy between the single and triplet excited states. This makes it impossible for single-photon absorption in the solute to describe the full temperature increase of the solvent and opens up the possibility for multiple photon absorption processes. Further, the analysis of the S_2 signal in **Paper III** does indeed suggest multiple photo absorption in the solute from the fact that a smaller percentage (1.8 %) of the excited molecules contribute to the anisotropic than to the isotropic scattering signal (2.8 %). Another explanation could be that the influence of the temperature signal in the fit is overestimated e.g. by correlations with the cage signal. The photo absorption of the solvent is considered insignificant due to the relatively small laser power of 0.03 Jm^{-2} [75].

4.3 The AgPtPOP XFEL Analysis

This section seeks to determine the ground and excited state structure of AgPtPOP and understand the structural changes of PtPOP induces by end-on coordination of Ag^+ atoms. The change in structural dynamics following photo excitation will also be investigated as the end-on coordination of Ag^+ effectively creates an asymmetric Pt-Pt-Ag three-body system in a rigid ligand cage in contrast to the very harmonic and symmetric Pt-Pt configuration of PtPOP. Further, AgPtPOP is dramatically more stable in the excited state configuration due to an increased affinity of the Ag^+ atoms, making the Pt-Ag bond changes an interesting study in itself. This will be investigated by analyzing Time-Resolved X-ray Scattering data from LCLS. The analysis is still on-going.

4.3.1 Structural Optimization of the Ground/Excited State

In this section a model based on the χ^2 maximum likelihood will be used to optimize the ground and excited state of AgPtPOP, starting from a DFT calculated structure of the excited state from Kong et al. (2012) [76]. These calculations assume an end-on coordination of Ag^+ even if some DFT calculations in literature suggest side-on coordination perpendicular to the Pt-Pt axis [77]. The latter is however inconsistent with experimental evidence [14, 43] and a preliminary analysis of the TR-WAXS data showed that end-on coordination is indeed much more likely.

Figure 4.11 (top-left) shows TR-WAXS scattering curves collected at LCLS. After 4 ps most of the dynamics have stabilized and hence by averaging the signal from, 4 ps < t < 5 ps, the signal should be representative for a relaxed excited state structure. It should be mentioned that *both* PtPOP and AgPtPOP molecules are present in the solution. Figure 4.10 (left) shows the averaged signal at, 4 ps < t < 5 ps, which can be analyzed according to the model described in *Section 4.2* with the addition of the AgPtPOP molecules in the population.

$$\Delta S(Q,t) = \Delta T S_{solvent,dT}(Q) + \alpha \Delta S_{PtPOP}(Q) + \beta \Delta S_{AgPtPOP}(Q) + \zeta \Delta S_{cage}(Q) \tag{4.19}$$

$\Delta S_{cage}(Q)$ is assumed to a first approximation to be similar to the cage of PtPOP. The most accurate estimation of $\Delta S_{PtPOP}(Q)$ is found by using the averaged signal from, 4 ps < t < 5 ps from the PtPOP experiment discussed in *Section 4.2*.

The remaining $\Delta S_{AgPtPOP}(Q)$ term is found from a simulation routine taking an

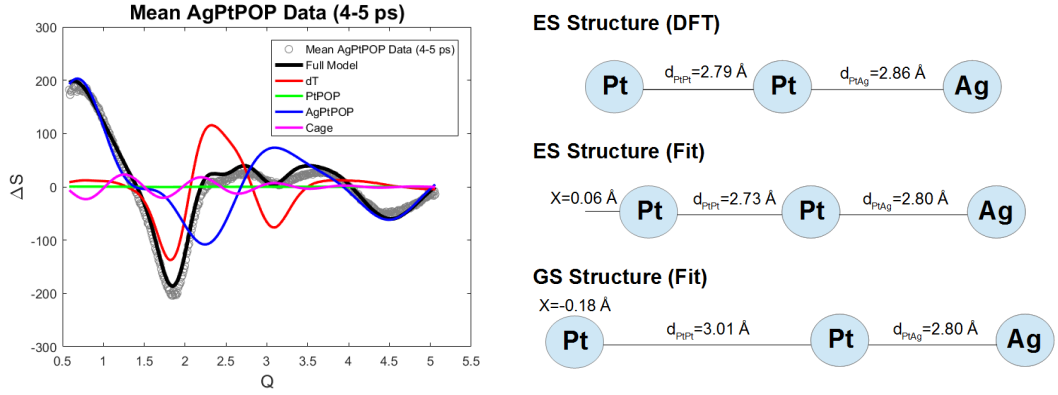

FIGURE 4.10: **Left:** The mean TR-WAXS scattering difference signal at, 4 ps < t < 5 ps, from the AgPtPOP experiment compared to the best structural fit using the χ^2 maximum likelihood framework and equation (4.19). **Right:** The structural model of the ground/excited state is based on variational parametrization of three atomic distances X, d_{PtPt} and d_{PtAg} compared to the DFT excited state structure calculated by Kong et al. (2012) [76]. The best-fit distances are indicated.

input consisting of geometrical structures of the ground and excited state molecules. These structures are based on the DFT calculations of both states and a variational parametrization of three atomic distances X, d_{PtPt} and d_{PtAg} in steps of 0.02 Å as illustrated in figure 4.10 (right). The distances were varied with $\pm$ 0.5 Å in the ground state and $\pm$ 0.1 Å in the excited state in comparison with the DFT structure for the excited state structure. Around 180 million different structures of which the scattering pattern can be calculated by the Debye equation. The output is the best estimate of the structures in comparison with the measured scattering curve based on the χ^2 framework introduced in *Section 3.4* and equation (4.19).

Figure 4.10 (left) shows the best fit using the full structural variation model with the structural best-fit values presented in Figure 4.10 (right). A slightly smaller excited state structure was found from the structural optimization of AgPtPOP, compared to the structure calculated by DFT, with $X^{ES} = 0.06 \pm 0.06$ Å, $\Delta d^{ES}_{PtPt} = -0.06 \pm 0.05$ Å and $\Delta d^{ES}_{PtAg} = -0.06 \pm 0.07$ Å corresponding to $d^{ES}_{PtPt} = 2.73 \pm 0.05$ Å and $d^{ES}_{PtAg} = 2.80 \pm 0.07$ Å. The optimized ground state structure was found to be given by $X^{GS} = -0.18 \pm 0.06$ Å, $d^{GS}_{PtPt} = 3.01 \pm 0.04$ Å and $d^{GS}_{PtAg} = 2.80 \pm 0.03$ Å.

The excitation fraction of AgPtPOP was found to be $\alpha \approx 10\%$ and the contribution of PtPOP was almost non-existent. The concentration of AgPtPOP/PtPOP molecules can be calculated from the initial concentration of $[Ag^+] = 80$ mM and $[PtPOP] = 20$ mM by the rate equation:

$$K = \frac{[\text{AgPtPOP}]}{[\text{Ag}^+][\text{PtPOP}]} \tag{4.20}$$

Where K is the rate constant $K = 320 \pm 40$ M^{-1} [78] giving a scattering ratio of excited AgPtPOP-to-PtPOP of ~ 40. The small concentration explain the almost non-existent contribution from PtPOP.

The cage contribution has a value of $\zeta \approx 9\%$ which corresponds very well with the

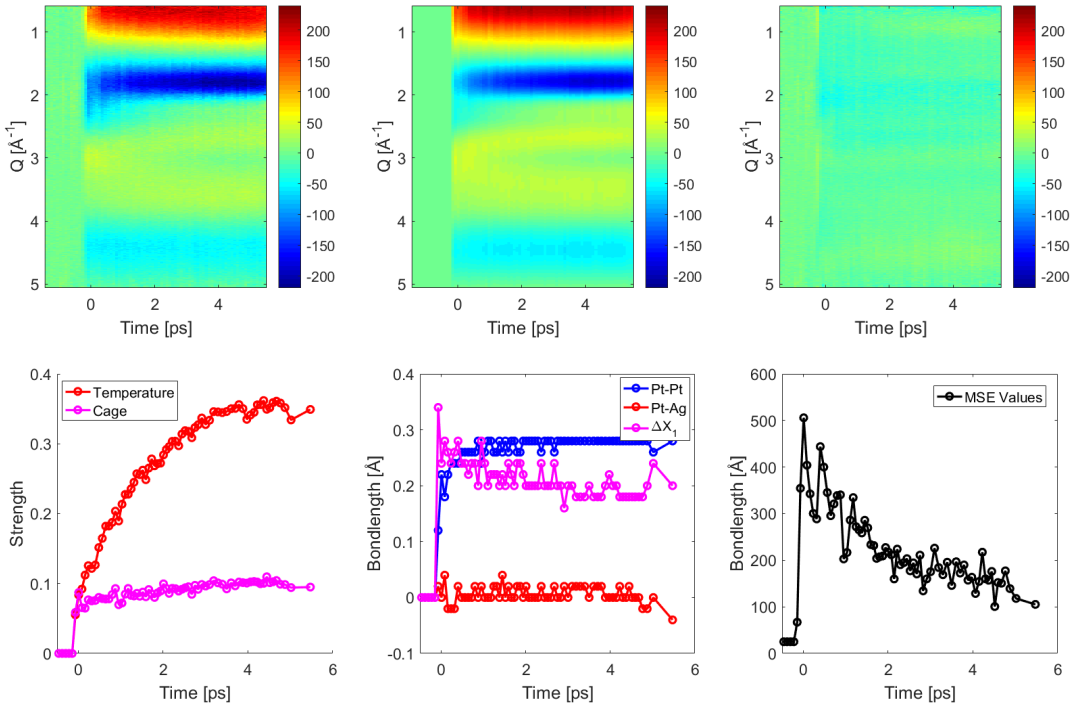

FIGURE 4.11: **Top:** The TR-WAXS scattering data (left), calculated scattering data based on the structural analysis framework presented in *Section 4.2.1* (middle) and their residuals (right). **Bottom:** The calculated values using the structural analysis for solvent temperature and cage signal (left), structural solute parameters for AgPtPOP (middle) and uncertainties presented as unbiased Mean Square Error (MSE) values (right).

AgPtPOP excitation fraction $\alpha \approx 10\%$. This is expected as the cage term is calculated for a single photo excited PtPOP molecule.

4.3.2 Pt-Pt-Ag Bond Dynamics

Having done the structural optimization of the molecule in the previous section, the ground state structure and the excitation fractions of PtPOP and AgPtPOP - and thus α and β - can be kept fixed in the temporal analysis of the TR-WAXS data. The structural analysis framework based on equation (4.19) can then be used for every single time delay. Figure 4.11 shows the resulting temporal dynamics of the experimental parameters using this method (bottom) and the model is in good agreement with the TR-WAXS scattering data (top). As of this point a MATLAB-based unbiased estimator (*lscov* routine) of the real MSE (Mean Square Error) values are used as an estimate of the fit quality and an oscillating decaying amplitude of the MSE values is observed as a function of time (bottom,right). Figure 4.12 shows an SVD analysis of the residual scattering signal, and a clear dominant component ($\approx$ 5 times stronger than the second component) is observed with a similar temporal evolution as the one observed for the MSE values. SVD decomposes the signal into an orthonormal basis, where the individual basis vectors represents a fraction of the signal that shows common temporal evolution.

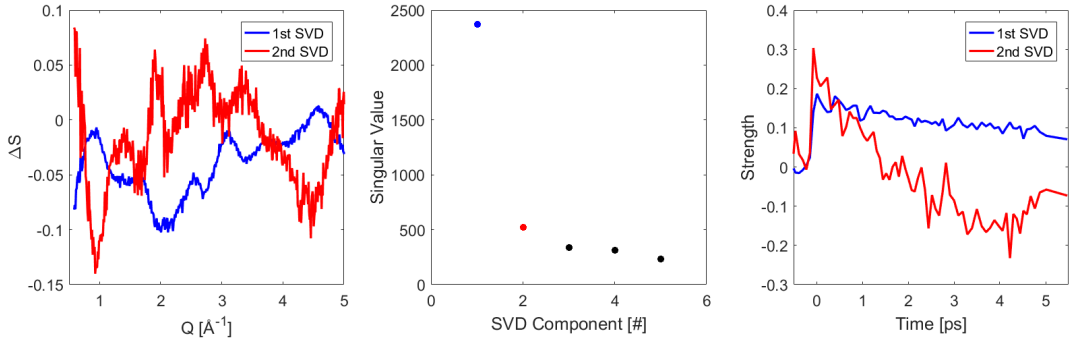

FIGURE 4.12: Shows the result of a singular value decomposition of the data with the two strongest components highlighted by colors. The left singular vectors **U** describes the shape of the signals, the middle singular values **S** the strength of the components and the right singular Vectors **V** the time evolution of the vectors in **U**.

4.3.3 Discussion

The structural changes of PtPOP have been directly measured in *Section 4.2* and in literature both in the crystal phase [79, 80] and in solution [9, 10], where the molecular structure has been found to start from a ground state Pt-Pt distance of 2.9-3.0 Å to an excited state Pt-Pt distance of 2.7-2.8 Å. These values are very similar to ones measured for AgPtPOP ($d^{ES}_{PtAg} = 2.80 \pm 0.07$ Å, $d^{GS}_{PtAg} = 3.01 \pm 0.04$ Å) and well within the uncertainties.

Whereas the movement of the atoms in the photo excited Pt-Pt bond contraction are symmetric in the PtPOP molecule, the end-on addition of the Ag^+ atom seems to create an asymmetric movement of the Pt atoms during the Pt-Pt bond contraction where the uncoordinated Pt atom move 0.1 Å closer to the middle of the structure than the Ag-coordinated Pt atom. One reason could be an energy cost of bringing the Ag^+ closer to the ligand structure. The Ag-Pt bond itself does not seem to change much upon excitation of an electron from the anti-bonding $5d\sigma*$ HOMO orbital to the bonding $6d\sigma$ LUMO orbital of the Pt-Pt bond. This indicates that either these orbitals do not play a significant role in the Pt-Ag bond formation or that its significance is balanced out by the increased structural resistance of moving the Ag^+ closer to the ligand structure, of which the first reason would be unexpected. Also no significant difference was measured in the size of the Pt-Pt contraction upon end-on coordination of Ag^+. Further, it should be noted that no clear oscillation period of 220 fs/280 fs can be seen in the AgPtPOP experimental data, which could be due to a much stronger decoherence effect in the AgPtPOP molecule where the Pt-Pt bond symmetry is broken by the end-on coordination of Ag^+.

Figure 4.13 (left) illustrates that the temporal evolution of the model residual (MSE) seems to follow an exponential decaying oscillation with a period of $\approx$ 380 fs. The decrease in the MSE values point towards an increasingly better structural model over time that could be explained by an additional short lived component in the data. Figure 4.13 (right) shows a direct comparison of the scattering difference signal between measurements at, 1 ps $< t <$ 2 ps, and, 4 ps $< t <$ 5 ps. The solvent temperature signal is shown as well to signify that it is insufficient to describe the full difference between the two scattering signals and that part of the residual could be due to an additional effect in the system. The $\approx$ 380 fs points towards additional

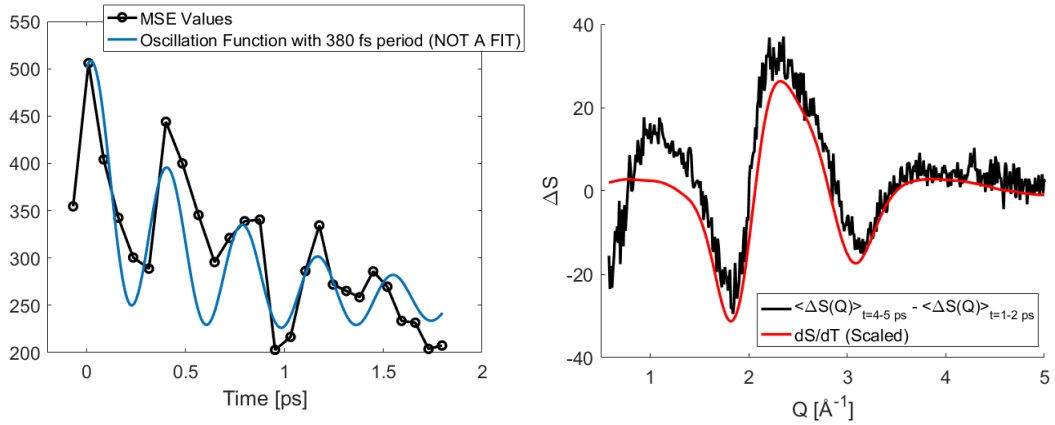

FIGURE 4.13: **Left:** The Mean Squared Errors (MSE) values from the structural analysis seem to behave according to an exponentially decaying oscillating function with a period of around 380 fs. The blue line illustrates this but is not a result of mathematical fitting. **Right**: The scattering difference signal for TR-WAXS data averaged over 1-2 ps and 4-5 ps cannot be fully described by a solvent temperature increase.

structural dynamics as well. It has been observed from Raman spectroscopy on Cl/Br/I coordinated PtPOP molecules that some complexes (Cl/Br) have a longer oscillation period (300/350 fs) than the Pt-Pt bond stretching mode, associated with the Pt-Pt-Cl/Br bending mode [81]. The QM/MM BOMD simulation method used in the PtPOP data analysis might give a better understanding of the underlying mechanisms in the AgPtPOP system.

The possible Ag-Pt-Pt bending mode is an obvious candidate to include in the structural model and the fitting at all time delays. It will however be difficult to increase the number of variables, due to the strong correlation between several of the parameters and the severe limitation caused by the available information content in one-dimensional scattering curves. For clearer observations of the oscillation periods, a data set with better quality and reduced time bins is needed. Another improvement could be the inclusion of a AgPtPOP cage instead of using the one for PtPOP as the geometry of the metal-solvent interaction may be a key component in understanding the photochemical reaction. It is however not expected to make significant differences in the current analysis.

A few limitations of the model will be addressed. First of all the structural model is based on atomic distance steps of 0.02 Å, which might be insufficient to clearly show subtle oscillations in the Pt-Pt/Pt-Ag bond lengths. The main issue is however, the strong correlations between several of the parameters in the model, which leads to a rather broad confidence interval in a full analysis and complications in determining small bond length changes. Excitation fraction and bond length changes are obviously correlated, but also changes in the Pt-Ag and Pt-Pt distance are correlated to some extend as the scattering signal is dominated by the distance between electron dense atoms in the molecule. The results from this analysis however shows that a geometrical optimization yielding realistic bond length distances are possible from the TR-WAXS data.

4.4 Summary

This chapter presented an experimental method to directly measure structural dynamics on a ground state potential surface by preparation of a vibrationally cold excited state through off-resonance photo excitation and subsequent measurement of the ground state "hole" dynamics. The method was successfully applied to the PtPOP transition metal complex in an XFEL solution experiment in order to measure the details of the sub-ps ground state Pt-Pt stretching mode by analysis of the X-ray scattering signal.

The experimental results were directly coupled to high-level QM/MM BOMD simulations to investigate the molecular details of the dynamics and the solvent-solute interactions. The analysis relied on assumptions of the population distributions but a direct comparison with the simulations allowed for an experimentally supported visualization of the dynamics on both the ground and excited state potential surfaces.

Further, an on-going analysis to optimize the ground and excited state structure of PtPOP with end-on coordination of Ag^+ was presented. An analysis of the excited state dynamics showed possible sub-ps dynamics of a structural vibrational mode yet to be determined.

We believe that the methods outlined in this chapter will have wide-ranging impact in the study of ground and excited state potential surfaces in chemical photoreactions.

Chapter 5

The Solvation Response to a Photo-Induced Solute Charge Change

This chapter describes the analysis of the Time-Resolved X-ray Scattering/Absorption XFEL data of the aqueous $I^- \rightarrow I^0$ photoreaction. The solvation shell changes in the reaction represents a simple case of solvent reorganizing upon a solute charge change in a chemical reaction and is a model system for a whole variety of chemical and biological systems. The time scale of the solvation changes are determined and the measured difference scattering signals are compared to classical MD simulations to give an experimentally supported visualization of the solvation dynamics. The electronic configuration is probed by the X-ray absorption measurements to couple the solvation dynamics to an increased electron back donation from the solvent to I^0. The chapter thus illustrates an example of how a combination of scattering and absorption XFEL data can be used to measure both ultrafast electronic and structural changes in the surrounding solvent shell (cage) of a chemical reaction.

5.1 Introduction

Solvation dynamics upon electronic structure changes in a solute, is one of the most studied phenomena in chemical physics [17, 18, 19], due to the solvation role in assisting, hindering or triggering chemical reactions. The dynamics have been studied both by using ultrafast optical measurements e.g. UV-VIS and IR laser techniques [17, 18] and by theoretical modelling [19, 83]. The femtosecond optical studies have traditionally been carried out on photo induced dipole moment changes in solvated dye molecules, probed by fluorescence, absorption or stimulated emission measurements. The optical studies can however not deliver the structure of the solvent shell before, during and after solvent rearrangement.

An approach based on solvated halides have been proposed as a simpler and more fundamental model system in order to gain a deeper insight into the solvent shell dynamics. Photo detachment of the valence p electron generates a free halogen atom with a dramatically different solvent shell structure due to changes in the electronic properties, as revealed by picosecond X-ray Absorption Fine Structure (XAFS) studies [84, 85]. The lack of further internal degrees of freedom for the simple system allows identification of the solvation dynamics in its purest form. Photo detachment of the halides leads to Charge-Transfer-To-Solvent (CTTS) states, which results in a well-separated halogen atom and a solvated electron (> 10 Å distance) well within the first picosecond [85].

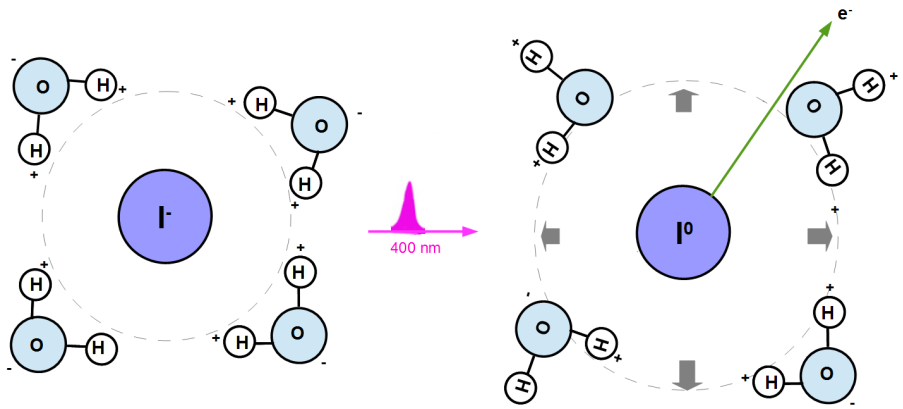

FIGURE 5.1: Illustration of the (simplified) structural dynamics of the $I^- \rightarrow I^0$ photoreaction pumped with 400 nm laser pulses. Upon photo-excitation of I^-, the surrounding water molecules reorient as a consequence of the photo abstraction of one electron from iodide. This will be investigated by combined time-resolved X-ray Absorption Spectroscopy and X-ray scattering with sub-ps resolution using an XFEL probe beam.

From a classical point of view, solvated halide atoms will affect the surrounding solvent shell molecules due to their charge. In the case of aqueous Iodide atoms (I^-) the negative charge will be solvated by the slightly positively charged hydrogens of the surrounding water molecules as illustrated in figure 5.1 (left). To a first approximation, it will give a solvation shell structure where all the hydrogen atoms in the nearest solvation shell will point inwards and move the whole solvent shell closer towards the Iodine atoms due to electrostatic interactions. There is however, a trade-off of this configuration with the energy cost in entropy and the mutual repulsion of hydrogens from different water molecules. The changes in the nearest solvent shell around a charged atom will in turn affect additional layers of the solvent.

Upon photo detachment of the electron in Iodide (I^0) and the loss of the negative charge, a dramatical change in the structure of the solvent shell is expected (figure 5.1, right). From a classical point of view the solute and solvent shell is no longer hold together by electrostatic interactions and the water molecules will lose their well-defined orientations. Therefore, the structural dynamics during the photo reaction is expected to be defined by two effects within the first picosecond; a rotation of the water molecules in the solvent shell and a dramatic expansion of the solvent shell. From a quantum mechanical point of view it may also be possible that I^0 receives a partial charge back donation from e.g. a few polar H_2O molecules, which thus are somewhat closer to the otherwise heavily expanded cage [85].

In this chapter the analysis of time-resolved X-ray scattering/absorption XFEL experiments aims to give direct structural/electronic information of the solvation dynamics in the aqueous $I^- \rightarrow I^0$ halide-halogen photoreaction. A direct comparison to the X-ray scattering calculated from MD simulations will allow for an experimentally supported visualization of the solvation dynamics.

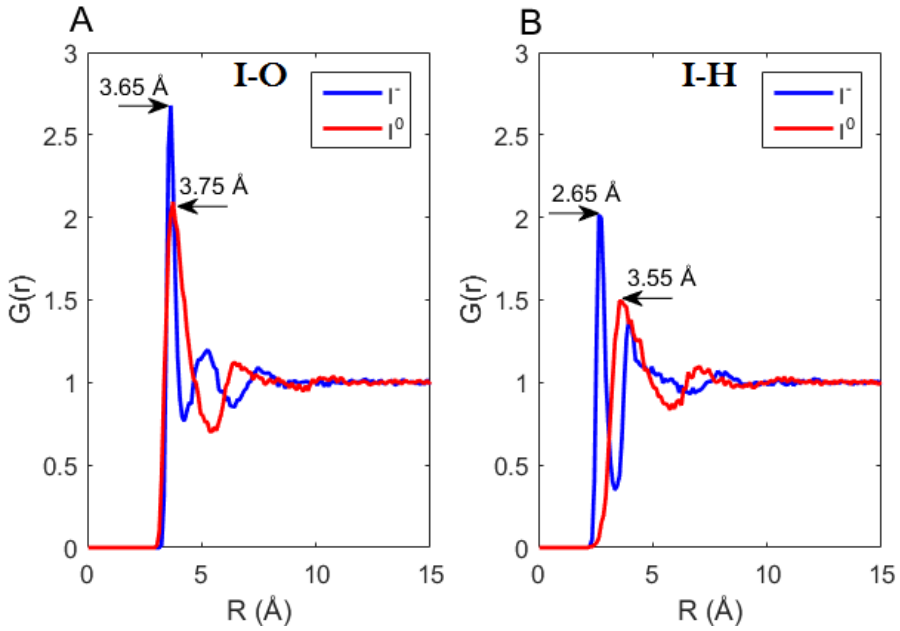

FIGURE 5.2: **A** and **B** show results from a classical Molecular Dynamics (MD) simulation of the $I^- \rightarrow I^0$ photoreaction. The I-O (**A**) and I-H (**B**) Radial Distribution Functions $g(r)$ (RDFs) show how the water molecules rotate away from their orientation in the very well-ordered solvation shell around I^- (blue) to an expanded and more disordered shell surrounding I^0 (red).

5.2 Classical MD Simulations

The classical Molecular Dynamics (MD) simulations were done by Elisa Biasin at the Technical University of Denmark. The purpose was to determine the Radial Distribution Functions $g(r)$ (RDFs) of the solvent shell around Iodine/Iodide (I^0/ I^-) and provide a visualization of the solvation dynamics. Calculations of the corresponding X-ray scattering patterns will allow for a direct comparison with the experiments.

The classical MD simulations of I^0/I^- were both (independently) solvated in a cubic box (30 Å size) of water molecules using the TIP4P-Ew potential. The I^0/I^- atoms were restrained at the center of the box and MD trajectories were calculated with a Nose-Hoover thermostat at 300 K. The RDFs were sampled in 0.1 Å radial bins and over 2000 individual simulation time steps over a total time interval of 2 ns.

Figure 5.2 shows the I-O and I-H RDFs of I^0/I^- atoms solvated in water, calculated from the classical MD simulations and a significant difference is observed in the solvation shell. The negatively charged I^- is solvated by the hydrogens of the surrounding water molecules that gives a well-defined solvation shell configuration where the hydrogen atoms in the nearest solvation shell points inward towards I^-. This can be seen by the first peak in the simulated I-H RDF being 1.0 Å closer to I^- than for the I-O RDF. The solvation shell of the neutral I^0 is less ordered with more similar I-O and I-H RDFs and the nearest water molecules no longer have a well-defined orientation.

With regards to the $I^- \rightarrow I^0$ photoreaction an expansion of the solvation cage is observed as the first peak in the I-H and I-O RDFs moves outward with $\sim$ 0.9 (from 2.65 Å to 3.55 Å) and $\sim$ 0.1 Å (from 3.65 Å to 3.75 Å) respectively. Previous

simulations performed by Pham et al. [85] shows some of the same trends, although the cage expansion was significant larger in these studies both for their classical MD ($\sim$ 1.6 Å and 0.7 Å) and QM/MM simulations ($\sim$ 1.0 Å and 0.3 Å). In the same study, an L3 EXAFS spectrum confirmed the general trends in the simulations, although the analysis did not allow for estimating the magnitude of the cage expansion.

5.3 Experimental Results

In the X-ray Absorption Spectroscopy (XAS) measurements the X-ray transient absorption through the sample was recorded by an X-ray diode around the L1 edge of $E = 5.188$ keV (using the XPP monochromator) and we denote $\Delta XAS(E,t)$ as the difference spectrum before and after hitting the sample.

The X-ray Diffraction Signal (XDS) was recorded in the forward direction by the large-area 2D CS-PAD detector [86] and undergone corrections as discussed in *Chapter 3*. Following these corrections, the 2D difference images were azimuthally integrated to yield one-dimensional $\Delta S(Q,t)$ difference scattering curves. The curves were then scaled to the liquid unit cell in electron units per solute molecule [87] to directly associate the magnitude of the change to an excitation fraction of the molecules.

5.3.1 L1-Edge Absorption Spectra

Figure 5.3 shows the recorded stationary L1-edge and the spectrum at 200 fs after laser excitation. Also shown is a selected subset of the transient spectra of the L1-edge recorded at time-delays between -300 fs and 1 ps together with a transient spectrum recorded at 10 ps time delay. In general, the transient signal shows a positive feature near 5.184 keV and a negative one at around 5.192 keV. The positive feature arises from the bound-bound 2s-5p transition, which is suddenly allowed after the electron has been expelled from the 5p orbital by the photo excitation of the sample [84]. The negative feature arises from the L1 absorption edge being shifted to higher energies as a result of the oxidation state as the less effective shielding of the core electrons leads to stronger binding energy.

The total amplitude of the transient spectra are increasing from 0, 50 to 200 fs which is a result of the IRF (Instrument Response Function) estimated to $\sigma \sim 40$ fs. The initial increase is followed by a slight decay on a ps timescale and the 10 ps trace is of lower amplitude than any other transients recorded after the full onset of the IRF.

5.3.2 X-ray Scattering Experiments

Figure 5.4 (A) shows the time-resolved XDS difference data rebinned in time intervals of 50 fs from -1 to 7 ps after laser excitation as $\Delta S(Q,t)$. The scattering analysis is based on a similar model as described in *Chapter 4*. The difference scattering signal arises mainly from two contributions, the local changes in the molecules in the proximity of the solute (ΔS_{cage}) and changes in the bulk solvent ($\Delta S_{solvent}$) [88]:

$$\Delta S_{total}(Q,t) = \Delta S_{cage}(Q,t) + \Delta S_{solvent}(Q,t) \tag{5.1}$$

The solvent term on a sub-10 ps timescale (before any significant thermal expansion occurs [45]) is generally well described by a difference signal $S_{dT}(Q) = (\partial S_{solvent}/\partial T)|_{\rho}$ which arrises from the molecular rearrangement due to solvent temperature increase

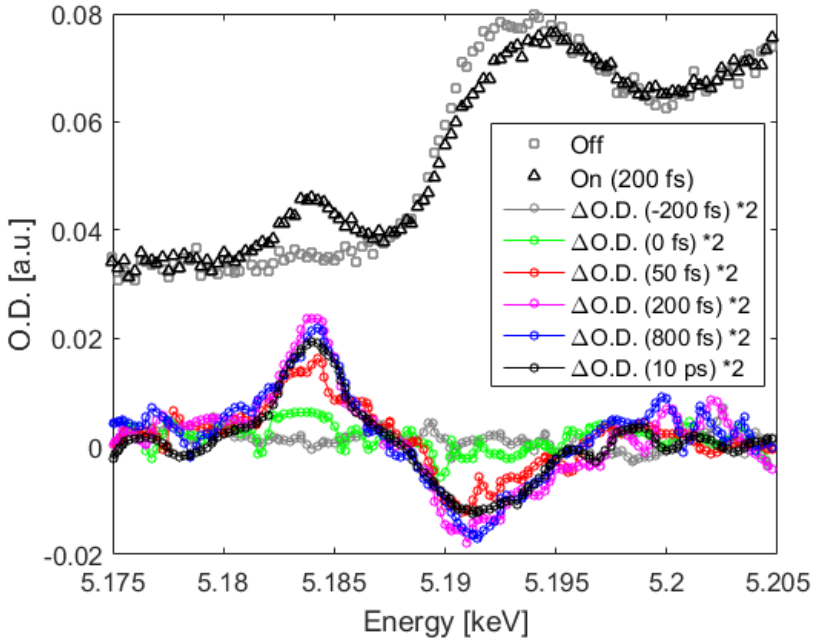

FIGURE 5.3: Time-resolved X-ray absorption data acquired at the iodide L1 edge. **Top:** X-ray absorption spectrum as a function of energy with (triangles) and without (squares) the pump laser pulse arriving before the probe X-ray pulse. A distinct pre-edge feature appears at 5.184 keV as electron abstraction leaves a hole in the 5p state and an edge shift related to the charge change. **Bottom:** Difference spectra at selected time delays, showing the prompt appearance and decay of the two features.

ΔT [44]. This term was measured in a separate experiment on neat water [43]. Further a $S_{dT2}(Q)$ term is included in the model which is a higher order heat effect and can be estimated from MD simulations [43].

The $\Delta S_{cage} \approx \alpha \Delta S_{cage,MD} = \alpha(S_{cage,I^0} - S_{cage,I^-})$ term is estimated by using the Debye equation on the pairwise RDFs [29] from the classical MD simulations of Iodine and Iodide in their "equilibrium"/"stationary" configuration (see figure 5.2). α is the scaling factor of the simulated cage signal. The total cage signal $\Delta S_{cage}(Q)$ is then to a first approximation assumed to be linearly related to the simulated signal $\Delta S_{cage,MD}(Q)$ at all time delays. The full difference signal can then be modelled as:

$$\Delta S_{tot}(Q,t) = \alpha(t)\Delta S_{cage,MD}(Q) + \Delta T(t) S_{dT}(Q) + \Delta T_2(t) S_{dT2}(Q) \qquad (5.2)$$

Figure 5.4 (A and B) shows the result of modelling the total scattering difference signal at all the investigated time delays with a linear combination of these three terms. Figure 5.4 (C) compares the XDS difference signal at 2 ps to the simulated difference signal. Very good agreement is observed from the residuals, supporting that the XDS signal is indeed monitoring the dynamics of the formation of the new solvent shell.

From the amplitude of the plateau at long time delays the excitation fraction has been estimated to $\sim$ 4 %, by comparing the magnitude of the difference scattering

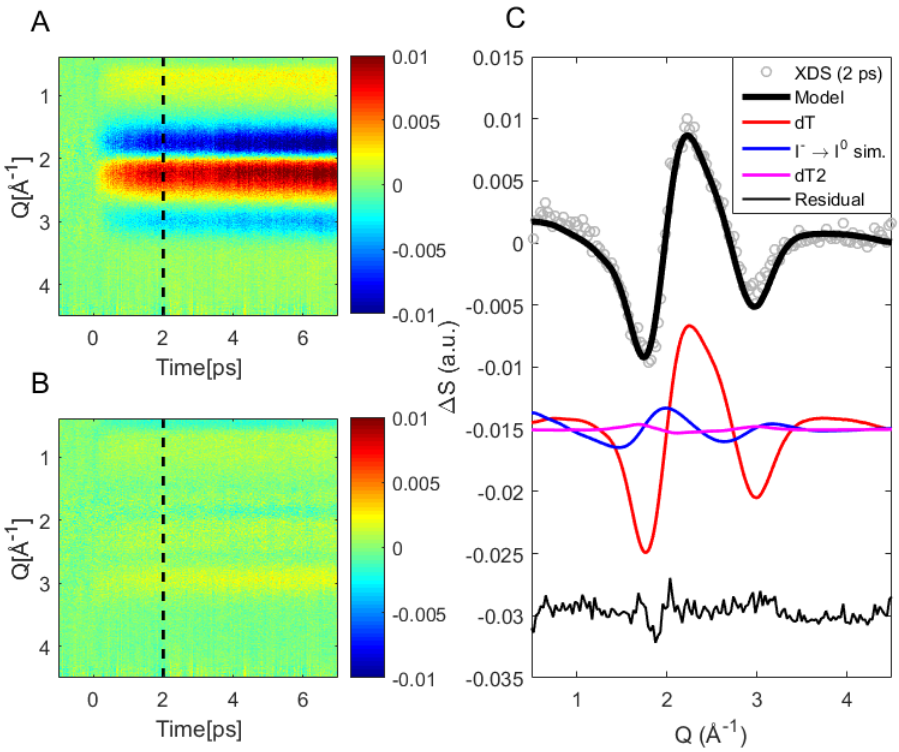

FIGURE 5.4: Time-resolved X-ray scattering (TR-XDS) difference signal and fit results. **A:** TR-XDS signal of the aqueous I^- to I^0 photo reaction as a function of time after laser excitation. **B:** The residual after subtracting the structural model. **C:** A comparison of the TR-XDS data (grey) at 2 ps and the structural model (black) and their residual (bottom, black). (middle) The structural model consist of contributions from the water heating (red and purple) and a change in the Iodine water cage estimated from the classical MD simulations (blue).

signal to the magnitude of the liquid water peak in the total scattering signal.

To provide a stronger argument for the existence of the cage component in the data set, the XDS data from a neat water experiment (prior to the Iodide experiment) was subtracted from the iodine XDS data (figure 5.5, top). Then the remaining signal was analyzed with an SVD analysis $\Delta S(Q,t) = \mathbf{USV^T}$ (see *Section 4.2.1*) with the strongest components shown in figure 5.5 (middle, bottom). Two clear SVD components can be seen from the analysis clearly resembling the simulated cage signal from the MD simulations (1st component) and the leftovers of the solvent temperature signal (2nd component).

5.3.3 Kinetics

Figure 5.6 (purple) shows the time evolution of the amplitude of the 5.184 keV peak from the L1 edge XAS experiments. The amplitude of the peak increases on a sub 100 fs timescale to its maximum value in agreement with the prompt creation of a 5p hole during the electron detachment and the IRF of $\sigma \sim 40$ fs.

A decay in intensity of this feature is observed and additional measurements at 9.5-10.5 ps (not shown here) show that the majority of this decay happens during the

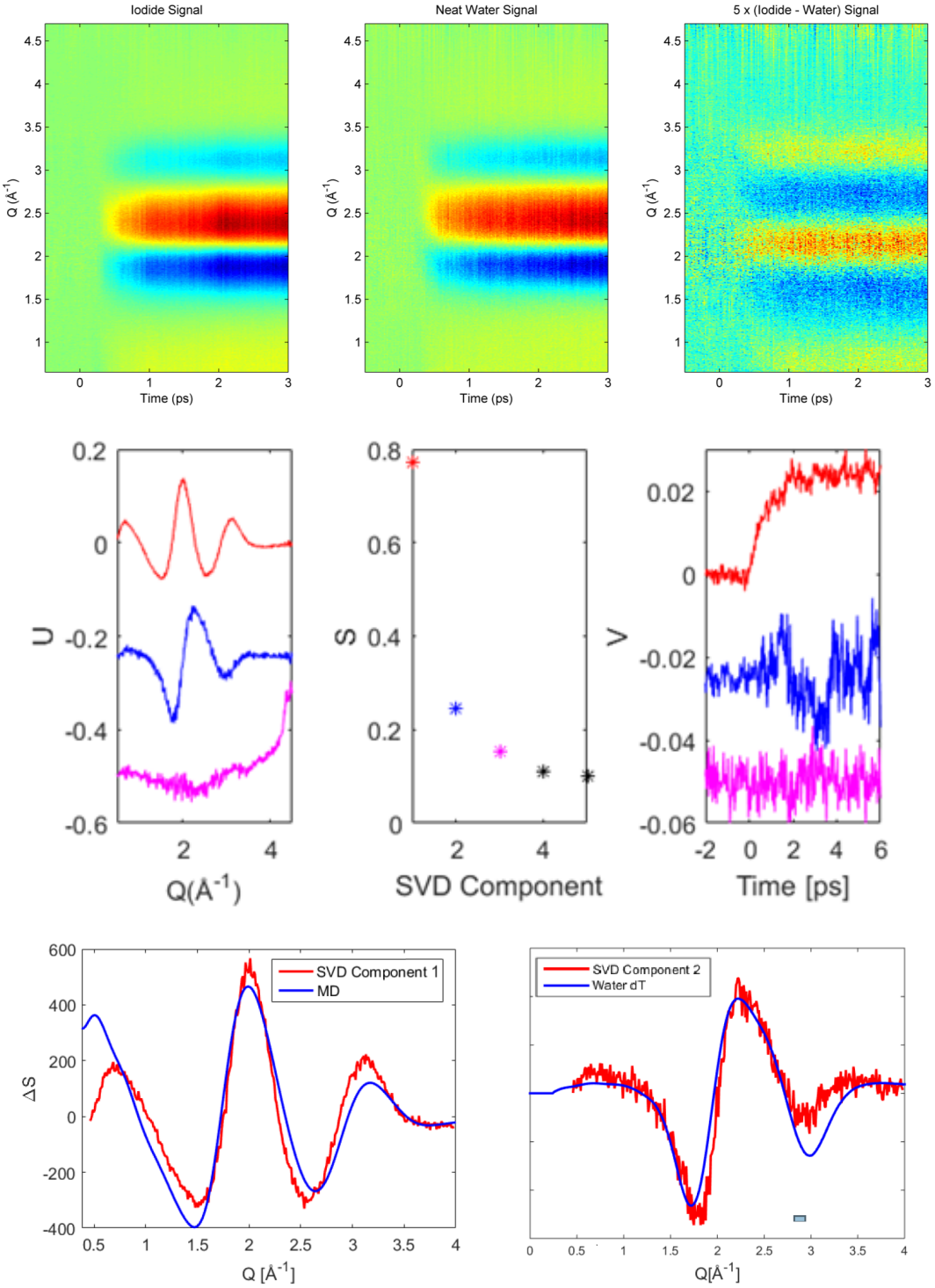

FIGURE 5.5: **Top:** XDS data from aqueous iodide (left) and neat water (middle) excited at 400 nm with 600 μJ per pulse. (right) shows the iodide signal after subtracting the water signal. **Middle:** A singular value decomposition (SVD) of the (iodide - water) signal with the three strongest components highlighted by colors (middle). **U** describes the fundamental Q-dependent components in the data (left) with a time revolution given by **V** (right). **Bottom:** The two strongest SVD components resembles the simulated cage signal from the MD simulations (left) and the leftovers of the solvent temperature (right).

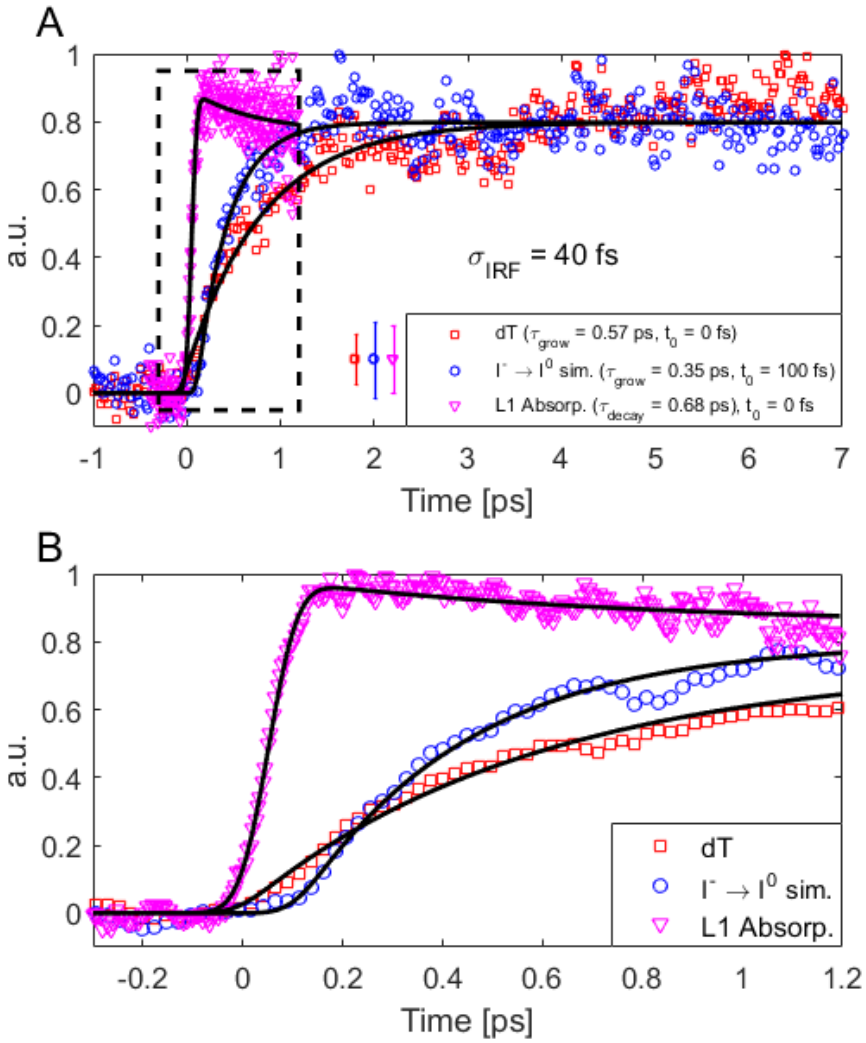

FIGURE 5.6: Results from the structural model fit (blue and red) to the TR-XDS data and the amplitude of the 5.184 keV peak (purple) from TR-XAS. **A:** The results from the first 7 ps after laser excitation scaled to maximum amplitude with the best exponential fits broadened by the IRF. **B:** shows the results from the featured box with a 5 pt smoothing. The cage contribution exhibits a possible delay of $\sim$ 100 fs compared to the solvent temperature increase.

first few picoseconds and that the signal at 10 ps has decreased to around 85 % of its maximum value. For those reasons the signal has been fitted with a step function at t_0, with an exponential decay to a baseline comprising 85 % of the signal, convoluted and broadened by the IRF (σ = 40 fs):

$$f_{XAS}(t) = \text{Gauss}(\sigma = 40 \text{ fs}) \otimes \begin{cases} 0 \text{ if } t < t_0 \\ A \cdot (0.85 + 0.15 \cdot e^{-\frac{(t-t_0)}{\tau_{XAS}}}) \text{ if } t > t_0 \end{cases} \tag{5.3}$$

The estimated decay time from the fit is $\tau_{XAS} = 0.68 \pm 0.40$ ps.

Figure 5.6 (blue and red) shows the solvent temperature increase and the cage contribution obtained from applying the structural model in equation (5.2) to fit the time-resolved XDS measurements (figure 5.4). Both these signals have been fitted with an IRF broadened single exponential grow-in at $t = t_0$ with t_0 as a free parameter.

$$f_{XDS}(t) = \text{Gauss}(\sigma = 40 \text{ fs}) \otimes \begin{cases} 0 \text{ if } t < t_0 \\ A \cdot (1 - e^{-\frac{(t-t_0)}{\tau}}) \text{ if } t > t_0 \end{cases} \tag{5.4}$$

The fit to the solvent temperature increase shows a time constant of $\tau_{\Delta T} = 0.57 \pm 0.07$ ps and a time-zero of $t_0 = -10 \pm 30$ fs. In general, the time-evolution is very similar to a neat water experiment measured subsequent to the Iodide experiment and no new features are observed in this signal on the measured timescale. The time constant for the cage term $\tau_{cage} = 0.35 \pm 0.04$ ps (at a time-zero of $t_0 = 100 \pm 30$ fs) represents the characteristic timescale of the grow-in of the XDS signal arising from the formation of the new solvent cage.

5.4 Discussion

The time-resolved XDS data (figure 5.4) was found to be dominated by a single component (apart from the components present in a pure water experiments) that strongly resembles the simulated signal from classical MD calculations of the solvent cage changes. This component grows in with a $\sim 0.35 \pm 0.04$ ps time constant (figure 5.6). The time-scale of the grow-in of the XDS signal could match the 0.68 ± 40 ps time scale (figure 5.3 and 5.6) of the $\sim 15\%$ (partial) decay of the amplitude of the L1-edge XAS difference signal, but the later is dominated by large uncertainties. These results could be significantly improved by obtaining XAS measurements at time delays of 1.2-7.0 ps, to reduce the uncertainties.

A simple explanation for both observations could be that the formation of the new solvation shell allows for a larger degree of back donation of electron oxygen lone-pairs from the solvent cage to the I^0 atoms, and that we are tracking both electronic and structural aspects of the solvation. The change in the solvation shell during the photoreaction does allow for a more direct interaction between I^0 and the oxygen lone pairs, due to the break-up of the more ordered shell around I^- (figure 5.1-2). Thus, the XDS data provides a direct handle on (in particular) the I-O RDF (allowing us to follow the structure as the new solvation shell forms), and the L1-edge amplitude provides a direct handle on the total back donation of charge from the oxygen atoms of the water molecules to the vacated 5p orbital of I^0 following the photoreaction.

Pham et al. [85] has reported that the sub-picosecond L1 transients exhibit a weak broadening (typically less than 1 eV) with respect to the 50 ps transient on the high energy side of both their positive and negative features. They assigned it to the creation of an intermediate $I^0(OH_2)$ complex on a sub 10 ps timescale and supported it with quantum simulations [85]. In our experiments, there are some differences between the shapes of the traces at different time delays but it is within the noise of the measurement and we do not see a similar L1 transient shift to higher energies on a sub 10 ps time scale. This indicates that the shape of the transient XAS spectra is completely controlled by the edge-shift upon oxidation of the I^-. Thus, it is the shift in position of these features with the oxidation that give rise to the difference signal, not structural changes in the solvation shell.

The time constant of the cage grow-in of 0.35 ± 0.04 ps corresponds reasonable well to QM/MM MD simulations which predicts a cage expansion with characteristic timescales of 200-300 fs [85]. The $\sim$ 100 fs delay of the onset of the cage term compared to the solvent heating could possibly be related to the time scale of ejecting the electron from the vicinity of the solvent cage. It is however likely that the linearity of the classical model predicted in equation (5.2) does not apply to the structural dynamics on ultrafast timescales (1-200 fs) or that the cage expansion happens in different steps which shows up differently in the scattering patterns (scattering is dominated by changes in the I-O RDF and e.g. rotations of the hydrogen bond will be much weaker).

Bradforth et al. [89, 90] and Laubereau et al. [91] have studied electron production under resonant single photon excitation and showed that for aqueous iodide the ejection of the electron from the solvation cage happens within 200 fs followed by solvent rearrangements around the electron completed at $\sim$ 2 ps. These studies only investigate the solvation effect around the free electron, which might have a significant different timescale than for the one around the neutral iodine atom.

In an ultrafast fluorescence spectroscopy experiments of Iodide [92] an initial short-lived emission from the sample of around $\sim$ 60 fs was observed together with a broad distribution of decays of 100-400 fs. This was related to an initial state relaxing to a broad distribution of lower-energy Charge-Transfer-To-Solvent (CTTS) states upon rearrangement of the solvent cage and with electron ejection occurring from these states. Studies with time-resolved photoelectron spectroscopy shows creation of an I/e^- contact pair on a time scale of $\sim$ 200 fs and a solvent-separated state on a timescale of $\sim$ 1 ps [93, 94]. None of these studies directly measures the solvation shell changes around the solute upon the photoexcitation.

5.5 Outlook - The Hydrated Electron

The model discussed in this chapter does only include the scattering signal from solvation shell changes around the solute atoms themselves and not the signal arising from the creation of a solvation shell around the photo-detached electrons. This is justified by considering the much higher number of electrons in the solute atoms and the data quality did not allow for identifying an additional (and small) component in the XDS data (figure 5.5).

Despite the hydrated electron being a very fundamental quantum mechanical system,

there is still considerable debate over the molecular structure. Different quantum simulations have produced different kinds of solvation shell structures in reasonable agreement with experiments [95]. The predicted structures can roughly be divided into two groups; i) The electron occupies a cavity due to the Pauli exclusion principle and the impossibility for the electrons to occupy the same space as the water molecules molecular orbitals [96, 97, 98]; ii) The hydrated electron acts as a diffuse ball of charge which can occupy multiple voids between the water molecules with very little direct overlap [99, 100]. The electron then occupies a region of enhanced water density with many molecules in the interior of the electrons charge density.

The improvements of XFEL facilities has been in a continuous progress for many years. The hope is that improved data quality will eventually allow us to provide real structural evidence of the solvation shell around a hydrated electron and conclude this much-debated problem in solvation chemistry.

5.6 Summary

This chapter described the analysis of the Time-Resolved X-ray Scattering/Absorption XFEL data of the aqueous $I^- \rightarrow I^0$ photoreaction. The time scale ($\approx$ 350 fs) of the solvation changes was determined and the measured difference scattering signals were compared to classical MD simulations to give an experimentally supported visualization of the structural solvation dynamics following the photoreaction. Based on this analysis the first solvation shell was found to expand upon photo-detachment of the electron, as the hydrogens of the water molecules are no longer interacting with negatively charged I^- atoms.

The electronic configuration was probed by the X-ray absorption measurements to couple the structural solvation dynamics to an increased electron back donation from the solvent to the I^0 atoms. An effect which is related to interactions with the oxygen lone pairs in the first solvation shell. The chapter thus illustrated an example of how a combination of scattering and absorption XFEL data can be used to measure both ultrafast (sub-ps) electronic and structural changes in the surrounding solvent shell of a photochemical reaction.

Chapter 6

Revealing Structural Information with Cross Correlation Analysis

X-ray Cross Correlation Analysis (XCCA) is a powerful tool to analyze the anisotropic part of the scattering signals from X-ray Free-Electron (XFEL) experiments. It often reveals additional information about the sample, as it takes advantage of the signal in the full 2-dimensional space of the detectors, instead of reducing the data to 1-dimensional scattering curves by azimuthal averaging. The aim of this chapter is to introduce the topic of angular intensity correlations in X-ray diffraction. Further, it will be shown how it can be applied to the PtPOP XFEL data introduced in *Chapter 4* and which results can be obtained from such an analysis. This chapter revisits the content of **Paper I**.

6.1 Introduction

The method of angular intensity correlations in X-ray diffraction has been around for almost 40 years, but has recently drawn an increased amount of attention due to development in X-ray sources and instrumentation. Imagine an X-ray scattering experiment from a solution of molecules as a collection of 2-dimensional detector images at different time delays, as discussed in *Chapter 2* and *Chapter 3*. These data has typically been analyzed as isotropic Debye-Scherrer rings which traditionally has been the case for disordered systems measured on relatively weak and low coherence sources [101, 102]. At such sources the necessary exposure time to get a sufficient signal, is typically longer than the characteristic rotational times of the molecules in question, which wash out any anisotropic signal on the detectors. The measured signals only consist of isotropic Debye-Scherrer rings from an average of all orientations of the solute molecules.

It is an entirely different story on a brilliant X-ray source with a high degree of coherence and a very short exposure time (pulses of few femtoseconds) as is obtainable on a X-ray Free-Electron Laser. Here the instantaneous positions and orientations of the solute molecules can be seen as a collection of speckles on the 2-dimensional detector images that opens up for a completely new type of experiments [21, 23, 103]. Due to the high penetration of X-rays on a solution of a few microns, the multiple scattering effects can be neglected which makes X-rays very attractive for these experiments compared to e.g. visible light or electrons. The Correlations between scattered intensity $I(\boldsymbol{q}, t)$ in different directions (e.g. $\boldsymbol{q_1}$,$\boldsymbol{q_2}$) at the same or different times (t) averaged over many measurements, can be defined as:

$$C(\boldsymbol{q}_1, \boldsymbol{q}_2, t, t') =< I(\boldsymbol{q}_1, t) I(\boldsymbol{q}_2, t') > \tag{6.1}$$

In this thesis the Cross-Correlation function (CCF) on a 2-dimensional detector image will be defined as calculated on the same scattering ring ($\|\boldsymbol{q}_1\| = \|\boldsymbol{q}_2\|$) and at the same time ($t = t'$), where $\boldsymbol{q}$ is defined in the polar coordinate system of the 2D detector (q, θ):

$$C(q, \Delta) =< \tilde{I}(q, \theta)\tilde{I}(q, \theta + \Delta) >_\theta \tag{6.2}$$

Where $\tilde{I}(q, \theta) = I(q, \theta) - < I(q, \theta)_\theta >$ is the intensity fluctuation, Δ is the angular coordinate and $< f(\theta) >_\theta$ is the angular average of the function.

The hope is that X-ray Cross Correlation Analysis (XCCA) can be developed as a tool to obtain additional information from a sample than has traditionally been extracted from the isotropic patterns (mainly average pair distribution functions) and thereby help solving structures of molecules in solution even to a high resolution [20]. Another useful application is the unveiling of hidden symmetries, as the technique is particularly sensitive to locate n-fold symmetries in a system [22, 104].

6.2 Theory

The CCFs presented in equation (6.2) provides information of the structure and symmetries of a system that will be investigated from a theoretical point of view in this section. It turns out to be convenient to decompose the CCFs using an angular Fourier series on a ring of radius q:

$$C(q, \Delta) = \sum_{n=-\infty}^{\infty} C_q^n e^{in\Delta} \tag{6.3}$$

$$C_q^n = \frac{1}{2\pi} \int_0^{2\pi} C(q, \Delta) e^{-in\Delta} d\Delta \tag{6.4}$$

By combining equation (6.2-4) and using the Fourier convolution theorem [26]:

$$C_q^n = I_q^{n*} \cdot I_q^n \tag{6.5}$$

Where I_q^n are the similar angular Fourier components of the scattered intensity:

$$I(q, \theta) = \sum_{n=-\infty}^{\infty} I_q^n e^{in\theta} \tag{6.6}$$

$$I_q^n = \frac{1}{2\pi} \int_0^{2\pi} I(q, \theta) e^{-in\theta} d\theta \tag{6.7}$$

As the scattered intensity is always a real value it follows that $I_q^{-n} = I_q^{n*}$ and $C_q^{-n} = C_q^{n*}$. Further $C_q^0 = 0$ by the definition of the CFF, so equation (6.3) can be rewritten as:

$$C(q, \Delta) = 2 \sum_{n=1}^{\infty} C_q^n cos(n\Delta) \tag{6.8}$$

$$C_q^n = \|I_q^n\|^2 \tag{6.9}$$

Which shows that for the values of q where one Fourier component dominates, a strong single cosine behavior can be observed in the CCF. These components are related to the structure and symmetry of the system [24, 25, 26].

As discussed in *Chapter 2* the Intensity from a disordered sample of N particles can be calculated from the electron densities ρ_k and be split into two terms; one from the collection of individual particles ($k_1 = k_2$) and one from the cross terms from correlations between the particles ($k_1 \neq k_2$):

$$I(\boldsymbol{q}) = [\sum_{k_1=k_2}^{N} + \sum_{k_1 \neq k_2}^{N}] \int\int \rho_{k_1}^{*}(\boldsymbol{r_1})\rho_{k_2}(\boldsymbol{r_2})e^{i\boldsymbol{q}\cdot(\boldsymbol{R}_{k_2,k_1}+\boldsymbol{r}_{21})}d\boldsymbol{r_1}d\boldsymbol{r_2} \tag{6.10}$$

Where $\boldsymbol{R}_{k_2,k_1} = \boldsymbol{R}_{k_2} - \boldsymbol{R}_{k_1}$ are the radius vectors between the particles (k_1 and k_2), and $\boldsymbol{r}_{21} = \boldsymbol{r}_2 - \boldsymbol{r}_1$ are the vectors internally in the particles. In this thesis the main interest are dilute samples, as in typical solution experiments, meaning that the cross terms can be ignored. The total scattered intensity is then given by a sum of the scattering intensities from the individual particles (only first term in equation (6.10) where $k_1 = k_2$):

$$I(\boldsymbol{q}) = \sum_{k}^{N} I_k(\boldsymbol{q}) = \sum_{k}^{N} \int\int \rho_k^{*}(\boldsymbol{r_1})\rho_k(\boldsymbol{r_2})e^{i\boldsymbol{q}\cdot\boldsymbol{r}_{21}}d\boldsymbol{r_1}d\boldsymbol{r_2} \tag{6.11}$$

To get a better understanding of the meaning of the Fourier components described in this section it is useful to first consider the 2-dimensional case. Here all radius vectors are defined in a 2D plane (x, y) with an angle θ, and the electron density of the particles transforms to a projected electron density $\tilde{\rho}_k(\boldsymbol{r}) = \int \rho_k(\boldsymbol{r}, z)dz$. It can be shown that for a plane wave front illumination of such a system, the uneven Fourier components of the intensity disappear [24].

Similar to equation (6.6) the scattered intensity from one individual reference particle k_1 can be decomposed in an angular Fourier transformation:

$$I_{k_1}(q, \theta) = \sum_{n=-\infty}^{\infty} I_{q,k_1}^{n} e^{in\theta} \tag{6.12}$$

Let us now consider the scattered intensity I_{k_2} from a particle k_2 rotated with the angle ψ_2 in the 2D plane compared to particle k_1. If all particles in the system are identical the intensity is then given by $I_{k_2}(q, \theta) = I_{k_1}(q, \theta - \psi_2)$. By applying the shift theorem for the Fourier transform [105] the Fourier components of the scattered intensity are given by $I_{q,k_2}^{n} = I_{q,k_1}^{n} e^{-in\psi_2}$. This relation can be used to calculate the total intensity Fourier components, for an ensemble of N particles with different orientations:

$$I_q^n = \sum_{k=1}^{N} I_{q,k}^{n} = I_{q,\Psi}^{n}(\sum_{k=1}^{N} e^{-in\psi_k}) = I_{q,\Psi}^{n} A_n \tag{6.13}$$

Where k_1 has been replaced with Ψ to signify its role as an atom with a reference orientation $\psi_1 = 0$. By using equation (6.9):

$$C_q^n = \|I_{q,\Psi}^{n}\|^2 \|A_n\|^2 \tag{6.14}$$

Where $A_n = \sum_{k=1}^{N} e^{-in\psi_k}$ is called the Random Phasor Sum. The Fourier components C_q^n are then a product of two terms. The first part depends on the internal structure through the electron density in equation (6.11), and the second part is the Random Phasor Sum that depends on the orientational distribution. The statistical behavior of the random phasor sum for e.g. Gaussian, completely oriented and uniform

distributions has been investigated in literature for 2-dimensional systems [26].

The first term of equation (6.13) can be related to the projected electron density of the reference particle $\tilde{\rho_\Psi}$ (defined earlier) as [24]:

$$I^n_{q,\Psi} = \int\int \tilde{\rho_\Psi}^*(\boldsymbol{r_1})\tilde{\rho_\Psi}(\boldsymbol{r_2})J_n(q\|\boldsymbol{r}_{21}\|)e^{-in\phi_{r_{21}}}d\boldsymbol{r_1}d\boldsymbol{r_2} \tag{6.15}$$

Where $\phi_{r_{21}}$ is the angle of the vector $\boldsymbol{r}_{21}$ in the detector plane, and $J_n(\rho)$ are Bessel functions. It can be seen from the structure of this equation that it is strongly dependent on the symmetry of the particles, and selection rules can be identified for the non-zero Fourier components which can be used to identify symmetries of the particles [24, 25, 26].

A more general solution to the Fourier components of the total scattered intensity for the 3-dimensional case in a dilute sample, can be shown to be [106]:

$$I^n(q^\perp, q^z) = (i)^n \sum_k^N e^{-iq^z z_{21}} \int\int \tilde{\rho}^*(\boldsymbol{r_1^\perp}, q^z)\tilde{\rho}(\boldsymbol{r_2^\perp}, q^z)J_n(q^\perp\|\boldsymbol{r}_{21}^\perp\|)e^{-in\theta_{r_{21}^\perp}}d\boldsymbol{r_1^\perp}d\boldsymbol{r_2^\perp} \tag{6.16}$$

Here the scattering vector $\boldsymbol{q} = (\boldsymbol{q}^\perp, q^z)$ has been split into a part q^z parallel to the beam and a part $\boldsymbol{q}^\perp$ perpendicular to the beam. Likewise the radius vectors has been split into a z-component z_{21} and a perpendicular component $\boldsymbol{r}_{21}^\perp$.

It can be shown that due to the curvature of the Ewald sphere (non-zero q^z component), the odd Fourier components will no longer be zero as in the case of a 2-dimensional analysis. This complicates the analysis of such 3-dimensional systems significantly even if it shares some of the same characteristics as the 2-dimensional case. However, it may also reveal new information and symmetries that cannot be observed in small-angle scattering [24], because these odd components become negligibly small for experimental conditions corresponding to a flat Ewald sphere (e.g. small-angle scattering).

6.3 Simulations: Scattering from a Solution of Molecules

To simulate the anisotropic scattering from a solution of molecules the Debye equation is no longer sufficient because it assumes a perfect orientational averaging, as was the assumption for the isotropic analysis described in *Chapter 4*. In fact in this chapter the point of interest are the variations from the Debye equation, either due to a non-isotropic distribution of molecular rotations or due to a statistical discrepancy from a complete well-defined distribution of rotations. For that reason it is more convenient to start out with the more fundamental equation of X-ray scattering intensity from a single molecule (*Chapter 2.2*), given by the atomic positions $\boldsymbol{r}_j$ and their atomic form factors $f_j(\boldsymbol{Q})$:

$$I^{mol}(\boldsymbol{Q}) = \|F^{mol}(\boldsymbol{Q})\|^2 = \|\sum_j f_j(\boldsymbol{Q})e^{i\boldsymbol{Q}\cdot\boldsymbol{r}_j}\|^2 \tag{6.17}$$

In the approximation of a dilute disordered sample where the mean distance between the molecules is larger than the coherence length of the incoming beam, interference between the X-rays scattered from different molecules can be neglected. The total scattered intensity can then be represented as a sum of intensities from the individual

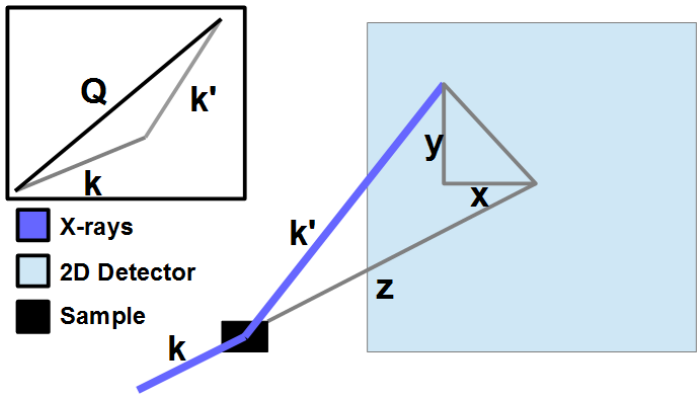

FIGURE 6.1: Shows the geometry of a typical scattering experiment. A horizontal beam of X-rays ($\boldsymbol{k}$) hits the sample and is scattered ($\boldsymbol{k'}$) unto a 2D pixel detector. The position of every pixel of the detector is given by the distance from the sample z and a set of coordinates (x, y).

molecules in the system:

$$I^{Total}(\boldsymbol{Q}) = \sum_{N} I^{mol}(\boldsymbol{Q}) \tag{6.18}$$

The excited and ground state PtPOP structures were modelled by DFT calculations as described in *Chapter 4*.

The next step is to consider the geometry of a typical scattering experiment. A horizontal beam of X-ray hits a sample and is scattered unto a 2D pixel detector as illustrated in figure 6.1. Every pixel on the detector corresponds to a specific $\boldsymbol{Q}$ value given by its position (x, y, z) and the wave length λ of the X-rays. The $\boldsymbol{Q}$ vector is defined by the wave vector of the incoming ($\boldsymbol{k}$) and scattered ($\boldsymbol{k'}$) X-rays:

$$\boldsymbol{Q} = \boldsymbol{k} - \boldsymbol{k'} \tag{6.19}$$

Now elastic Thomson scattering is assumed ($\|\boldsymbol{k}\| = \|\boldsymbol{k'}\|$) and by using the geometry on figure 6.1, the scattering vector is given by:

$$\boldsymbol{Q} = \frac{2\pi}{\lambda}\left(\begin{bmatrix}1\\0\\0\end{bmatrix} - \frac{1}{\sqrt{x^2+y^2+z^2}}\begin{bmatrix}x\\y\\z\end{bmatrix}\right) \tag{6.20}$$

By combining equation (6.17), (6.18) and (6.20) the scattering on every pixel of the detector can be calculated from a given molecule, using the positions $\boldsymbol{r}_j$ of all the j atoms in the molecules and the atomic form factors $f_j(\boldsymbol{Q})$. The positions have to be in the same coordinate system as the scattering experiment.

To calculate the scattering from a collection of molecules with different orientations, a new set of coordinates $\boldsymbol{r}_j^{rot}$ are calculated for every molecule by rotating it around the y and z axis of the experiment. For this purpose, the well-defined rotation matrices are used:

$$R_y(\theta) = \begin{bmatrix}\cos(\theta) & 0 & \sin(\theta)\\ 0 & 1 & 0\\ -\sin(\theta) & 0 & \cos(\theta)\end{bmatrix}, R_z(\theta) = \begin{bmatrix}\cos(\theta) & -\sin(\theta) & 0\\ \sin(\theta) & \cos(\theta) & 0\\ 0 & 0 & 1\end{bmatrix}$$

The overall structure of the program to simulate the anisotropic scattering is then to:

i) rotate a molecule given by $\boldsymbol{r_j}$ to obtain a new set of rotated coordinates $\boldsymbol{r_j^{rot}}$;
ii) calculate the scattered intensity on each pixel of the detector using the rotated coordinates and equation (6.17-20);
iii) repeat i)-ii) for molecule 2 to N (total number of molecules);
iv) sum up the scattered intensity for all the rotated molecules to obtain the total scattering.

Figure 6.2 shows the PtPOP molecule as an example (only Pt atoms shown for simplicity) of how to randomly rotate a molecule in an isotropic way. The first step will be to rotate the molecule around the z-axis, the axis of the Pt-Pt bond, choosing a rotation angle θ_{z1} randomly between 0 and 360 degrees. The next step is then to ensure that the molecule is rotated in such a way that for a huge collection of molecules, the Pt atoms are evenly distributed over a sphere as also illustrated on figure 6.2. This can be done by additional rotations around the y-axis (θ_y) and z-axis (θ_{z2}). However, if both these angles are picked randomly between 0 and 360 degrees, it will not give an isotropic distribution of orientations but a distribution with more orientations close to the poles of the sphere. The reason is that if the molecule is first rotated with a random angle around the y-axis, then the additional random rotation around the z-axis will be on a circle with a different circumference dependent on the first rotation, as illustrated on figure 6.2 (top,right). Therefore, there will be a denser population around the poles where the circumference is small.

It is then important to pick an angle θ_y that ensures an even distribution on the sphere. A way to do this was to develop an algorithm I called the SIC (Sphere-In-Cube) which can be described by the following steps:

i) pick a random point (x, y, z) inside a cube of dimensions $[-1, 1] \times [-1, 1] \times [-1, 1]$;
ii) if $x^2 + y^2 + z^2 > 1$ then repeat i). This ensures that the point is picked randomly within a sphere with a radius of one;
iii) read out the angle between the xz-plane and the vector going from $(0, 0, 0)$ to $(x, y, 0)$. Use it as θ_{z2} (it is now randomly distributed between 0 and 360 degrees);
iv) read out the angle between the vector from iii) and the vector from $(x, y, 0)$ to (x, y, z). Use this angle as the θ_y angle. This angle will not be randomly distributed between 0 and 360 degrees but instead have a distribution weighted according to the circumference of the circles illustrated in figure 6.2 (top, right).

In this way, an isotropic distribution of molecular rotations is ensured:

$$\boldsymbol{r}_j^{rot} = R_z(\theta_{z2}) R_y(\theta_y) R_z(\theta_{z1}) \boldsymbol{r}_j \tag{6.21}$$

If a random angle distribution but with e.g. a Gaussian, completely oriented or a cosine squared shape are desired around the y axis, then this can be implemented by adding it as an additional condition to selection rules of the θ_y angle. Figure 6.3 shows examples of simulations of such distributions for the PtPOP molecules. The difference scattering patterns are calculated by subtracting the simulation results of the ground state from the simulation results of the excited state.

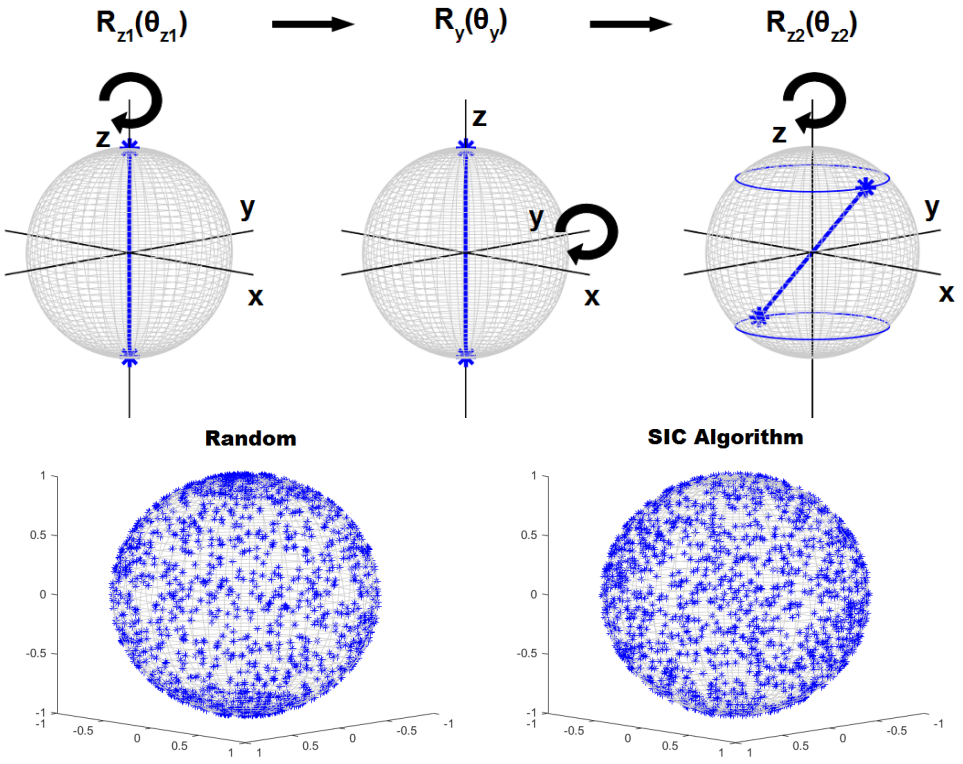

FIGURE 6.2: **Top:** Rotation of the PtPOP molecule (only Pt-Pt bond is shown) using the rotation matrices $R_z(\theta_{z2})R_y(\theta_y)R_z(\theta_{z1})\boldsymbol{r}_j$. **Bottom:** Pt atom positions plotted for 700 different orientation using a random selection of θ_y from 0-360 degrees (left) and a selection using the SIC algorithm (right), where the probability is weighted according to the length of the circumferences shown on the sphere to the top right. Notice the denser population at the poles in the first case.

6.4 X-ray Cross-Correlation Analysis

To perform an X-ray Cross-Correlation Analysis a number (M) of diffraction patterns are used. For a practical application one would normally need to average a large number (M typically of the order of 1,000 to 10,000) of 2D detector images to obtain reliable information about symmetry and structure due to statistical variations of the CCFs [107]:

$$C(q,\Delta)_M = \frac{1}{M}\sum_{m=1}^{M}\{C(q,\Delta)\}^m \tag{6.22}$$

The intensities $I(q,\theta)^i$ and $I(q,\theta)^j$ are the measured intensities on two different diffraction images (i and j). From that, the two-point CCF is then calculated for every diffraction pattern ($i = j$) and between every diffraction pattern ($i \neq j$) using the definition in equation (6.2):

$$C(q,\Delta)^{ij} =< \tilde{I}^i(q,\theta)\tilde{I}^j(q,\theta+\Delta) >_\theta \tag{6.23}$$

With the Fourier decomposition given by equation (6.8):

$$C(q,\Delta)^{ij} = 2\sum_{n=1}^{\infty} C_n^{ij}(q)cos(n\Delta) \tag{6.24}$$

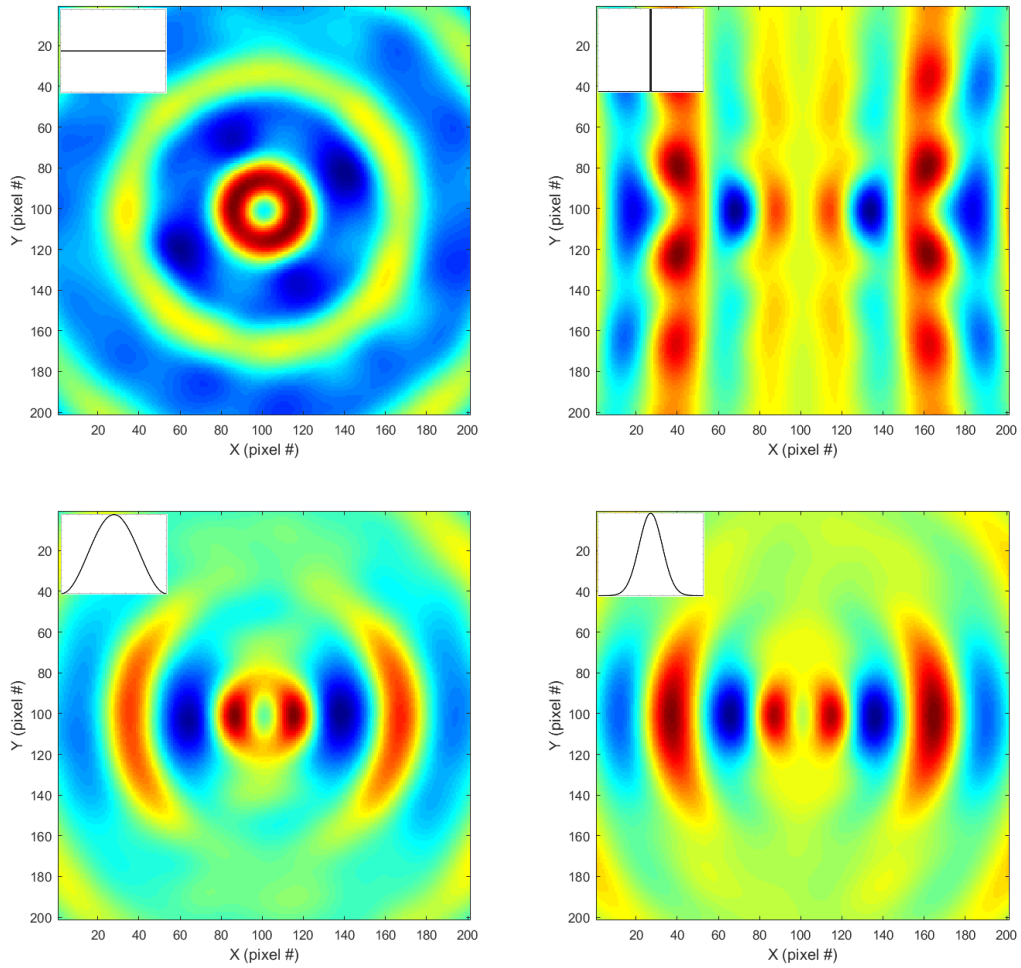

FIGURE 6.3: Simulations of X-ray difference scattering intensity on a 2D detector from 20,000 rotated ground/excited state PtPOP molecules. The molecular orientations are distributed with an isotropic (**top, left**), completely oriented (**top, right**), cosine squared (**bottom, left**) and a Gaussian (**bottom, right**) distribution around the y-axis as discussed in *Section 6.3*. The inserts illustrates the shape of the distributions.

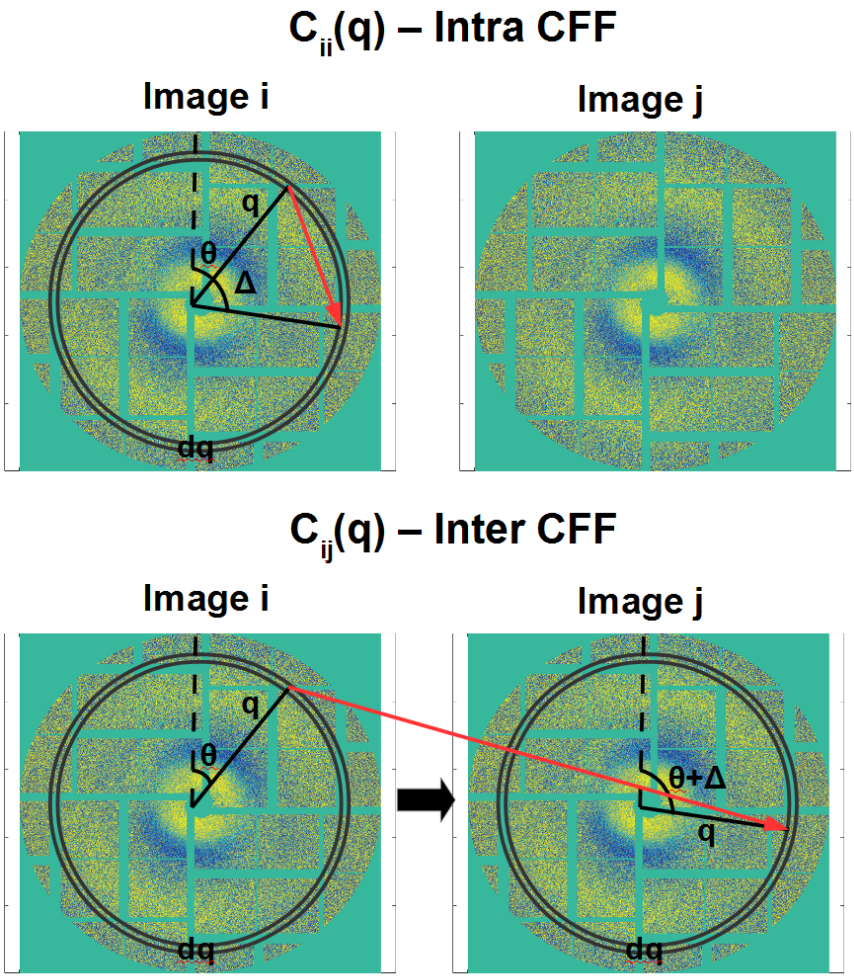

FIGURE 6.4: Illustrates how the CCFs are calculated at a specific q value. The Intra CCF is calculated as the Intensity correlation at an angle θ and $\theta + \Delta$ on the same diffraction pattern ($i = j$), and the Inter CCF as the correlation on different scattering patterns ($i \neq j$). The Fourier components are then found by Fourier decompositions.

The ensemble-averaged Fourier components, for all the M diffraction images, are then calculated according to [24, 25, 26]:

$$\tilde{C}_n^{ii}(q) = < C_n^{ii}(q) >_M \quad \text{(Inter CCF)} \tag{6.25}$$

$$\tilde{C}_n^{ij}(q) = < C_n^{ij}(q) >_M \quad \text{(Intra CCF)} \tag{6.26}$$

$$\tilde{C}_n^{ii-ij}(q) = < C_n^{ii}(q) >_M - < C_n^{ij}(q) >_M \quad \text{(Intra-Inter CCF)} \tag{6.27}$$

Figure 6.4 illustrates the differences between these CCFs. It is a powerful tool to calculate both the average of the Inter ($i = j$) and Intra ($i \neq j$) CFFs of the ensemble of scattering patterns, as they provide different kind of information and can be used to distinguish the contributions to the Fourier components. The Fourier components describing the anisotropic signal comes mainly from three different contributions - The Random Phasor Sum, The Internal Contribution and Background (the first two terms were introduced in *section 6.2*, through equation (6.13-16)):

The Random Phasor Sum Is present whenever there is a non-isotropic distribution of orientations of the molecules in the sample, as demonstrated in figure 6.3 and discussed in *section 6.2*, through equation (6.13-14). This is most visible for a large ensemble of molecules as the distribution of angles will then be almost complete. This term is generally proportional to the number of particles N as it adds up linearly for every diffraction pattern. A smaller ensemble will have "holes"/statistical variations from the complete distribution of angles that will show up as statistical variations in the Fourier components compared to the full complete distribution. This contribution due to the Random Phasor Sum will be similar for the Inter and Intra CCFs as the shape and orientation of this anisotropic signal does not change from shot-to-shot.

The Internal Contribution The statistical variations in the Fourier components discussed in "The Random Phasor Sum" above are not completely random. They are highly dependent on the internal structure and symmetries of the particles and were introduced in *section 6.2*, through equation (6.13-16) as the internal term. It comes from the "holes"/variations from a complete angular distribution, and each of these "holes" will have a scattering intensity on the 2D detector similar to the scattering from a single particle with the same orientation as the "hole". Therefore, this contribution will show the same symmetries as the individual particles as e.g. seen from the 4-fold PtPOP symmetry in the simulated scattering signal from an isotropic angle distribution in figure 6.3 (top, left). As the shape and orientation of this anisotropic signal changes from shot-to-shot it will show up differently for all the scattering patterns. It will therefore not have the same contribution to the Inter and Intra CCFs. Because it is a statistical variation from a well-defined distribution this term is expected to be proportional to $\sqrt{N}$.

Background The background contribution from the experimental setup. It will in general be similar from shot-to-shot (at least part of it) and therefore it will also show up similar for both the Intra and Inter CCFs.

The advantage of using the Intra-Inter CCF is that it will cancel out most of the contributions from the Random Phasor Sum and the Background, as these show up similar in both the Inter and Intra CFF. The only remaining contributions are then signals that changes its shape from shot-to-shot. That includes the Internal Contribution that gives information of the symmetries of the individual molecules themselves, and possibly contributions from experimental artifacts that change from shot-to-shot. Especially the Internal Contribution is of interest, and the identification of this term works best for a relatively small amount of molecules, as this signal is expected to be proportional to $\sqrt{N}$ whereas the total scattering signal goes as N.

6.5 Analysis of PtPOP XFEL Data

The experimental XFEL data from the PtPOP sample, consists of a large amount of 2D 2.3M pixel detector images at different time delays which undergoes data corrections as described in *Chapter 3*. The difference scattering images are then created by subtracting laser-off (all ground state) images from laser-on images (some

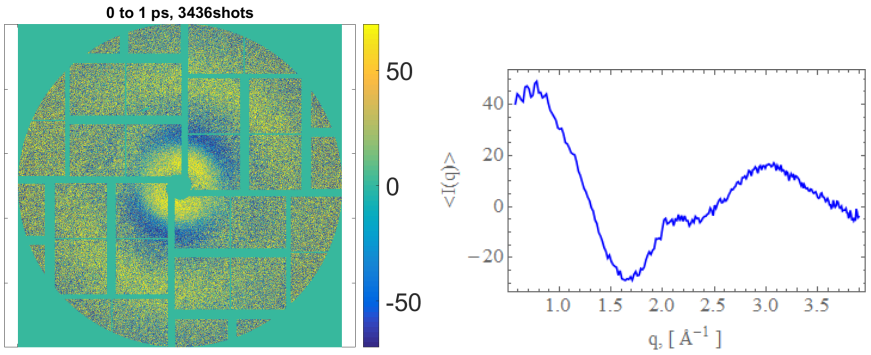

FIGURE 6.5: **Left:** An example of a difference scattering detector image (On - Off) averaged over 3436 shots in the 0-1 ps interval. The anisotropy is clearly visible, **Right:** The azimuthally averaged Intensity. The isotropic component is insufficient to describe the details of the image.

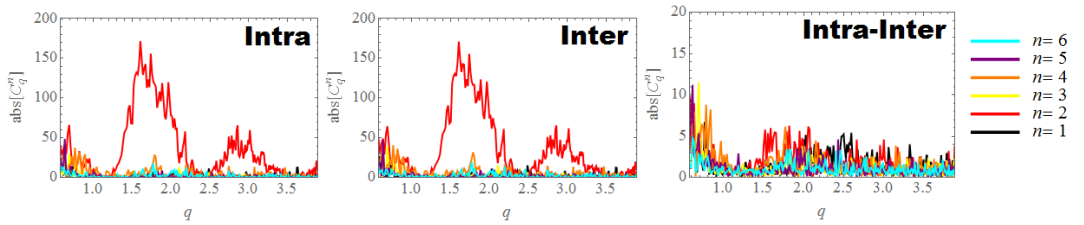

FIGURE 6.6: Calculated Fourier components of the Intra, Inter and Intra-Inter CFFs from 10 averaged images of 340 shots in the 0-1 ps interval (PtPOP experiment). A dominant $n = 2$ components can be seen in both the Intra and Inter analysis, which almost cancels out in the Intra-Inter analysis.

excited states). Figure 6.5 shows an average of 3436 corrected difference scattering images in the 0-1 ps time delay interval of the experiment, with the isotropic part of the signal derived from an azimuthal average of the intensity $< I(q, \theta) >_\theta$. It can be seen that an anisotropic part of the signal is clearly needed to fully describe the signal.

6.5.1 The CCF Fourier Components

To calculate the Fourier components of the CCFs (Intra, Inter and Intra-Inter) of a difference scattering image averaged over e.g. 3436 shots/images (and temporally rebinned into 1 ps bins as in figure 6.5), the image is first divided into 10 detector images of approximately 340 shots each from which the CCFs can be calculated. Figure 6.6 shows the Fourier components of these CCFs and a strong $n = 2$ component is clearly visible in both the Inter and Intra analysis, but not in the Intra-Inter analysis. This is a clear indication that the component arises due to an anisotropic signal with a similar shape and orientation in all the images. As discussed in the previous section this means that it is not a result of the internal symmetry of the individual molecules but rather a result of a non-isotropic orientational distribution of the excited state molecules. In this work the diffraction patterns were masked prior to the CCF calculations to exclude irregular, beam stop, edge and shadowed pixels on the detector and the pixels were rebinned in 4×4 pixel groups, to decrease the noise of the CCF Fourier components.

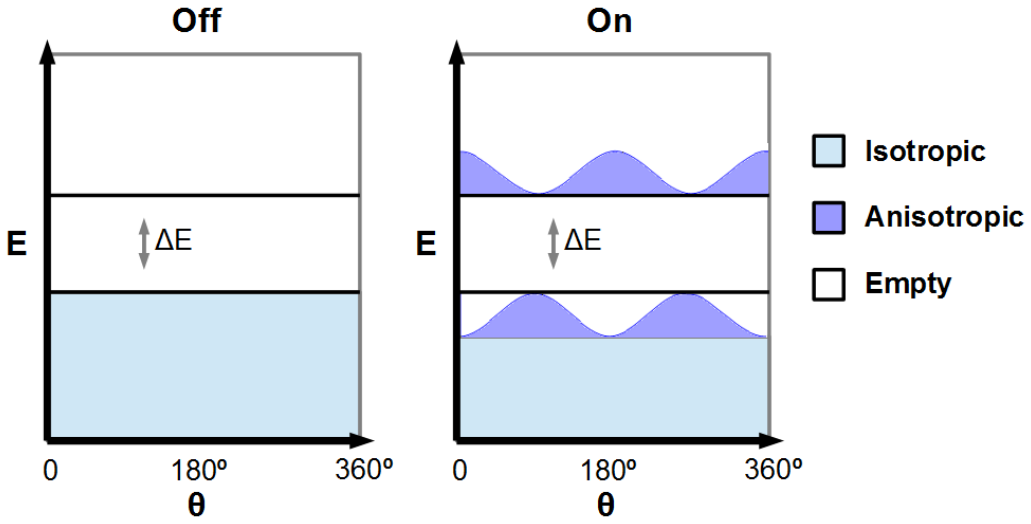

FIGURE 6.7: Model of the azimuthal distribution of the PtPOP molecules with regard to the laser polarization, before (Off) and immediately after laser excitation (On). The model is based on an initial $\cos^2(\theta)$ distribution of excited state molecules, expected from linear molecules excited by one-photon absorption. This leaves a "hole" in the ground state population with a similar azimuthal distribution.

6.5.2 The "Linear Molecule" Model

In this thesis, a simple model is proposed for the excitation of PtPOP. The molecules are considered as linear molecules because the Pt-Pt bond is essential for the photo excitation and the molecule is symmetric around this axis. When such linear molecules are excited from thermal equilibrium by one-photon absorption, the population of excited molecules will have a cosine squared orientational distribution with respect to the polarization of the incoming photons [108]. As the laser pulses in the experiment are linearly polarized, such an orientational distribution of the molecules is expected immediately after laser excitation. This is also evident from the experimental results as e.g. shown in figure 6.6. Figure 6.7 illustrates this simple "Linear Molecule" model and the ground/excited state populations expected from the PtPOP experiment, before and (immediately) after photo excitation. In the simulations of the difference scattering signals it is then important to consider the two different azimuthal distributions of molecules in the ground and excited state populations.

Figure 6.8 shows the calculated Fourier components of the Inter CCFs from a simulation of 20,000 PtPOP molecules (left) and a comparison of the $n = 2$ Fourier component (scaled accordingly) with that measured from the XFEL experiment (right) at a time delay of 0-1 ps. The simulations were based on the "Linear Molecule" model and the scaling factor is dependent on the number of molecule in the actual experiment. A good agreement was found between the experimental results and the model, and the discrepancy can possibly be explained from the lack of a cage in the simulations (the solvation shell around PtPOP, which will have the same azimuthal distribution as the molecules) and errors in the best estimation of the PtPOP structures. The $n = 2$ component was the only dominant component in both simulation and experiment, and the very weak $n = 4$ component in the simulations can be explained by the 4-fold symmetry of the PtPOP molecules, due to the relatively small amount of

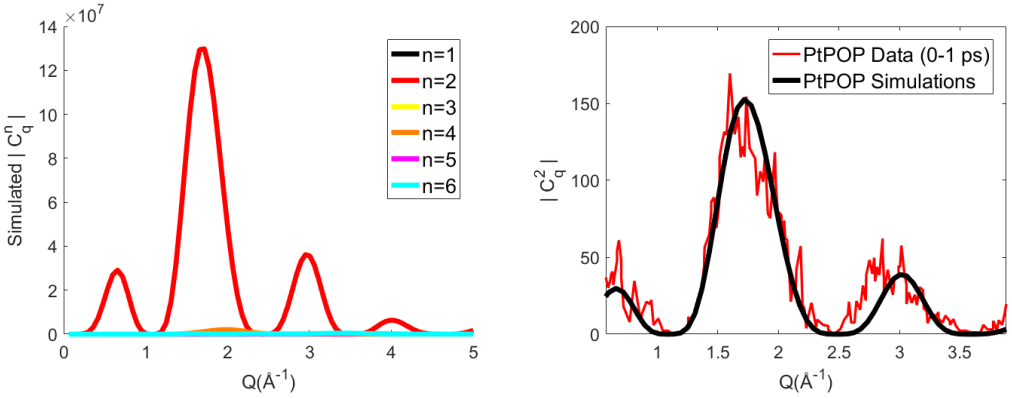

FIGURE 6.8: **Left:** Calculated Fourier components of the Inter CFFs from an ensemble of 5 five simulations of 20,000 PtPOP molecules with a cosine squared orientational distribution. **Right:** Comparison of the $n = 2$ angular Fourier component from the simulation to the one calculated from 10 images of 340 shots in the 0-1 ps interval of the experiment.

molecules in the simulation (Internal Contribution). Overall, the proposed model of a cosine squared azimuthal distribution seems to fit the data very well.

Weak but consistent $n = 4$ and $n = 6$ components can also be seen in the Intra and Inter analysis of the experimental data around $q = 1.8$ Å^{-1}. These components could arise either from a background signal, an artifact in the analysis or possibly that a small fraction of the excited molecules have a different distribution of rotation angles - but there is no clear indication of that. These components are disregarded in the analysis due to their small significance. Other Fourier components are seen at very low q (<1 Å^{-1}) which is a result of the very few detector pixels on these q rings.

6.5.3 Time Dynamics

It is interesting to look at the temporal evolution of the experimentally determined $n = 2$ angular Fourier component. The anisotropic contribution to the signal will decay over time, as the population of molecules eventually will settle back into an isotropic orientational distribution. This decay time will be dependent on the rotational correlation time of the molecules in the solution, which for inorganic molecules normally varies from 10-200 picoseconds [109], but also of the lifetime of the excited state (~ 10 µs) as the excited state molecules eventually return to their initial distribution in the ground state population. A combination of two life times is then expected which can be on very different time scales.

The measured difference scattering images at two different time delays and their corresponding Fourier components of the angular CCFs are shown in Figure 6.9. To average over sufficient number of diffraction patterns ($M \sim 3000$) and increase the signal-to-noise ratio, the collected diffraction patterns were temporally rebinned into 1 ps bins. A dominant $n = 2$ angular Fourier component in the difference scattering images, parallel to the laser polarization (~ 20 degrees to vertical), is clearly visible and its contribution have decreased significantly after 10 ps. Taking into consideration the rapid decay of the dominant component, this is strong evidence that the observed $n = 2$ signal arises from a 2-fold symmetric orientational distribution

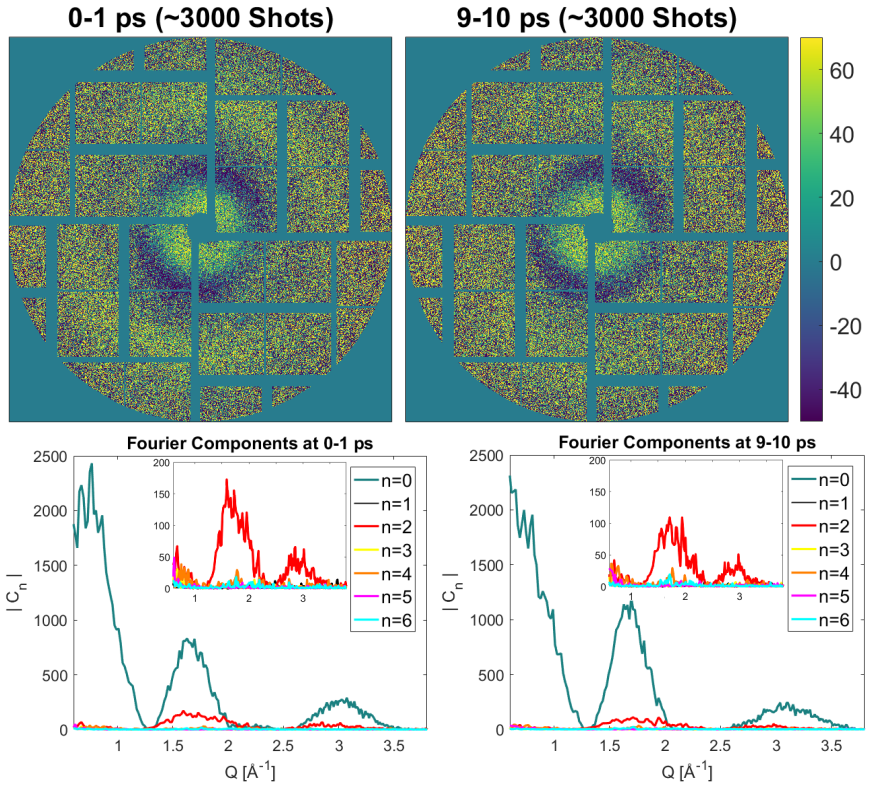

FIGURE 6.9: **Top:** Difference scattering detector images (On - Off) averaged over $\approx$ 3000 shots for two different 1 ps time intervals, **Bottom:** Calculated Fourier components of the CCFs. The insets highlight the dominant and temporally decreasing $n = 2$ contribution on top of the isotropic $n = 0$ signal.

of excited state molecules induced by the laser excitation at $\Delta t = 0$.

Figure 6.10 (left) follows the temporal evolution of the integrated area under the peak at $q \sim 1.8$ Å^{-1} of the $n = 2$ intensity Fourier component $|I_n(q)| = \sqrt{C_n(q)}$ (equation (6.14)), to clearly illustrate the decay of the anisotropic detector signal over time. An additional short decay is clearly visible on top of the longer decay in the inset of Figure 6.10 (left) when the images are rebinned into 250 fs time bins. This analysis is as such independent on any structural modelling of the system. The total decay was modelled as a sum of two exponents:

$$f(\Delta t) = Ae^{-\frac{\Delta t}{\tau_1}} + Be^{-\frac{\Delta t}{\tau_2}} + \sigma_B \tag{6.28}$$

Where σ_B is related to the general noise level of the averaged images. Based on least-square fitting $79 \pm 5\%$ of the signal was found to decrease with a time constant of $\tau_1 = 46 \pm 10$ ps, and $21 \pm 5\%$ with $\tau_2 = 1.9 \pm 1.5$ ps. Rebinning into 100 fs time bins reveals oscillatory behavior of the decay during the first few picoseconds (figure 6.12), which we relate to the Pt-Pt bond stretching mode with a sub-300 fs period as discussed in *Chapter 4*. The rebinning however results in a much reduced signal-to-noise ratio due to fewer images per time delay.

The observed model-independent time dynamics can be directly compared to our structural model and simulation. Figure 6.11 shows a comparison of the measured

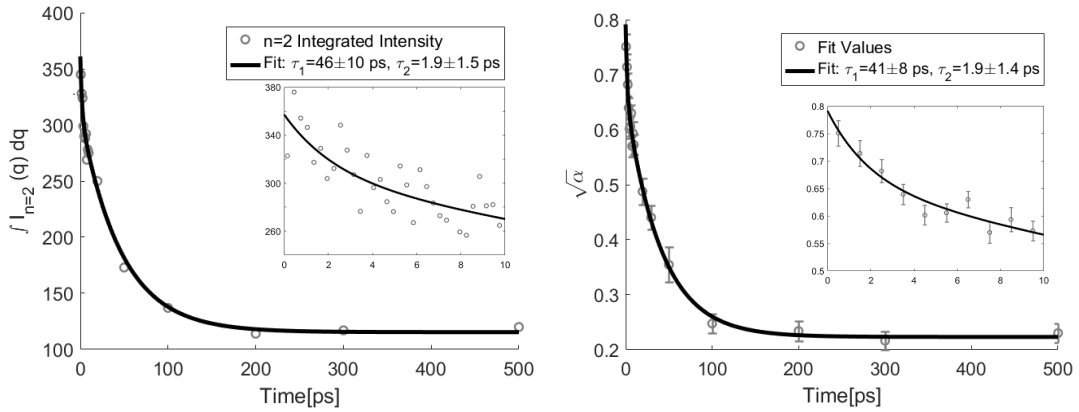

FIGURE 6.10: **Left:** A double exponential decay fit to the measured $I_{n=2}(q, \Delta t)$ Fourier components integrated in q space, as a measure of the changes in the $n = 2$ signal strength over time. The intensity Fourier components were calculated from the averaged images binned in 1 ps bins. The model-independent analysis reveals two different time scales as highlighted in the inset with 250 fs time bins. **Right:** Similar figure but with the best-fit scaling value $\sqrt{\alpha}$ between simulation and measurements.

$n = 2$ CCF Fourier component at different time delays with the $n = 2$ component calculated from our simulation scaled accordingly. The results from the simulations are scaled with scaling factors α to account for the total number of excited PtPOP molecules in the probed volume of the sample and their orientational distribution at the specific time delay. The scaling factor α (figure 6.10, right) has a similar temporal decay behavior as observed for the integrated $n = 2$ intensity Fourier component (figure 6.10, left).

6.5.4 Correlated Parameters

Until now the data has been analyzed simply by considering the averaged relaxed ground and excited state structures of PtPOP while the fundamental modes of oscillations in e.g. the Pt-Pt bond length has been ignored. It has blindly been assumed that the strength of the $n = 2$ Fourier component in the intensity, is linear with the change in the Pt-Pt bond length Δd_{PtPt}. The sub-ps oscillations has been handled by assuming linearity and the whole analysis was carried out by considering averaged structures. A way to verify this assumption is to carry out simulations with Pt-Pt bond length changes of e.g. 0.2 and 0.3 Å respectively, and see if the differences in the Fourier components can be described by a scaling factor of $\zeta = \frac{0.3\text{ Å}}{0.2\text{ Å}} = 1.5$. Figure 6.13 shows the results from such a procedure, and the assumption seems to works well for these bond length changes. Further, the molecule is assumed to be otherwise completely rigid and other possible atomic oscillations has been ignored, an assumption that is justified by DFT simulations and the results presented in *Chapter 4*.

The fact that there is an approximately linear relation between the strength of the $n = 2$ Fourier component and the bond length change means that it is very hard to determine an exact value for the bond length contraction from the anisotropic scattering signal. This is because the strength of the $n = 2$ Fourier component is also linearly related to the excitation fraction of the molecules and these two parameters

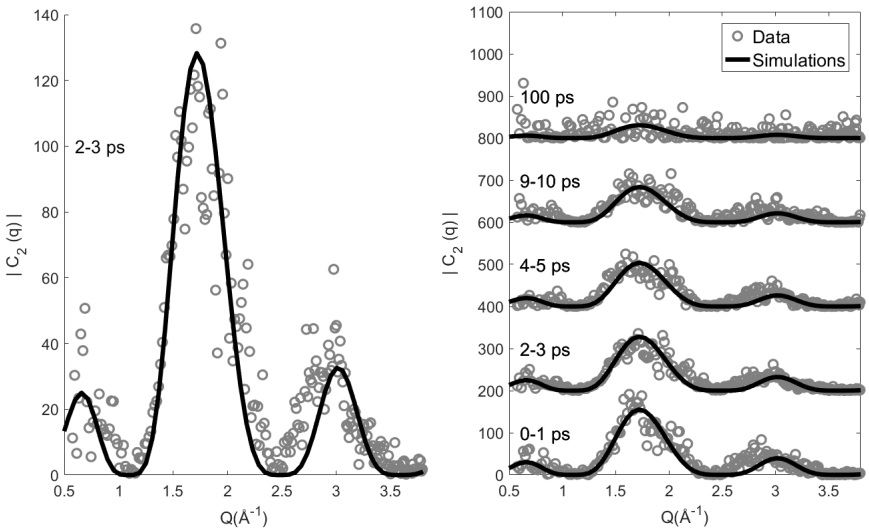

FIGURE 6.11: **Left:** The calculated $n = 2$ CCF Fourier component (black) from the simulation of 10^5 PtPOP molecules with a cosine squared orientational distribution, fitted to the measured $n = 2$ component (gray) in the 2-3 ps time delay interval with a scaling factor $\alpha(\Delta t)$. **Right:** The same comparison for a variety of time delays; at 100 ps the molecules have almost lost their preferred orientation.

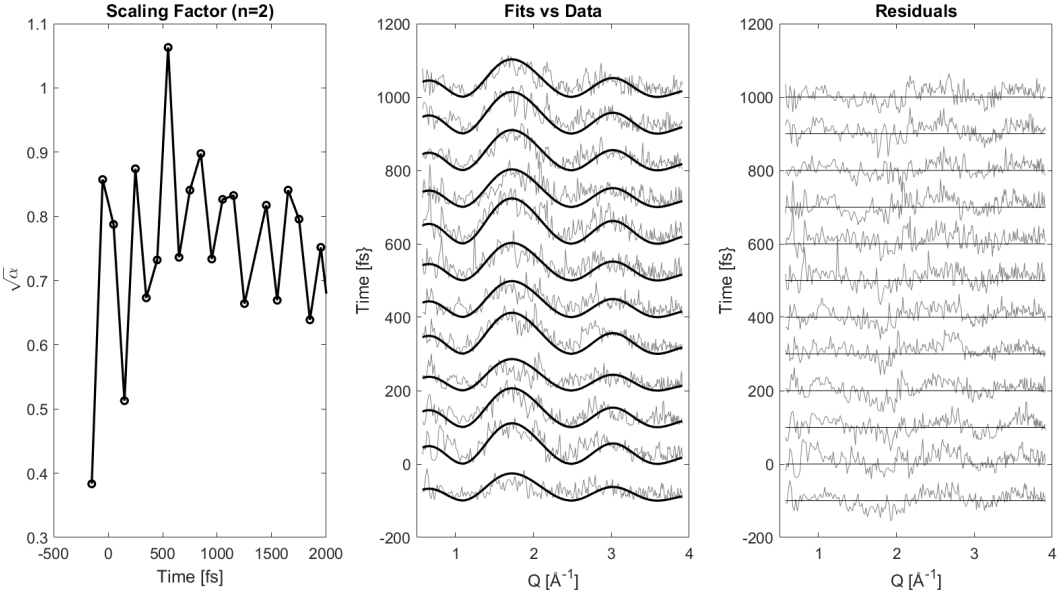

FIGURE 6.12: A direct comparison of the calculated $n = 2$ CCF Fourier components from the simulation, fitted to the measured components (bins of 100 fs) with a scaling factor $\alpha(\Delta t)$ (**middle**) and residuals (**right**). The temporal evolution of $\alpha(\Delta t)$ shows sub-ps oscillations (**left**).

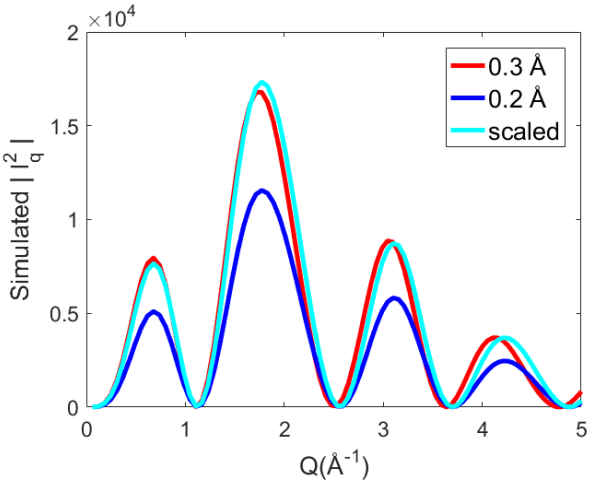

FIGURE 6.13: Comparison of the $n = 2$ intensity Fourier component in the difference scattering signal, from "Linear Molecule" simulations of Pt-Pt bond length changes of Δd_{PtPt}=0.2 (blue) and 0.3 Å (red) respectively. A scaling factor of $\zeta = \frac{0.3\text{ Å}}{0.2\text{ Å}} = 1.5$ multiplied to the $\Delta d_{PtPt} = 0.2$ Å curve (cyan) agrees well with the $\Delta d_{PtPt} = 0.3$ Å curve. The structures are assumed to be otherwise completely rigid.

are then directly correlated. A similar problem was observed in the isotropic analysis described in *Chapter 4*.

6.5.5 The Random Phasor Sum vs. Internal Contributions

An anisotropic signal was only found in the experiment from the initial cosine squared orientational distribution of the excited state molecules (Random Phasor Sum). No contributions were observed from the internal symmetry of the molecules themselves (discussed in *Section 6.4* and *Section 6.5.1*). It was however seen as e.g. a weak $n = 4$ component in the simulations (figure 6.8). This is expected due to the large number N_{exp} of molecules in the actual experiment compared to the simulations ($N_{sim} = 20,000$), as the signal from the Random Phasor Sum generally is proportional to N and the Internal Contribution goes as $\sqrt{N}$.

A way to demonstrate this is to simulate the behavior of the intensity Fourier components $\|I_q^n\|$ as a function of N_{sim}, using the Intra-Inter CCF (very sensitive to the internal symmetries) and the Inter CCF (includes the Random Phasor Sum). As an estimate of the strength of a particular Fourier component, the maximum value of the main peak is used. Figure 6.14 (top) shows the result of such an analysis for the Inter and Intra-Inter $\|I_q^n\|$ components up to 20,000 molecules. From the Inter CCF analysis the linear dependence of the $n = 2$ components can clearly be seen, and was fitted with a function $f_I^n(N_{sim}) = \alpha_n N_{sim}$. Likewise a square root dependence was seen for all the components in the Intra-Inter analysis and fitted with $f_{I-I}^n(N_{sim}) = \beta_n\sqrt{N_{sim}}$. A simple and rough estimation of the ratio of contributions to the Intensity, from these two effects (Random Phasor Sum and Internal Contribution) is done by comparing their strongest components as:

$$f(N_{sim}) = \frac{f_I^2(N_{sim})}{f_{I-I}^4(N_{sim})} = \frac{\alpha_2}{\beta_4}\sqrt{N_{sim}} \sim 0.06 \times \sqrt{N_{sim}} \tag{6.29}$$

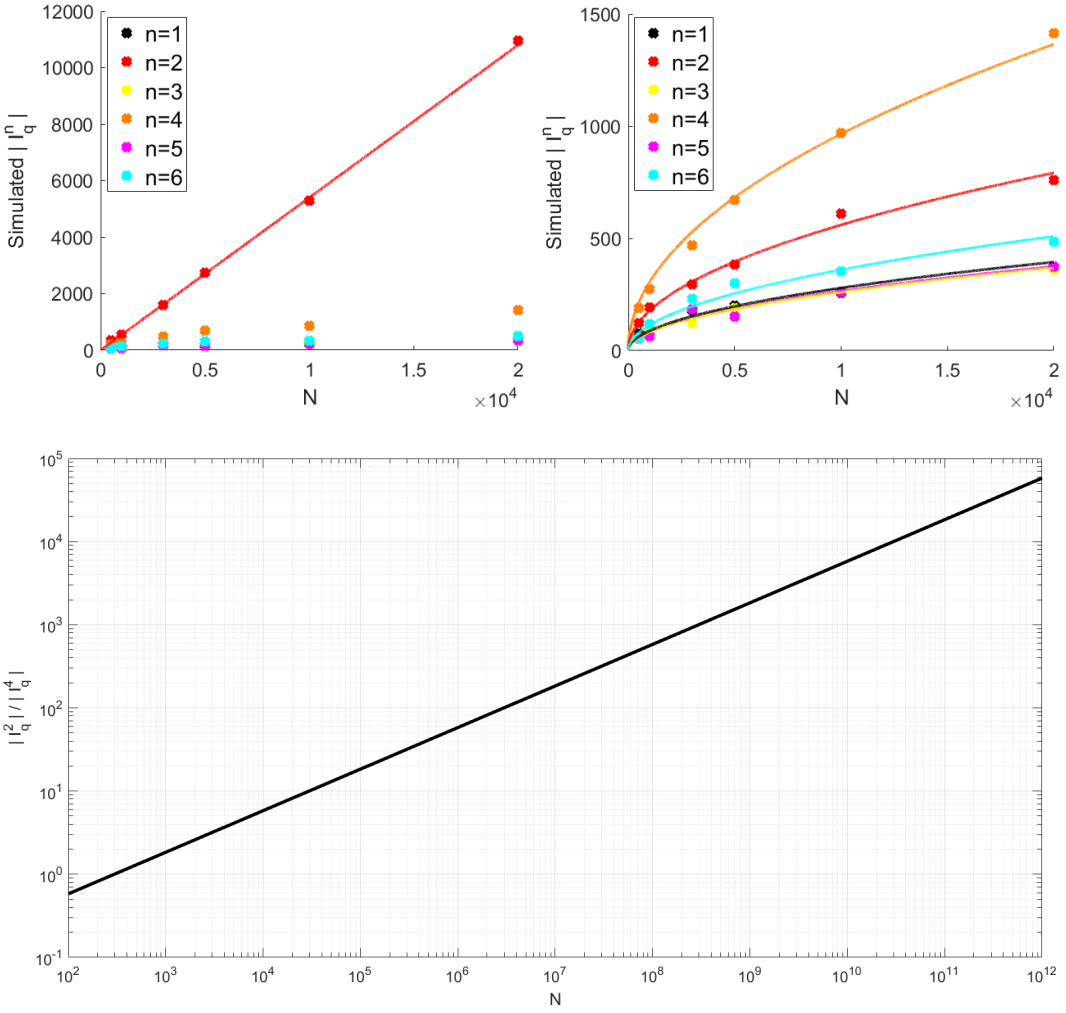

FIGURE 6.14: **Top:** The main peak height of the calculated $\|I_q^n\|$ Fourier components for an Intra (left) and Intra-Inter (right) analysis of the PtPOP simulations, as a function of the number of molecules N_{sim} in the simulation. The fits are $f_I^n(N_{sim}) = \alpha_n N_{sim}$ (left) and $f_{I-I}^n(N_{sim}) = \beta_n \sqrt{N_{sim}}$ (right), **Bottom:** Plot of $f(N_{sim}) = \frac{f_I^2(N_{sim})}{f_{I-I}^4(N_{sim})} = \frac{\alpha_2}{\beta_4}\sqrt{N_{sim}}$ which gives a roughly estimated value of the ratio between the Random Phase Sum and Internal Contribution parts of the anisotropic intensity signal.

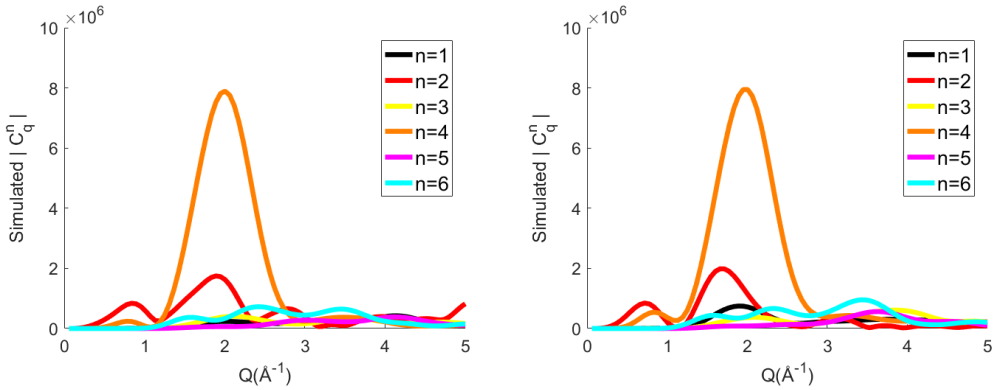

FIGURE 6.15: Simulation of the Fourier components of the Intra-Inter CCFs in the difference scattering images for 20,000 PtPOP molecules. Shown for a bond length change of $\Delta d_{PtPt} = 0.2$ Å (**left**) and $\Delta d_{PtPt} = 0.3$ Å (**right**). Notice the dominance of the $n = 2$ and $n = 4$ components, due to the 2-fold and 4-fold symmetries in the molecules.

This function is displayed in figure 6.14 (bottom), and the fitting parameters are found from the best-fit values in figure 6.14 (top). It can be seen from this equation that a simulation of 20,000 molecules gives a ratio of $f(20,000) \sim 8.5$ in the intensity Fourier components and $\|f(20,000)\|^2 \sim 72$ in the CCF Fourier components, which explains the very weak $n = 4$ component in the simulation shown in figure 6.8.

The number of excited molecules in the experiment is of the order of $N_{exp} = 5 \times 10^{10}$, estimated from the experimental setup. A comparison with equation (6.29) shows that the ratio $f(N_{exp})$ for the C_q^n and I_q^n components are of the order of 10^4 and 10^8 respectively. This is the reason why only the Random Phasor Sum contribution of the signals can be seen from the experimental measurements, as the signal-to-noise value is around 50 at the best for the measured C_q^n. This concludes that the Internal Contribution is only measurable for experiments designed with a significantly smaller amount of molecules.

6.5.6 Investigating the Internal Contributions

Figure 6.15 (left) shows an example of the simulated Fourier components of the Intra-Inter C_q^n for 20,000 molecules (primarily Internal Components as discussed earlier) where it is clear that the most visible component is $n = 4$ followed by $n = 2$. It is not surprising as the PtPOP molecule has exactly those two symmetries, a 4-fold symmetry expected to be dominated in the scattering by the 8 Pt-P bonds and a 2-fold symmetry expected to be dominated by the single Pt-Pt bond. The $n = 6$ Fourier component is slightly stronger than the rest of the components (attributed to the general noise level) but could not be related to any direct symmetries in the molecules.

Figure 6.15 (right) shows the results of the simulation when the Pt-Pt bond length change is 0.3 Å instead of 0.2 Å, in an otherwise completely rigid molecule. There is a small shift of the main peak in the $n = 2$ component to lower q-values probably due to the dominance of the Pt-Pt bond for this scattering symmetry and the fact that the bond length changes with additional 0.1 Å. The $n = 4$ component remains almost unchanged, as the Pt-P bond length only changes with additional 0.005 Å

due to the geometry of the molecule. More simulations with different bond length changes (Pt-Pt, Pt-P, Pt-O etc.) and structural changes (rotations, different modes of oscillations etc.) can be carried out to reach conclusions that are more concrete. These results are expected to be summarized in a future article.

It should be mentioned that the simulations has only been considering the anisotropic population of the molecules, which only makes out around 3 % of the molecules according to the excitation fraction estimated in *Chapter 4*. As illustrated previously in figure 6.7 there is also a huge population ($\sim 97\%$) of molecules with an isotropic orientational distribution which are not directly influenced by the laser excitation pulse in the experiment. It is enough to only investigate the anisotropic population if you are solely interested in the orientational distribution (Random Phasor Sum) of molecules in the experiment, as it will greatly dominate the signal due to the large amount of molecules in a typical solution experiment. However if one are interested in investigating the Internal Contribution, the symmetries of the ground state molecules in the isotropic distribution will contribute as well. This means that it will be even harder to design experiments to measure the Internal Contribution, as the signal from the 97 % ground state molecules in the laser On images (+ 100 % ground state molecules in laser Off) will dominate over the 3 % of molecules in the exited state (only laser-On). For these reasons, molecules with a high excitation fraction will work better for this purpose.

6.6 Discussion and Outlook

An inclination of $\sim$ 20 degrees of the $n = 2$ signal can be directly observed at short time delays from the time-binned and averaged scattering difference detector images (figure 6.9), which corresponds to the inclination of the laser polarization direction with respect to the vertical direction. This is strong evidence that the observed $n = 2$ signals arise from a 2-fold symmetric orientational distribution of excited state molecules induced by the laser excitation at $\Delta t = 0$. In the simulation model one can see that the internal structure of the molecule results in the fact that the $n = 0$ and $n = 2$ Fourier components have slightly different q-positional of the scattering peaks (figure 6.9). This indicates that additional information on the exact structures and symmetries of the system is available from the higher order scattering curves. The strong contribution from the 2-fold symmetry is also a convincing argument for the "linear molecule" model presented in section 6.5.2 and that such molecules, excited from thermal equilibrium by one-photon absorption, will have a short-living cosine squared orientational distribution with respect to the laser polarization as calculated by van Kleef and Powis [108].

A direct model-independent analysis of the temporal decay of the $n = 2$ integrated signal revealed two dominant time scales of $\tau_1 = 46 \pm 10$ ps and $\tau_2 = 1.9 \pm 1.5$ ps respectively (figure 6.10). The longer time scale is interpreted as the rotational dephasing of the initial cosine squared distribution of orientations to a completely random and isotropic distribution. The reorientation time τ_r for a molecule in solution can be estimated from the Stokes-Einstein-Debye hydrodynamic theory in a classical dynamical framework without electrical interactions [110]:

$$\tau_r = \frac{\eta V}{k_b T}(fC) \tag{6.30}$$

Which includes the Boltzmann constant k_b, temperature T, molecule volume V, solvent viscosity η and a shape factor f to take into account for non-spherical molecules [111] . C is a value between 0 and 1 for different boundary condition and depends on the axial ratio of the molecule [112]. For a spherical molecule $VfC = \frac{4}{3}\pi r^3$ which gives a value of $r = 3.6 \pm 0.3$ Å from the measured decay time. This is only slightly less than the longest interatomic distance in PtPOP of 4.0 Å from the DFT calculations. The uncertainty is expected to be significantly reduced by performing more measurements at time delays of tens of picoseconds.

To take the specific molecular shape into account the van der Waals volume V can be evaluated using the Edwards increment method [113]. The shape factor f can be found from the axial ratio estimated from the molecule as the longest interatomic length parallel and perpendicular to the Pt-Pt axis ($\approx 10\%$ difference for PtPOP, which could explain the good result from a spherical approximation). The boundary condition C can be obtained by interpolating numerical tabulations [114, 115]. Potential electrical contributions for a polar molecule from the relaxing long-range dipolar interactions can be taken into account using a dielectric friction contribution calculated from e.g. the Nee-Zwanzig [116] and van der Zwan-Hynes models [117].

Since coefficients C and f depend on the molecular radius and shape, estimations of the molecular size and shape can be made by measuring the rotational dephasing times τ_r. This can be used to benchmark values obtained from radially integrated SAXS curves and help distinguish between size and shape effects of the scattering signal. If the laser excitation involves a change in size, shape or dielectric properties a different rotational dephasing time can be expected for the excited state molecules compared to the ground state molecules. This means that the $n = 2$ contribution from the ground and excited state can be distinguished by following the temporal evolution of the $n = 2$ signal as the molecules with a longer dephasing time constant will dominate the signal at longer time delays. This applies as well to experiments where different species (or same species of different sizes) in the same sample volume are excited with an orientational preferred direction. The molecular rotational dephasing time obtained from the $n = 2$ signal cannot be determined from radially integrated $n = 0$ curves and can help refine structural models and gain new insight in time-resolved SAXS/WAXS experiments.

Concerning the shorter time constant of $\tau_2 = 1.9 \pm 1.5$ a direct interpretation is slightly more complicated as it is assumed to arise from the internal dynamics of the PtPOP molecules. The strength of the two dominant peaks in the measured $n = 2$ signal both decreases with a similar time constant indicating that the shape of the signal remains almost unchanged (Figure 6.12). Possible explanation could be; 1) a fast structural relaxation of the dominant Pt-Pt bond contraction, through interactions with other modes or the solvent-solute cage; 2) the time-scale for the ground state hole to reach equilibrium. This shorter time constant directly revealed by XCCA could in principle be obtainable from radially averaged scattering curves but will be intermixed with contributions from e.g. the bulk solvent.

In general the radially integrated $n = 0$ signal consist of contributions from both solute, solvent cage, bulk solvent (heating and density changes) and background variations. On the other hand the $n = 2$ signal is not influenced by bulk solvent contributions and only include contributions from background variations with the same symmetry as the orientational distribution of the molecules. This significantly

reduces the amount of free parameters in a structural analysis and makes the interpretation of the time constants more clear and based on fewer assumptions about the system. A combination of both the $n = 0$ and $n = 2$ curves will give two slightly different signals to benchmark the structural models, where one is dependent and one is independent of the solvent contribution and therefore gives the possibility to enhance the structural information from a SAXS/WAXS experiment.

A direct comparison of our model to the measured $n = 2$ signal (figure 6.11) confirms the validity of the assumed model of the system. The small discrepancies are associated with the lack of a simulated solvent cage signal and slight variations between the DFT calculated structure and the actual structure of the molecule. Further, the temporal decay of the scaling factor (figure 6.10, right) follows the same behavior as the decay in the integrated $n = 2$ signal (figure 6.10, left). This indicates that direct structural modelling of these signals are possible and reliable.

The observation of oscillations on a sub-300 fs timescale (figure 6.12) in the signal related to the Pt-Pt bond stretching mode, illustrates the potential of XCCA to observe structural changes on shorter time scales. This opens up the potential to investigate e.g. the Kerr effect [118, 119, 120] that happens during the first few hundred femtoseconds. The Kerr effect is the rotational dephasing of laser aligned solvent molecules and can reveal information of solvation dynamics.

Experiments with transition dipole moment along a particular axis are suitable for XCCA, which uses Cross- Correlation Functions (CCFs) to analyze the non-isotropic part of the scattered intensities, and extract fine-structure information, going beyond radially integrated intensity analysis. The Fourier analysis of the CCFs allows revealing additional structural information about the system, particularly symmetries and their lifetimes. Therefore, we expect that XCCA will significantly improve the information content accessible in such experiments. At the same time, we also expect that by varying such parameters as sample concentration and laser power we will explore the capabilities of XCCA, which is crucial for method development. Experiments with smaller X-ray beam and at higher flux facilities might reveal higher order XCCA components for the studies of internal symmetries of the molecules.

XCCA offers a model independent approach for investigations of the anisotropic scattering from systems of a photo-aligned sub-population of molecules in solution that can be applied to various disordered samples of molecules, proteins, particles and biomolecules. While such methods currently are working best in dilute systems, our studies of PtPOP metal complex molecules show that similar methods may let us significantly enhance the information content of scattering images, even in denser systems, such as solvated molecules in case of a predominant orientation of the molecules. This technique and anisotropic scattering is of great importance in many solid-state and chemical systems as it can provide information of both orientational symmetries in an ensemble and of the internal structural symmetries in molecules and solid-state systems. These symmetries are often essential to understand the physical and chemical properties.

The PtPOP system represents an excellent model system to further develop the XCCA method and investigate fundamental chemical processes, due to e.g. the significant structural changes in the Pt-Pt bondlength and the strong scatters (Pt-Pt) along the excitation axis of the molecules.

6.7 Summary

In this chapter, it was shown how X-ray Cross-Correlation Analysis (XCCA) can be applied as an model independent approach to study the structural symmetries and their timescale of disordered samples of solvated molecules, with the PtPOP molecule as an example. Important steps in the analysis are Fourier decomposition of the Cross-Correlation Functions (CCFs) and averaging over thousands of detector images.

We revealed hidden symmetry on a very short ($\sim$ 1 ps) time scale and rotational dephasing at longer ($\sim$ 50 ps) times that was compared to theoretical estimations. Analysis of the $n = 2$ angular Fourier component in XCCA helps to distinguish size and shape effects and enhance structural information, which is otherwise difficult to obtain in a conventional SAXS approach. Further, the results were successfully compared to simulations confirming the validity of our model. The study presented here illustrates the potential of XCCA as an additional tool to reveal hidden structural information and time scales in a SAXS/WAXS experiment and enhance the information content of scattering images.

It was however not possible to investigate the Internal Contribution in the experiment, due to the large number of molecules and the poor signal-to-noise ratio. Experiments with a smaller X-ray beam and at high flux facility might reveal higher order XCCA components for the studies of internal symmetries of the molecules.

We believe that the technique presented here can be widely used in the SAXS/WAXS experiments to enhance structural information from a disordered sample of molecules, proteins or biomolecules and to reveal hidden symmetries and their time evolution in a model independent approach.

Chapter 7

Conclusions

This thesis presented a systematic review of the data analysis from Time-Resolved Wide-Angle Scattering (TR-WAXS) solution experiments at X-ray Free Electron Laser (XFEL) facilities. It demonstrated the analysis of structural dynamics of transition metal complexes and solvation systems.

Compared to more traditional synchrotron experiments, the successful XFEL analysis relied on a robust non-linear SVD-based method to adjust the recorded scattering images for the characteristic shot-to-shot fluctuations in e.g. X-ray intensity and energy in addition to a solid model framework for comparing the results to high-level quantum simulations of complex molecular dynamics.

An innovative experimental method based on off-resonance optical excitation of the PtPOP transition metal complex was developed, to prepare a vibrationally cold excited state to record subsequent images of the coherent ground state "hole" dynamics on the ground state potential surface. The method clearly revealed the fundamental ≈ 280 fs Pt-Pt ground state stretching mode with a decoherence time of $\tau \approx 1.5$ ps, and quenched excited state dynamics. In addition to traditional methods of investigating excited state dynamics, it provides a complete set of tools to investigate the potential energy landscape in transition metal complexes. Combined with modern QM/MM BOMD simulations it allows for an experimentally supported visualization of the molecular dynamics. We believe these methods will have a wide-ranging impact on studies of energy states in chemical photoreactions and optimizations of DFT simulations.

The aqueous $I^- \rightarrow I^0$ photoreaction was studied by simultaneously measurements of the X-ray scattering and L1-edge absorption spectrum. The time scale (≈ 350 fs) of the solvent shell expansion was determined and successfully compared to recent quantum simulations. The structural dynamics was directly coupled to an increased electron back donation to I^0 as a result of the structural changes in the solvent shell. The study illustrated the strength of combining X-ray absorption to study the electronic configurations and X-ray scattering to deduce the structural dynamics.

X-ray Cross Correlation Analysis (XCCA) was introduced as a powerful tool to analyze the angular intensity correlations in the full detector space and reveals additional structural information in solution samples prepared with a photo-aligned sub-population of molecules. The scattering patterns from the PtPOP molecule were successfully compared to XCCA simulations to confirm the validity of the model and a hidden timescale (~ 50 ps) was identified and related to the rotational dephasing of the molecules. We believe the method can be widely used in SAXS/WAXS to enhance

the information content from XFEL solution scattering experiments to obtain better structural models in biology and chemistry.

7.1 Outlook

The analysis framework can be optimized in several ways. First, a χ^2 statistical framework for data-model comparison is not without problems, as it requires the explicit estimation of experimental errors and if done correctly, the comparison might not be valid. An alternative statistical method based on Correlation Maps (CorMap) might be worth considering, as it only uses data point correlations for data-model comparisons. Secondly, the data reduction process is still very time consuming in XFEL experiments and there can easily be years between data acquisition and published articles. The upcoming XFEL facilities (European XFEL / upgraded LCLS) will enter the MHz regime, and might record an order of magnitude bigger data sets. There is therefore a need for more standardized methods e.g. based on artificial intelligence and machine learning for the sorting and corrections of the scattering images to more quickly deal with the reduction and analysis part of XFEL experiments.

The combination of several different methods (e.g. scattering/absorption) allows for the disentanglement of different contributions in the multi-variable optimization problem of determining molecular dynamics. In combination with increased data quality and regions of Q-space in upcoming XFELs, the available information content will increase. This will allow for determination of even smaller difference scattering signals as e.g. from the solvation dynamics around a photo detached electron following the aqueous $I^- \rightarrow I^0$ photoreaction, to determine this much debated question in chemical physics.

As the XCCA method is still in its infancy in XFEL experiments it is crucial for method development with a more dedicated study, where the XCCA capabilities will be explored by variations of such parameters as sample concentration and laser power. Our recent beam time proposal **Proposal I** which suggested such a XCCA study on a transition metal complex, has just been accepted by the European XFEL in fierce competition with other research groups ($\sim 10\%$ acceptance rate). XCCA can potentially lead to direct reconstruction of the molecular structure, directly from the correlations functions.

Bibliography

[1] K. Glusac (2016), *Nature Chemistry*, volume 8, 734-73

[2] E. Muybridge (1878), *Scientific American*, Volume 39, Issue 16.

[3] A. H. Zewail (2000), *Pure Appl. Chem.*, Vol 72, no. 12, pp. 2219-2231.

[4] B. Perman, V, Srajer, Z. Ren, T. Teng, C. Pradervand, T. Ursby, D. Bourgeois, F. Schotte, M. Wulff, R. Kort, K. Hellingwerf and K. Moffat (1998), *Science*, 279, 1946-1950.

[5] E. Collet, M.H. Lemee-Cailleau, M. Buron-Le Cointe, H. Cailleau, M. Wulff, T. Luty, S.Y. Koshihara, M. Meyer, L. Toupet, P. Rabiller, S. Techert (2003), *Science*, 300, 612-615.

[6] J. Feldhaus, J. Arthur and J.B. Hastings (2005), *Journal of Physics B: Atomic, Molecular and Optical Physics*, 38 (9): S799.

[7] Parts of the figure are kindly borrowed from Greg Stewart at SLAC.

[8] M. Christensen, K. Haldrup, K.S. Kjær, M. Cammarata, M. Wulff, K. Bechgaard, H. Weihe, N.H. Harrit and M.M. Nielsen (2010), *Phys. Chem. Chem. Phys.*, 6921-6923.

[9] M. Christensen, K. Haldrup, K. Bechgaard, R. Feidenhansl, Q. Kong, M. Cammarata, M. Lo Russo, M. Wulff, N. Harrit and M.M. Nielsen (2009), *J. Am. Chem. Soc.*, 131, 502-508.

[10] R.M. van der Veen, C. Milne, A. El Nahhas, F.A. Lima, V.T. Pham, J. Best, J.A. Weinstein, C.N. Borca, R. Abela, C. Bressler and M.C. Chergui (2009), *Angew. Chem. Int. Ed.*, 48, 2711-2714

[11] D.M. Roundhill, H.B. Gray and C.M. Che (1989), *Accounts of Chemical Research*, vol. 22, no. 2, pp. 55-61.

[12] H.B. Gray and A.W. Maverick (1981), *Science*, 214.

[13] T.B. van Driel et al. (2016), *Nature Communications*, 7.

[14] K. Haldrup, M. Christensen, M. Cammarata, Q. Kong, M. Wulff, S.O. Mariager, K. Bechgaard, R. Feidenhansl, N. Harrit, M.M. Nielsen (2009), *Angewandte Chemie International Edition*, Vol 48, Iss 23, pages 4180-4184.

[15] T. Harlang, Y. Liu, O. Gordivska, L.A. Fredin, C.S. Ponseca, P. Huang, P. Chabera, K.S. Kjær, H. Mateos, J. Uhlig, R. Lomoth, R. Wallenberg, S. Styring, P. Persson, V. Sundstrom and K. Warnmark (2015), *Nature Chemistry*, Vol. 7, No. 11, p. 883-889.

[16] Biasin et al. (2016), *Physical Review Letters*, 117(1), [013002].

[17] M. Maroncelli (1993). *J. Mol. Liq.*, 57, 1.

[18] G.R. Fleming and M.H. Cho (1996), *Annu. Rev. Phys. Chem.*, 47,109.

[19] N. Nandi, K. Bhattacharyya and B. Bagchi (2000), *Chem. Rev.*, 100, 2013.

[20] Z. Kam (1977), *Macromolecules*, 10, 927.

[21] T. Ishikawa et al. (2012), *Nature Photonics*, 6, 540.

[22] X.J. Liu, Y. Xu, X. Hui, Z.P. Lu, F. Li, G.L. Chen, J. Lu and C.T. Liu (2010), *Phys. Rev. Lett.*, 105 ,155501.

[23] P. Emma (2010), *Nature Photonics*, 4, 641.

[24] M. Altarelli, R.P. Kurta and I.A. Vartanyants (2010), *Physical Review B*, vol. 82, no. 10.

[25] M. Altarelli, R.P. Kurta and I.A. Vartanyants (2012), *Physical Review B*, vol. 86, no. 17, 179904, 2012.

[26] R. P. Kurta, M. Altarelli, E. Wecker and I.A. Vartanyants (2012), *Physical Review B*, vol. 85, no. 18, 184204.

[27] J. Als-Nielsen and D. McMorrow (2011). *Elements of Modern X-ray Physics*. Wiley. Second Edition.

[28] P. Debye (1915). *Ann. Physik.*, 46:809.

[29] A. Dohn, E. Biasin, K. Haldrup, M.M. Nielsen, N.E. Henriksen and K.B. Møller (2015), *Journal of Physics B: Atomic, Molecular and Optical Physics*, Volume 48, Number 24.

[30] J.H. Jensen (2010). *Molecular Modeling Basics*. CRC Press.

[31] S.R. Bahn and K.W. Jacobsen (2002), *Computing in Science and Engineering*, 4:55.

[32] A.H. Larsen et al. (2017), *Journal of Physics: Condensed Matter*, 29(7):273002.

[33] J. Kohanoff (2006). *Electronic Structure Calculations for Solids and Molecules*. Cambrige Univ. Press.

[34] `https://wiki.fysik.dtu.dk/ase/` and `https://wiki.fysik.dtu.dk/gpaw/`

[35] J.J. Mortensen, L.B. Hansen and K.W. Jacobsen (2005), *Physical Review B*, 71:035109.

[36] J. Enkovaara et al. (2010), *Journal of Physics: Condensed Matter*, 22:253202.

[37] A. Brandt (1977), *Mathematics of Computation*, 31, 333

[38] E.L. Briggs, D.J. Sullivan and J. Bernholc (1996), *Physical Review B*, 54, 14362

[39] P.E. Blöchl (1994), *Physical Review B*, 50, 17953

[40] P.E. Blöchl, C. Forst and J. Schimpl (2003), *Bulletin of Materials Science*, 26, 33.

[41] P. Hohenberg and W. Kohn (1964). *Inhomogeneous Electron Gas*. Phys. Rev. 136. B864-867

[42] C. Lee, W. Yang and R. Parr (1988). *Physical Review B*, 37, 785.

[43] K.S. Kjaer, T.B. van Driel, J. Kehres, K. Haldrup, D. Khakhulin, K. Bechgaard, M. Cammarata, M. Wulff, T.J. Soerensen and M.M. Nielsen (2013), *Phys. Chem. Chem. Phys.*, 15(36):15003-16.

[44] M. Cammarata, M. Lorenc, T.K. Kim, J.H. Lee, Q. Kong, E. Pontecorvo, M. Lo Russo, G. Schiro, A. Cupane, M. Wulff (2006), *The Journal of Chemical Physics*, 124.

[45] P.R. Longaker and M.M. Litwak(1969). *J. Appl. Phys.* 40, 4033.

[46] The figure is kindly borrowed from Frank Horst.

[47] T. B. van Driel, K. S. Kjaer, E. Biasin, K. Haldrup, H. T. Lemke, and M. M. Nielsen (2015), *Faraday Discuss.*, 177, 443.

[48] C. Pellegrini (2012), *The European Physical Journal H*, vol. 37, pp. 659-708.

[49] G. Hura, J. Sorenson, R. Glaeser and T. Head-Gordon (2000), *J. Chem. Phys.*, 113, 9140.

[50] P. Bosecke and O. Diat (1997), *J. Appl. Cryst.*, 30, 867-871.

[51] J.R. Taylor (1997). *An Introduction to Error Analysis*. Second Edition. University Science Books.

[52] U. Lorenz, K.B. Møller and N.E. Henriksen (2010), *New Journal of Physics*, 12.

[53] W. Press, S. Teukolsky, W.T. Vetterling and B.P. Flannery (1988). *Numerical Recipes*. Cambridge University Press.

[54] A. Dent, P. Stephenson and G. Greaves(1991). *Rev. Sci. Instrum.* 63, 856-858.

[55] H. Ihee, M. Wulff, J. Kim and S. Adachic (2010), *International Reviews in Physical Chemistry*, 29(3):453-520.

[56] D. Franke, C.M. Jeffries and D.I. Svergun (2015), *Nature Methods*, vol.12 No.5.

[57] M.F. Schilling (1990), *Coll. Math. J.*, 21, 196-207.

[58] V.E. Johnson (2013), *Proc. Natl. Acad. Sci.*, USA 110, 19313-19317.

[59] U. Banin, A. Bartana, S. Ruhman and R. Kosloff (1994), *Journal Chemical Physics*, 101(10):8461-8481.

[60] E. Gershgoren, J. Vala, R. Kosloff and S. Ruhman (2001), *Journal of Physical Chemistry A*, 105(21):5081-5095.

[61] A.M. Zheltikov (2000), *Journal of Raman Spectroscopy*, 31(8-9):653-667.

[62] M.T. Zanni, T.R. Taylor, B.J. Greenblatt, B. Soep and D. Neumark (1997), *Journal of Chemical Physics*, 107(19):7613-7619.

[63] R.W. Hartsock, W. Zhang, M.G. Hill, B. Sabat and K.J. Gaffney (2011), *Journal of Physical Chemistry A*, 115(14):2920-2926.

[64] R.R. Frontiera and R.A. Mathies (2011), *Laser and Photonics Reviews*, 5(1):102-113.

[65] C.M. Che, L.G. Butler and H.B. Gray (1981), *Journal of the American Chemical Society*, vol 103, no. 26, p. 7796-7797.

[66] K.H. Leung, D.L. Phillips, C.M. Che and V. Miskowski (1999), *Journal of Raman Spectroscopy*, 30(11):987-993.

[67] R. Monni, G. Aubrock, D. Kinchel, K.M. Aziz-Lange, H.B. Gray, A. Vlcek and M. Chergui (2017), *Chemical Physics Letters*, 1, 112-120.

[68] A. Dohn et al. (2017), *J. of Chem. Theory Comput.*, 13 (12), pp 6101–6107.

[69] T. Ziegler and A. Rauk (1977), *Theoretica Chimica Acta*, 43(3):261-271.

[70] J. Gavnholt, T. Olsen, M. Engelund and J. Schiotz (2008), *Physical Review B*, 78(7),

[71] Q. Liu, J.K. Wang and A.H. Zewail (1993), *Nature*, 364, 427-430.

[72] A. Nitzan (2006), *A. Chemical Dynamics in Condensed Phases*, 1st edn (Oxford Graduate Texts).

[73] J.T. Hynes (2015), *Annu. Rev. Phys. Chem.*, 66, 1-20.

[74] R. M. van der Veen, A. Canizzo, F. van Mourik, A. Vlcek and M. Chergiu (2011), *Journal of the American Chemical Society*, 133(2):305-315.

[75] A.N. Tarnovsky, W. Gawelda, M. Johnson, C. Bressler and M. Chergui (2006), *The Journal of Physical Chemistry B*, vol. 110, no. 51, pp 26497-26505.

[76] Q. Kong, K.S. Kjær, K. Haldruo, S. Sauer, T.B. van Driel, M. Christensen, M.M. Nielsen and M. Wulff (2012), *Chemical Physics*, 393, 117-122.

[77] S. Kruppa, Y. Nosenko, M.O. Winghart, S.P. Walb, M.M. Kappes and C. Riehn (2016), *International Journal of Mass Spectroscopy*, 395, 7-19.

[78] Measured by Kasper Skov Kjaer at the Technical University of Denmark.

[79] C.D. Kim, S. Pillet, G. Wu, W.K. Fullagur and P. Coppens (2002), *Acta Crystallographica*, 58(2):133-137.

[80] N. Yasuda, M. Kanazawa, H. Uekusa and Y. Ohashi (2002), *Chemistry Letters*, (11):1132-1133.

[81] P. Stein, M.K. Dickson and M. Roundhill (1983), *J. Am. Chem. Soc.*, 105, 3489-3494.

[82] *International Tables for Crystallography* (2014), John Wiley and Sons.

[83] S. Mukamel (1995), *Principles of Nonlinear Optical Spectroscopy*. Oxford: Oxford Univ. Press.

[84] V.T. Pham, W. Gawelda, Y. Zaushitsyn, M. Kaiser, D. Grolimund, S.L. Johnson, R. Abela, C. Bressler and M.J. Chergui (2007), *Am. Chem. Soc.*, 129, 1530.

[85] V.T. Pham, T.J. Penfold, R.M. van der Veen, F. Lima, A. El Nahhas, S.L. Johnson, P. Beaud, R. Abela, C. Bressler, I. Tavernelli, C.J. Milne and M. Chergui (2011), *J. Am. Chem. Soc.*, 133, 12740-12748.

[86] P. Hart, S. Boutet, G. Carini, M. Dubrovin, B. Duda, D. Fritz, G. Haller, R. Herbst, S. Herrmann and C. Kenney (2012), The Cornell-SLAC Pixel Array Detector at LCLS. Proc. SPIE, 85040C, 538-541.

[87] K. Haldrup, M. Christensen, and M.M. Nielsen (2010), *Acta Crystallogr. Sect. A*, 66, 261.

[88] K. Haldrup, G. Vankó, W. Gawelda, A. Galler, G. Doumy, A. M. March, E. P. Kanter, A. Bordage, A. Dohn, T. B. van Driel, K. S. Kjær, H. T. Lemke, S. E. Canton, J. Uhlig, V. Sundström, L. Young, S. H. Southworth, M. M. Nielsen and C. Bressler (2012), *J. Phys. Chem. A*, 116, 9878.

[89] X.Y. Chen and S.E. Bradforth (2008), *S. E. Annu. Rev. Phys. Chem.*, 59, 203.

[90] J.A. Kloepfer, V.H. Vilchiz, V.A. Lenchenkov, X.Y. Chen and S.E. Bradforth (2002), *Chem. Phys.*, 117, 766.

[91] H. Iglev, A. Trifonov, A. Thaller, I. Buchvarov, T. Fiebig and A. Laubereau (2005), *A. Chem. Phys. Lett.*, 403, 198.

[92] F. Messina, O. Bram, A. Canizzo and M. Chergui (2013), *Nature Communications*, 4, 2119.

[93] H. Okuyama, Y. Suzuki, S. Karashima and T. Suzuki (2016), *The Journal of Chemical Physics*, 145, 074502.

[94] Y.I. Suzuki, H. Shen, Y. Tang, N. Kurahashi, K. Sekiguchi, T. Mizuno and T. Suzuki (2011), *Chem. Sci.*, 2, 1094-1102

[95] J.R. Casey, A. Kahros and B.J. Schwartz (2013), *The Journal of Physical Chemistry B*, 117, 14173-15182.

[96] J. Schnitker and P.S. Rossky (1984), *The Journal of Chemical Physics*, 86, 3462.

[97] L. Turi, M.P. Gaigeot, N. Levy and D. Borgis (2001), *J. Chem. Phys.*, 114, 7805-7815.

[98] L. Turi and D. Borgis (2002), *J. Chem. Phys.*, 117, 6186-6195.

[99] R.E. Larsen, W.J. Glover and B.J. Schwartz (2010), *Science*, 329, 65-69.

[100] F. Uhlig, O. Marsalek and P. Jungwirth (2012), *J. Phys. Chem. Lett.*, 3, 3071-3075.

[101] B.E. Warren (1990), *X-ray Diffraction*, Dover Publications, New York.

[102] A. Guinier (1994), *X-ray Diffraction in Crystals, Imperfect Crystals, and Amorphous Bodies*, Dover Publications, New York.

[103] M. Altarelli et al. (2007), *The European X-ray Free-Electron Laser - Technical Design Report*, DESY, 2006-098.

[104] P.J. Steinhardt, D.R. Nelson and M. Ronchetti (1983), *Phys. Rev. B*, 28, 784.

[105] A.V. Oppenheim and R.W. Schafer (1999), *Discrete-Time Signal Processing*, Prentice Hall, New Jersey.

[106] R. P. Kurta, M. Altarelli and I.A. Vartanyants (2016), *Advances in Chemical Physics*, vol. 161, 2016.

[107] D. K. Saldin, V. L. Shneerson, M. R. Howells, S. Marchesini, H. N. Chapman, M. Bogan, D. Shapiro, R. A. Kirian, U. Weierstall, K. E. Schmidt and J. C H Spence (2010), *New J. Physics*, 12 035014.

[108] E. H. van Kleef and I. Powis (1996), *Mol. Phys.*, 96, 757.

[109] J. R. Lakowicz (2006), *Principle of Fluorescence spectroscopy*, Springer.

[110] P. Debye (1929), *Polar Molecules*, Dover, New York.

[111] F. Perrin (1934), *J. Phys. Radium*, 5, 497.

[112] C.M. Hu and R. Zwanzig (1974), *J. Chem. Phys*, 60, 4354.

[113] J.T. Edward (1970), *J. Chem. Educ*. 47, 261.

[114] E.W. Small and I. Isenberg (1977), *Biopolymers*, 16, 1907.

[115] R.J. Sension and R.M. Hochstrasser (1993), *J. Chem. Phys.*, 98, 2490.

[116] T.W. Nee an R. Zwanzig (1970), *J. Chem. Phys.*, 52, 6353.

[117] G. van der Zwan and J.T. Hynes (1985), *J. Phys. Chem.*, 89, 4181.

[118] S. Palese, L. Schilling, R. Miller, P.R. Staver and W.T. Lotshaw (1994), *The Journal of Physical Chemistry*, vol 98, no. 25, pp. 6308-6316.

[119] R. Jimenez, R.F. Fleming, P.V. Kumar and M. Maroncelli (1994), *Nature*, vol. 369, pp. 417-473.

[120] E.W. Castner and Y.J. Chang (1995), *The Journal of Chemical Physics*, vol 102, no 2.

Paper I

Ultrafast Structural Dynamics of Photo-Reactions Revealed by Model-Independent X-ray Cross-Correlation Analysis

Peter Vester,[1] Ivan A. Zaluzhnyy,[2, 3, a)] Ruslan P. Kurta,[4] Klaus B. Møller,[5] Elisa Biasin,[1, 6] Kristoffer Haldrup,[1] Martin Meedom Nielsen,[1, b)] and Ivan A. Vartanyants[2, 3, c)]

[1)]*Department of Physics, Technical University of Denmark, DK-2800 Lyngby, Denmark*

[2)]*Deutsches Elektronen-Synchrotron DESY, Notkestraße 85, D-22607 Hamburg, Germany*

[3)]*National Research Nuclear University MEPhI (Moscow Engineering Physics Institute), Kashirskoe shosse 31, 115409 Moscow, Russia*

[4)]*European XFEL, Holzkoppel 4, D-22869 Schenefeld, Germany*

[5)]*Department of Chemistry, Technical University of Denmark, DK-2800 Lyngby, Denmark*

[6)]*PULSE Institute, SLAC National Accelerator Laboratory, CA 94025, Menlo Park, USA*

(Dated: 24 October 2018)

We applied angular X-ray Cross-Correlation analysis (XCCA) to scattering images from a femtosecond resolution LCLS X-ray free-electron laser (XFEL) pump-probe experiment with solvated PtPOP ($[Pt_2(P_2O_5H_2)_4]^{4-}$) metal complex molecules. The molecules were pumped with linear polarized laser pulses creating an excited state population with a preferred orientational (alignment) direction. Two time scales of 1.9 ± 1.5 ps and 46 ± 10 ps were revealed by model-independent XCCA, associated with an internal structural changes and rotational dephasing, respectively. Our studies illustrate the potential of XCCA to reveal hidden structural information in a model independent analysis of time evolution of solvated metal complex molecules.

[a)]Present address: Department of Physics, University of California San Diego, La Jolla, CA 92093, USA

[b)]Electronic mail: mmee@fysik.dtu.dk

[c)]Electronic mail: ivan.vartaniants@desy.de

Pump-probe XCCA studies of PtPOP dymanics

I. INTRODUCTION

Recent development of coherent X-ray sources, such as synchrotrons and X-ray free-electron lasers (XFELs), led to a substantial progress in time-resolved X-ray scattering techniques, which allows one to study structural dynamics on femtosecond scale, making it possible to track chemical reactions in real time[1]. Despite a significant progress of X-ray scattering methods over the last decades, investigations of molecular structure and dynamics remains a challenging experimental task. A general problem within the structural analysis framework of small- and wide-angle X-ray scattering (SAXS/WAXS) experiments from molecules in solution is to deduce a large number of structural parameters, including three-dimensional (3D) structural model of the molecules and their interactions with the surrounding solvent molecules, from a single azimuthally integrated one-dimensional (1D) scattering curve. Moreover, the key structural parameters deduced from conventional SAXS/WAXS experiments are known to be strongly correlated with experimental parameters[2], which further complicates evaluation of molecular structure from the experimental data.

A possible way to enhance the structural information obtained in X-ray experiments is to excite molecules by a polarized pump laser which to a certain degree orients these molecules[3] and utilize anisotropic information recorded by the two-dimensional (2D) X-ray detectors for better optimization of the structural models. In this respect an angular X-ray cross-correlation analysis (XCCA)[4–10] has a significant potential to extract and utilize anisotropic information contained in 2D diffraction patterns to provide additional constraints for structural models in the framework of conventional SAXS/WAXS analysis, and, importantly, reveal otherwise hidden information on structure and dynamics of molecules under investigation.

The method of angular intensity correlations in X-ray diffraction goes back to a pioneering work of Z. Kam[11] and recently further developed in a number of publications (see for a review[12]). This method can, in principle, reveal information about the structure of an individual particle in solution not available from azimuthally integrated SAXS/WAXS measurements. Moreover, the angular distribution of scattered X-ray intensity also contains information about the spatial orientation of molecules. The ultra-bright femtosecond X-ray pulses from XFELs provide an opportunity to measure scattering signals with a time resolution much higher than rotational relaxation times, enabling studies of molecular rotational dynamics by laser pump/X-ray probe experiments. In this case, XCCA offers a model independent approach for investigation of structural dynamics

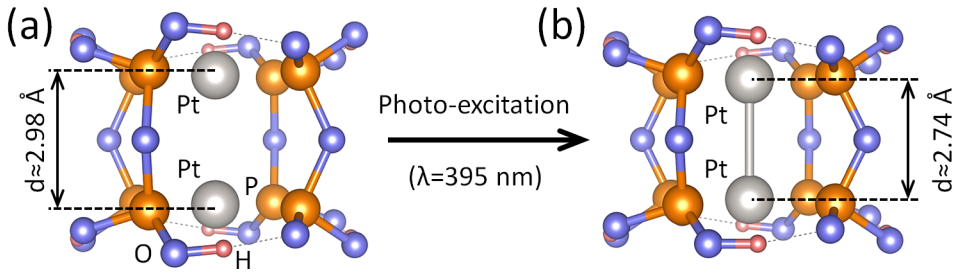

FIG. 1. (a) Structure of PtPOP molecule in ground state. (b) Structure of PtPOP molecule in excited state. Contraction of about 0.24 Å between two Pt atoms is shown.

of photo-excited ensembles of particles (molecules, proteins, etc) in solution. In contrast to conventional SAXS/WAXS techniques XCCA automatically separates scattering of bulk (isotropic) solvent from anisotropic solute in the experimental data. Our studies show that XCCA may significantly enhance the information content of scattering images in systems of partially oriented solvated molecules. The present work is a novel application of XCCA to investigate the structure and dynamics of solvated molecules.

This work is focused on the analysis of the experimental data obtained in the pump-probe X-ray scattering experiment performed at the Linear Coherent Light Source (LCLS)[13,14]. In contrast to these publications where the interpretation was based on a theoretical model of the molecular structure in solution, XCCA allowed us to study the molecular dynamics without any *a priori* knowledge or assumptions (cosine squared distribution of photo-excited molecules, symmetric top shape of the molecules, etc.). This work is a test bench to prove the validity of the XCCA technique to elucidate the structure and dynamics on molecular level. To verify our findings we compare experimental results with simulated X-ray diffraction patterns obtained from density functional theory (DFT) calculations of molecular structure.

II. EXPERIMENT

A. Photo-excitation of PtPOP molecules

The investigated metal complex molecules tetrakis-μ-pyrophosphitodiplatinate(II) anion ($[Pt_2(P_2O_5H_2)_4]^{4-}$, PtPOP) consist of a bi-planar Pt-Pt pair held together by four pyrophosphito ligands (Figure 1(a)). It belongs to a family of binuclear d^8-d^8 transition metal complexes exhibiting photophysical properties of both fundamental and applied interest[15] and shows intense luminescence with a total

quantum efficiency very close to unity, a property which has made the system very amenable to investigation by time-resolved optical methods in both frequency and time domains. It is now very well established, that upon photo-excitation at or near the 370 nm absorption peak, an electron is promoted from an anti-bonding $5d\sigma^*$ highest occupied molecular orbital (HOMO) to the bonding $6p\sigma$ lowest unoccupied molecular orbital (LUMO). This chemical transition leads to a pronounced structural change in the form of contraction[16,17] of the Pt atoms along the Pt-Pt axis by 0.24(4) Å (Figure 1(b)). Further, as the transition dipole moment lies along the Pt-Pt axis, the molecules will be selectively photo excited as a function of the Pt-Pt axis orientation relative to the polarization of the optical pump pulse[3], all of which makes it an excellent candidate for exploring the potential of XCCA (Figure 2(a)).

Following the photo-excitation event, the molecule is in a singlet state, and on a time scale of 1-10 ps undergoes inter-system crossing (ISC) to a triplet state. The excited singlet- and triplet states, are well separated, both in their respective lifetimes (1-10 ps and 10 μs, respectively) as well as in terms of their potential energy surfaces, which are highly harmonic, nested potentials shifted 0.24(4) Å along the Pt-Pt coordinate with respect to the also highly harmonic ground state potential surface[15,18]. The quantum yield close to unity and well-separated optical signatures of the two states make PtPOP an almost ideal system for studying the fundamental phenomenon of non-radiative singlet-triplet transitions in the case where no intersections along the main reaction coordinate are immediately apparent. However, to this day the intermediate state(s) and mechanism mediating the spin-state change remains elusive despite much recent work[19–21]. From these optical studies both direct interaction with the solvent, as well as deformation of the POP ligands, have been suggested as possible mechanisms. However, the suggested intermediate states are optically "dark" and methods directly sensitive to structure are needed.

B. Pump-probe experiment

The dynamics following photo-excitation of aqueous PtPOP molecules was tracked in time-resolved pump-probe X-ray diffuse scattering (XDS) experiments at the XPP beamline of the LCLS XFEL facility as schematically illustrated in Figure 2(b) (for details of the experimental setup see[22,23]). The investigated sample was a 80 mM aqueous solution of PtPOP in a vertical free flowing cylindrical liquid jet of 50 μm in diameter at a flow rate sufficient to fully replace the sample between successive pump-probe events (120 Hz). The sample was excited by a short 50

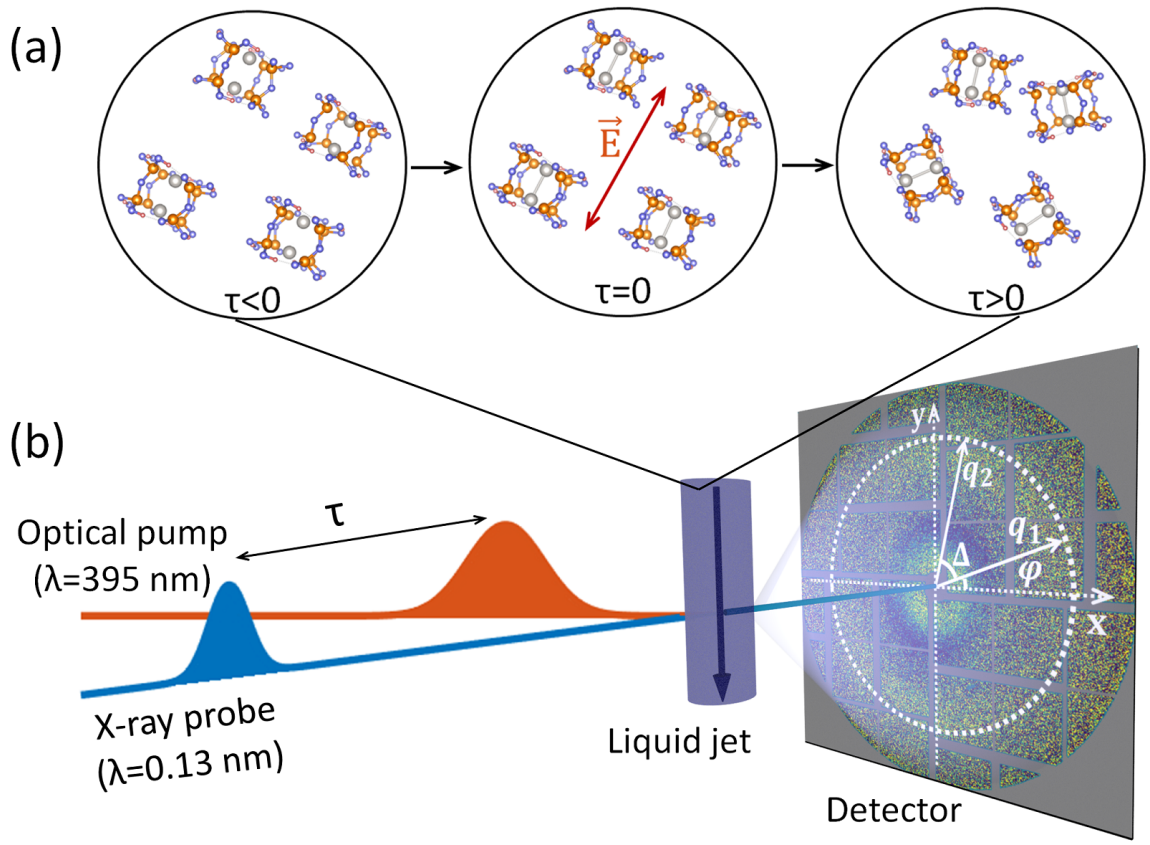

FIG. 2. (a) Temporal evolution of an ensemble of randomly oriented PtPOP molecules before ($\tau < 0$) and after ($\tau \geq 0$) excitation. The optical pump selectively excites PtPOP molecules with a dipole moment parallel to the laser electric field $\mathbf{E}$ at $\tau = 0$ and the population of excited molecules eventually evolves ($\tau > 0$) to a random orientational distribution on a timescale of tens of picoseconds. (b) Scheme of the pump-probe experiment at LCLS. The experiment utilizes the optical pump laser/X-ray probe detection scheme on a circular liquid jet system with the time resolution given by the time delay τ of the femtosecond X-ray pulse. On the detector momentum transfer vectors q_1 and q_2 are shown with the angular coordinates φ and $\varphi + \Delta$.

fs 5 μJ laser pulse with wavelength of 395 nm (pump) followed by a 50 fs 9.5 keV X-ray pulse (probe) at a well-defined time delay. The nearly collinear laser beam with a circular spot size of approximately 50 μm and the X-ray beam with an estimated spot size of 30 μm at full width at half maximum (FWHM) were spatially and temporally overlapped at the sample position in the middle of the liquid jet. The X-ray probe pulses were polarized in the horizontal direction, whereas the laser pump pulses had a linear polarization 20 degrees off the vertical. Thus, a single pump-

probe event gives a snapshot of the configuration after photo-excitation at a single time-delay τ, and by combining snapshots at different time-delays the dynamics of the excited molecules can be followed.

XDS signals were recorded in the forward direction by the large-area 2D CS-PAD detector[24] positioned 10 cm behind the sample and corrected for such effects as polarization, solid angle, absorption, background/dark image subtraction and outlier rejection as previously described[23]. The sensitivity of the diffraction patterns to structural changes in the sample is increased by considering difference scattering images, which are created by subtracting a laser-off (all molecules in the ground state) image from the nearest laser-on images (some molecules in the excited state) in the sequence of collected detector images. The difference scattering images contain only a change in diffraction signal from ground- and excited-state PtPOP molecules and their interaction with solvent cage, while the constant background arising from solvent scattering cancels out. To increase signal-to-noise ratio the collected diffraction patterns were temporally binned into 1 ps bins using the timing tool at LCLS, which allowed us to collect sufficiently many diffraction patterns ($M \approx 3,000$) within each time bin for reliable XCCA analysis. The measured difference scattering images averaged over 1 ps intervals of two different time delays $\tau = 0-1$ ps and $\tau = 9-10$ ps are shown in Figure 3(a,b). One can see slight anisotropy in the intensity of the difference scattering images, parallel to the laser polarization (about 20 degrees to vertical direction), which appears due to the photo-excitation selectively occurring in molecules with Pt-Pt axis oriented along the polarization vector of the pump laser pulse[3].

III. X-RAY CROSS-CORRELATION ANALYSIS

Angular anisotropy of difference diffraction patterns was analyzed by XCCA, which is based on evaluation of two-point angular cross-correlation functions (CCFs). In this work, we apply the CCF defined on the scattering ring of radius q, where $\mathbf{q} = (q, \varphi)$ is the momentum transfer vector defined in the polar coordinate system of the 2D detector[12,25],

$$C(q,\Delta) = \langle I^{dif}(q,\varphi) I^{dif}(q,\varphi+\Delta)\rangle_{\varphi}\,, \tag{1}$$

where $I^{dif}(q,\varphi) = I^{On}(q,\varphi) - I^{Off}(q,\varphi)$ is the measured difference intensity between the laser on $I^{On}(q,\varphi)$ and laser off $I^{Off}(q,\varphi)$ diffraction patterns, Δ is the angular coordinate, and $\langle f(\varphi)\rangle_{\varphi}$ denotes the angular average of the function $f(\varphi)$. In this work, the diffraction patterns were

masked prior to the calculation of the CCF to exclude beamstop area, gaps between detector tiles as well as not responding pixels on the detector. The pixels were also binned in 4×4 pixel groups to increase signal to noise ratio.

It is convenient to decompose the CCFs using an angular Fourier series on a ring of radius q

$$C(q,\Delta) = \sum_{n=-\infty}^{\infty} C_n(q) e^{in\Delta}, \tag{2}$$

$$C_n(q) = \frac{1}{2\pi} \int_0^{2\pi} C(q,\Delta) e^{-in\Delta} \mathrm{d}\Delta, \tag{3}$$

where $C_n(q)$ are the angular Fourier components of the CCF. It can be shown[25] that Fourier components of the CCFs are directly related to Fourier components of the difference intensities as

$$C_n(q) = \left| I_n^{dif}(q) \right|^2. \tag{4}$$

In practical applications, due to statistical variations of the CCFs, one needs to average the Fourier components (4) over a large number M (typically of the order of 10^3 to 10^6) of diffraction patterns to obtain reliable information about symmetry and structure of the system[25]. Averaged values of the Fourier components $\langle C_n(q) \rangle$ are directly related to the structure of molecules and their orientational distribution[26].

IV. RESULTS

A. Analysis of the angular anisotropy

XCCA provides an excellent tool for model-independent analysis of angular anisotropy of difference diffraction patterns (Figure 3). The averaged Fourier components of the angular CCF (4) from the experimental difference scattering intensities at two different time delays evaluated according to definition (3) are shown in Figure 3(c,d). According to equations (1)-(3) the zero-order angular Fourier component ($n = 0$) can be considered as the square of an azimuthally integrated difference intensity $I^{dif}(q,\varphi)$

$$\langle C_0(q) \rangle \propto \left| \int I^{dif}(q,\varphi) \mathrm{d}\varphi \right|^2. \tag{5}$$

The first two peaks of $\langle C_0(q) \rangle$ at $q \approx 0.7$ Å^{-1} and $q \approx 1.8$ Å^{-1} (see Fig. 3(c,d)) correspond to internal concentric rings with positive and negative signal on the difference scattering images in

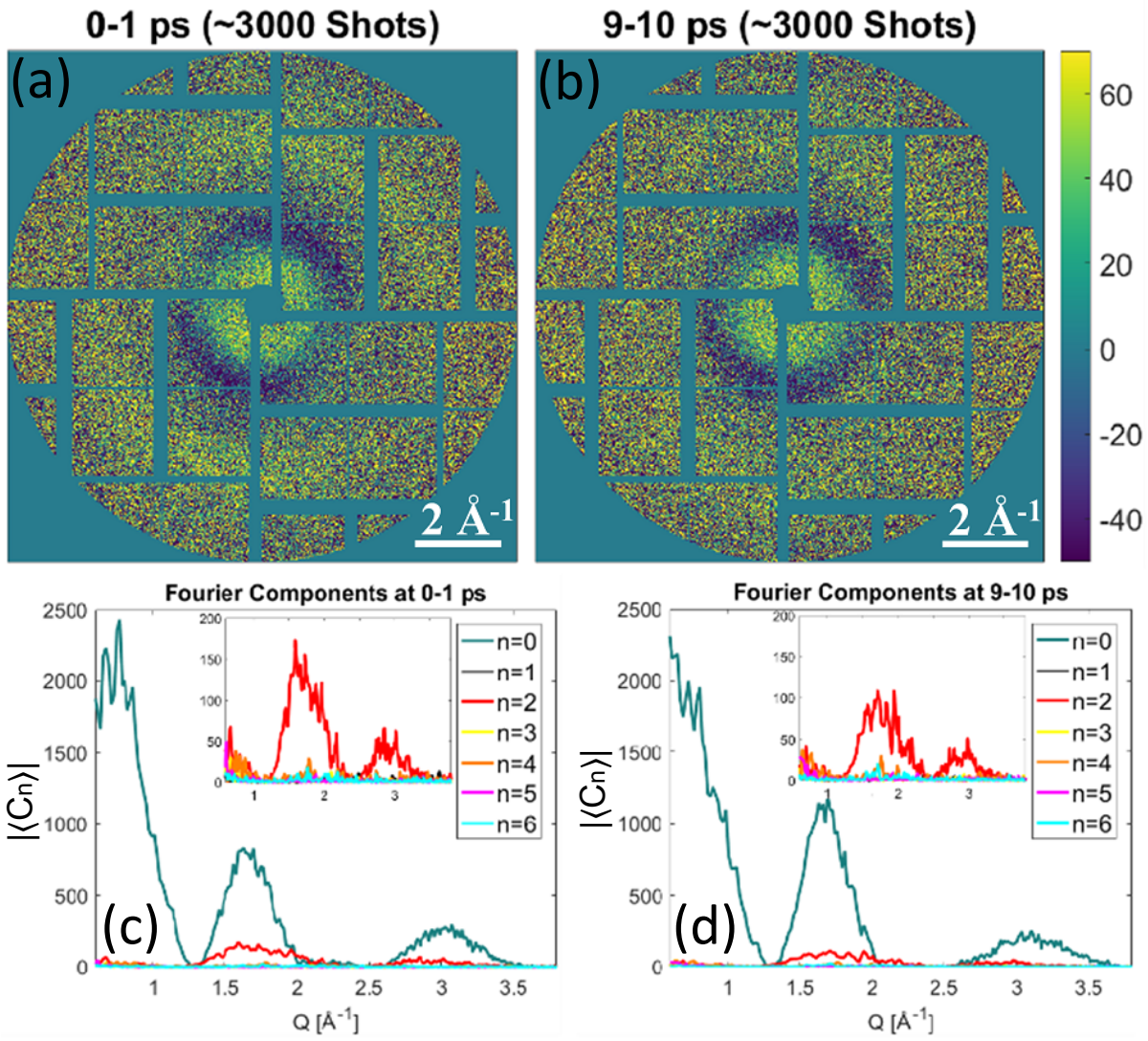

FIG. 3. (a-b) Difference scattering detector images (laser On - laser Off) for two different one picosecond time delay intervals. For better visualisation shown diffraction patterns were averaged over about 3,000 pulses within each time delay interval. (c-d) Calculated averaged Fourier components of the CCFs. The insets show the dominant anisotropic $n = 2$ Fourier component contribution (the isotropic $n = 0$ Fourier component is removed from the insets).

Fig. 3(a,b). A clearly visible peak of the same Fourier component in Fig. 3(c,d) at $q \approx 3.0$ Å^{-1} (see Fig. 3(c,d)) corresponds to the broad anisotropic external scattering ring in Figure 3(a,b).

Information about angular anisotropy in diffraction can be conveniently accessed by evaluation of the higher-order Fourier components of the CCF $\langle C_n(q)\rangle$, i.e. for $n = 2,4,6,\ldots$. A dominant $n = 2$ angular Fourier component in the diffraction pattern is clearly visible in the inset of Figure

3(c,d). A rapid decay of the dominant component after optical pump pulse is a strong evidence that the observed $n = 2$ signal arises from a twofold symmetric orientational distribution of the excited state of the molecules induced by the laser excitation at time delay $\tau = 0$. Weak but consistent $n = 4$ and $n = 6$ components can be also seen at around $q \approx 1.8$ Å^{-1}. In principle, higher order intensity Fourier components in the X-ray scattering may originate from the internal symmetry of the individual molecules (see Figure 1(a)), which was directly observed in simulations with a relatively small number of illuminated particles[27].

In general, the azimuthally averaged $n = 0$ signal contains contributions from the solute, solvent cage and bulk solvent (heating and density changes caused by optical pump)[28]. The latter two should be subtracted from the azimuthally average data to extract the signal corresponding to the changes in solute structure[29]. In contrast, the $n = 2$ signal is not influenced by the bulk solvent contributions but includes contributions from variations with the same symmetry as the orientational distribution of the molecules, e.g. solvent cage. This significantly reduces the amount of free parameters in any structural analysis and makes the interpretation of the time constants more clear and requires less assumptions about the system. A combination of both the $n = 0$ and $n = 2$ curves will give two different signals to benchmark the structural models, where one is dependent and one is independent of the bulk solvent contribution and therefore gives the possibility to enhance the structural information from a SAXS/WAXS experiment.

B. Analysis of molecular dynamics

The values of non-zero CCF Fourier components contain all available information about the orientational distribution of photo-excited molecules. To study the dynamics of excited PtPOP we considered the temporal evolution of the $n = 2$ Fourier component. To quantify the fraction of excited molecules within the cosine squared orientational distribution the normalized integrated area $S_2(\tau) = \int \sqrt{\langle C_2(q,\tau)\rangle} dq$ under the peak at $q \approx 1.8$ Å^{-1} of the averaged second-order Fourier component cross-correlation function was considered (integration over q was performed within the range 1.1 Å^{-1} - 2.3 Å^{-1}). The temporal evolution of this quantity as a function of delay time $\tau = 0 - 500$ ps is shown by dots in Figure 4. One can clearly see a significant decay of the anisotropic signal after 10 ps. Binning of the same data into 250 fs time bins, shown in the inset of Figure 4, reveals an additional short-time decay, which is clearly visible on top of the longer

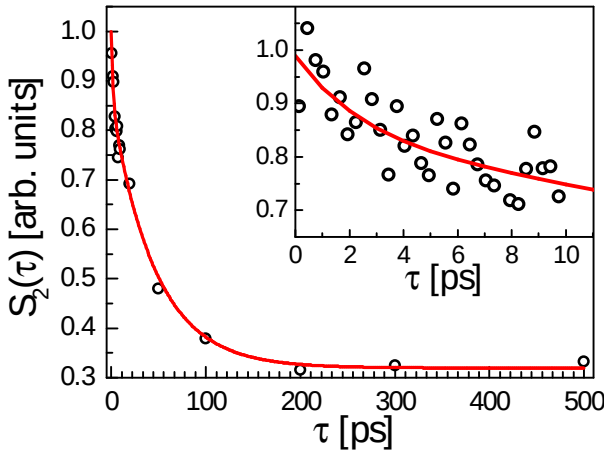

FIG. 4. A double exponential decay with the time constants $\tau_1 = 1.9 \pm 1.5$ ps and $\tau_2 = 46 \pm 10$ of the normalized area $S_2(\tau) = \int \sqrt{\langle C_2(q,\tau)\rangle} dq$ under the peak at $q = 1.8$ Å^{-1}. The average Fourier components of CCF $\langle C_2(q,\tau)\rangle$ were calculated according to equation (4) binned in 1 ps bins. In inset binning into 250 fs time bins reveals short time decay. Points experimental data, solid line fit to equation (6).

decay. Thus, the total decay was approximated by a sum of two exponential terms

$$S_2(\tau) = Ae^{-\tau/\tau_1} + Be^{-\tau/\tau_2} + C, \tag{6}$$

where $A = 21 \pm 5\%$ and $B = 79 \pm 5\%$ are scale constants and C is related to the general noise level of the averaged images. Based on least-square fitting (see solid line in Figure 4), the values of time constants were found to be $\tau_1 = 1.9 \pm 1.5$ ps and $\tau_2 = 46 \pm 10$ ps. We would like to stress here that the values of time constants were obtained without any modeling or *a priory* knowledge of system behavior.

The longer time scale $\tau_2 = 46 \pm 10$ ps may be interpreted as the rotational dephasing of the initial cosine squared distribution of orientations to a completely random and isotropic distribution. The reorientation time τ_r for a molecule in solution can be estimated from the Stokes-Einstein-Debye hydrodynamic theory in a classical dynamical framework without electrical interactions as $\tau_r \approx 50$ ps[13]. The specific molecular shape of PtPOP can be taken into account (here we approximated the shape of PtPOP molecule by a sphere with the radius $r = 4$ Å), which would lead to a slight change of the value of rotational time constant τ_r. If the laser excitation involves a change in size, shape or dielectric properties of a molecule, a different reorientation time can be expected for the excited species. It means that the $n = 2$ contribution from the ground and excited states can be distinguished by following the temporal evolution of the $n = 2$ signal as the

molecules with a longer time constant will dominate the signal at longer time delays. This applies as well to experiments where different species (or same species of different sizes) in the same sample volume are excited with a preferred orientational direction. The molecular reorientation time obtained from the $n = 2$ signal can not be determined from radially integrated $n = 0$ curves and can be used to refine structural models and gain new insight in time-resolved SAXS/WAXS experiments.

A direct interpretation of the shorter time constant $\tau_1 = 1.9 \pm 1.5$ ps is more challenging as it is assumed to arise from the internal dynamics of the molecule on short time scales. The area under the two dominant peaks at $q \approx 1.8$ Å^{-1} and $q \approx 3.0$ Å^{-1} in the measured $n = 2$ signal decreases with a similar time constant indicating that the shape of the signal remains almost unchanged. Therefore, we interpret the short time constant as possibly reflecting the time scales for vibrational decoherence of the PtPOP molecule[18,21,30], but the underlying mechanism is at present unknown.

C. Model of the scattering signal

The time-dynamics results of XCCA can be directly compared to simulations based on a DFT structural model. In this work we utilize a simple model for the excited state population of PtPOP, where they are considered as linear molecules. Such model can be justified by rotational symmetry of PtPOP molecule around the Pt-Pt axis and the fact that the excitation of the molecule can be approximated to a high accuracy by Pt-Pt bond contraction. When such symmetric top molecules are excited from thermal equilibrium by one-photon absorption, the orientational distribution of excited molecules will have a cosine squared distribution with respect to the polarization of the incoming optical photons[31], which was indeed observed in the collected X-ray diffraction patterns (Figure 3).

As a model system for simulation we assume a 3D disordered sample consisting of $N = 10^5$ molecules. In the approximation of a dilute disordered sample where the mean distance between the molecules is larger than the coherence length of the incoming beam, interference between the X-rays scattered from different molecules can be neglected and the total scattered intensity can be represented as a sum of intensities from the individual molecules in the system. The X-ray intensity scattered from one molecule can be evaluated as

$$I_{mol}(\mathbf{q}) = \left| \sum_i f_i(q) e^{i\mathbf{q}\mathbf{r}_i} \right|^2, \tag{7}$$

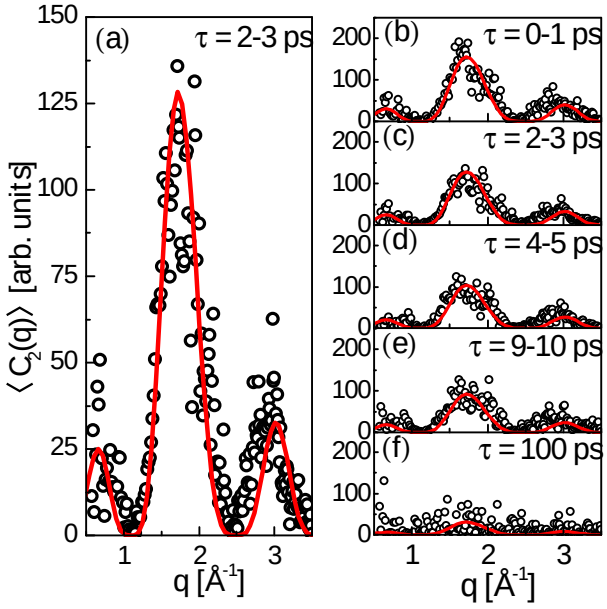

FIG. 5. (a) Direct comparison of the calculated $n = 2$ CCF Fourier components from the simulation of 10^5 PtPOP molecules with a cosine squared angular distribution, fitted to the measured components in the $2-3$ ps time delay interval with a scaling factor $\alpha(\tau)$. (b-e) Same comparison for different time delays; at $\tau = 100$ ps (f) the molecules have almost completely lost their preferred orientation. Here dots are experimental data obtained from XCCA analysis, solid lines are theoretical fit.

where $\mathbf{r}_i$ are the atomic positions and $f_i(q)$ are the atomic form factors of the i-th atom in the PtPOP molecule.

The coordinates of atoms in excited and ground state PtPOP structures were calculated by DFT simulations (see for details[18,32]). This gives a Pt-Pt bond contraction of 0.24 Å, while the ligand cage structure remains rigid, which is in agreement with experimental X-ray scattering results[16,17].

To obtain the diffraction patterns from an ensemble of molecules in excited state, we simulated our sample as one in which each molecule was rotated within the cosine squared distribution. The positions of the atoms in rotated photo-excited PtPOP molecule were used to calculate a diffuse X-ray scattering signal from a single molecule using equation (7). Then the diffraction signal was averaged over $N = 10^5$ molecules and a difference scattering signal was calculated to obtain similar diffraction patterns as we observed in the XDS experiment.

Figure 5 shows a comparison of the experimentally observed and simulated $n = 2$ Fourier component of the CCF at different time delays. The model signal was scaled with a factor $\alpha(\tau)$ to account for the total number of excited PtPOP molecules in the probed volume of the sample and

their orientational distribution at the specific time delay. The scaling factor $\alpha(\tau)$ has a similar temporal decay behavior as observed for the $S_2(\tau)$ factor shown in Figure 4, with two time constants of 1.9 ± 1.4 ps and 41 ± 8 ps.

In this work we assumed that excited singlet and triplet states of PtPOP molecule are characterized by almost the same Pt-Pt distance within the accuracy of 0.01 Å[18,33], which means that we could not observe singlet-to-triplet ISC in our pump-probe experiment. Therefore, the temporal evolution of the scaling coefficient $\alpha(\tau)$ can be attributed only to the orientational dephasing of the excited molecules and not to the relaxation of the molecules to ground state, since the lifetime of triplet excited state is estimated to be about 10 μs. A direct comparison confirms the validity of the assumed model of the system, and the small discrepancies are interpretated as arising from the lack of a simulated solvent cage signal and slight variations between the DFT simulated structure and the actual structure of the molecule. This demonstrates how the direct structural modeling of these signals is possible in a straightforward and robust manner.

V. DISCUSSION

In this work by applying XCCA we show that the difference signal from photo-excited PtPOP molecules can be well represented by contribution of two (zero- and second-order) Fourier components. The dominant anisotropic signal of the $n = 2$ Fourier component of the CCF clearly indicates that orientation of the photo-excited PtPOP molecules can be approximated by a cosine squared distribution. This is in agreement with theoretical predictions[3,34], assuming a single-photon excitation and initially non-occupied rotational and vibrational degrees of freedom of the PtPOP molecules[13]. Observation of small values of higher-order Fourier components, indicates the possibility of XCCA to go beyond the common assumption about cosine squared distribution of molecular orientations and gain new insight on the structure of molecules.

Time-dependent analysis of the anisotropic scattering signal reveals that its shape remains unchanged, while the amplitude exponentially decreased to the noise level with two characteristic time-scales $\tau_1 = 1.9 \pm 1.5$ ps and $\tau_2 = 46 \pm 10$ ps. Taking into account the long lifetime of photo-excited state of PtPOP molecules and the fact that the ISC from the singlet to the triplet state occurs with near-unity efficiency, this decay can be attributed exclusively to rotational dephasing of molecules (longer time constant) and internal dynamics of molecules (shorter time constant). Our analysis is supported by simulation of the difference scattering signal, which shows that the

anisotropic scattering can be modelled by difference scattering signal from excited- and ground-state molecules at any time-delay. In principle, it should be possible to observe oscillations on a sub-300 fs timescale in the difference scattering signal, which is directly related to the Pt-Pt bond stretching mode[18,30]. The direct studies of the bond dynamics would require collecting significantly more scattering patterns with short time delays to accumulate sufficient statistics for the XCCA. This opens up the possibility to investigate, for example, the optical Kerr effect[35–37], which is based on creation of induced dipoles in the solvent molecules by the oscillating light field during the first few hundred femtoseconds after the pump pulse.

VI. CONCLUSIONS

In summary, we have shown how XCCA can be applied as a model independent approach to study the structural symmetries and their timescale of a disordered sample of solvated photo-excited PtPOP molecules with a preferred photo-induced orientation. We revealed two time scales that may be attributed to internal structural changes on short time scales and rotational dephasing at longer times. Analysis of $n = 2$ angular Fourier component of CCF enhance structural information, which is otherwise difficult to access in a conventional SAXS approach. In an ultrafast experiment with a smaller X-ray beam and at high flux facility it might be possible to detect higher order scattering terms necessary for studies of dynamics of internal symmetries of the molecules. We believe that the technique presented here can be widely used in SAXS/WAXS experiments to enhance structural information from a disordered sample of molecules, proteins or biomolecules and to reveal hidden symmetries and their time evolution in a model independent approach.

ACKNOWLEDGMENTS

We acknowledge E. Weckert for fruitful discussions and support of the project and L. Gelisio for a careful reading of the manuscript. RPK and IAV acknowledge support from the Helmholtz Association's Initiative and Networking Fund and the Russian Science Foundation (project No. 18-41-06001). The authors would like to acknowledge Henrik T. Lemke, Silke Nelson, Mike Glownia, T.B. van Driel and Morten Christensen for fruitful scientific discussions. The DTU-affiliated authors would like to gratefully acknowledge DANSCATT for funding the beam time efforts. MMN, KBM, and EB gratefully acknowledge support from the Danish Council For Inde-

pendent Research under grant no. DFF 4002-00272B. MMN and KBM gratefully acknowledge support from the Independent Research Fund Denmark under grant no. 8021-00347B. Use of the Linac Coherent Light Source (LCLS), SLAC National Accelerator Laboratory, is supported by the U.S. Department of Energy, Office of Science, Office of Basic Energy Sciences under Contract No. DE-AC02-76SF00515.

REFERENCES

[1]M. P. Minitti, J. M. Budarz, A. Kirrander, J. S. Robinson, D. Ratner, T. J. Lane, D. Zhu, J. M. Glownia, M. Kozina, H. T. Lemke, M. Sikorski, Y. Feng, S. Nelson, K. Saita, B. Stankus, T. Northey, J. B. Hastings, and P. M. Weber, "Imaging molecular motion: Femtosecond x-ray scattering of an electrocyclic chemical reaction," Phys. Rev. Lett. **114**, 255501 (2015).

[2]K. Haldrup, T. Harlang, M. Christensen, A. Dohn, T. B. van Driel, K. S. Kjær, N. Harrit, J. Vibenholt, L. Guerin, M. Wulff, and M. M. Nielsen, "Bond Shortening (1.4 Å) in the Singlet and Triplet Excited States of $[Ir_2(dimen)_4]^{2+}$ in Solution Determined by Time-Resolved X-ray Scattering," Inorg. Chem. **50**, 9329–9336 (2011).

[3]U. Lorenz, K. B. Møller, and N. E. Henriksen, "On the interpretation of time-resolved anisotropic diffraction patterns," New J. Phys. **12**, 113022 (2010).

[4]P. Wochner, C. Gutt, T. Autenrieth, T. Demmer, V. Bugaev, A. D. Ortiz, A. Duri, F. Zontone, G. Grübel, and H. Dosch, "X-ray cross correlation analysis uncovers hidden local symmetries in disordered matter," Proc. Natl. Acad. Sci. USA **106**, 11511 LP – 11514 (2009).

[5]R. P. Kurta, B. I. Ostrovskii, A. Singer, O. Y. Gorobtsov, A. Shabalin, D. Dzhigaev, O. M. Yefanov, A. V. Zozulya, M. Sprung, and I. A. Vartanyants, "X-ray cross-correlation analysis of liquid crystal membranes in the vicinity of the hexatic-smectic phase transition," Phys. Rev. E **88**, 044501 (2013).

[6]D. Mendez, T. J. Lane, J. Sung, J. Sellberg, C. Levard, H. Watkins, A. E. Cohen, M. Soltis, S. Sutton, J. Spudich, V. Pande, D. Ratner, and S. Doniach, "Observation of correlated x-ray scattering at atomic resolution," Philos. Trans. Royal Soc. B Biol. Sci. **369**, 20130315 (2014).

[7]R. Kurta, L. Grodd, E. Mikayelyan, O. Gorobtsov, I. Zaluzhnyy, I. Fratoddi, I. Venditti, M. Russo, M. Sprung, I. Vartanyants, and S. Grigorian, "Local structure of semicrystalline P3HT films probed by nanofocused coherent X-rays," Phys. Chem. Chem. Phys. **17**, 7404–7410 (2015).

[8]F. Lehmkühler, B. Fischer, L. Müller, B. Ruta, and G. Grübel, "Structure beyond pair correlations: X-ray cross-correlation from colloidal crystals," J. Appl. Crystallogr. **49**, 2046–2052 (2016).

[9]I. Zaluzhnyy, R. Kurta, E. Sulyanova, O. Gorobtsov, A. Shabalin, A. Zozulya, A. Menushenkov, M. Sprung, A. Krówczyński, E. Górecka, B. Ostrovskii, and I. Vartanyants, "Structural studies of the bond-orientational order and hexatic-smectic transition in liquid crystals of various compositions," Soft Matter **13**, 3240–3252 (2017).

[10]I. Zaluzhnyy, R. Kurta, A. André, O. Gorobtsov, M. Rose, P. Skopintsev, I. Besedin, A. Zozulya, M. Sprung, F. Schreiber, I. Vartanyants, and M. Scheele, "Quantifying Angular Correlations between the Atomic Lattice and the Superlattice of Nanocrystals Assembled with Directional Linking," Nano Lett. **17**, 3511–3517 (2017).

[11]Z. Kam, "Determination of Macromolecular Structure in Solution by Spatial Correlation of Scattering Fluctuations," Macromolecules **10**, 927–934 (1977).

[12]R. Kurta, M. Altarelli, and I. A. Vartanyants, "Structural analysis by x-ray intensity angular cross correlations," Adv. Chem. Phys. **161**, 1–39 (2016).

[13]E. Biasin, T. B. van Driel, G. Levi, M. G. Laursen, A. O. Dohn, A. Moltke, P. Vester, F. B. K. Hansen, K. S. Kjaer, T. Harlang, R. Hartsock, M. Christensen, K. J. Gaffney, N. E. Henriksen, K. B. Møller, K. Haldrup, and M. M. Nielsen, "Anisotropy enhanced X-ray scattering from solvated transition metal complexes," J. Synchrotron Radiat. **25**, 306–315 (2018).

[14]K. Haldrup, G. Levi, E. Biasin, P. Vester, M. Laursen, F. Beyer, K. S. Kjær, T. B. van Driel, T. Harlang, A. O. Dohn, R. J. Hartsock, S. Nelson, J. M. Glownia, H. T. Lemke, M. Christensen, K. J. Gaffney, N. E. Henriksen, K. B. Møller, and M. M. Nielsen, "Ultrafast X-ray scattering measurements of coherent structural dynamics on the ground-state potential energy surface of a diplatinum molecule," Submitted to Phys. Rev. Lett. (2018).

[15]H. B. Gray, S. Záliš, and A. Vlček, "Electronic structures and photophysics of d8-d8 complexes," Coord. Chem. Rev. **345**, 297–317 (2017).

[16]M. Christensen, K. Haldrup, K. Bechgaard, R. Feidenhans'l, Q. Kong, M. Cammarata, M. L. Russo, M. Wulff, N. Harrit, and M. M. Nielsen, "Time-Resolved X-ray Scattering of an Electronically Excited State in Solution. Structure of the $^3A_{2u}$ State of Tetrakis-μ-pyrophosphitodiplatinate(II)," J. Am. Chem. Soc **131**, 502–508 (2009).

[17]R. M. van der Veen, C. J. Milne, A. El Nahhas, F. A. Lima, V.-T. Pham, J. Best, J. A. Weinstein, C. N. Borca, R. Abela, C. Bressler, and M. Chergui, "Structural Determination of a Photochem-

ically Active Diplatinum Molecule by Time-Resolved EXAFS Spectroscopy," Angew. Chem. Int. Ed. **48**, 2711–2714 (2009).

[18]G. Levi, M. Pápai, N. E. Henriksen, A. O. Dohn, and K. B. Møller, "Solution Structure and Ultrafast Vibrational Relaxation of the PtPOP Complex Revealed by ΔSCF-QM/MM Direct Dynamics Simulations," J. Phys. Chem. C **122**, 7100–7119 (2018).

[19]Y. C. Lam, H. B. Gray, and J. R. Winkler, "Intersystem Crossing in Diplatinum Complexes," J. Phys. Chem. A **120**, 7671–7676 (2016).

[20]R. Monni, G. Auböck, D. Kinschel, K. M. Aziz-Lange, H. B. Gray, A. Vlček, and M. Chergui, "Conservation of vibrational coherence in ultrafast electronic relaxation: The case of diplatinum complexes in solution," Chem. Phys. Lett. **683**, 112–120 (2017).

[21]R. Monni, G. Capano, G. Auböck, H. B. Gray, A. Vlček, I. Tavernelli, and M. Chergui, "Vibrational coherence transfer in the ultrafast intersystem crossing of a diplatinum complex in solution," Proc. Natl. Acad. Sci. USA (2018).

[22]H. T. Lemke, C. Bressler, L. X. Chen, D. M. Fritz, K. J. Gaffney, A. Galler, W. Gawelda, K. Haldrup, R. W. Hartsock, H. Ihee, J. Kim, K. H. Kim, J. H. Lee, M. M. Nielsen, A. B. Stickrath, W. Zhang, D. Zhu, and M. Cammarata, "Femtosecond X-ray Absorption Spectroscopy at a Hard X-ray Free Electron Laser: Application to Spin Crossover Dynamics," J. Phys. Chem. A **117**, 735–740 (2013).

[23]T. B. van Driel, K. S. Kjær, E. Biasin, K. Haldrup, H. T. Lemke, and M. M. Nielsen, "Disentangling detector data in XFEL studies of temporally resolved solution state chemistry," Faraday Discuss. **177**, 443–465 (2015).

[24]P. Hart, S. Boutet, G. Carini, A. Dragone, B. Duda, D. Freytag, G. Haller, R. Herbst, S. Herrmann, C. Kenney, J. Morse, M. Nordby, J. Pines, N. van Bakel, M. Weaver, and G. Williams, "The Cornell-SLAC pixel array detector at LCLS," in *2012 IEEE Nuclear Science Symposium and Medical Imaging Conference Record (NSS/MIC)* (2012) pp. 538–541.

[25]M. Altarelli, R. P. Kurta, and I. A. Vartanyants, "X-ray cross-correlation analysis and local symmetries of disordered systems: General theory," Phys. Rev. B **82**, 104207 (2010); "Erratum: X-ray cross-correlation analysis and local symmetries of disordered systems: General theory [Phys. Rev. B 82, 104207 (2010)]," **86**, 179904(E) (2012).

[26]R. P. Kurta, M. Altarelli, and I. A. Vartanyants, "X-ray cross-correlation analysis of disordered ensembles of particles: potentials and limitations," Adv. Cond. Matter Phys. **2013** (2013).

[27]R. P. Kurta, M. Altarelli, E. Weckert, and I. A. Vartanyants, "X-ray cross-correlation analysis applied to disordered two-dimensional systems," Phys. Rev. B **85**, 184204 (2012).

[28]K. Haldrup, M. Christensen, and M. Meedom Nielsen, "Analysis of time-resolved X-ray scattering data from solution-state systems," Acta Crystallogr. A **66**, 261–269 (2010).

[29]K. S. Kjær, T. B. van Driel, J. Kehres, K. Haldrup, D. Khakhulin, K. Bechgaard, M. Cammarata, M. Wulff, T. J. Sørensen, and M. M. Nielsen, "Introducing a standard method for experimental determination of the solvent response in laser pump, X-ray probe time-resolved wide-angle X-ray scattering experiments on systems in solution," Phys. Chem. Chem. Phys. **15**, 15003–15016 (2013).

[30]R. M. van der Veen, A. Cannizzo, F. van Mourik, A. Vlček, and M. Chergui, "Vibrational Relaxation and Intersystem Crossing of Binuclear Metal Complexes in Solution," J. Am. Chem. Soc **133**, 305–315 (2011).

[31]E. H. van Kleef and I. Powis, "Anisotropy in the preparation of symmetric top excited states. I. One-photon electric dipole excitation," Mol. Phys. **96**, 757–774 (1999).

[32]A. O. Dohn, E. O. Jónsson, G. Levi, J. J. Mortensen, O. Lopez-Acevedo, K. S. Thygesen, K. W. Jacobsen, J. Ulstrup, N. E. Henriksen, K. B. Møller, and H. Jónsson, "Grid-based projector augmented wave (gpaw) implementation of quantum mechanics/molecular mechanics (qm/mm) electrostatic embedding and application to a solvated diplatinum complex," J. Chem. Theory Comput. **13**, 6010–6022 (2017).

[33]A. E. Stiegman, S. F. Rice, H. B. Gray, and V. M. Miskowski, "Electronic spectroscopy of d^8-d^8 diplatinum complexes. $^1A_{2u}$ ($d\sigma^* \rightarrow p\sigma$), ^3E_u ($d_{xz}, d_{yz} \rightarrow p\sigma$), and $^{3,1}B_{2u}$ ($d\sigma^* \rightarrow d_{x^2-y^2}$) excited states of tetrakis(diphosphonato)diplatinate(4-), $Pt_2(P_2O_5H_2)_4^{4-}$," Inorg. Chem. **26**, 1112–1116 (1987).

[34]J. S. Baskin and A. H. Zewail, "Oriented ensembles in ultrafast electron diffraction," Chem. Eur. J. of Chem. Phys. **7**, 1562–1574 (2006).

[35]S. Palese, L. Schilling, R. J. D. Miller, P. R. Staver, and W. T. Lotshaw, "Femtosecond optical Kerr effect studies of water," J. Phys. Chem. **98**, 6308–6316 (1994).

[36]R. Jimenez, G. R. Fleming, P. V. Kumar, and M. Maroncelli, "Femtosecond solvation dynamics of water," Nature **369**, 471 (1994).

[37]E. W. Castner, Y. J. Chang, Y. C. Chu, and G. E. Walrafen, "The intermolecular dynamics of liquid water," J. Chem. Phys. **102**, 653–659 (1995).

[38]F. Lehmkühler, F. Schulz, M. A. Schroer, L. Frenzel, H. Lange, and G. Grübel, "Heterogeneous local order in self-assembled nanoparticle films revealed by X-ray cross-correlations," IUCrJ **5**, 354–360 (2018).

[39]R. J. Sension, S. T. Repinec, A. Z. Szarka, and R. M. Hochstrasser, "Femtosecond laser studies of the cis-stilbene photoisomerization reactions," J. Chem. Phys. **98**, 6291–6315 (1993).

[40]F. Perrin, "Mouvement brownien d'un ellipsoide-I. Dispersion diélectrique pour des molécules ellipsoidales," J. phys. radium **5**, 497–511 (1934).

[41]P. J. W. Debye, *Polar Molecules* (Dover, New York, 1929).

[42]G. van der Zwan and J. T. Hynes, "Time-dependent fluorescence solvent shifts, dielectric friction, and nonequilibrium solvation in polar solvents," J. Phys. Chem. **89**, 4181–4188 (1985).

[43]C.-M. Hu and R. Zwanzig, "Rotational friction coefficients for spheroids with the slipping boundary condition," J. Chem. Phys. **60**, 4354–4357 (1974).

[44]M.-L. Horng, J. A. Gardecki, and M. Maroncelli, "Rotational Dynamics of Coumarin 153: Time-Dependent Friction, Dielectric Friction, and Other Nonhydrodynamic Effects," J. Phys. Chem. A **101**, 1030–1047 (1997).

[45]R. P. Kurta, J. J. Donatelli, C. H. Yoon, P. Berntsen, J. Bielecki, B. J. Daurer, H. DeMirci, P. Fromme, M. F. Hantke, F. R. Maia, A. Munke, C. Nettelblad, K. Pande, H. K. Reddy, J. A. Sellberg, R. G. Sierra, M. Svenda, G. van der Schot, I. A. Vartanyants, G. J. Williams, P. L. Xavier, A. Aquila, P. H. Zwart, and A. P. Mancuso, "Correlations in Scattered X-Ray Laser Pulses Reveal Nanoscale Structural Features of Viruses," Phys. Rev. Lett. **119**, 158102 (2017).

[46]T. Nee and R. Zwanzig, "Theory of Dielectric Relaxation in Polar Liquids," J. Chem. Phys. **52**, 6353–6363 (1970).

[47]D. Starodub, A. Aquila, S. Bajt, M. Barthelmess, A. Barty, C. Bostedt, J. D. Bozek, N. Coppola, R. B. Doak, S. W. Epp, B. Erk, L. Foucar, L. Gumprecht, C. Y. Hampton, A. Hartmann, R. Hartmann, P. Holl, S. Kassemeyer, N. Kimmel, H. Laksmono, M. Liang, N. D. Loh, L. Lomb, A. V. Martin, K. Nass, C. Reich, D. Rolles, B. Rudek, A. Rudenko, J. Schulz, R. L. Shoeman, R. G. Sierra, H. Soltau, J. Steinbrener, F. Stellato, S. Stern, G. Weidenspointner, M. Frank, J. Ullrich, L. Strüder, I. Schlichting, H. N. Chapman, J. C. H. Spence, and M. J. Bogan, "Single-particle structure determination by correlations of snapshot X-ray diffraction patterns," Nat. Commun. **3**, 1276 (2012).

[48]B. Pedrini, A. Menzel, M. Guizar-Sicairos, V. A. Guzenko, S. Gorelick, C. David, B. D. Patterson, and R. Abela, "Two-dimensional structure from random multiparticle X-ray scattering

images using cross-correlations," Nat. Commun. **4**, 1647 (2013).

[49]E. W. Small and I. Isenberg, "Hydrodynamic properties of a rigid molecule: Rotational and linear diffusion and fluorescence anisotropy," Biopolymers **16**, 1907–1928 (2018).

[50]J. T. Edward, "Molecular volumes and the Stokes-Einstein equation," J. Chem. Educ. **47**, 261 (1970).

Paper II

Ultrafast X-ray scattering measurements of coherent structural dynamics on the ground-state potential energy surface of a diplatinum molecule

Kristoffer Haldrup,[1] Gianluca Levi,[2,3] Elisa Biasin,[1,4] Peter Vester,[1] Mads Goldschmidt Laursen,[1] Frederik Beyer,[1] Kasper Skov Kjær,[1,5,4] Tim Brandt van Driel,[1,6] Tobias Harlang,[1,5] Asmus O. Dohn,[2,7] Robert J. Hartsock,[4] Silke Nelson,[6] James M. Glownia,[6] Henrik T. Lemke,[6,8] Morten Christensen,[1] Kelly J. Gaffney,[4] Niels E. Henriksen,[2] Klaus B. Møller,[2] and Martin M. Nielsen[1]

[1] *Technical University of Denmark, Department of Physics, Fysikvej 307, DK-2800 Kongens Lyngby, Denmark.*
[2] *Technical University of Denmark, Department of Chemistry, Kemitorvet 207, DK-2800 Kongens Lyngby, Denmark.*
[3] *Current address: Science Institute of the University of Iceland, VR-III, 107 Reykjavik, Iceland*
[4] *PULSE Institute, SLAC National Accelerator Laboratory, Menlo Park, California 94025, USA*
[5] *Department of Chemical Physics, Lund University, Box 118, S-22100 Lund, Sweden*
[6] *LCLS, SLAC National Accelerator Laboratory, Menlo Park, California 94025, USA*
[7] *Science Institute of the University of Iceland, VR-III, 107 Reykjavik, Iceland*
[8] *SwissFEL, Paul Scherrer Institut, 5232 Villigen PSI, Switzerland*

We report XFEL experiments addressing ground-state structural dynamics of the di-platinum anion Pt_2POP_4 following photoexcitation. The structural dynamics are tracked with <100 femtosecond time resolution by X-ray scattering, utilizing the anisotropic component to suppress contributions from the bulk solvent. The X-ray data exhibits a strong oscillatory component with period $T = 0.28$ picoseconds and lifetime 2.2 picoseconds, and structural analysis of the difference signal directly shows this as arising from ground-state dynamics along the PtPt coordinate. The results are compared with QM/MM BOMD simulations and demonstrate how off-resonance excitation can be used to prepare a vibrationally cold excited-state population complemented by a structure-dependent depletion of the ground-state population which subsequently evolves in time, allowing direct tracking of ground-state structural dynamics.

Optical lasers with femtosecond pulse lengths have enabled a host of studies of the excited-state kinetics and dynamics. With the arrival of X-ray and electron sources with pulse lengths in the sub-picosecond regime, the bond-length and -angle dynamics of the photoexcited molecules can now be directly measured [1–3]. However, the majority of chemical reactions take place between molecular species in their electronic ground states and the energy landscape of ground-state molecules is therefore of fundamental interest. The dynamics of ground-state molecules have mainly been investigated through time-resolved optical methods based on preparing non-equilibrium, coherent vibrational states through combined absorption and Raman processes involving an excited-state potential surface. This is today a mature field spanning several methodologies, e.g. Resonant Impulsive Stimulated Raman Scattering (RISRS) and Coherent Anti-Stokes Raman scattering (CARS) [4–8]. These spectroscopy methods provide a powerful approach to characterizing vibrational eigenfrequencies for harmonic modes, but do not directly access bond lengths and angles. Similar limitations apply to the so-called *Lochfrass* or '*R*-dependent ionization' spectroscopies, where the ground state is selectively depleted as a function of some key structural parameter [9–12].

The reliance on indirect, albeit powerful, spectroscopic methods to probe the potential energy landscape of ground-state molecules has been due to a lack of structurally-sensitive probes with the requisite time resolution. Here we show how hard X-ray Free Electron Laser (XFEL) sources [13] now make it possible to directly map the structural dynamics of an ensemble of molecules as it evolves on the ground-state potential surface. illustrating this approach we investigate how the ground-state population of the much-studied di-platinum anion Pt-POP $[Pt_2(P_2O_5H_2)_4]^{4-}$ (Figure 1) [14–23] evolves following Pt-Pt distance-dependent photo-depletion of the ground-state population.

Our structural analysis of the X-ray data is compared with Born-Oppenheimer Molecular Dynamics (BOMD) simulations using quantum mechanics/molecular mechanics (QM/MM) calculated forces [24–26]. Following Fleming and co-workers [27], the simulations are used to model the dynamics of a ground-state non-equilibrium density created by the pump pulse through propagation of a so-called hole in the classical ground-state equilibrium distribution mirroring at time zero the distribution promoted to the excited state. The ground-state dynamics predicted this way becomes increasingly accurate in the high temperature limit ($T >> \Theta$, where $\Theta = h\nu/k_B$ is the vibrational temperature) as more vibrational levels of the ground state are initially populated (for PtPOP the ground-state vibrational temperature is 170 K giving a vibrational excitation fraction [28] of ≈0.6 at 300 K).

The photophysics of PtPOP have been studied for four decades [22] and it is well established that excitation in

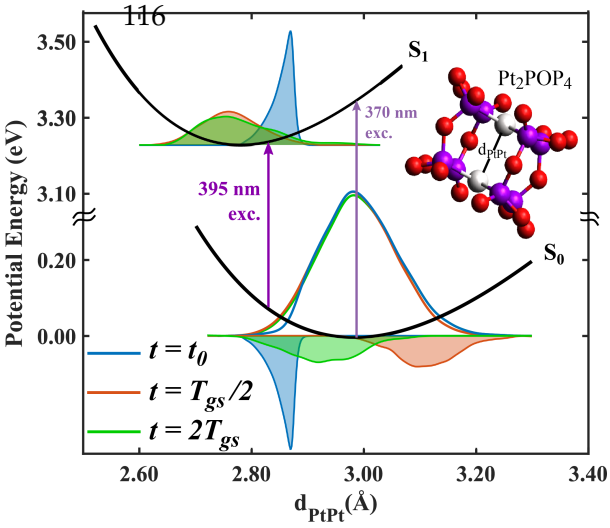

Figure 1. FIG. 1. Ground- and excited-state potential surfaces and QM/MM BOMD simulation of the structural dynamics following photoexcitation at 395 nm. The distribution of Pt-Pt distances is given by blue/red/green lines, representing the time steps $t = 0$, $t = T_{gs}/2$ and $t = 2T_{gs}$. An animation of the time evolution can be found in the SI.

the absorption band centered at 370 nm promotes an electron from the anti-bonding $5d\sigma^*$ HOMO orbital to the bonding $6p\sigma$ LUMO orbital [14]. Excitation to the $p\sigma$ orbital, located between the two Pt atoms, leads to a shortening of the Pt-Pt equilibrium distance from $d^{\rm gs}_{\rm PtPt}$ =2.9-3.0 Å to $d^{\rm es}_{\rm PtPt}$ =2.7-2.8 Å, with the bond shortening being closely similar in both the singlet (τ_{S_1} = 10-30 ps) and triplet (τ_{T_1} = 10 μs) excited states [15–18, 23]. Figure 1 shows the potential surfaces of the ground and S_1 excited state, the shape and positions of which determine the structural dynamics following photoexcitation. Excitation around $\lambda = 370$ nm leads to well-defined harmonic oscillations with period $T^{\rm es}$ close to 0.225 ps [19, 21, 23] as molecules near the bottom of the ground-state potential surface are promoted to S_1.

Low-temperature optical spectroscopy in the crystal phase [14] and Raman spectroscopy in solution [29, 30] determined the ground-state potential to be also highly harmonic but slightly softer than the singlet- and triplet-state potentials with a Pt-Pt oscillation with period $T^{\rm gs}$ = 0.285 ps. Whereas much effort has been devoted towards investigating the energy dissipation mechanisms and structural dynamics of the excited-state structure(s) of PtPOP [26, 31–33], no studies have directly addressed the ground-state dynamics. Here, we utilize off-resonance excitation at 395 nm to selectively excite solute molecules near the excited-state equilibrium geometry, see Figure 1.

To complement the experiments, the structural evolution following off-resonance excitation of PtPOP was also investigated via hybrid QM/MM BOMD simulations. Full descriptions of the methods are given in references [25] and [26]. Briefly, PtPOP was modelled using DFT with the BLYP functional [34, 35], and a representation of the Kohn-Sham (KS) orbitals in terms of tzp basis set for the Pt atoms and dzp for the rest of the atoms [36]. The TIP4P force field [37] was used for the surrounding solvent. The simulations were realized using the BOMD code and QM/MM interfacing scheme [25] implemented in ASE [38, 39] and GPAW [40, 41].

To model the off-resonance excitation process, the simulation procedure first established a large set of ground-state configurations. From these, a subset with sufficiently short Pt-Pt distances to allow excitation to the singlet excited state by a 395 nm (≈3.14 eV) photon was selected. Photoexcitation to the S_1 singlet state of PtPOP was modelled by starting 50 independent trajectories from this subset of ground-state configurations using the ΔSCF method [26, 42]. The procedure thus established two sets of trajectories, representing propagation of a depleted ground-state ensemble and of an excited-state ensemble. Figure 1 shows the $d_{\rm PtPt}$ distributions following the excitation event. We note that the semi-classical picture used to predict the dynamics taking place in the ground state after interaction with a short pump pulse implicitly incorporates effects that are commonly thought of as originating from a combination of absorption and impulsive stimulated Raman scattering [27].

Laser-pump/X-ray probe experiments were conducted at the LCLS facility. The XFEL delivered <50 fs 9.5 keV X-ray pulses at 120 Hz to the XPP experiment station [43], where the X-ray beam was focused to 30 × 30 μm^2. Laser excitation was by <50 fs 395(5) nm pulses, focused to a circular spot of <50 μm diameter and with a pulse energy of 3 μJ/pulse. The sample consisted of a 50 μm diameter free-flowing cylindrical jet of an 80 mM aqueous solution of PtPOP, with a flow speed sufficient to ensure full replenishment between pump/probe events. Scattered X-rays were detected by the 2D CSPAD [44] detector placed ≈5 cm behind the sample, allowing a Q-space coverage up to Q= 5 Å^{-1}, with $Q = \frac{4\pi}{\lambda}\sin(2\theta/2)$ where 2θ is the scattering angle and λ is the X-ray wavelength (1.31 Å). Following detector corrections, background subtraction and outlier rejection as previously described [45], 2D difference scattering images were constructed by subtracting laser-*off* images from laser-*on* images, where the laser had interacted with the sample at time t relative to the X-ray probe. Designating the scattering patterns with and without the excitation laser interacting with the sample as 'On' and 'Off' the difference signal is:

$$\Delta S(t) = S^{\rm On}(t) - S^{\rm Off} \quad (1)$$

For the experiments and analysis described here, the individual difference scattering images were rebinned and subsequently averaged in 10 fs time bins according to the upstream Timing Tool [46] with approximately 150 images in each bin.

The contribution to the scattering patterns from the solute molecules is designated as either *gs* or *es* corresponding to ground- and excited-state molecules, the 'Off' signal is the scattering from just the ground-state equilibrium distribution of structures whereas the 'On'-signal arises from two contributions:

$$\begin{aligned} S^{\mathrm{Off}} &= S^{\mathrm{gs,eq}}; \\ S^{\mathrm{On}}(t) &= \alpha S^{\mathrm{es}}(t) + (S^{\mathrm{gs,eq}} - \alpha S^{\mathrm{gs,hole}}(t)) \end{aligned} \tag{2}$$

where α denotes the fraction of photoexcited PtPOP molecules in the probed sample volume at the given time delay. The term in the parentheses describes the population of ground-state molecules, of which the fraction α has been promoted to the excited state. The difference scattering signal is thus given by:

$$\Delta S(t) = \alpha[S^{\mathrm{es}}(t) - S^{\mathrm{gs,hole}}(t)] \tag{3}$$

As such, the acquired difference scattering signal arises from both the excited-state population as well as from the 'hole' that the excitation pulse created in the ground state.

The 2D difference images as acquired are anisotropic, with the anisotropic contribution to the scattering arising from preferential excitation of molecules with the transition dipole moment aligned parallel with the polarization of the excitation laser pulse. When the subsequent structural changes have a specific orientation with respect to the transition dipole moment, then the resulting scattering patterns will necessarily be anisotropic. This is the case here, as the $d\sigma^* p\sigma$ absorption peak has a transition dipole moment aligned along the Pt-Pt axis along which the Pt nuclei contract following photoexcitation. The difference scattering signal from such a distribution of solute molecules is described by [47, 48, 50]

$$\Delta S(Q,t) = \Delta S_0(Q,t) + P_2(\cos(\theta_q))\Delta S_2(Q,t); \tag{4}$$

-where the geometry of the experiment is introduced through θ_q, the angle between the laser polarization axis and $\mathbf{Q}$ with P_2 being a second-order Legendre polynomium.

Assuming that the solute in each of the vibrational ensembles *es* and *gs*, *hole* can be represented by a single average structure, the isotropic ΔS_0 and anisotropic ΔS_2 parts of the solute contributions to the difference scattering signal are calculated from [49, 50]:

$$\begin{aligned} S_0(Q) &= \sum_{i,j}^{N} f_i(Q) f_j(Q) \frac{\sin(Qr_{ij})}{Qr_{ij}}; \\ S_2(Q) &= -c_2 \sum_{i,j}^{N} f_i(Q) f_j(Q) P_2(\cos(\xi_{ij})) j_2(r_{ij}); \end{aligned} \tag{5}$$

-where we have suppressed the time-dependence for clarity of presentation. In these expressions, r_{ij} is the length of the vector $\mathbf{r_{ij}}$ connecting atoms i and j and ξ_{ij} is the angle between $\mathbf{r_{ij}}$ and the transition dipole moment of the molecule. j_2 the second-order spherical Bessel function and f_i refers to the form factor of atom i in the molecule consisting of N atoms. The time evolution of the orientational distribution is described by the pre-factor $c_2(t)$[50].

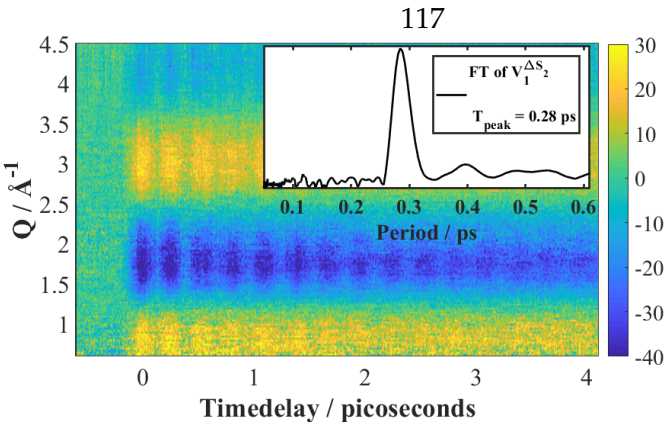

Figure 2. FIG. 2. $\Delta S_2(Q,t)$ with the color scale given in ‰-units of total signal. The inset shows the Fourier transform of the first right-singular vector of an SVD analysis, $|\mathcal{F}(V_1^{\Delta S_2})|$. A sharp peak at the T=0.28 ps ground-state period of PtPOP is observed.

For the structural analysis presented here, the isotropic $\Delta S_0(Q)$ and anisotropic $\Delta S_2(Q)$ contributions to the difference signal were separated [48, 50]. The analysis presented below is focused on $\Delta S_2(Q,t)$, as this part of the full difference signal arises only from structural changes with a well-defined relationship to the excitation laser polarization axis and as such contains no contribution from the (isotropic) heating of the bulk solvent. The analysis of $\Delta S_0(Q,t)$ is shown in the SI, with key results reported in Figures 3 and 4.

Figure 2 shows $\Delta S_2(Q,t)$, where following photoexcitation at $t = 0$ a positive feature appears at low Q, indicative of a decrease in the average Pt-Pt distance in the probed sample volume. In the following picoseconds, the difference signal oscillates in intensity with little change in signal shape. Applying a Singular Value Decomposition to $\Delta S_2(Q,t)$ (SI), the inset shows the fourier transform of the time dependence of the acquired signal as described by the first right-singular vector of the difference signal, $|\mathcal{F}(V_1^{\Delta S_2})|$. From this, we find that structural dynamics of the photoexcited sample gives rise to a difference scattering signal exhibiting a pronounced oscillatory behavior with a period T close to 0.285 ps. This value is in very good agreement with the ground-state frequency of the Pt-Pt oscillations and significantly different from the T = 0.210-0.225 ps period of the singlet and triplet excited states [14, 19, 21]. From time-domain fourier transforms of ΔS_0 and ΔS_2 (SI), we estimate that contributions from excited-state dynamics (T=0.21-0.23 ps) to the observed difference signals is at most around 10%.

118

We ascribe this to two main factors: (i) off-resonance excitation, and (ii) within-pulse motion of the Pt nuclei smearing out the dynamics in the excited state more significantly than in the ground state. As such, photoexcitation at 395 nm preferentially excites the sub-population of PtPOP molecules with short Pt-Pt distances, that is, near the potential energy minimum of the singlet excited state (Figure 1). The photoexcited molecules therefore exhibit little or no coherent vibrational dynamics. Simultaneously, the ground-state population as characterized by the distribution of Pt-Pt distances is now no longer in equilibrium, as molecules with short Pt-Pt bond lengths have been preferentially excited. As the ensemble of molecules evolves, the ground-state population of molecules characterized at $t = 0$ by long Pt-Pt distances ($d_{\mathrm{PtPt}} \sim 3.1$ Å) will after $T^{\mathrm{gs}}/2$ have moved to short Pt-Pt distances, thus filling the 'hole' at $d_{\mathrm{PtPt}} = 2.77$ Å, which consequently moves to long Pt-Pt distances. In the following picoseconds, the hole propagates on the ground-state potential surface, eventually broadening to reflect the equilibrium ground-state distribution of Pt-Pt distances.

The difference signal $\Delta S(Q,t)$ was analyzed by structural fitting, employing a model incorporating a Pt-Pt distance-dependent depletion of the ground-state population as described above.

Within this analysis framework [17, 52], the excitation fraction and key structural parameters (here d_{PtPt}) are known to be strongly correlated [53]. To enable the robust determination of bond-length dynamics, the excitation fraction was first estimated by analyzing the difference signal at t= 5 ps where both the excited- and ground-state populations have reached their equilibrium distributions. The model applied in this step utilizes DFT-derived structures for the ground and excited state of PtPOP while maintaining the excitation fraction α as a free parameter. Obtaining a photoexcitation fraction $\alpha = 0.018(2)$, the second step of the structural analysis relies on locking this parameter in the analysis of the full data set. The difference signal modeling further assumes the excited-state population to have d_{PtPt}=2.77 Å for all time delays, while the ground-state distribution is assumed to be given by a combination of the ground-state equilibrium structure minus a hole characterized by a time-dependent Pt-Pt distance $d^{hole}_{\mathrm{PtPt}}(t)$. The model with which the observed time-dependent difference scattering signal was fit is thus:

$$\Delta S_2(Q,t) = \alpha[S_2^{\mathrm{es}}(Q) - S_2^{gs,hole}(Q, d^{hole}_{\mathrm{PtPt}}(t))] \qquad (6)$$

-with all structural dynamics parameterized through the position of the ground-state hole, $d^{hole}_{\mathrm{PtPt}}(t)$ and with the scattering signals calculated through Eq. 5.

Figure 3 shows the fit at a representative time delay, $t = 0.25$ ps, and Figure 4A shows the best-fit value for d^{hole}_{PtPt} as a function of time delay t. d^{hole}_{PtPt} is observed to move towards larger values immediately after excitation and then oscillates around the ground-state equilibrium distance in agreement with the discussion above. The time dependence is well described by an (IRF-broadened) exponentially damped sine function convoluted with a step function centered at $t = 0$. Fitting this function to $d^{hole}_{\mathrm{PtPt}}(t)$ we find a period T^{hole}=0.283(1) ps and decay time $\tau^{hole} = 2.2(2)$ ps.

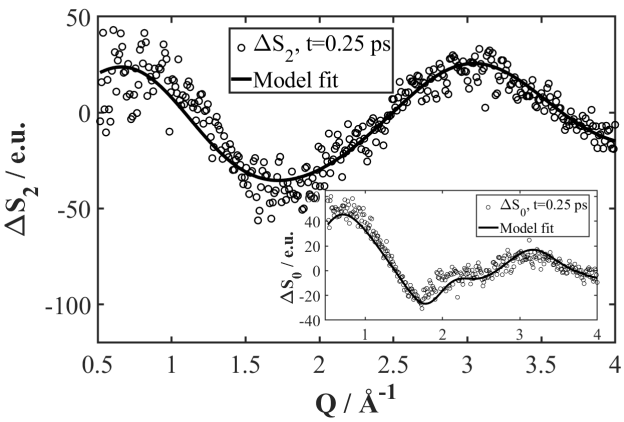

Figure 3. FIG. 3. ΔS_2 and model fit at $t = 0.25$ ps after photoexcitation. Inset shows the corresponding fit of ΔS_0 at the same time delay.

Figure 4B shows the corresponding results of our QM/MM BOMD simulations. From these, we obtain a period of $T^{\mathrm{gs}}_{\mathrm{sim}} = 0.271$ ps, which agrees to within 5% with the experimental data. The decay of the oscillations takes place in $\tau_{gs,sim}$=0.7 ps, which is three times faster than observed experimentally. We tentatively ascribe this difference as arising from the simulations overestimating the anharmonicity of the Pt-Pt potential. This is supported by the observation that the period of the simulated oscillations changes by around 20 fs from the first oscillation to the last, while no change can be discerned from the analysis of the experimental data.

The period and decay time of the observed oscillations derived from the ΔS_2 analysis, $T^{\mathrm{gs}}_{\mathrm{hole}} = 0.284(1)$ ps and $\tau = 2.2(2)$ ps, are in very good agreement with optical studies of PtPOP in ethylen glycole and in acetonitrile where $T^{\mathrm{gs}} = 0.281(3)$ ps and $\tau = 2.2(2)$ ps were found [19, 23]. The slightly faster decay time observed in the ΔS_0 analysis ($\tau = 1.7(3)$ ps) is likely spurious and arising from a small contribution from 2-photon excitation of PtPOP to $\Delta S_0(Q,t)$ as discussed in the SI.

The amplitude of the d^{hole}_{PtPt} oscillation is 0.06(1) Å, which is somewhat shorter than inferred from optical data [19] but in full agreement with the simulation result shown in Figure 4. The lower amplitude can thus be interpreted as due to the analysis tracking only the central position of the $d^{\mathrm{hole}}_{\mathrm{PtPt}}$ distribution which rapidly broadens (Figure 1).

The results presented demonstrate the preparation of a

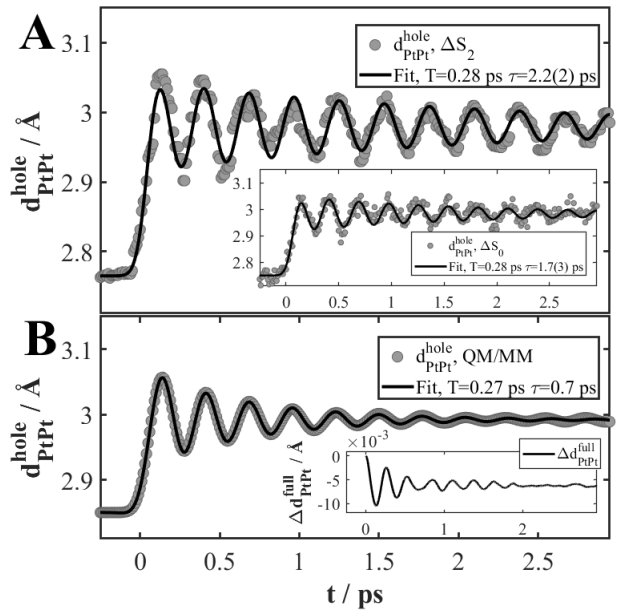

Figure 4. FIG. 4**A**: Time-dependent evolution of d^{hole}_{PtPt} (Gray circles). The dynamics have been fit (black line) with an IRF-broadened, exponentially damped sine function convoluted with a step function. Inset shows the ΔS_0 results. FIG. 4**B**: Time-dependent position of the hole (gray circles) from the simulations fitted with the same function (black line) as the experimental results. Inset shows the average Pt-Pt distance for the entire simulated ensemble.

vibrationally cold excited-state population and the evolution of a ground-state hole. Comparison with simulations allows direct and experimentally supported visualization of how the population distributions evolve on both the ground- and excited-state potential surfaces. Future experiments with better Q-space coverage will allow us to follow these dynamics in more detail, as recently discussed from a theoretical point of view [54] and experimentally realized for the $Fe(bpy)_3$ system using XAFS [55]. A key feature of the present experiment is the controlled preparation of a vibrationally cold excited state and we suggest that further studies utilizing vibrationally cold excited states may shed light on the temperature-dependent and highly elusive [22] mechanism of the singlet-triplet transition in PtPOP.

In summary, excitation with ultrashort optical laser pulses in combination with SASE-based X-ray laser sources can be used to prepare and track well-defined populations on the ground- and excited-state potential surfaces of molecules in solution. By choosing off-resonance excitation, the excited population can be prepared in a vibrationally cold state, allowing tracking of the ground-state dynamics alone.

[1] Thomas Elsaesser. Introduction: Ultrafast Processes in Chemistry. *CHEMICAL REVIEWS*, 117(16, SI):10621–10622, AUG 23 2017.

[2] Majed Chergui and Eric Collet. Photoinduced Structural Dynamics of Molecular Systems Mapped by Time-Resolved X-ray Methods. *CHEMICAL REVIEWS*, 117(16, SI):11025–11065, AUG 23 2017.

[3] Eric Collet and Marco Cammarata. Disentangling ultrafast electronic and structural dynamics with x-ray lasers. *Chemistry A European Journal*, 0(0), 2018.

[4] U. Banin, A. Bartana, S. Ruhman, and R. Kosloff. Impulsive excitation of coherent vibrational motion ground state surface dynamics induced by intense short pulses. *Journal of Chemical Physics*, 101(10):8461–8481, NOV 15 1994.

[5] E. Gershgoren, J. Vala, R. Kosloff, and S. Ruhman. Impulsive control of ground surface dynamics of I-3(-) in solution. *Journal of Physical Chemistry A*, 105(21):5081–5095, MAY 31 2001.

[6] A.M. Zheltikov. Coherent anti-Stokes Raman scattering: from proof-of-the-principle experiments to femtosecond CARS and higher order wave-mixing generalizations. *Journal of Raman Spectroscopy*, 31(8-9):653–667, AUG-SEP 2000.

[7] Robert W. Hartsock, Wenkai Zhang, Michael G. Hill, Bridgett Sabat, and Kelly J. Gaffney. Characterizing the Deformational Isomers of Bimetallic $Ir_2(dimen)_4{}^{2+}$ (dimen=1,8-diisocyano-p-menthane) with Vibrational Wavepacket Dynamics. *Journal of Physical Chemistry A*, 115(14):2920–2926, APR 14 2011.

[8] Renee R. Frontiera and Richard A. Mathies. Femtosecond stimulated Raman spectroscopy. *Laser & Photonics Reviews*, 5(1):102–113, JAN 2011.

[9] Th. Ergler, B. Feuerstein, A. Rudenko, K. Zrost, C. D. Schroeter, R. Moshammer, and J. Ullrich. Quantum-phase resolved mapping of ground-state vibrational D-2 wave packets via selective depletion in intense laser pulses. *Physical Review Letters*, 97(10), SEP 8 2006.

[10] Erich Goll, Gunter Wunner, and Alejandro Saenz. Formation of ground-state vibrational wave packets in intense ultrashort laser pulses. *Physical Review Letters*, 97(10), SEP 8 2006.

[11] L. Fang and G. N. Gibson. Strong-field induced vibrational coherence in the ground electronic state of hot I(2). *Physical Review Letters*, 100(10), MAR 14 2008.

[12] Johann Foerster, Etienne Plesiat, Alvaro Magana, and Alejandro Saenz. Imaging of the umbrella motion and tunneling in ammonia molecules by strong-field ionization. *Physical Review A*, 94(4), OCT 5 2016.

[13] Christoph Bostedt, Sebastien Boutet, David M. Fritz, Zhirong Huang, Hae Ja Lee, Henrik T. Lemke, Aymeric Robert, William F. Schlotter, Joshua J. Turner, and Garth J. Williams. Linac Coherent Light Source: The first five years. *Reviews of Modern Physics*, 88(1), MAR 9 2016.

[14] S.F. Rice and H.B. Gray. Electronic absorption and emission spectra of binuclear platinum(II) complexes - characterization of the lowest singlet and triplet excited states of $Pt_2(H_2P_2O_5)_4{}^{4-}$. *Journal of the American Chemical Society*, 105(14):4571–4575, 1983.

[15] C.D. Kim, S. Pillet, G. Wu, W.K. Fullagar, and P. Cop-

120
pens. Excited-state structure by time-resolved X-ray diffraction. *Acta Crystallographica Section A*, 58(2):133–137, MAR 2002.

[16] N. Yasuda, M. Kanazawa, H. Uekusa, and Y. Ohashi. Excited-state structure of a platinum complex by X-ray analysis. *Chemistry Letters*, pages 1132–1133, NOV 5 2002.

[17] Morten Christensen, Kristoffer Haldrup, Klaus Bechgaard, Robert Feidenhans'l, Qingyu Kong, Marco Cammarata, Manuela Lo Russo, Michael Wulff, Niels Harrit, and Martin Meedom Nielsen. Time-Resolved X-ray Scattering of an Electronically Excited State in Solution. Structure of the (3)A(2u) State of Tetrakis-mu-pyrophosphitodiplatinate(II). *Journal of the American Chemical Society*, 131(2):502–508, JAN 21 2009.

[18] Renske M. van der Veen, Chris J. Milne, Amal El Nahhas, Frederico A. Lima, Van-Thai Pham, Jonathan Best, Julia A. Weinstein, Camelia N. Borca, Rafael Abela, Christian Bressler, and Majed Chergui. Structural Determination of a Photochemically Active Diplatinum Molecule by Time-Resolved EXAFS Spectroscopy. *Angewandte Chemie - International Edition*, 48(15):2711–2714, 2009.

[19] Renske M. van der Veen, Andrea Cannizzo, Frank van Mourik, Antonin Vlcek, Jr., and Majed Chergui. Vibrational Relaxation and Intersystem Crossing of Binuclear Metal Complexes in Solution. *Journal of the American Chemical Society*, 133(2):305–315, JAN 19 2011.

[20] Marc-Oliver Winghart, Ji-Ping Yang, Matthias Vonderach, Andreas-Neil Unterreiner, Dao-Ling Huang, Lai-Sheng Wang, Sebastian Kruppa, Christoph Riehn, and Manfred M. Kappes. Time-resolved photoelectron spectroscopy of a dinuclear Pt(II) complex: Tunneling autodetachment from both singlet and triplet excited states of a molecular dianion. *Journal of Chemical Physics*, 144(5), FEB 7 2016.

[21] Roberto Monni, Gerald Aubck, Dominik Kinschel, Kathrin M. Aziz-Lange, Harry B. Gray, Antonn Vlek, and Majed Chergui. Conservation of vibrational coherence in ultrafast electronic relaxation: The case of diplatinum complexes in solution. *Chemical Physics Letters*, pages –, 2017.

[22] Harry B. Gray, Stanislav Zalis, and Antonin Vlcek. Electronic structures and photophysics of d(8)-d(8) complexes. *Coordination Chemistry Reviews*, 345:297–317, AUG 15 2017.

[23] Roberto Monni, Gloria Capano, Gerald Auböck, Harry B. Gray, Antonín Vlček, Ivano Tavernelli, and Majed Chergui. Vibrational coherence transfer in the ultrafast intersystem crossing of a diplatinum complex in solution. *Proceedings of the National Academy of Sciences*, 2018.

[24] Asmus Ougaard Dohn, Elvar Örn Jonsson, Kasper Skov Kjær, Tim Brandt van Driel, Martin Meedom Nielsen, Karsten Wedel Jacobsen, Niels Engholm Henriksen, and Klaus Braagaard Møller. Direct Dynamics Studies of a Binuclear Metal Complex in Solution: The Interplay Between Vibrational Relaxation, Coherence, and Solvent Effects. *Journal of Physical Chemistry Letters*, 5(14):2414–2418, JUL 17 2014.

[25] A. O. Dohn, Elvar Örn Jonsson, G. Levi, J. J. Mortensen, O. Lopez-Acevedo, K. S. Thygesen, K. W. Jacobsen, J. Ulstrup, N. E. Henriksen, K. B. Møller, and H. Jonsson. Grid-based projector augmented wave (gpaw) implementation of quantum mechanics/molecular mechanics (qm/mm) electrostatic embedding and application to a solvated diplatinum complex. *Journal of Chemical Theory and Computation*, 13(12):6010–6022, 2017. PMID: 29083921.

[26] Gianluca Levi, Matyas Papai, Niels E. Henriksen, Asmus O. Dohn, and Klaus B. Møller. Solution Structure and Ultrafast Vibrational Relaxation of the PtPOP Complex Revealed by Delta SCF-QM/MM Direct Dynamics Simulations. *Journal of Physical Chemistry C*, 122(13):7100–7119, APR 5 2018.

[27] DM Jonas, SE Bradforth, SA Passino, and GR Fleming. Femtosecond wavepacket spectroscopy - influence of temperature, wavelength and pulse duration. *Journal of Physical Chemistry*, 99(9):2594–2608, MAR 2 1995.

[28] Donald A. McQuarrie. *Statistical Mechanics*. Harper & Row, 1975.

[29] C.M. Che, F.H. Herbstein, W.P. Schaeffer, R.E. Marsh, and H.B. Gray. Binuclear platinum diphosphite complexes - crystal-structures of $K_4[Pt_2(POP)_4Br]$-$3H_2O$, a new linear-chain semiconductor, and $K_4[Pt_2(POP)_4Cl_2]$-$2H_2O$. *Journal of the American Chemical Society*, 105(14):4604–4607, 1983.

[30] K.H. Leung, D.L. Phillips, C.M. Che, and V.M. Miskowski. Resonance Raman intensity analysis investigation of metal-metal bonded transitions: an examination of the $_1A^{2u}$ ¡- $_1A^{1g}$ (5d σ^* -¿ 6p σ) transition of $Pt_2(H_2P_2O_5)_4$ $^{4-}$. *Journal of Raman Spectroscopy*, 30(11):987–993, NOV 1999.

[31] Alec C. Durrell, Gretchen E. Keller, Yan-Choi Lam, Jan Sykora, Antonin Vlcek, Jr., and Harry B. Gray. Structural Control of (1)A(2u)-to-(3)A(2u) Intersystem Crossing in Diplatinum(II,II) Complexes. *Journal of the American Chemical Society*, 134(34):14201–14207, AUG 29 2012.

[32] Stanislav Zalis, Yan-Choi Lam, Harry B. Gray, and Antonin Vlcek. Spin-Orbit TDDFT Electronic Structure of Diplatinum(II,II) Complexes. *Inorganic Chemistry*, 54(7):3491–3500, APR 6 2015.

[33] Yan Choi Lam, Harry B. Gray, and Jay R. Winkler. Intersystem Crossing in Diplatinum Complexes. *Journal of Physical Chemistry A*, 120(39):7671–7676, OCT 6 2016.

[34] A. D. Becke. Density-functional exchange-energy approximation with correct asymptotic behavior. *Physical Review A*, 38:3098, 1988.

[35] C. Lee, W. Yang, and R. G. Parr. Development of the colle-salvetti correlation-energy formula into a functional of the electron density. *Physical Review B*, 37:785–789, 1988.

[36] A. H. Larsen, M. Vanin, J. J. Mortensen, K. S. Thygesen, and K. W. Jacobsen. Localized atomic basis set in the projector augmented wave method. *Phys. Rev. B*, 80:195112, 2009.

[37] W. L. Jorgensen. Quantum and statistical mechanical studies of liquids. 10. transferable intermolecular potential functions for water, alcohols, and ethers. application to liquid water. *Journal of the American Chemical Society*, 103:335–340, 1981.

[38] S. R. Bahn and K. W. Jacobsen. An object-oriented scripting interface to a legacy electronic structure code. *Computing in Science & Engineering*, 4:55, 2002.

[39] Ask Hjorth Larsen, Jens Jørgen Mortensen, Jakob Blomqvist, Ivano E Castelli, Rune Christensen, Marcin Dułak, Jesper Friis, Michael N Groves, Bjørk Ham-

mer, Cory Hargus, Eric D Hermes, Paul C Jennings, Peter Bjerre Jensen, James Kermode, John R Kitchin, Esben Leonhard Kolsbjerg, Joseph Kubal, Kristen Kaasbjerg, Steen Lysgaard, Jón Bergmann Maronsson, Tristan Maxson, Thomas Olsen, Lars Pastewka, Andrew Peterson, Carsten Rostgaard, Jakob Schiøtz, Ole Schütt, Mikkel Strange, Kristian S Thygesen, Tejs Vegge, Lasse Vilhelmsen, Michael Walter, Zhenhua Zeng, and Karsten W Jacobsen. The atomic simulation environmenta python library for working with atoms. *Journal of Physics: Condensed Matter*, 29(27):273002, 2017.

[40] J.J. Mortensen, L.B. Hansen, and K. W. Jacobsen. Real-space grid implementation of the projector augmented wave method. *Physical Review B*, 71:035109, 2005.

[41] J. Enkovaara, C. Rostgaard, J. J. Mortensen, J. Chen, M. Dulak, L. Ferrighi, J. Gavnholt, C. Glinsvad, V. Haikola, H. A. Hansen, H. H. Kristoffersen, M. Kuisma, A. H. Larsen, L. Lehtovaara, M. Ljungberg, O. Lopez-Acevedo, P. G. Moses, J. Ojanen, T. Olsen, V. Petzold, N. A. Romero, J. Stausholm-Møller, M. Strange, G. A. Tritsaris, M. Vanin, M. Walter, B. Hammer, H. H.äkkinen, G. K. H. Madsen, R. M. Nieminen, J. K. Nørskov, M. Puska, T. T. Rantala, J. Schiøtz, K. S. Thygesen, and K. W. Jacobsen. Electronic structure calculations with gpaw: a real-space implementation of the projector augmented-wave method. *Journal of Physics: Condensed matter*, 22:253202, 2010.

[42] Jeppe Gavnholt, Thomas Olsen, Mads Engelund, and Jakob Schiotz. Delta self-consistent field method to obtain potential energy surfaces of excited molecules on surfaces. *Physical Review B*, 78(7), AUG 2008.

[43] Matthieu Chollet, Roberto Alonso-Mori, Marco Cammarata, Daniel Damiani, Jim Defever, James T. Delor, Yiping Feng, James M. Glownia, J. Brian Langton, Silke Nelson, Kelley Ramsey, Aymeric Robert, Marcin Sikorski, Sanghoon Song, Daniel Stefanescu, Venkat Srinivasan, Diling Zhu, Henrik T. Lemke, and David M. Fritz. The X-ray Pump-Probe instrument at the Linac Coherent Light Source. *Journal of Synchrotron Radiation*, 22(3, SI):503–507, MAY 2015.

[44] Hugh T. Philipp, Marianne Hromalik, Mark Tate, Lucas Koerner, and Sol M. Gruner. Pixel array detector for X-ray free electron laser experiments. *Nuclear Instruments & Methods in Physics Research Section A - Accelerators, Spectrometers, Detectors and associated equipment*, 649(1):67–69, SEP 1 2011. 16th Pan-American Conference on Synchrotron Radiation Instrumentation (SRI2010), Chicago, IL, SEP 21-24, 2010.

[45] Tim Brandt van Driel, Kasper Skov Kjaer, Elisa Biasin, Kristoffer Haldrup, Henrik Till Lemke, and Martin Meedom Nielsen. Disentangling detector data in XFEL studies of temporally resolved solution state chemistry. *Faraday Discussions*, 177:443–465, 2015.

[46] M. Harmand, R. Coffee, M. R. Bionta, M. Chollet, D. French, D. Zhu, D. M. Fritz, H. T. Lemke, N. Medvedev, B. Ziaja, S. Toleikis, and M. Cammarata. Achieving few-femtosecond time-sorting at hard X-ray free-electron lasers. *Nature Photonics*, 7(3):215–218, MAR 2013.

[47] J. Spencer Baskin and Ahmed H. Zewail. Oriented ensembles in ultrafast electron diffraction. *ChemPhysChem*, 7(7):1562–1574, JUL 17 2006.

[48] U. Lorenz, K. B. Møller, and N. E. Henriksen. On the interpretation of time-resolved anisotropic diffraction patterns. *New Journal of Physics*, 12, NOV 10 2010.

[49] Asmus O. Dohn, Elisa Biasin, Kristoffer Haldrup, Martin M. Nielsen, Niels E. Henriksen, and Klaus B. Møller. On the calculation of x-ray scattering signals from pairwise radial distribution functions (vol 48, 244010, 2015). *Journal of Physics B - Atomic, Molecular and Optical Physics*, 49(5), MAR 14 2016.

[50] Elisa Biasin, Tim B. van Driel, Gianluca Levi, Mads G. Laursen, Asmus O. Dohn, Asbjorn Moltke, Peter Vester, Frederik B. K. Hansen, Kasper S. Kjaer, Tobias Harlang, Robert Hartsock, Morten Christensen, Kelly J. Gaffney, Niels E. Henriksen, Klaus B. Møller, Kristoffer Haldrup, and Martin M. Nielsen. Anisotropy enhanced X-ray scattering from solvated transition metal complexes. *Journal of Synchrotron Radiation*, 25(2):306–315, MAR 2018.

[51] Elisa Biasin, Tim Brandt van Driel, Kasper S. Kjaer, Asmus O. Dohn, Morten Christensen, Tobias Harlang, Pavel Chabera, Yizhu Liu, Jens Uhlig, Matyas Papai, Zoltan Nemeth, Robert Hartsock, Winnie Liang, Jianxin Zhang, Roberto Alonso-Mori, Matthieu Chollet, James M. Glownia, Silke Nelson, Dimosthenis Sokaras, Tadesse A. Assefa, Alexander Britz, Andreas Galler, Wojciech Gawelda, Christian Bressler, Kelly J. Gaffney, Henrik T. Lemke, Klaus B. Møller, Martin M. Nielsen, Villy Sundstrom, Gyorgy Vanko, Kenneth Warnmark, Sophie E. Canton, and Kristoffer Haldrup. Femtosecond X-Ray Scattering Study of Ultrafast Photoinduced Structural Dynamics in Solvated $[Co(terpy)_2]^{2+}$. *Physical Review Letters*, 117(1), JUN 30 2016.

[52] Kristoffer Haldrup, Tobias Harlang, Morten Christensen, Asmus Dohn, Tim Brandt van Driel, Kasper Skov Kjaer, Niels Harrit, Johan Vibenholt, Laurent Guerin, Michael Wulff, and Martin Meedom Nielsen. Bond Shortening (1.4 angstrom) in the Singlet and Triplet Excited States of $[Ir_2(dimen)_4]^{2+}$ in Solution Determined by Time-Resolved X-ray Scattering. *Inorganic Chemistry*, 50(19):9329–9336, OCT 3 2011.

[53] Kristoffer Haldrup, Morten Christensen, and Martin Meedom Nielsen. Analysis of time-resolved X-ray scattering data from solution-state systems. *Acta Crystallographica Section A*, 66(2):261–269, MAR 2010.

[54] Adam Kirrander and Peter M. Weber. Fundamental Limits on Spatial Resolution in Ultrafast X-ray Diffraction. *Applied Sciences*, 7(6), JUN 2017.

[55] Henrik T. Lemke, Kasper S. Kjaer, Robert Hartsock, Tim B. van Driel, Matthieu Chollet, James M. Glownia, Sanghoon Song, Diling Zhu, Elisabetta Pace, Samir F. Matar, Martin M. Nielsen, Maurizio Benfatto, Kelly J. Gaffney, Eric Collet, and Marco Cammarata. Coherent structural trapping through wave packet dispersion during photoinduced spin state switching. *Nature Communications*, 8, MAY 24 2017.

Supplementary Material

...

Ultrafast X-ray scattering measurements of coherent structural dynamics on the ground-state potential energy surface of a diplatinum molecule

Kristoffer Haldrup,[1] Gianluca Levi,[2,3] Elisa Biasin,[1,4] Peter Vester,[1] Mads Laursen,[1] Frederik Beyer,[1] Kasper Skov Kjær,[1,5,4] Tim Brandt van Driel,[1,6] Tobias Harlang,[1,5] Asmus O. Dohn,[2,3] Robert G. Hartsock,[4] Silke Nelson,[6] James M. Glownia,[6] Henrik T. Lemke,[6,7] Morten Christensen,[1] Kelly J. Gaffney,[4] Niels E. Henriksen,[2] Klaus B. Møller,[2] and Martin M. Nielsen[1]

[1] *Technical University of Denmark, Department of Physics, Fysikvej 307, DK-2800 Kongens Lyngby, Denmark.*

[2] *Technical University of Denmark, Department of Chemistry, Kemitorvet 207, DK-2800 Kongens Lyngby, Denmark.*

[3] *Science Institute of the University of Iceland, VR-III, 107 Reykjavik, Iceland*

[4] *PULSE Institute, SLAC National Accelerator Laboratory, Menlo Park, California 94025, USA*

[5] *Department of Chemical Physics, Lund University, Box 118, S-22100 Lund, Sweden*

[6] *LCLS, SLAC National Accelerator Laboratory, Menlo Park, California 94025, USA*

[7] *SwissFEL, Paul Scherrer Institut, 5232 Villigen PSI, Switzerland*

I. SAMPLE SYNTHESIS AND PREPARATION

Following the procedure presented by C.-M. Che *et al.*, [1] a deoxygenated aqueous solution of K_2PtCl_4 and phosphorous acid was heated in a boiling water bath for several hours before being slowly heated to dryness at 110 °C in nitrogen/argon atmosphere resulting in a yellow powder with a greenish tint. The compound was washed with methanol and acetone and recrystallized in order to remove excess phosphorous acid. If the sample is exposed to air, the colour changes from almost yellow to a more olive green, and darkens further as the degradation proceeds. The dry, slightly sticky, bright yellow-green powder was stored in carefully sealed containers purged with argon. Purity of the compound was confirmed by absorption and emission spectroscopy.

A. Preparation of solutions

Since atmospheric oxygen causes degradation of PtPOP handling of the sample was to the widest possible extent done in a protective Ar- or N_2-environment. The water used for making solutions (milli-Q, 5.5 μS/m) was purged with argon through a Drechsel bubbler for at least two hours prior to dissolution of the PtPOP salt. Flushing of the solution with water-saturated inert gas was maintained after preparation. During the XFEL experiments, which were carried out under a helium atmosphere, the sample container was continuously bubbled with solvent-saturated helium.

II. DATA REDUCTION

A. Detector corrections and S_0/S_2 separation

The data reduction procedures necessary to go from as-acquired 2D detector images from the CS-PAD detector to ΔS_0 and ΔS_2 are described in detail in reference [2]. Very briefly, the key steps are:

- Correct for solid angle coverage, detector efficiency and polarization of X-ray beam
- Normalize to total scattered intensity and calculate 2-dimensional difference signals from nearest $On - Off$-pairs of 2D scattering patterns

- Rebin the set of 2D difference images according to the Timing Tool information
- Rebin the 2D difference signals according to azimuthal angle ϕ
- Perform ΔS_0 and ΔS_2 decomposition by plotting $\Delta S(P_2)$, where P_2 is a second-order Legendre polynomium as a function $\theta_q(\phi)$, the angle between the laser polarization and the Q-vector as described in the main text.

B. $S(Q)$ scaling

To allow quantitative interpretation of the fit results described below, an initial scaling of the azimuthally integrated signal $S(Q)$ was carried out as described in detail in [3]. Briefly, this approach relies on scaling the acquired and corrected signals (in detector units) to that simulated for a "'liquid Unit Cell"', corresponding to the smallest stoichiometrically representative unit of the sample. In the present case of an 80 mM solution of PtPOP, this Liquid Unit Cell consists of 1 PtPOP molecule, 4 K^+ ions and 694 water molecules and both elastic (Thompson) and inelastic (Compton) scattering was included. Figure 4 shows the result of this procedure which yields a single number with which all the normalized signals can be multiplied to be put on an absolute scale of electron units per liquid unit cell.

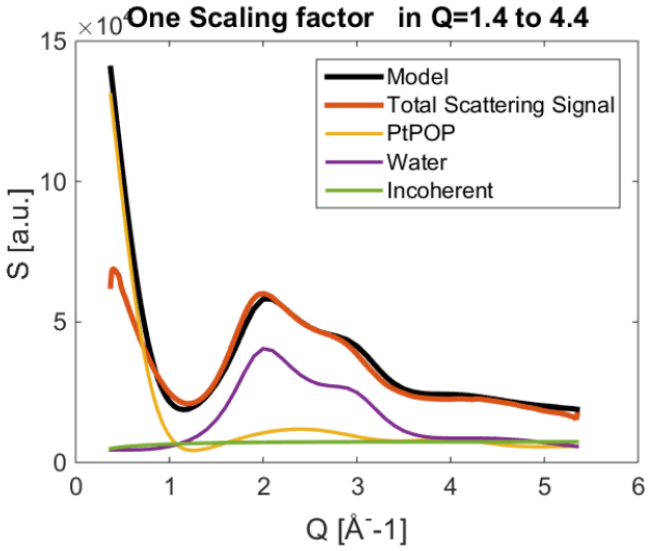

Figure 1. Components of the full scattering signal (black) and a scaled scattering pattern $S(Q)$ (red).

III. MODEL-INDEPENDENT ANALYSIS OF $\Delta S_0(Q,t)$ AND $\Delta S_2(Q,t)$

Figure 4 shows the $\Delta S_0(Q,t)$ and $\Delta S_2(Q,t)$ after the data reduction described above.

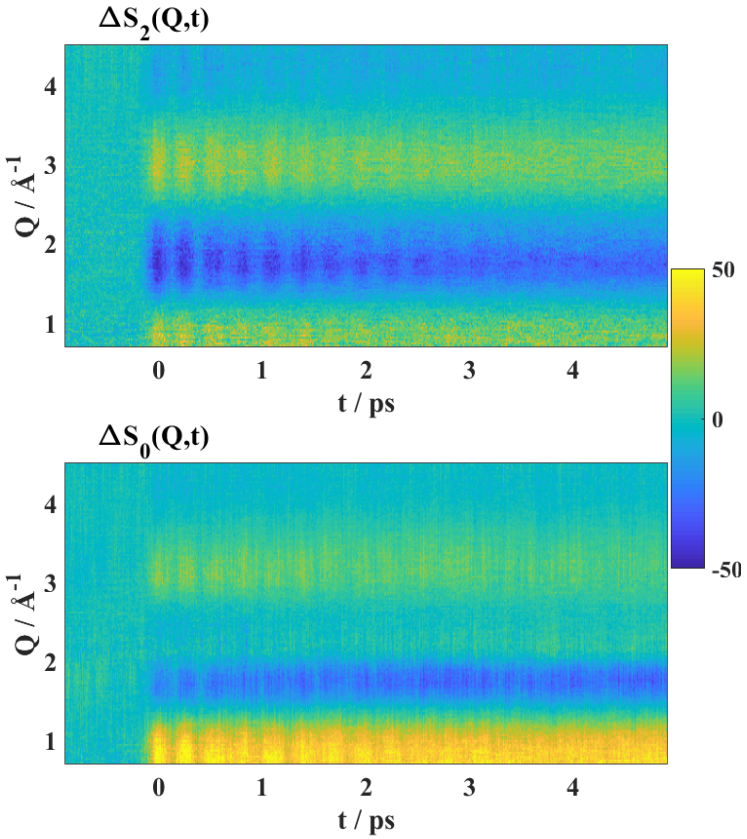

Figure 2. ΔS_2 (top) and ΔS_0 (bottom) data sets.

A. Time-domain Fourier transforms of $\Delta S_0(Q,t)$ and $\Delta S_2(Q,t)$

As a starting point for understanding the information contained in the data sets, Figure 3 shows absolute squared value of time-domain Fourier Transforms of the low-Q ($Q < 1.08\mathring{A}^{-1}$, a region where difference signal strength is approximately linear in Δd_{PtPt}) part of difference signals in the $t = -1 - 3$ ps region, after applying a Hann window to eliminate truncation artifacts.

Based on an estimate of the areas of the peaks arising from either ground-state or excited-state dynamics (within T= 0.21-0.23 ps and T = 0.25-0.32 ps, respectively) we estimate the

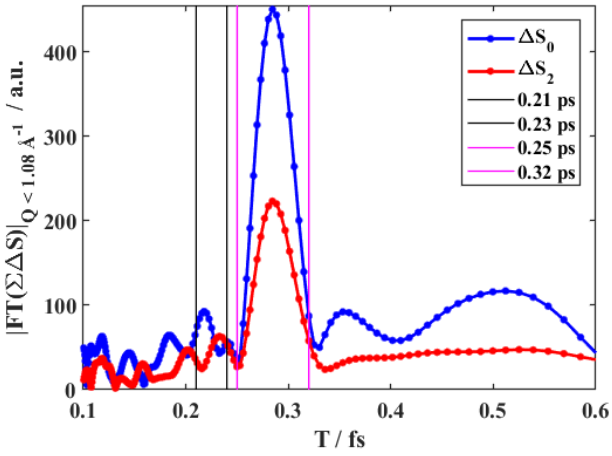

Figure 3. Power spectra of the low-Q part of the acquired difference signals. Vertical lines delineate the regions arising from either excited state (black) or ground-state dynamics (magenta), here chosen as 0.21-0.23 ps and 0.25-0.32 ps, respectively.

observed dynamics as being dominated ($\sim$ 90 %) by ground-state dynamics.

B. Singular Value Decomposition of $\Delta S_0(Q,t)$ and $\Delta S_2(Q,t)$

As a preliminary investigation initial to the structural analysis of $\Delta S(Q,t)$, a Singular Value Decomposition (SVD) of the data sets was carried out. Within the SVD framework, the matrix **A** is decomposed as

$$\mathbf{A} = \mathbf{SUV^T} \tag{1}$$

If the matrix **A** represents a time-varying signal with time along the row dimension and scattering vector Q along the column dimension, then the left-singular vectors **S** will contain the 'typical' shapes of the signal (often termed topograms) and the right-singular vectors **V** (often termed chronograms) will hold the information on the time evolution of the left-singular vectors. The diagonal elements of the matrix **U** are the Singular Values, expressing the relative magnitude of each of the left-singular vectors.

Figure 2 shows the corresponding Singular Value Decompostions of the the two data sets.

By comparison with Figure 4 in the main article and with Figure 5 below, the first topogram of each SVD can be identified as arising primarily from the solute response to

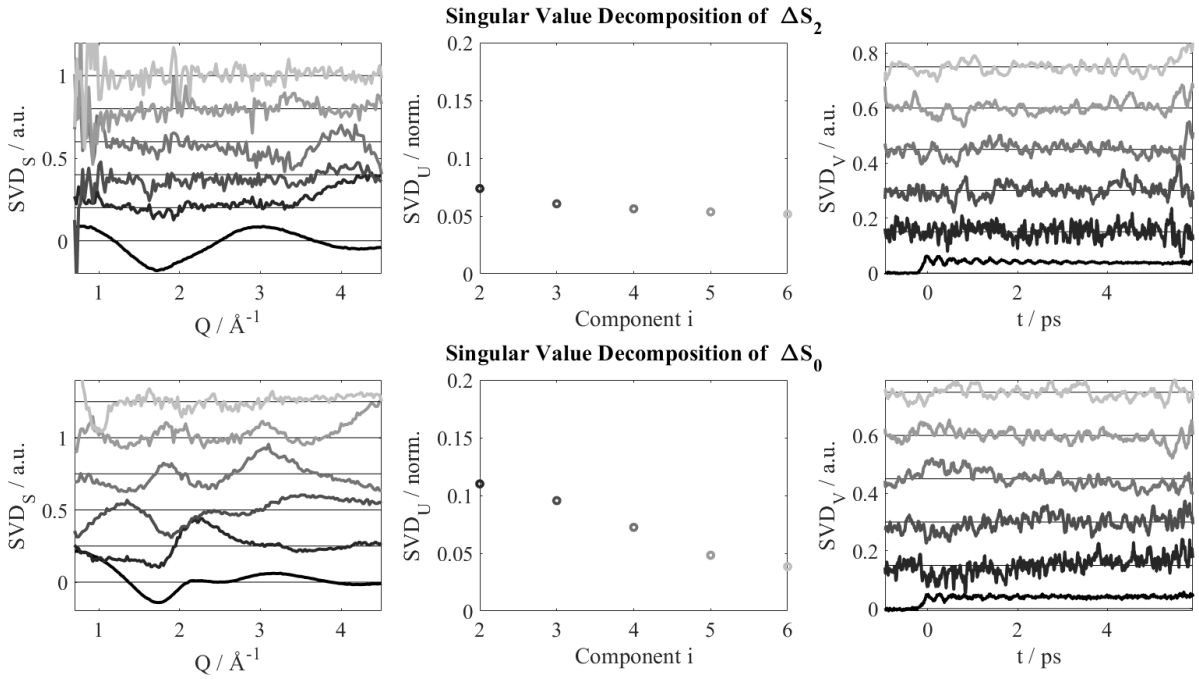

Figure 4. Graphical representation of the first 6 components of the Singular Value Decomposition of the two data sets. From left to right the first six components of **S**, **U** and **V** are shown. Color scale from black to light gray indicates components 1 – 6. For **U**, the singular values have been normalized to 1 by dividing all values with $\mathbf{U}_{1,1}$, and only 2-6 are shown.

photoexcitation. For ΔS_2, the remaining components are all less than 10% of the magnitude of the first component (Figure 2, middle panels) and in general have signal shapes inconsistent with difference signals arising from sample dynamics. In contrast, the first 5 topograms of ΔS_0 as well as their corresponding Singular Values and chronograms exhibit signal shapes and a characteristic grow-in around $t = 0$ consistent with difference signals arising from photoinduced dynamics. This is in agreement with ΔS_2 arising primarily from single-photon excited PtPOP with no contribution from the bulk solvent, with ΔS_0 arising from a combination of one- and two photon excited PtPOP (see below) as well as from solvent dynamics.

Focusing now on only the first left-singular vectors of the two data sets, these are shown in Figure 3.

As discussed in the main article, the pronounced oscillatory behavior observed is interpreted as arising from structural dynamics along the Pt-Pt coordinate due to distance-

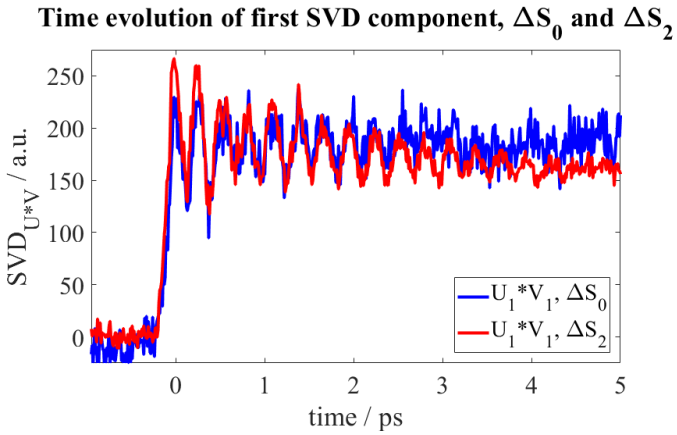

Figure 5. First right-singular vector (chronogram) of ΔS_0 and ΔS_2 Singular Value Decompostions

dependent excitation of PtPOP. Figure 4 shows the power spectra (shown as a function of period T) obtained through fourier transforms of these two signals, utilizing a Hann window centered at $t = 2$ ps.

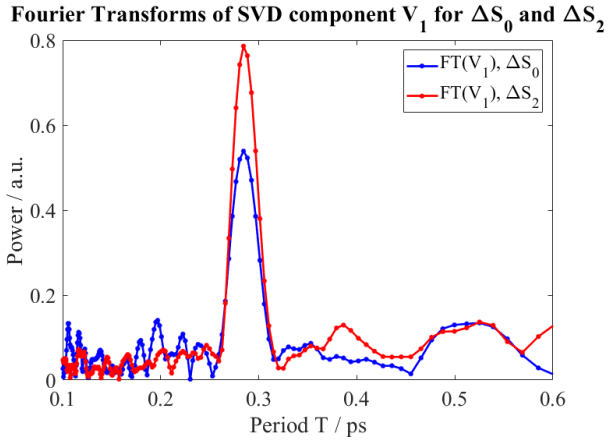

Figure 6. Fourier transforms of V1 for both data sets. A Hann window centered at t = 2 ps has been applied to V.

The two power spectra are highly similar, with both showing a very distinct peak at a period of $T = 0.285$ ps.

IV. STRUCTURAL ANALYSIS OF $\Delta S_0(Q,t)$

As described in the main text, the analysis of $\Delta S_2(Q,t)$ relies on only a single component, namely the difference signal arising from structural changes in the solute system only. In contrast, and as also suggested by the SVD analysis introduced above, a full description of $\Delta S_0(Q,t)$ includes more components as indicated in Equation 2:

$$\Delta S_{model}(t) = \alpha_{\Delta S_0}\Delta S_{Solute}(d_{\mathrm{PtPt}}(t)) + \beta(t)\Delta S_{cage} + \Delta T(t)\Delta S_{\Delta T} \tag{2}$$

Here, as in the analysis of ΔS_2, $\Delta S_{Solute}(d_{PtPt})$ describes the difference signal arising from changes in the PtPt coordinate in the ensemble of solute molecules. As for the ΔS_2 analysis, the excitation fraction α was determined at $t = 5$ ps and $\alpha_{\Delta S_0} = 0.026(2)$ was found, somewhat more than $\alpha_{\Delta S_2} = 0.018(2)$, as discussed in more detail below. The term $\beta(t)\Delta S_{cage}$ arises from changes in scattering due to (primarily) changes in the solvent immediately around the PtPOP solute, as described in detail in [4], and was simulated using solute-solvent radial pair distribution functions calculated in the QM/MM BOMD framework described in the main text and in further detail below. The final contribution to the difference scattering signal within this modeling framework is $\Delta T(t)\Delta S_{\Delta T}$, which describes the changes in scattering due to a temperature increase of the bulk solvent of the sample, $\Delta S_{\Delta T} = \frac{\partial S}{\partial T}|_\rho$. This contribution to the difference signal can be determined from reference measurements [5] or from MD simulations and the ΔT pre-factor represents the average temperature increase in the probed volume following thermalization as discussed in detail in the Supplementary Information of reference [6].

The insert of Figure 3 in the main text shows the quality of fit acquired using this model, and Figure 7 shows both the fit and the individual fit contributions at two different time delays.

As observed for the ΔS_2 analysis, the agreement between fit and model is quite good, and the main difference between the fit result at t= 0.25 ps and $t = 4$ ps is the magnitude of the contribution from solvent heating. This is discussed further in the next section.

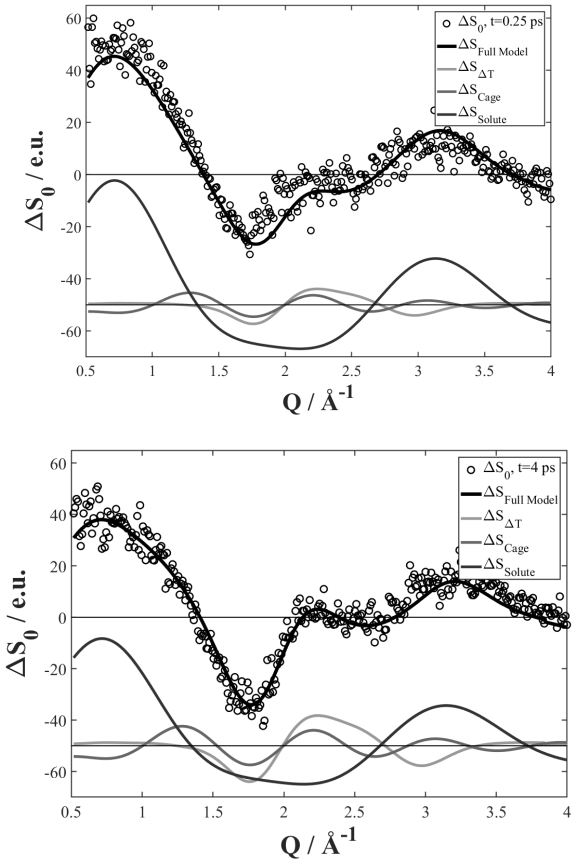

Figure 7. ΔS_0 data and fit after 0.25 ps and 4 ps.

A. Time evolution of $d_{PtPt}(t)$, ΔT and β_{cage}

Figure 8 shows the time evolution of each of the three fit components included in the model described by Equation 2. As discussed in the main text, the position of the hole in the ground-state population shows pronounced oscillations after $t = 0$. By fitting the same exponentially damped sinusoidal function as applied for the ΔS_2 analysis the period is found to be 0.28 ps, with a time constant for the damping of 1.7 ps in reasonable agreement with the ΔS_2 result, although somewhat faster. We tentatively attribute the faster decay to be due to excited state dynamics following 2-photon excitation [7] as discussed further below.

Figure 9 (left panel) shows the residuals after fitting d_{PtPt} as determined from the ΔS_2 (red lines) and ΔS_0 (blue lines) analysis.

The power spectrum of the fourier transform of the residual of the ΔS_0 and ΔS_2 fits are shown in the right-hand panel of Figure 9. The power spectrum for ΔS_0 exhibits a

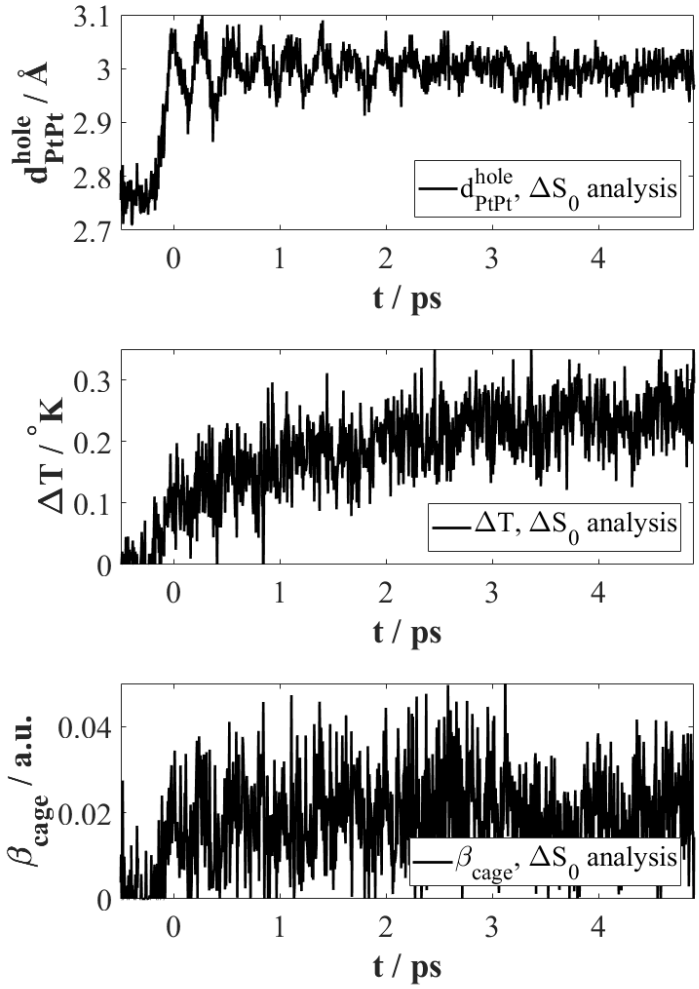

Figure 8. Time evolution of the fit components

weak peak at $T = 0.213$ ps (157 cm^{-1}) corresponding to the triplet state vibrational period, but no peak corresponding to the singlet state period (∼0.225 ps, 147 cm^{-1}) is evident. This indicates that some (small) population of the triplet state takes place sufficiently fast to launch wave packets, in agreement with recent results based on optical spectroscopy following UV excitation [7, 8] where coherent dynamics on the triplet potential surface was observed following 260 nm excitation. In the present case this excitation to high-lying states is via two-photon excitation. A similar fourier analysis of the ΔS_2-fit residual, shown in red, shows a weak peak at $T = 0.225$ ps but no peak around 0.213 ps, consistent with direct population of the singlet state only, with subsequent small-amplitude dynamics on

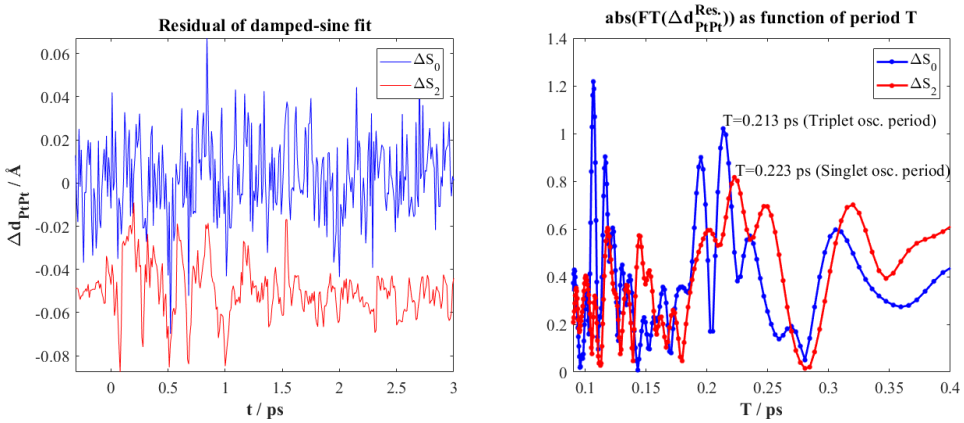

Figure 9. Residuals (left) and power spectra of the fourier transforms of the residuals (right)

that potential surface.

The third panel of Figure 8 shows the time evolution of the magnitude of the so-called cage component of the fit model. From previous optical [9] and QM/MM BOMD investigations [10] this effect is expected to be quite small, in agreement with the fit results in Figure 7 and the noisy appearance of the time dependence seen in Figure 8. Nevertheless, as the solvent has been implicated in the relaxation dynamics from high-lying states as well as in the intersystem crossing processes, this contribution to the signal could be an interesting target for further experimental investigations.

The second panel of Figure 8 shows the time evolution of energy deposition to the bulk solvent. An immediate increase of ΔT close to 0.15 K with a grow-in time of τ = 0.5-1 ps is observed, followed by a further grow-in of 0.1 K on a time scale of a few picoseconds. This indicates impulse heating followed by a slower transfer of energy from the solute to the solvent as discussed further in the section on solvent heating below. The uncertainty on this parameter is well represented by the bin-to-bin fluctuations, ± 0.05 K.

The bulk solvent heating affords an opportunity to directly investigate the energy flow in the molecular system with picosecond resolution [11]. Turning first to the prompt increase in temperature observed in Figure 8 the immediate increase of 0.05 K is likely an artifact of the fit as the structural changes due to changes in temperature take ∼ to be established. However, the ∼0.1 K increase on the 0.1-1 ps time scale is in good agreement with previous observations in experiments with ultrafast energy release to the surrounding solvent [6]. On slightly longer time scales a further temperature increase is observed, likely related

to energy release associated with the non-radiative transition of PtPOP from the initially excited singlet to the triplet state. More quantitatively and introducing the heat capacity of water as C_{H_2O}, the observed ~ 0.1 K increase within the first picosecond corresponds to an energy release per water molecule of

$$\Delta E_{H_2O} = \frac{C_{H_2O}\Delta T}{N_{H_2O}} = 0.1K * \frac{4187 \frac{J}{L \cdot K}}{3.34 \cdot 10^{25} \frac{H_2O}{L}} = 1.25 \cdot 10^{-23} \quad J = 0.08 \quad meV/H_2O \qquad (3)$$

At a concentration of 80 mM, there are 695 water molecules per solute, and with a photo-excitation fraction of 0.026(2) determined from the t=5 ps analysis of ΔS_0 [2], this leads to a calculated prompt energy release per excited-state solute of 3.0 eV. Given the 3.1 eV photon energy of the 395 nm excitation, this is quite significantly more than expected.

This observation, however, points to a resolution of the seeming discrepancy between the 0.018(2) excitation fraction concluded from the ΔS_2 analysis and the 0.026(2) excitation fraction from the ΔS_0 analysis by suggesting that a relatively large fraction of the photoexcited PtPOP molecules have undergone two-photon excitation followed by fast relaxation to the lowest-lying triplet state [8]. Transitions in the (quite unstructured) < 250 nm absoprtion bands of PtPOP in general do not have transition dipole moments parallel to the Pt-Pt axis as for the $d\sigma^* p\sigma$ band centered at 370 nm [12, 13], and therefore the difference signal arising from PtPOP molecules excited via this channel is not expected to have an anisotropic component. Based on these considerations, one would therefore expect a population fraction of ~ 0.01 to have undergone 2-photon excitation with a subsequent fast release of $E_{2\gamma} - E_{triplet}$ = 2*3.1 eV - 2.4 eV = 3.6 eV per excited solute molecule. The temperature increase due to energy release from the 2-photon excited population can be calculated as

$$\Delta T = \frac{N_{H_2O}\Delta E_{H_2O}}{C_{H_2O}} = \frac{3.34 \cdot 10^{25} \frac{H_2O}{L} \times (3.6 \text{ eV} * 0.01 * 1/695 \text{ PtPOP}/H_2O * 1.602 \cdot 10^{-19} \text{ J/eV})}{4187 \frac{J}{L \cdot K}} = 0.07 \text{ K} \qquad (4)$$

-in reasonable agreement with the observed temperature increase on the ~ 1 ps time scale.

V. STRUCTURAL ANALYSIS WITH NO CONSTRAINTS ON d^{ES}_{PtPt}

As a check that the $d^{ES}_{PtPt} = 2.77$ Å constraint applied in the analysis presented in main text does not impose a certain structural interpretation, Figure 10 shows the corresponding analysis carried out without constrains on d^{ES}_{PtPt}:

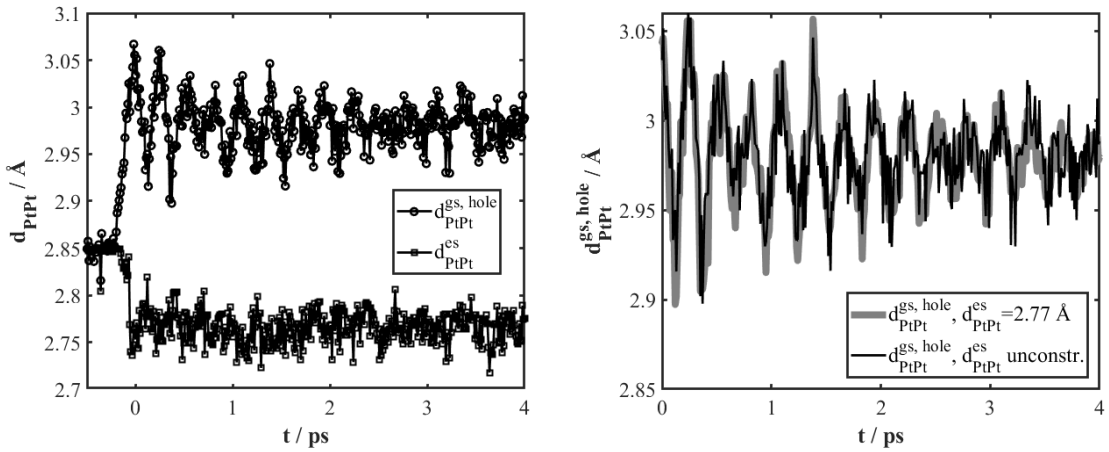

Figure 10. d^{ES}_{PtPt} and d^{hole}_{PtPt} as a function of time with no constraints on d^{ES}_{PtPt}.

As evident from Figure 10, right panel, the main difference compared to the results shown in the main text is an increase in the noise and it is interesting to note how the analysis immediately converges on $d^{ES}_{\mathrm{PtPt}} = 2.77$ Å with essentially all dynamics contained in d^{hole}_{PtPt}.

VI. LINEARITY OF RESPONSE

To identify a regime with good difference signal from single-photon excited solute and with little or no contamination from two-photon processes, several series of so-called power titration scans were carried out. In these, the difference signal was acquired at $t = 2$ ps while varying the laser fluence. The set of difference signals was subsequently analyzed and the ratio between the components of the difference signal arising from solute and solvent was calculated as a function of laser fluence. This allows an identification of when two-photon processes begin to influence the signal under the given experimental conditions, as this ratio will change when contributions from two-photon processes become appreciable as more

energy is then transferred to the solvent per photoexcited solute. The estimated threshold using this method was 5-10 μJ/pulse, with the measurements reported here carried out at 3 μJ/pulse and still showing some contributions from two-photon processes as discussed above. Direct excitation of the aqueous solvent was observed around 40 μJ/pulse.

VII. SIMULATION DETAILS

The QM/MM Born-Oppenheimer Molecular Dynamics (BOMD) simulations were realized using the implementation of electrostatic embedding QM/MM [14] in the Atomic Simulation Environment (ASE) [15, 16] and the Grid-based Projector Augmented Wave (GPAW) DFT code [17, 18]. In the simulations, the QM part comprised the PtPOP complex alone and employed a representation of the Kohn-Sham orbitals in a basis of linear combination of atomic orbitals (LCAO) [19]. Within the GPAW QM cell, the complex was described with the BLYP functional [20, 21], while the basis functions were tzp [19] for Pt and dzp [19] for the rest of the atoms. We employed a grid spacing of the GPAW cell of 0.18 Å. This choice of LCAO basis set and grid spacing ensured converged structural parameters, as demonstrated in references [10, 22]. The MM part included water molecules at a density of 1 g/cm^3 modelled through the TIP4P force field [23].

Photoexcitation to the lowest-lying singlet excited state by the optical pump pulse and the subsequent dynamics were described in a picture [24] of instantaneous promotion of ground-state molecules from a 300 K equilibrium distribution of Pt-Pt distances and evolution of the resulting nonequilibrium ground- and excited-state ensembles. The thermally equilibrated QM/MM BOMD data for the ground state were collected in a previous work [14], where the simulations are extensively described. Here, we sum up the main aspects of the QM/MM BOMD simulation setup. We used a cubic QM/MM simulation box with a side length of 35 Å. The box included 1383 classical TIP4P [23] water molecules and four K^+ counter ions to neutralize the total charge. Throughout the dynamics, the positions of the counter ions were restrained as described in [14]. Non-bonded dispersion and exchange repulsion interactions between the solute and the solvent were modelled through the standard Lennard-Jones (LJ) potential, using for the atoms of the complex LJ parameters from the universal force field (UFF) [25]. Thermalization at 300 K was realized by employing the Langevin thermostat implemented in ASE, which was applied only to the solvent. Stability of the simulations

while using a time step of 2 fs for the BOMD propagation was ensured by constraining all OH bonds and hydrogen bonds in the complex with the ASE implementation of RATTLE [26]. In total, the ground-state thermal equilibrium distribution included around 230000 QM/MM BOMD snapshots accounting for ∼460 ps of simulation time.

The initial conditions for the nonequilibrium dynamics following laser excitation were drawn from the underlying ground-state thermal distribution of Pt-Pt distances $P^{\mathrm{gs,eq}}(d_{\mathrm{PtPt}})$ using a spatial filtering (SF) approximation [10, 24, 27–30] of the pump-pulse transition. The ultrashort pump pulse was assumed to have a Gaussian frequency profile $\epsilon(t) \propto \mathrm{e}^{-\frac{t^2}{2\tau^2}}\mathrm{e}^{-i\omega_1 t}$, where ω_1 and τ are respectively the center frequency and temporal width of the pulse. Under this assumption, the standard equation of the SF approximation giving the initial (unnormalized) excited-state distribution is:

$$P^{\mathrm{es}}(d_{\mathrm{PtPt}}, t_0) = F^2(d_{\mathrm{PtPt}})P^{\mathrm{gs,eq}}(d_{\mathrm{PtPt}}) \tag{5}$$

in which the excitation window $F(d_{\mathrm{PtPt}})$ takes the following form:

$$F(d_{\mathrm{PtPt}}) = A\exp\left[-\frac{\tau^2\left(\Delta V(d_{\mathrm{PtPt}}) - \hbar\omega_1\right)^2}{2\hbar^2}\right] \tag{6}$$

where $\Delta V(d_{\mathrm{PtPt}})$ is the potential energy difference between the ground and excited states. Following Fleming [24], we approximate the change in the ground-state distribution induced by the laser, the ground-state hole distribution at time zero $P^{\mathrm{gs,hole}}(d_{\mathrm{PtPt}}, t_0)$, with $P^{\mathrm{es}}(d_{\mathrm{PtPt}}, t_0)$, i.e. we assume that the hole burned in ground-state by the pulse has the same form of the non-stationary distribution created in the excited state. To achieve the experimental excitation fraction α, the parameter A in the expression of the excitation window, Eq. 6, is increased until the desired value of α is obtained. However, this procedure can lead to complete depopulation of the ground-state equilibrium ensemble at specific Pt-Pt distances. Since the experiment employed a linearly polarized excitation pulse, the orientation dependence of the absorption probability [31] limits the number of molecules that can be excited. Thus, in order to avoid the unphysical situation of depopulating entirely the ground-state equilibrium distribution at a particular Pt-Pt distance, $P^{\mathrm{es}}(d_{\mathrm{PtPt}}, t_0)$ given by Eq. 5, and hence $P^{\mathrm{gs,hole}}(d_{\mathrm{PtPt}}, t_0)$ were replaced by:

$$P_0^{\mathrm{es}}(d_{\mathrm{PtPt}}, t_0) = P_0^{\mathrm{gs,hole}}(d_{\mathrm{PtPt}}, t_0) = \begin{cases} \frac{1}{B}P^{\mathrm{es}}(d_{\mathrm{PtPt}}, t_0) & \text{if } P^{\mathrm{es}}(d_{\mathrm{PtPt}}, t_0) > \frac{1}{B}P^{\mathrm{gs,eq}}(d_{\mathrm{PtPt}}) \\ P^{\mathrm{es}}(d_{\mathrm{PtPt}}, t_0) & \text{if } P^{\mathrm{es}}(d_{\mathrm{PtPt}}, t_0) \leq \frac{1}{B}P^{\mathrm{gs,eq}}(d_{\mathrm{PtPt}}) \end{cases} \tag{7}$$

with $B > 1$. The normalization factor of $P_0^{\mathrm{es}}(d_{\mathrm{PtPt}}, t_0)$, given by $\int P_0^{\mathrm{es}}(d_{\mathrm{PtPt}}, t_0)\mathrm{d}(d_{\mathrm{PtPt}})$, represents the simulated excitation fraction. $\Delta V(r)$ was taken as the difference between two harmonic potentials with force constants calculated from the reduced mass of Pt_2 and the vibrational frequencies obtained by van der Veen et al. using femtosecond transient absorption measurements in water solution [32], which in wavenumbers are 119 and 149 cm^{-1} for the ground and excited states, respectively. For the position of the minima of the potentials, the Pt-Pt distances of the ground- and excited-state gas-phase optimized geometries (3.00 and 2.80 Å [10], respectively) were used; finally, the two potentials were shifted relative to each other such that the energy difference at the Pt-Pt distance of the optimized ground-state geometry was equal to 3.35 eV (corresponding to a wavelength of ∼370 nm), i.e. the transition energy at the maximum of the $S_0 \rightarrow S_1$ band of the experimental absorption spectrum in aqueous solution. The parameters for the excitation field were obtained from a Gaussian fit to the spectral intensity profile of the pump pulse that was used in the experiment. Under the assumption that the pulse is Fourier-transform limited, the fit delivered a τ of 20 fs and an $\hbar\omega_1$ of 3.14 eV (∼370 nm). The parameters A and B defining the form of $P_0^{\mathrm{es}}(d_{\mathrm{PtPt}}, t_0)$ were chosen such to give the estimated experimental excitation fraction and most closely match the initial position of the ground-state hole as obtained from the fit of the experimental data. The distributions used to sample initial conditions for the dynamics in the ground and excited states are shown in Figure 11.

The dynamics in the excited state following laser excitation was modelled by propagating 50 excited-state QM/MM BOMD trajectories starting from ground-state configurations reflecting the distribution $P_0^{\mathrm{es}}(d_{\mathrm{PtPt}}, t_0)$. These trajectories were collected with a time step of 2 fs, and keeping the thermostat applied to the solvent molecules. The singlet excited-state was described with a recent implementation of the ΔSCF method in GPAW [10, 22] in conjunction with the spin unpolarized formalism [33, 34]. To ensure stable convergence of the electronic density at each step in the dynamics the ΔSCF constrains on the occupation numbers of the Kohn-Sham orbitals were smeared with Gaussian functions with a width of 0.01 eV, as explained in details in references [10, 22]. In total, around 200 ps of excited-state QM/MM BOMD trajectories were collected.

The dynamics taking place in the ground state was described by the evolution of the hole left in the ground-state distribution of Pt-Pt distances. The present model of ground-state dynamics has been shown to give accurate results in the high temperature limit ($T >> \Theta$,

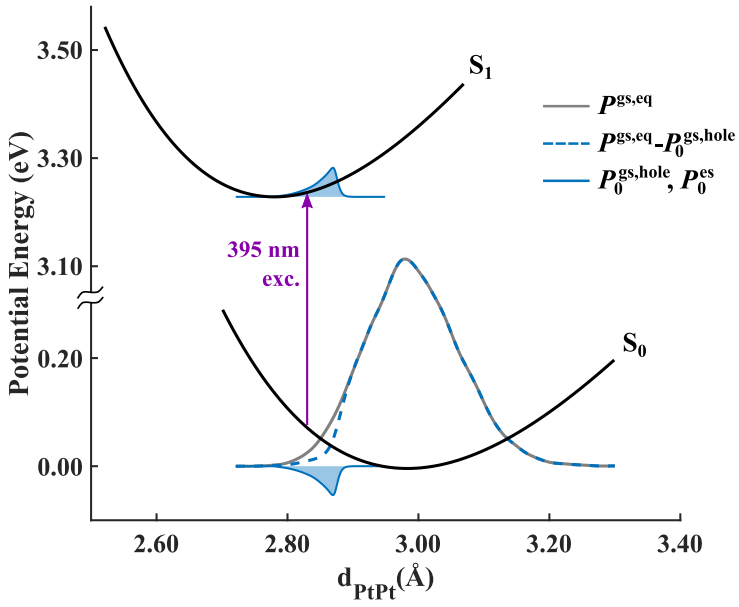

Figure 11. The photoexcitation event simulated within the classical SF approximation using the ground-state equilibrium distribution of Pt-Pt distances obtained from around 460 ps of QM/MM BOMD at 300 K [14]. A definition of the distributions used to set up initial conditions for the nonequilibrium dynamics following laser excitation is provided in the text. The black curves are Morse-potential fits to the potential of mean force (PMF) calculated using the pairwise Pt-Pt radial distribution functions (RDF) obtained from the equilibrated QM/MM BOMD data for ground and excited states, respectively. All distributions were smoothed with a cubic smoothing spline.

where $\Theta = h\nu/k_b$ is the vibrational temperature), as more vibrational levels of the ground state are initially populated [24]. For PtPOP, this classical picture is applicable since the Pt-Pt ground-state vibrational period of 285 fs provides a vibrational temperature of ∼170 K and, therefore [35], at room temperature the fraction of molecules in excited vibrational states is $\exp(-\Theta/T)$∼0.6. Further considerations regarding the SF approximation and the adequacy of the picture of ground-state hole dynamics for PtPOP can be found in [22].

VIII. SIMULATED ENSEMBLE DYNAMICS

Figure 12 shows the time evolution of the out-of-equilibrium excited-state (blue density plot) and ground-state hole (red) distributions of Pt-Pt distances, together with their instantaneous averages (black curves), as obtained from the QM/MM BOMD simulations.

Both ground- and excited-state distributions describe coherent oscillations on the respective potentials(for the hole, the coherent oscillations are a result of the remaining ground-state molecules vibrating in phase following laser excitation). As is evident from the comparison

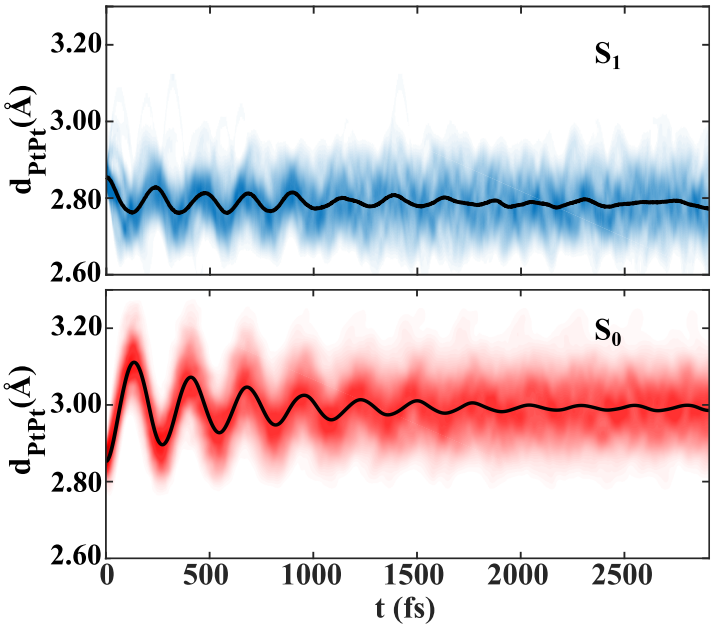

Figure 12. Density plots of the time-dependent Pt-Pt distance distributions from the nonequilibrium ΔSCF-QM/MM trajectories in S_1 (Top) and S_0 nonequilibrium hole distributions (Bottom)obtained following photoexcitation of PtPOP in water by an ultrashort pulse selectively depleting the ground-state ensemble at short d_{PtPt}. The distributions were smoothed with a cubic smoothing spline. The superimposed black curves represent the instantaneous averages of Pt-Pt distances.

in Figure 12, the amplitude of the ground-state hole oscillations are by far larger than the amplitude of the coherent vibrations described by the excited-state ensemble of molecules.

This is shown more clearly in Figure 13 where the variation $\Delta d^{\mathrm{full}}_{\mathrm{PtPt}}(t)$ of the average Pt-Pt distance of the full simulated ensemble of PtPOP molecules (Left)and its Fourier transform (FT)(Right) are plotted. $\Delta d^{\mathrm{full}}_{\mathrm{PtPt}}(t)$ was computed from:

$$\begin{aligned}\Delta d^{\mathrm{full}}_{\mathrm{PtPt}}(t) =& < d_{\mathrm{PtPt}}(t) > - < d_{\mathrm{PtPt}}(t_0) > \\ &= \int d_{\mathrm{PtPt}} \left[P_0^{\mathrm{es}}(d_{\mathrm{PtPt}}, t) + P^{\mathrm{gs,eq}}(d_{\mathrm{PtPt}}) - P_0^{\mathrm{gs,hole}}(d_{\mathrm{PtPt}}, t) \right] \mathrm{d}(d_{\mathrm{PtPt}}) \\ &\quad - \int d_{\mathrm{PtPt}} P^{\mathrm{gs,eq}}_{\mathrm{GS}} \mathrm{d}(d_{\mathrm{PtPt}}) \end{aligned} \tag{8}$$

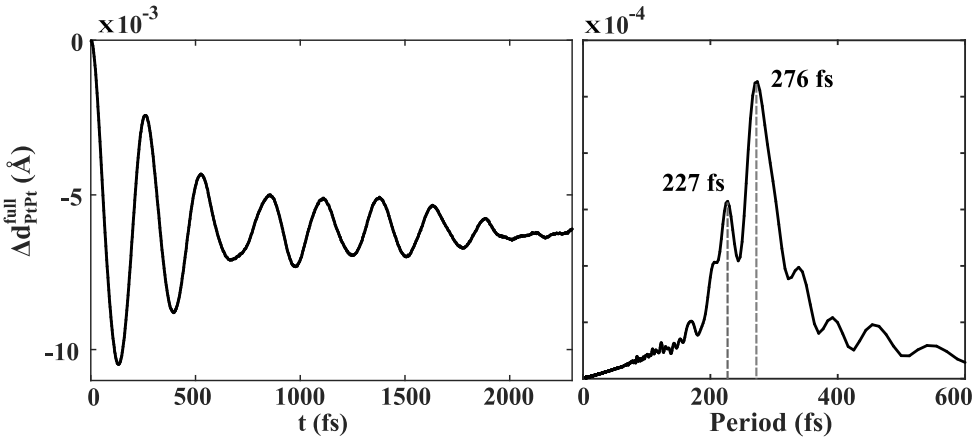

Figure 13. Evolution of the Pt-Pt average distance computed from the ground- and excited-state time-dependent distributions of Pt-Pt distances (Left), and its Fourier transform (FT) (Right) showing peaks at the two vibrational periods characteristic of motion in S_0 (276 fs) and S_1 (227 fs).

where the ground- and excited-state distributions of Pt-Pt distances and their normalizations have been defined in the previous section. The peak of the FT associated to the period of vibrations in S_1 (227 fs) has a significantly smaller intensity than the peak of the S_0 period (276 fs). The classical picture of the photoexcitation event described in the previous section permits us to gain a qualitative understanding of the predominance of the ground-state vibrational signature in the outcome dynamics: as shown in Figure 11, and detailed extensively in the main text, the photon energy of the excitation pulse ensures that the excited-state distribution is created very close to the equilibrium Pt-Pt distance of the S_1 state. Thus, while the photoexcited molecules experience a small gradient along the Pt-Pt coordinate, the hole starts its motion on the ground-state potential from a position far from the equilibrium ground-state Pt-Pt distance. Accordingly, the amplitude of the coherent vibrations in the excited-state are comparatively much smaller than those described by the ground-state hole.

We note that the classical picture used here to describe the dynamics following photoexcitation neglects the motion of ground-state molecules during the pulse, which would lead to a broadening of the initial excited- and ground-state hole distributions, and hence to a smearing of the coherent oscillations [22, 24]. Since the oscillations in the Pt-Pt distance are faster in S_1 than S_0, we expect that the smearing due to the finite duration of the pulse is more

significant for the excited state than for the ground-state hole. This could be a plausible explanation of why the experimental data contain no trace at all of excited-state dynamics, while the simulations predict the presence of a (comparatively very small) contribution.

IX. ANIMATIONS

Movie of the Pt-Pt bond length distributions can be found here:

---

[1] C.M. Che, L.G. Butler, P.J. Grunthaner, and H.B. Gray. Chemistry and spectroscopy of binuclear diplatinum complexes. *Inorganic Chemistry*, 24(26):4662–4665, DEC 18 1985.

[2] Elisa Biasin, Tim B. van Driel, Gianluca Levi, Mads G. Laursen, Asmus O. Dohn, Asbjorn Moltke, Peter Vester, Frederik B. K. Hansen, Kasper S. Kjaer, Tobias Harlang, Robert Hartsock, Morten Christensen, Kelly J. Gaffney, Niels E. Henriksen, Klaus B. Møller, Kristoffer Haldrup, and Martin M. Nielsen. Anisotropy enhanced X-ray scattering from solvated transition metal complexes. *Journal of Synchrotron Radiation*, 25(2):306–315, MAR 2018.

[3] Kristoffer Haldrup, Morten Christensen, and Martin Meedom Nielsen. Analysis of time-resolved X-ray scattering data from solution-state systems. *Acta Crystallographica Section A*, 66(2):261–269, MAR 2010.

[4] Asmus O. Dohn, Elisa Biasin, Kristoffer Haldrup, Martin M. Nielsen, Niels E. Henriksen, and Klaus B. Møller. On the calculation of x-ray scattering signals from pairwise radial distribution functions (vol 48, 244010, 2015). *Journal of Physics B - Atomic, Molecular and Optical Physics*, 49(5), MAR 14 2016.

[5] Kasper Skov Kjær, Tim B. van Driel, Jan Kehres, Kristoffer Haldrup, Dmitry Khakhulin, Klaus Bechgaard, Marco Cammarata, Michael Wulff, Thomas Just Sorensen, and Martin M. Nielsen. Introducing a standard method for experimental determination of the solvent response in laser pump, X-ray probe time-resolved wide-angle X-ray scattering experiments on systems in solution. *Physical Chemistry Chemical Physics*, 15(36):15003–15016, 2013.

[6] Kristoffer Haldrup, Wojciech Gawelda, Rafael Abela, Roberto Alonso-Mori, Uwe Bergmann, Amelie Bordage, Marco Cammarata, Sophie E. Canton, Asmus O. Dohn, Tim Brandt van Driel, David M. Fritz, Andreas Galler, Pieter Glatzel, Tobias Harlang, Kasper S. Kjaer, Hen-

rik T. Lemke, Klaus B. Møller, Zoltan Nemeth, Matyas Papai, Norbert Sas, Jens Uhlig, Diling Zhu, Gyoergy Vanko, Villy Sundstroem, Martin M. Nielsen, and Christian Bressler. Observing Solvation Dynamics with Simultaneous Femtosecond X-ray Emission Spectroscopy and X-ray Scattering. *Journal of Physical Chemistry B*, 120(6):1158–1168, FEB 18 2016.

[7] Roberto Monni, Gerald Aubck, Dominik Kinschel, Kathrin M. Aziz-Lange, Harry B. Gray, Antonn Vlek, and Majed Chergui. Conservation of vibrational coherence in ultrafast electronic relaxation: The case of diplatinum complexes in solution. *Chemical Physics Letters*, pages –, 2017.

[8] Roberto Monni, Gloria Capano, Gerald Auböck, Harry B. Gray, Antonín Vlček, Ivano Tavernelli, and Majed Chergui. Vibrational coherence transfer in the ultrafast intersystem crossing of a diplatinum complex in solution. *Proceedings of the National Academy of Sciences*, 2018.

[9] J.R. Peterson and K. Kalyanasundaram. Energy-transfer and electron-transfer processes of the lowest triplet excited-state of tetrakis(diphosphito)diplatinate(II). *Journal of Physical Chemistry*, 89(12):2486–2492, 1985.

[10] Gianluca Levi, Matyas Papai, Niels E. Henriksen, Asmus O. Dohn, and Klaus B. M œller. Solution Structure and Ultrafast Vibrational Relaxation of the PtPOP Complex Revealed by Delta SCF-QM/MM Direct Dynamics Simulations. *Journal of Physical Chemistry C*, 122(13):7100–7119, APR 5 2018.

[11] Denis Leshchev, Tobias C. B. Harlang, Lisa A. Fredin, Dmitry Khakhulin, Yizhu Liu, Elisa Biasin, Mads G. Laursen, Gemma E. Newby, Kristoffer Haldrup, Martin M. Nielsen, Kenneth Warnmark, Villy Sundstrom, Petter Persson, Kasper S. Kjaer, and Michael Wulff. Tracking the picosecond deactivation dynamics of a photoexcited iron carbene complex by time-resolved X-ray scattering. *Chemical Science*, 9(2):405–414, JAN 14 2018.

[12] A.E. Stiegman, S.F. Rice, H.B. Gray, and V.M. Miskowski. Electronic spectroscopy of diplatinum complexes - excited states of $Pt_2(P_2O_5H_2)_4^{4-}$. *Inorganic Chemistry*, 26(7):1112–1116, APR 8 1987.

[13] Stanislav Zalis, Yan-Choi Lam, Harry B. Gray, and Antonin Vlcek. Spin-Orbit TDDFT Electronic Structure of Diplatinum(II,II) Complexes. *Inorganic Chemistry*, 54(7):3491–3500, APR 6 2015.

[14] A. O. Dohn, E. . Jnsson, G. Levi, J. J. Mortensen, O. Lopez-Acevedo, K. S. Thygesen, K. W. Jacobsen, J. Ulstrup, N. E. Henriksen, K. B. Mller, and H. Jnsson. Grid-based projector aug-

mented wave (gpaw) implementation of quantum mechanics/molecular mechanics (qm/mm) electrostatic embedding and application to a solvated diplatinum complex. *Journal of Chemical Theory and Computation*, 13(12):6010–6022, 2017. PMID: 29083921.

[15] S. R. Bahn and K. W. Jacobsen. An object-oriented scripting interface to a legacy electronic structure code. *Computing in Science & Engineering*, 4:55, 2002.

[16] A. H. Larsen, J. J. Mortensen, J. Blomqvist, I. E. Castelli, R. Christensen, M. Dułak, J. Friis, M. N. Groves, B. Hammer, C. Hargus, E. D. Hermes, P. C. Jennings, P. B. Jensen, J. Kermode, J. R. Kitchin, E. L. Kolsbjerg, J. Kubal, K. Kaasbjerg, S. Lysgaard, J. B. Maronsson, T. Maxson, T. Olsen, L. Pastewka, A. Peterson, C. Rostgaard, J. Schiøtz, O. Schütt, M. Strange, K. S. Thygesen, T. Vegge, L. Vilhelmsen, M. Walter, Z. Zeng, and K. W. Jacobsen. The atomic simulation environmenta python library for working with atoms. *Journal of Physics: Condensed Matter*, 29(27):273002, 2017.

[17] J. J. Mortensen, L. B. Hansen, and K. W. Jacobsen. Real-space grid implementation of the projector augmented wave method. *Physical Review B*, 71:035109, 2005.

[18] J. Enkovaara, C. Rostgaard, J. J. Mortensen, J. Chen, M. Dulak, L. Ferrighi, J. Gavnholt, C. Glinsvad, V. Haikola, H. A. Hansen, H. H. Kristoffersen, M. Kuisma, A. H. Larsen, L. Lehtovaara, M. Ljungberg, O. Lopez-Acevedo, P. G. Moses, J. Ojanen, T. Olsen, V. Petzold, N. A. Romero, J. Stausholm-Møller, M. Strange, G. A. Tritsaris, M. Vanin, M. Walter, B. Hammer, H. Häkkinen, G. K. H. Madsen, R. M. Nieminen, J. K. Nørskov, M. Puska, T. T. Rantala, J. Schiøtz, K. S. Thygesen, and K. W. Jacobsen. Electronic structure calculations with gpaw: a real-space implementation of the projector augmented-wave method. *Journal of Physics: Condensed matter*, 22:253202, 2010.

[19] A. H. Larsen, M. Vanin, J. J. Mortensen, K. S. Thygesen, and K. W. Jacobsen. Localized atomic basis set in the projector augmented wave method. *Phys. Rev. B*, 80:195112, 2009.

[20] A. D. Becke. Density-functional exchange-energy approximation with correct asymptotic behavior. *Physical Review A*, 38:3098, 1988.

[21] C. Lee, W. Yang, and R. G. Parr. Development of the colle-salvetti correlation-energy formula into a functional of the electron density. *Physical Review B*, 37:785–789, 1988.

[22] G. Levi. *Photoinduced Molecular Dynamics in Solution.* PhD thesis, Technical University of Denmark, 2018.

[23] W. L. Jorgensen, J. Chandrasekhar, J. D. Madura, R. W. Impey, and M. L. Klein. Comparison of simple potential functions for simulating liquid water. *Journal of Chemical Physics*, 79:926–935, 1983.

[24] DM Jonas, SE Bradforth, SA Passino, and GR Fleming. Femtosecond wavepacket spectroscopy - influence of temperature, wavelength and pulse duration. *Journal of Physical Chemistry*, 99(9):2594–2608, MAR 2 1995.

[25] A.K. Rappe, C.J. Casewit, K.S. Colwell, W.A. Goddard III, and W.M. Skiff. Uff, a full periodic table force field for molecular mechanics and molecular dynamics simulations. *Journal of the American Chemical Society*, 114:10024–10035, 1992.

[26] H. C. Andersen. Rattle: A "velocity" version of the shake algorithm for molecular dynamics calculations. *Journal of Computational Physics*, 52:24, 1983.

[27] J. Petersen, N. E. Henriksen, and K. B. Møller. Validity of the Bersohn-Zewail model beyond justification. *Chemical Physics Letters*, 539-540:234–238, 2012.

[28] Klaus B. Møller, Rossend Rey, and James T. Hynes. Hydrogen bond dynamics in water and ultrafast infrared spectroscopy: A theoretical study. *Journal of Physical Chemistry A*, 108:1275–1289, 2004.

[29] V. A. Ermoshin and V. Engel. Femtosecond pump-probe fluorescence signals from classical trajectories: Comparison with wave-packet calculations. *European Physical Journal D*, 15:413–422, 2001.

[30] Z. Li, J.-Y. Fang, and C. C. Martens. Simulation of ultrafast dynamics and pump-probe spectroscopy using classical trajectories. *The Journal of Chemical Physics*, 104(18):6919, 1996.

[31] E.H. Van Kleef and I. Powis. Anisotropy in the preparation of symmetric top excited states. I. One-photon electric dipole excitation. *Molecular Physics*, 96(5):757–774, 1999.

[32] Renske M. van der Veen, Andrea Cannizzo, Frank van Mourik, Antonin Vlcek, Jr., and Majed Chergui. Vibrational Relaxation and Intersystem Crossing of Binuclear Metal Complexes in Solution. *Journal of the American Chemical Society*, 133(2):305–315, JAN 19 2011.

[33] Reinhard J. Maurer and Karsten Reuter. Assessing computationally efficient isomerization dynamics: ??sCF density-functional theory study of azobenzene molecular switching. *Journal of Chemical Physics*, 135(22):224303, 2011.

[34] Burak Himmetoglu, Alex Marchenko, Isma??la Dabo, and Matteo Cococcioni. Role of electronic localization in the phosphorescence of iridium sensitizing dyes. *Journal of Chemical Physics*, 137(15):154309, 2012.

[35] D. A. McQuarrie. *Statistical Mechanics*. Harper & Row, 1976.

Paper III

research papers

JOURNAL OF SYNCHROTRON RADIATION

ISSN 1600-5775

Anisotropy enhanced X-ray scattering from solvated transition metal complexes

Elisa Biasin,[a,b]* Tim B. van Driel,[a,f] Gianluca Levi,[c] Mads G. Laursen,[a] Asmus O. Dohn,[d] Asbjørn Moltke,[a] Peter Vester,[a] Frederik B. K. Hansen,[a] Kasper S. Kjaer,[a,b,e] Tobias Harlang,[a] Robert Hartsock,[b] Morten Christensen,[a] Kelly J. Gaffney,[b] Niels E. Henriksen,[c] Klaus B. Møller,[c] Kristoffer Haldrup[a] and Martin M. Nielsen[a]

[a]Department of Physics, Technical University of Denmark, Fysikvej 307, DK-2800 Kongens Lyngby, Denmark, [b]PULSE Institute, SLAC National Accelerator Laboratory, Menlo Park, CA 94025, USA, [c]Department of Chemistry, Technical University of Denmark, Kemitorvet 207, DK-2800 Kongens Lyngby, Denmark, [d]Faculty of Physical Sciences, University of Iceland, Reykjavik, Iceland, [e]Department of Chemical Physics, Lund University, Box 118, S-22100 Lund, Sweden, and [f]Linac Coherent Light Source, SLAC National Accelerator Laboratory, Menlo Park, CA 94025, USA. *Correspondence e-mail: elbia@fysik.dtu.dk

Received 2 August 2017
Accepted 24 November 2017

Edited by G. Grübel, HASYLAB at DESY, Germany

Keywords: time-resolved; anisotropic scattering; orientational selection; XFEL; ultrafast; molecular structure.

Supporting information: this article has supporting information at journals.iucr.org/s

Time-resolved X-ray scattering patterns from photoexcited molecules in solution are in many cases anisotropic at the ultrafast time scales accessible at X-ray free-electron lasers (XFELs). This anisotropy arises from the interaction of a linearly polarized UV–Vis pump laser pulse with the sample, which induces anisotropic structural changes that can be captured by femtosecond X-ray pulses. In this work, a method for quantitative analysis of the anisotropic scattering signal arising from an ensemble of molecules is described, and it is demonstrated how its use can enhance the structural sensitivity of the time-resolved X-ray scattering experiment. This method is applied on time-resolved X-ray scattering patterns measured upon photoexcitation of a solvated di-platinum complex at an XFEL, and the key parameters involved are explored. It is shown that a combined analysis of the anisotropic and isotropic difference scattering signals in this experiment allows a more precise determination of the main photoinduced structural change in the solute, *i.e.* the change in Pt—Pt bond length, and yields more information on the excitation channels than the analysis of the isotropic scattering only. Finally, it is discussed how the anisotropic transient response of the solvent can enable the determination of key experimental parameters such as the instrument response function.

1. Introduction

Time-resolved X-ray diffuse scattering (XDS) experiments give insight into the photoinduced structural dynamics of solvated molecules. In these experiments, a laser pulse initiates the dynamic process, which is subsequently probed by an X-ray probe pulse arriving at specific time delays after the pump event. If the laser pulse is ultra-short, the ensuing structural dynamics are coherently initiated in the molecular ensemble (Zewail, 2000), and the scattering signal can be used to retrieve structural changes occurring in the molecule after the electronic excitation (Borfecchia *et al.*, 2013; Biasin *et al.*, 2016; Haldrup *et al.*, 2012; Kim *et al.*, 2015*a*; van Driel *et al.*, 2016; Chergui & Collet, 2017; Kong *et al.*, 2008). Such experiments are of fundamental importance for understanding the structure–function relationship of, for instance, transition metal complexes whose photochemical and photophysical properties can be applied in technologies such as solar energy conversion and photocatalysis (Takeda *et al.*, 2017; Esswein & Nocera, 2007; White, 1982).

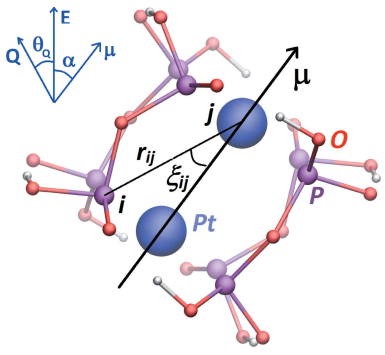

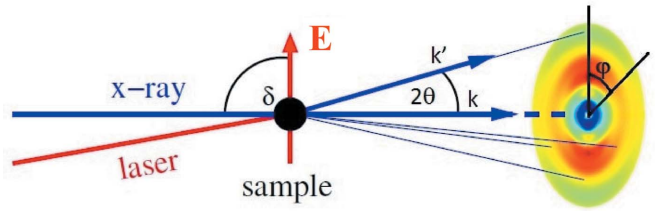

Figure 1
Experimental setup for a standard time-resolved XDS experiment. δ is the angle between the direction of propagation of the X-ray beam and the laser polarization axis **E**; 2θ is the scattering angle, *i.e.* the angle between the incoming (**k**) and outgoing (**k′**) momentum of the X-ray beam; φ is the angle between the projection of the laser polarization and the scattering vector $\mathbf{Q} = \mathbf{k}' - \mathbf{k}$ on the detector surface.

In typical time-resolved XDS experiments, laser pump and X-ray probe pulses are focused onto a thin liquid jet, which is produced by pumping the liquid sample through a nozzle. The diffuse X-ray scattering is collected on a two-dimensional (2D) detector placed after the sample on the plane perpendicular to the propagation direction of the X-ray beam (Fig. 1). The measured scattering signal contains information about all the inter-nuclear distances of the sample at a specific time delay and it is usually dominated by the scattering from the solvent. The sensitivity to the solute is enhanced in the difference scattering signal, which is constructed by subtracting the signal collected without photoexciting the sample from the signal collected after photoexcitation. In this way the unchanging background contributions cancel out, and the difference scattering signal arises from the changes in the inter-atomic distances in the probed sample volume (Borfecchia *et al.*, 2013; Ihee *et al.*, 2010). The established procedure for analysing scattering data from liquid samples consists of an azimuthal integration of the 2D difference scattering patterns, since the signal is usually assumed to arise from an isotropically distributed ensemble of molecules (Ihee *et al.*, 2010; Haldrup *et al.*, 2010). If the sample is isotropic, the azimuthal integration allows for an improvement of the signal-to-noise (S/N) without loss of information. This procedure was first established with synchrotron data and it is justified when the time resolution is longer than the molecular rotational correlation time in solution, which ranges in the 10–100 ps time scale for transition metal complexes (Lakowicz, 2006; Kim *et al.*, 2015*b*).

At X-ray free-electron lasers (XFELs), that can deliver femtosecond X-ray pulses, the photoinduced structural changes in the sample can be captured at the time scale of atomic motions. This enables the observation of vibrational and rotational molecular dynamics in, for instance, solvated transition metal complexes (Biasin *et al.*, 2016; Kim *et al.*, 2015*b*; Lemke *et al.*, 2017; Chergui & Collet, 2017). If the photoselection process (illustrated in Fig. 2 and further described below) creates an aligned excited-state ensemble of molecules, anisotropic 2D scattering patterns can be observed on time scales shorter than the rotational correlation time of the molecules (Kim *et al.*, 2011; Kim *et al.*, 2015*b*; Yang *et al.*, 2016*a*,*b*; Glownia *et al.*, 2016). Anisotropic scattering patterns contain information on the molecular preferred orientation, and thus can add sensitivity to spatial degrees of freedom compared with isotropic patterns (Hensley *et al.*, 2012; Burger *et al.*, 2010; Küpper *et al.*, 2014). The theoretical foundation for interpreting anisotropic scattering contributions from aligned ensembles of molecules in time-resolved experiments has been laid out in some detail over the past ten years (Baskin & Zewail, 2006; Lorenz *et al.*, 2010; Brinkmann & Hub, 2015; Penfold *et al.*, 2012). However, quantitative structural analysis of anisotropic scattering data from molecular ensembles where a photoselected sub-population has been promoted to an electronic excited state has been demonstrated only in a very few cases in the gas phase (Yang *et al.*, 2016*a*,*b*; Glownia *et al.*, 2016), and a robust methodology for such cannot yet be said to have been fully established as the debate surrounding the work of Glownia *et al.* shows (Bennett *et al.*, 2017; Glownia *et al.*, 2017). Specifically with respect to solution-state molecular systems, only qualitative analysis of time-resolved anisotropic scattering data have been reported, and the anisotropic contributions to the observed scattering patterns have been mostly used only to obtain the rotational correlation time of the molecules in solution (Kim *et al.*, 2011; Kim *et al.*, 2015*b*).

In this article, we revisit the formalism derived by Lorenz *et al.* (2010) for analysing scattering from a photo-aligned ensemble of molecules. We use this formalism to extract the isotropic and anisotropic contribution from 2D scattering patterns measured at an XFEL upon photoexcitation of a transition metal complex in solution and we explore a few of the key parameters involved in this procedure. We show that, in the presence of anisotropic scattering, the separation of the two contributions can, and should, replace the standard azimuthal integration in the data reduction procedures. As a key point, we demonstrate that the anisotropic contribution

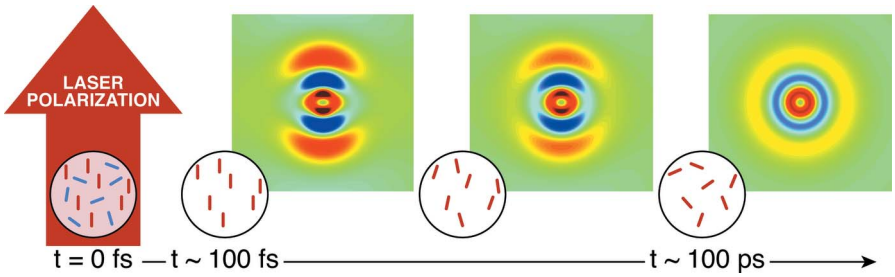

Figure 2
Illustration of the photoselection process. Before the arrival of the laser pump ($t < 0$), the molecules are randomly oriented in solution. The laser pulse preferentially excites the molecules with the transition dipole moments parallel to the laser polarization axis. Thus, the excited-state population is created as an aligned ensemble (at $t = 0$ the distribution of the transition dipole moment in molecules being excited is a cosine-squared distribution with respect to the laser polarization axis) yielding anisotropic difference scattering patterns. After the excitation event ($t > 0$), the rotation of both the excited and unexcited populations causes rotational dephasing of the alignment.

can be quantitatively analysed in order to extract structural information about the photoexcited ensemble of molecules. These results are discussed in the framework of how the information extracted from a combined analysis of the isotropic and anisotropic contributions to the measured difference scattering signals can potentially help disentangle the many inter- and intra-nuclear degrees of freedom involved in photoinduced structural dynamics of molecules in solution.

The method is exemplified on scattering data collected at the X-ray Pump Probe (XPP) instrument (Chollet *et al.*, 2015) at the Linac Coherent Light Source upon photoexcitation of the tetrakis-μ-pyrophosphitodiplatinate(II) ion $[Pt_2(P_2O_5H_2)_4]^{4-}$, here abbreviated as PtPOP. Fig. 3 shows the molecular structure of PtPOP: a Pt–Pt dimer is held together by four pyrophosphito ligands. The compound belongs to the C_{4h} point group, with approximately fourfold symmetry along the Pt–Pt axis (Zipp, 1988; Gray *et al.*, 2017). Thus, the Pt–Pt axis has higher rotational symmetry than the other two axes, and the molecule is a symmetric top (*i.e.* two principal moments of inertia have the same value and the third has a unique value). This compound was first synthesized in 1977 and has been the subject of a vast amount of studies, due to its characteristic photophysical properties and activity as a photocatalyst (Roundhill *et al.*, 1989; Stiegman *et al.*, 1987). In the last decades, PtPOP has become a model compound for time-resolved X-ray studies, due to its high scattering power, its long singlet excited-state lifetime, and its high symmetry (Christensen *et al.*, 2009; van der Veen *et al.*, 2009). For this experiment, an 80 m*M* aqueous solution of PtPOP was circulated through a nozzle producing a 50 µm round liquid jet. Each photocycle was initiated by a 3 µJ laser pulse at 395 nm and with 50 fs pulse width (FWHM), focused onto a 150 µm-diameter spot. The scattering from the 9.5 keV X-ray probe pulses was detected by the Cornell–SLAC Pixel Array Detector (CSPAD) (Philipp *et al.*, 2011) covering scattering vectors up to 4.5 Å^{-1}. The time delay t between the laser and the X-ray pulses was determined for every pump–probe event with ∼10 fs (FWHM) resolution using the XPP timing-tool (Minitti *et al.*, 2015). The detector signal was corrected according to the procedure described by van Driel *et al.* (2015), including corrections for the detector geometry and the horizontal polarization of the X-ray beam. The corrected scattering signal was scaled to the liquid unit cell reflecting the stoichiometry of the sample (Haldrup *et al.*, 2010), yielding the acquired signal in electron units per solute molecule (e.u. molec^{-1}). Individual 2D difference scattering patterns were then time-sorted and averaged. Movie S1 of the supporting information shows averaged measured difference scattering patterns upon photoexcitation of PtPOP as a function of increasing time delay: a strongly anisotropic difference scattering signal is visible at an early time delay and decays on a ∼100 ps time scale. The signal is expected to arise predominantly from the shortening of the Pt–Pt distance since the 395 nm transition, which has polarization along the Pt—Pt bond, involves the promotion of an electron from the antibonding $d\sigma^*$ to the bonding $p\sigma$ orbital (Stiegman *et al.*, 1987). Christensen *et al.* investigated the structure of the excited state of PtPOP in water with time-resolved XDS and obtained a Pt—Pt contraction of 0.24 ± 0.06 Å with respect to the ground state of the molecule (Christensen *et al.*, 2009). van der Veen *et al.* concluded a 0.31 ± 0.05 Å Pt—Pt contraction upon excitation of the complex in ethanol, with X-ray absorption spectroscopy (van der Veen *et al.*, 2009). The well defined transition dipole moment and the strong scattering signal arising from the contraction of the Pt—Pt bond makes PtPOP an ideal model system to benchmark the formalism required in order to interpret anisotropic difference scattering patterns.

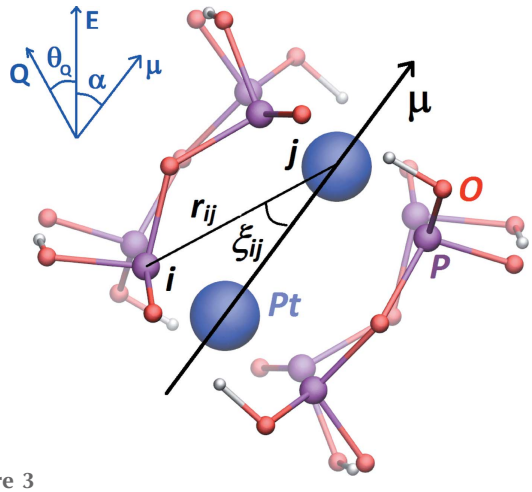

Figure 3
Molecular structure of PtPOP and relevant angles. PtPOP is a symmetric top molecule with the main axis of symmetry parallel to the Pt–Pt axis (Zipp, 1988; Gray *et al.*, 2017). In the molecular fixed frame (black arrows): ξ_{ij} is the angle between the internuclear displacement $\mathbf{r}_{ij}$ and the transition dipole moment $\boldsymbol{\mu}$ of the molecule, which is parallel to the main axis of symmetry of the molecule. In the laboratory frame (blue arrows): α is the angle between the laser polarization axis **E** and the transition dipole vector $\boldsymbol{\mu}$ of the molecule, θ_Q is the angle between the laser polarization axis and the scattering vector.

2. Methods

In time-resolved XDS experiments, the molecules in solution are randomly oriented before the arrival of the laser pump. If the linearly polarized ultrashort laser pulse interacts with a single transition dipole moment $\boldsymbol{\mu}$ of the molecule, the angular distribution D of this transition dipole moment in molecules being excited displays cylindrical symmetry with respect to the laser polarization **E**. Therefore, this distribution can be expressed through an expansion in Legendre polynomials $P_n(\cos\alpha)$ of only the angle α between the laser polarization axis and the transition dipole moment (Baskin & Zewail, 2006),

$$D(\alpha, \eta) = D(\alpha) = \sum_{n=0}^{\infty} c_n P_n(\cos\alpha), \qquad (1)$$

where α and η are the polar and azimuthal angles, respectively, in a spherical coordinates system with polar axis **E**, and c_n are expansion coefficients. In the case of one-photon absorption of linearly polarized radiation by an isotropic molecular

ensemble in thermal equilibrium, the distribution of the transition dipole moment in molecules being excited is a cosine-squared distribution with respect to the laser polarization axis (Møller & Henriksen, 2012; Baskin & Zewail, 2006). Cast into the generic form of equation (1), the distribution of excited-state molecules immediately after the excitation event can be expressed as a sum of two terms,

$$D(\alpha) = c_0 P_0(\cos\alpha) + c_2 P_2(\cos\alpha), \tag{2}$$

where $P_0(x) = 1$ and $P_2(x) = (3x^2 - 1)/2$, with $c_2 = 2c_0$. Properly normalizing (Kleef & Powis, 1999) the angular distribution in equation (1) on unit sphere gives

$$1 = \frac{1}{2}\int_0^\pi D(\alpha)\sin\alpha\,\mathrm{d}\alpha = c_0, \tag{3}$$

where the last equality is a consequence of the orthogonality of the Legendre polynomials.

Assuming ultrashort laser pump and X-ray probe pulses, the differential scattering cross section from an ensemble of excited molecules, at a specific pump–probe delay time t, can be expressed by weighting the squared molecular form factor with the instantaneous distribution ρ of nuclear geometries (Lorenz *et al.*, 2010),

$$\frac{\mathrm{d}\sigma}{\mathrm{d}\Omega}(\mathbf{Q}, t) = \sigma_\mathrm{T}\int \mathrm{d}\mathbf{R}\,\rho(\mathbf{R}, t)\left|F_\mathrm{mol}(\mathbf{Q}, \mathbf{R})\right|^2, \tag{4}$$

where $\mathbf{R}$ has dimensions $3N$ and describes the nuclear coordinates in the laboratory frame, σ_T is the Thomson scattering cross section and $\mathbf{Q}$ is the scattering vector. After assuming that rotational and vibrational degrees of freedom of the molecule are uncoupled (Lorenz *et al.*, 2010), we express the rotational part of the distribution through $D(\alpha)$ in equation (1) and the vibrational distribution as a δ-distribution. Under these assumptions, the scattering from an ensemble of molecules with their transition dipole moments aligned with respect to the laser polarization axis can be calculated through

$$\frac{\mathrm{d}\sigma}{\mathrm{d}\Omega}(\mathbf{Q}, t) = 2\pi\sigma_\mathrm{T}\int_0^\pi \mathrm{d}\alpha\sin\alpha D(\alpha, t)\left|F_\mathrm{mol}[\mathbf{Q}, \alpha, \mathbf{r}(t)]\right|^2, \tag{5}$$

where $\mathbf{r}$ is the vector of inter-nuclear distances. Furthermore, this expression [equation (5)] can be simplified by utilizing the fact that the molecule is a symmetric top with the transition dipole moment parallel to the unique axis of symmetry. Under this assumption, as detailed by Baskin & Zewail (2005), the angular distribution of each intra-molecular distance $\mathbf{r}_{ij}$ with respect to the laser polarization axis can be expressed through the angle ξ_{ij} between $\mathbf{r}_{ij}$ and the main axis of symmetry of the molecule. These parameters are illustrated in Fig. 3: PtPOP is a symmetric top molecule with the main axis of symmetry parallel to the Pt—Pt bond, which is also the direction of the transition dipole moment photoselected in this experiment and therefore meets the above assumptions. As described by Lorenz *et al.* (2010), under the described assumptions, the integral in equation (5) has the analytical form

$$\frac{\mathrm{d}\sigma}{\mathrm{d}\Omega}(Q, \theta_Q, t) = 2(2\pi)^2\sigma_\mathrm{T}\sum_n P_n(\cos\theta_Q)\,S_n(Q, t), \tag{6}$$

where θ_Q is the angle between the laser polarization axis and $\mathbf{Q}$ (see Fig. 3) and

$$S_n(Q, t) = (-1)^{n/2}\,c_n(t)\sum_{i,j}^{N} f_i(Q) f_j(Q)\,P_n\left[\cos\xi_{ij}(t)\right] j_n\left[Qr_{ij}(t)\right], \tag{7}$$

where j_n are the spherical Bessel functions and f_i is the atomic form factor of atom i, which is used to express the molecular form factor within the independent atom model (Møller & Henriksen, 2012). Assuming one-photon absorption [and thus the angular distribution in equation (2)], only the $n = 0$ and $n = 2$ terms contribute in equation (6) (Lorenz *et al.*, 2010) and the scattering signal can be written as

$$\frac{\mathrm{d}\sigma}{\mathrm{d}\Omega}(Q, \theta_Q, t) \propto S_0(Q, t) + P_2(\cos\theta_Q) S_2(Q, t). \tag{8}$$

Since $j_0(x) = (\sin x)/x$, S_0 is recognized as the Debye formula for isotropic ensembles,

$$S_0(Q, t) = \sum_{i,j}^{N} f_i(Q) f_j(Q)\,\frac{\sin\left[Qr_{ij}(t)\right]}{Qr_{ij}(t)}, \tag{9}$$

while S_2 contains information about the orientation of the single bond $\mathbf{r}_{ij}$ with respect to the transition dipole moment of the molecule,

$$S_2(Q, t) = -c_2(t)\sum_{i,j}^{N} f_i(Q) f_j(Q)\,P_2\left[\cos\xi_{ij}(t)\right] j_2\left[Qr_{ij}(t)\right], \tag{10}$$

with $j_2(x) = [(3/x^2) - 1][(\sin x)/x] - 3[(\cos x)/x^2]$. From here, S_0 and S_2 will be referred to as the isotropic and anisotropic part of the scattering signal, respectively. c_2 decays from its initial value of 2 to 0 according to the rotational correlation time of the molecules in solution.

The excitation will leave a hole in the ground-state distribution of the same rotational anisotropy as the excited-state ensemble (Baskin & Zewail, 2006; Jonas *et al.*, 1995). Starting from equation (8), the difference scattering signal ΔS including both excited-state and ground-state contributions can, therefore, be decomposed as (Lorenz *et al.*, 2010)

$$\Delta S(Q, \theta_Q, t) \propto \Delta S_0(Q, t) + P_2(\cos\theta_Q)\Delta S_2(Q, t), \tag{11}$$

where $\Delta S_0(Q, t)$ and $\Delta S_2(Q, t)$ are, respectively, the isotropic and anisotropic difference scattering signals arising from the photoinduced structural changes in the sample at a specific pump–probe time delay t.

With respect to equation (11), S_0 and S_2 depend only on internal coordinates of the molecule, while $P_2(\cos\theta_Q)$ depends only on the geometry of the experiment. Specifically, as detailed by Baskin & Zewail (2006), $\cos\theta_Q$ can be expressed as a function of the angles δ, θ and φ, as defined in Fig. 1,

$$\cos\theta_Q = \sin\theta\cos\delta - \cos\theta\cos\varphi\sin\delta. \tag{12}$$

In the case of most standard XDS experiments, and for the PtPOP experiment presented here, the laser beam is nearly

collinear to the X-ray beam. This is one of the possible configurations that yields a 90° angle between the laser polarization axis and the direction of propagation of the X-ray beam (δ in Fig. 1), and equation (12) simplifies to

$$\cos\theta_Q = -\cos\theta\cos\varphi. \qquad (13)$$

Since φ is the azimuthal angle on the detector surface, $\cos\theta_Q$ maps P_2 anisotropically onto the detector surface. The second-order Legendre polynomial, and hence the anisotropic contribution to the scattering, vanishes when θ_Q in equation (12) is equal to the magic angle. However, as extensively described by Baskin & Zewail (2006), it is not possible to simultaneously remove anisotropic contributions from the entire scattering pattern for a given choice of δ. The linear relation between scattering intensity and P_2 in equation (11) can be used to retrieve, for a specific Q value, the isotropic and anisotropic difference scattering signal, as described in the following.

Fig. 4 illustrates the extraction of the isotropic and anisotropic difference scattering signals from a difference scattering pattern measured 4.5 ps after the photoexcitation of PtPOP in water. The scattering pattern is shown in Fig. 4(*b*) and it is

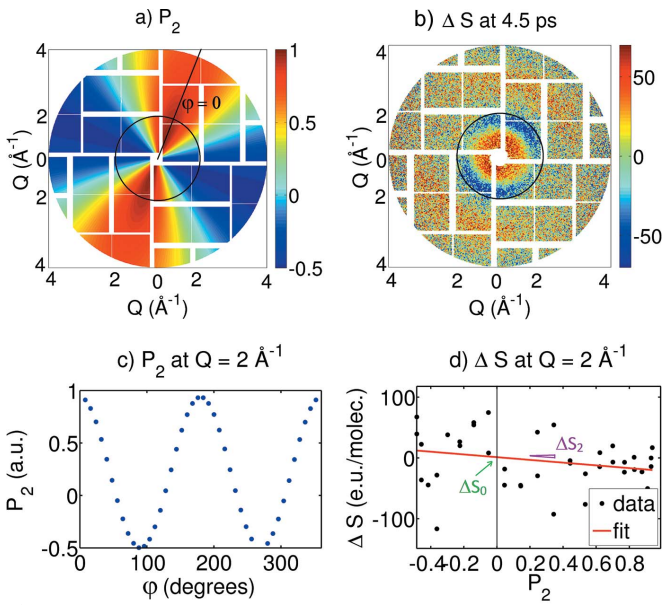

Figure 4
(*a*) $P_2(\cos\theta_Q)$, with θ_Q as in equation (13), mapped on the CSPAD. The azimuthal angle (φ) is defined to be zero at the projection of the laser polarization axis on the detector surface. A radial bin corresponding to $Q = 2$ Å^{-1} is selected. (*b*) Averaged difference scattering pattern at 4.5 ps after photoexcitation of PtPOP in water. For comparison, a full scattering pattern is shown in Fig. S1 of the supporting information. (*c*) Value of P_2 for the specific radial bin selected in panel (*a*) as a function of azimuthal angle φ, corresponding to $Q = 2$ Å^{-1}. (*d*) Difference scattering signal ΔS at $Q = 2$ Å^{-1} *versus* P_2 (black dots) and straight line fit (red). The intercept with $P_2 = 0$ yields the isotropic scattering signal and the slope yields the anisotropic scattering signal, according to equation (11). The uncertainties ($\sigma_{\Delta S_0}$ and $\sigma_{\Delta S_2}$) are also estimated from the fit and further described in the text.

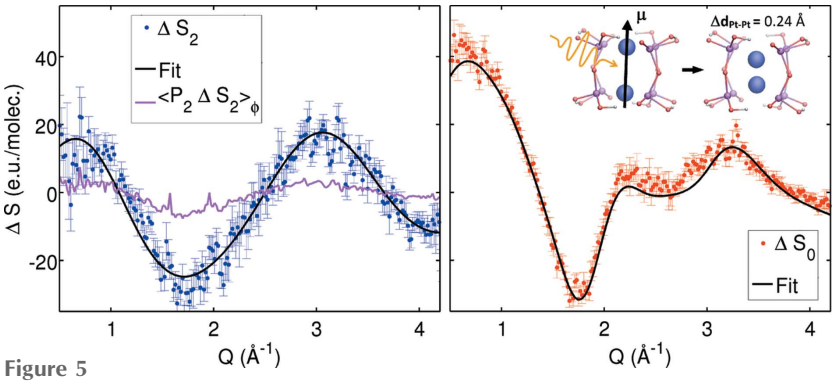

Figure 5
ΔS_2 (left, blue points) and ΔS_0 (right, red points) extracted from the pattern in Fig. 4(*b*) through equation (11). The black line shows the simulated difference scattering signal through equations (9) and (10) using as parameters the best-fit results obtained by a combined fit of ΔS_2 and ΔS_0. The magenta line in the left panel shows the azimuthal average of the anisotropic signal $[\langle -P_2(\cos\theta_Q)\Delta S_2\rangle_\varphi]$.

an average of 50 difference scattering patterns collected in a ~40 fs-wide time bin centred at 4.5 ps after the arrival of the laser pump pulse. As introduced above, such a signal arises mainly from the photoinduced contraction of the Pt atoms along their connecting vector. In the excited-state ensemble, this vector has a cosine-squared distribution with respect to the laser polarization axis, since the transition dipole moment is parallel to the Pt–Pt axis. Fig. 4(*a*) shows P_2 [$P_2 = (3\cos^2\theta_Q - 1)/2$ and $\cos\theta_Q$ as in equation (13)] mapped onto the CSPAD, with $\varphi = 0$ along the direction of the projection of the laser polarization axis on the detector surface, which was found to be inclined by 20° with respect to the vertical for the experiment described here.

For the analysis, the scattering pattern in Fig. 4(*b*) was divided into 500 radial bins and 45 azimuthal bins, and the signal in each bin was calculated as the average value of the pixels. The difference scattering signal corresponding to the radial bin centred at $Q = 2$ Å^{-1} (black circle) is plotted in Fig. 4(*d*) as a function of $P_2(\cos\theta_Q)$ at the same Q value. The red line is a least-squares fit of a straight line to the data points. This fit, according to equation (11), yields ΔS_2 ($Q = 2$ Å^{-1}) as the slope and ΔS_0 ($Q = 2$ Å^{-1}) as the intercept with the $P_2 = 0$ axis. Repeating the procedure for all the radial bins yields the one-dimensional isotropic and anisotropic difference scattering curves for the full Q range at this specific time delay, as Fig. 5 shows.

3. Results and discussion

Fig. 5 shows the isotropic and anisotropic difference scattering signals extracted from the scattering pattern measured at 4.5 ps as a function of Q. The uncertainty estimates for ΔS_0 and ΔS_2 at each Q point are calculated from the covariance matrix of the coefficients of the straight-line fit. Since the difference scattering signal is usually of the order of 0.1–1% of the total scattering signal [see comparison between Fig. S1 of the supporting information and Fig. 4(*b*) for this experiment], averaging several difference scattering patterns acquired at the same nominal time delay allows the improvement of the

S/N ratio before the extraction of the isotropic and anisotropic contributions. Experimental parameters such as the magnitude of the differential scattering cross section and the X-ray photon flux, as well as the number of radial bins considered for each 2D pattern, determine the optimum number of images to be averaged for a specific experiment. The number of radial bins should be higher than the number of independent data points in the Q range [$\sim$tens of points (Haldrup *et al.*, 2010)] and can be chosen arbitrarily high since re-binning can be done at a later stage of the analysis. For the present experiment, we set the number of radial bins to 500 and, for each time bin, we choose the number of images to be averaged by inspection of the decreasing uncertainties σ on the coefficients of the straight-line fit [ΔS_0 and ΔS_2 in equation (11)] as a function of number of averaged images. This is exemplified in Fig. 6(*a*) for the signal extracted at 4.5 ps: up to 50 averaged images, $\sigma_{\Delta S}$ decreases as the inverse square root of the number of averaged images, as expected for Gaussian noise; after 50 images, $\sigma_{\Delta S}$ converges to a constant value ($\sim$4 e.u. molec^{-1}) since the noise is then dominated by systematic errors due to contributions from a non-constant background and the non-linear response of the detector rather than counting statistics (van Driel *et al.*, 2015). Therefore averaging more than 50 images will not further decrease the uncertainties on the measured signal.

Fig. 6(*b*) shows the number of unique P_2 values that are sampled for a specific Q value as a function of the number of azimuthal bins into which the 2D diffraction patterns is divided. The plot shows that choosing an odd number of azimuthal bins maximizes the number of unique points available for the fitting of ΔS *versus* P_2. This behaviour arises from the dependency of P_2 on the azimuthal angle φ, as shown in Fig. 4(*c*), and from choosing equi-angular azimuthal bins. Moreover, since P_2 is non-linear as a function of φ, we introduce an error by calculating P_2 as the central value rather than the mean value in each azimuthal bin. This error can cause a significant decrease of the magnitude of the anisotropic difference scattering signal when decreasing the number of

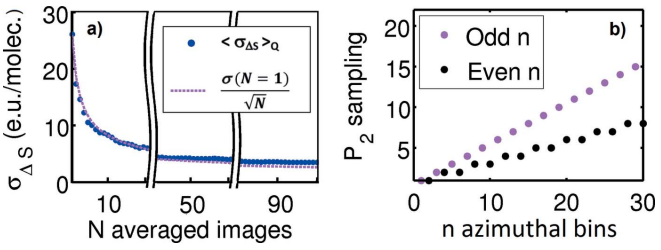

Figure 6
(*a*) Average of the uncertainties $\sigma(Q)$ on ΔS_2 over the full Q-range (500 radial bins) as a function of number of images averaged in the time bin centred at 4.5 ps. The uncertainties are estimated from the covariance matrix of the straight-line fit [equation (11)]. The dashed line shows that the magnitude of the uncertainties up to $\sim$50 averaged images follows the behaviour of counting noise expected for a Gaussian distribution ($\sigma \propto N^{-1/2}$). (*b*) Number of different P_2 values that are sampled as a function of number of azimuthal bins. This parameter is maximized if the number of azimuthal bins is odd.

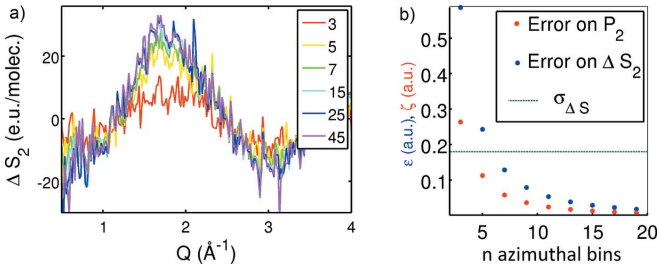

Figure 7
(*a*) Anisotropic difference scattering signals extracted from the 2D scattering patterns in Fig. 4(*d*) as a function of number of azimuthal bins. A significant decrease in the intensity of the signal is observed when decreasing the number of azimuthal bins below 5. (*b*) The red dots show the difference (ζ) between P_2 calculated as the central value in the azimuthal bins or as in equation (14): $\zeta = \langle P_2(\cos\theta_Q)\rangle_{2\delta\varphi} - P_2(\cos\theta_Q) = (3/4)\cos^2\theta\cos 2\varphi[1-(\sin 2\varphi/2\delta\varphi)]$. With respect to this, the blue dots show the resulting difference (ε) in the magnitude of ΔS_2 (at $Q = 2$ Å^{-1}): $\varepsilon = (\langle\Delta S_2\rangle_{2\delta\varphi} - \Delta S_2)/\langle\Delta S_2\rangle_{2\delta\varphi}$. The dashed black line shows the averaged experimental uncertainty $\sigma_{\Delta S_2}$ (divided by the measured signal).

azimuthal bins, as shown in Fig. 7(*a*). In order to calculate the mean value of P_2, we should use the following expression,

$$\langle P_2(\cos\theta_Q)\rangle_{2\delta\varphi} = \frac{1}{2\delta\varphi}\int_{\varphi-\delta\varphi}^{\varphi+\delta\varphi} P_2(\cos\theta,\cos\varphi)\,\mathrm{d}\varphi$$

$$= \frac{3}{4}\cos^2\theta\left(1-\frac{\sin 2\delta\varphi}{\delta\varphi}\cos 2\varphi\right)-\frac{1}{2}, \qquad (14)$$

where $\delta\varphi$ is half the size of the azimuthal bins. Fig. 7(*b*) shows the difference between the values of P_2 (red dots) and of the magnitude of ΔS_2 (blue dots) obtained when calculating P_2 either as the central or the mean value of the azimuthal bins. From this observation, if the 2D scattering pattern is divided into more than five azimuthal bins, such a difference is within the uncertainty of the measurements ($\sigma_{\Delta S}$, the dashed green line) and can therefore be neglected, thus simplifying the calculations.

Since the isotropic difference scattering signal arises from the changes in the radial distribution functions (RDFs) of the sample (Dohn *et al.*, 2015), ΔS_0 in Fig. 5 comprises contributions arising from the changes in the structure of the solute and of the solvation shells, as well as from the changes in temperature and density of the bulk solvent (Haldrup *et al.*, 2010; Kjaer *et al.*, 2013; Ihee *et al.*, 2010; Cammarata *et al.*, 2006). The anisotropic scattering signal in Fig. 5 arises from the changes in the structure of the solute and potentially anisotropic changes in the solvation shell structure. The anisotropic response of the bulk solvent is discussed at the end of the section and, in the case of water, its contributions are negligible at time scales longer than a few hundred femtoseconds after excitation. In this experiment, the signal arising from the changes in the structure of the solute ($\Delta S^{\mathrm{solute}}$) is strongly dominated by the contraction of the Pt—Pt bond due to the very electron-rich Pt atoms. As Fig. S2 shows, in the limited Q-range available for this experiment, possible contributions to $\Delta S^{\mathrm{solute}}$ arising from intramolecular changes

other than the Pt—Pt bond contraction are found within the uncertainties of the measured signal. Based on these considerations, we construct a modelling framework where the photoinduced structural changes in the structure of the solute are parametrized through a single structural parameter, $\Delta d_{\text{Pt-Pt}}$, which describes the changes in the Pt–Pt distance from the ground to the excited state of the molecule. Specifically, ΔS^{solute} is simulated from a set of structures derived by varying only the Pt–Pt distance of the density functional theory (DFT) optimized ground-state geometry of PtPOP. Details of the DFT calculations are provided in the supporting information. The full model used to fit the difference scattering signal measured at 4.5 ps after the photoexcitation of PtPOP is

$$\Delta S^{\text{model}}(Q, \Delta d_{\text{Pt-Pt}}) = \alpha \Delta S^{\text{solute}}(Q, \Delta d_{\text{Pt-Pt}}) + \beta \Delta S^{\text{cage}}(Q) + \Delta S^{\text{solvent}}(Q), \quad (15)$$

where the first term on the right-hand side is $\alpha_0 \Delta S_0^{\text{solute}}$, in the case of the isotropic signal, and $\alpha_2 \Delta S_2^{\text{solute}}$, in the case of the anisotropic signal. $\Delta S_0^{\text{solute}}$ and $\Delta S_2^{\text{solute}}$ are calculated using equations (9) and (10), respectively; α_0 and α_2 represent the fraction of excited-state molecules contributing to the isotropic and anisotropic scattering, respectively. ΔS^{cage} describes the changes in the structure of the solvation shells and β is a scaling factor. For the isotropic case, ΔS^{cage} was calculated from the RDFs of the solute–solvent atom pairs (Dohn *et al.*, 2015), as further described in the supporting information, while it was not necessary to include this term in the analysis of the anisotropic signal, given the good quality of the fit without the inclusion. Finally, $\Delta S^{\text{solvent}}$ describes the changes arising from the heating of the bulk water and its calculation is detailed in the supporting information. We note that, since the anisotropic signal is insensitive to the isotropic changes of the bulk solvent, fewer degrees of freedom are used in the description of the anisotropic data compared with the isotropic contribution. Equation (15) was fit to the measured difference scattering signal within a standard χ^2 minimization framework (Jun *et al.*, 2010). From a simultaneous fit of the isotropic and the anisotropic scattering signal, we find $\Delta d_{\text{Pt-Pt}} = 0.24 \pm 0.04$ Å, $\alpha_0 = 2.6 \pm 0.2\%$, $\alpha_2 = 1.5 \pm 0.2\%$. The black line in Fig. 5 shows the model constructed from the best-fit results, which well describe the data ($\chi^2 = 1.9$). $\Delta d_{\text{Pt-Pt}}$ is found in agreement with previous studies (Christensen *et al.*, 2009); the 1σ confidence interval on this parameter (0.04 Å) is found to be smaller than that obtained from fitting the isotropic and the anisotropic signals separately (which gives 1σ confidence intervals of 0.05 Å and 0.09 Å, respectively). Since changes in population fraction are not expected on these single-ps time scales (Gray *et al.*, 2017) and taking into account the decay of the anisotropic signal, as described below, we find that following the excitation event ~2.6% of the molecules have been photoexcited and contribute to the isotropic signal, and approximately 1.8 % contribute to the anisotropic scattering. We interpret this difference as an indication of multi-photon excitation of PtPOP, where the multi-photon excitation takes place through transitions where the dipole moment is not parallel to the Pt–Pt axis (Stiegman *et al.*, 1987). This combined analysis may further allow the disentanglement of the contributions to the difference scattering signal arising from structural changes parallel or perpendicular with respect to the transition dipole moment. Specifically to PtPOP, the structural changes contributing to ΔS_2 depend directly on their displacement with respect to the Pt–Pt axis (ξ_{ij} in Fig. 3): equation (10) is maximum (and positive) when $\xi_{ij} = 0°$ (*i.e.* when the structural change is displaced parallel to the Pt–Pt axis) and minimum (and negative) when $\xi_{ij} = 90°$ (*i.e.* when the structural changes occur in the plane perpendicular to the Pt–Pt axis). However, as detailed above, the difference scattering signal is mainly dominated by the Pt–Pt contraction, and this hinders the investigation of additional structural parameters in the analysis described here.

The magenta line in Fig. 5 shows the signal obtained from an azimuthal integration of the anisotropic contribution reprojected onto the detector surface $[\langle -P_2(\cos\theta_Q)\Delta S_2\rangle_\varphi]$. According to equation (11), this trace corresponds to the difference between the difference scattering signal obtained from an azimuthal integration of the 2D scattering pattern and the isotropic signal ($\langle \Delta S - \Delta S_0\rangle_\varphi$). For the PtPOP data, such a difference is found to be ~20% of the magnitude of the isotropic contribution at time delays immediately after the excitation event, where the anisotropy is most pronounced. These observations show that the azimuthally integrated signal, at time scales shorter than the rotational correlation time of the solute, may not be a good approximation of the scattering arising from an isotropic ensemble of photoexcited molecules. This implies that at such time scales the use of azimuthally integrated scattering signals in subsequent analysis should be justified by comparing S_0 and azimuthally integrated signals.

Following the procedure described above, the anisotropic difference scattering signals were extracted from measured difference scattering patterns up to 1 µs after photoexcitation of PtPOP (see Movie S1). Fig. 8 shows the decay of the

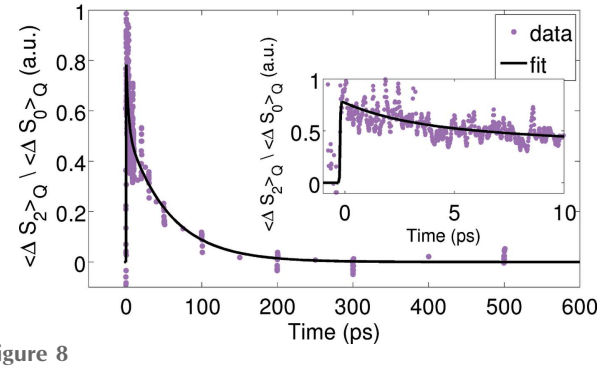

Figure 8
Ratio between the magnitudes (calculated as averages of the absolute values of the signal in the full Q-range) of the anisotropic and isotropic difference scattering signals as a function of pump–probe time-delay, up to 600 ps after the photoexcitation of PtPOP in water. A broadened bi-exponential decay is fit to the data (black line), with time constants of 3 ps ± 2 ps and 60 ps ± 10 ps. The latter is interpreted as the rotational correlation time of PtPOP in water.

anisotropy as a function of increasing pump–probe time delay. We find that 20% of the anisotropic contribution to the signal decays with a time constant of 3 ps ± 2 ps; while 80% decays with a time constant of 60 ps ± 10 ps. The latter is interpreted as the rotational correlation time of the PtPOP molecule in water. Using the Stokes–Einstein–Debye model (Horng *et al.*, 1997), the rotational correlation time of a sphere can be described as

$$\tau_{\rm r} = \frac{4\pi\eta r^3}{3k_{\rm B}T}, \qquad (16)$$

where η is the viscosity of water, $k_{\rm B}$ is the Boltzmann constant, T is the temperature and r is the radius of the sphere. Approximating the PtPOP molecule to a sphere, and taking r as half the longest inter-atomic distance in the PtPOP molecule (r = 4 Å), the rotational correlation time at room temperature can be estimated as 50 ps. This value is in agreement with the ∼60 ps found in this analysis.

Finally, we note that the neat solvent may exhibit anisotropic scattering independently of the photoexcited solute molecules: the laser pulse weakly perturbs the equilibrium structure of the solvent through non-resonant excitations predominantly aligned with the polarization of the laser, and the X-ray pulse probes the induced structural dynamics. Optically, the sample becomes birefringent, with different indices of refraction for light polarized parallel or perpendicular to the laser polarization axis. From an X-ray point of view, the scattering patterns are observed to be anisotropic and the analysis described above can be applied to extract the anisotropic scattering as a function of Q and time delay. The time evolution of the anisotropic X-ray scattering signal can be directly compared with the impulsive nuclear-coordinate response measured through techniques such as Raman-induced Kerr effect spectroscopy (Palese *et al.*, 1994; Castner *et al.*, 1995). Since the time scales of this nuclear response are known from optical Kerr effect studies, the anisotropic solvent scattering signal can be used to estimate the time-zero (the arrival time of the laser pulse at the sample) and the instrument response function (IRF) of the experiment (Biasin *et al.*, 2016). The separate determination of these parameters significantly improves the analysis of the isotropic part of the scattering signal, by reducing the number of free parameters in the model used to fit the data (Biasin *et al.*, 2016). This method of extracting the IRF and time-zero can be used as a diagnostic for any time-resolved XDS experiment on solvated molecules where the anisotropic solvent response can be clearly identified.

4. Conclusions

In summary, the formalism introduced by Baskin & Zewail (2006) and expanded by Lorenz *et al.* (2010) has been applied here to separate isotropic and anisotropic contributions from 2D difference scattering patterns measured upon photoexcitation of the solvated PtPOP molecule at an XFEL. The presented formalism has been directly implemented in quantitative structural analysis and we find that a combined analysis of the isotropic and anisotropic difference scattering signals helps the disentanglement of the many degrees of freedom involved in the structural response of the sample to photoexcitation and enhances the structural sensitivity. This analysis approach is generally applicable for all molecular systems with a well defined transition dipole moment and asymmetric structural response to photoexcitation, provided a time-resolution shorter than the rotational dephasing time. Furthermore, we have discussed how the quantitative analysis of the anisotropic scattering signal can provide access to anisotropic solvent dynamics induced by the linearly polarized pump pulse and how these measurements can lead to independent determination of time-zero and the IRF of the experiment. In conclusion, we have demonstrated a method that allows quantitative interpretation of anisotropic scattering signals measured at XFELs from aligned ensembles of molecules. The information delivered by this method can benefit the overall interpretation of high-content scattering data from solution-state molecular systems.

5. Related literature

The following references, not cited in the main body of the paper, have been cited in the supporting information: Bahn & Jacobsen (2002); Becke (1988); Che *et al.* (1983); Dohn *et al.* (2017); Enkovaara *et al.* (2010); Himmetoglu *et al.* (2012); Larsen *et al.* (2009, 2017); Lee *et al.* (1988); Maurer & Reuter (2011); Mortensen *et al.* (2005); Ozawa *et al.* (2003); Pinto *et al.* (1980). Sørensen & Kjaer (2013); Yasuda *et al.* (2004); Ziegler *et al.* (1977).

Acknowledgements

The authors would like to acknowledge the beamline scientists of the XPP Instrument at LCLS. Use of the Linac Coherent Light Source (LCLS), SLAC National Accelerator Laboratory, is supported by the US Department of Energy, Office of Science, Office of Basic Energy Sciences under Contract No. DE-AC02-76SF00515.

Funding information

Funding for this research was provided by: DANSCATT; Danish Council For Independent Research (grant No. DFF 4002-00272B to MMN, KBM, EB, MGL and AOD).

References

Bahn, S. R. & Jacobsen, K. W. (2002). *Comput. Sci. Eng.* **4**, 56–66.
Baskin, J. S. & Zewail, A. H. (2005). *ChemPhysChem*, **6**, 2261–2276.
Baskin, J. S. & Zewail, A. H. (2006). *ChemPhysChem*, **7**, 1562–1574.
Becke, A. D. (1988). *Phys. Rev. A*, **38**, 3098–3100.
Bennett, K., Kowalewski, M. & Mukamel, S. (2017). *Phys. Rev. Lett.* **119**, 069301.
Biasin, E., van Driel, T. B., Kjaer, K. S., Dohn, A. O., Christensen, M., Harlang, T., Chabera, P., Liu, Y., Uhlig, J., Pápai, M., Németh, Z., Hartsock, R., Liang, W., Zhang, J., Alonso-Mori, R., Chollet, M., Glownia, J. M., Nelson, S., Sokaras, D., Assefa, T. A., Britz, A.,

Galler, A., Gawelda, W., Bressler, C., Gaffney, K. J., Lemke, H. T., Møller, K. B., Nielsen, M. M., Sundström, V., Vankó, G., Wärnmark, K., Canton, S. E. & Haldrup, K. (2016). *Phys. Rev. Lett.* **117**, 013002.
Borfecchia, E., Garino, C., Salassa, L. & Lamberti, C. (2013). *Philos. Trans. R. Soc. London A*, **371**, 20120132.
Brinkmann, L. U. L. & Hub, J. S. (2015). *J. Chem. Phys.* **143**, 104108.
Burger, C., Hsiao, B. S. & Chu, B. (2010). *Polym. Rev.* **50**, 91–111.
Cammarata, M., Lorenc, M., Kim, T., Lee, J., Kong, Q., Pontecorvo, E., Lo Russo, M., Schiró, G., Cupane, A., Wulff, M. & Ihee, H. (2006). *J. Chem. Phys.* **124**, 124504.
Castner, E. W., Chang, Y. J., Chu, Y. C. & Walrafen, G. E. (1995). *J. Chem. Phys.* **102**, 653–659.
Che, C. M., Herbstein, F. H., Schaefer, W. P., Marsh, R. E. & Gray, H. B. (1983). *J. Am. Chem. Soc.* **105**, 4604–4607.
Chergui, M. & Collet, E. (2017). *Chem. Rev.* **117**, 11025–11065.
Chollet, M., Alonso-Mori, R., Cammarata, M., Damiani, D., Defever, J., Delor, J. T., Feng, Y., Glownia, J. M., Langton, J. B., Nelson, S., Ramsey, K., Robert, A., Sikorski, M., Song, S., Stefanescu, D., Srinivasan, V., Zhu, D., Lemke, H. T. & Fritz, D. M. (2015). *J. Synchrotron Rad.* **22**, 503–507.
Christensen, M., Haldrup, K., Bechgaard, K., Feidenhans'l, R., Kong, Q., Cammarata, M., Russo, M. L., Wulff, M., Harrit, N. & Nielsen, M. M. (2009). *J. Am. Chem. Soc.* **131**, 502–508.
Dohn, A. O., Biasin, E., Haldrup, K., Nielsen, M. M., Henriksen, N. E. & Møller, K. B. (2015). *J. Phys. B*, **48**, 244010.
Dohn, A. O., Jonsson, E. O., Levi, G., Mortensen, J. J., Lopez-Acevedo, O., Thygesen, K. S., Jacobsen, K. W., Ulstrup, J., Henriksen, N. E., Mller, K. B. & Jonsson, H. (2017). *J. Chem. Theory Comput.* Accepted.
Driel, T. B. van, Kjaer, K. S., Biasin, E., Haldrup, K., Lemke, H. T. & Nielsen, M. M. (2015). *Faraday Discuss.* **177**, 443–465.
Driel, T. B. van, Kjaer, K. S., Hartsock, R. W., Dohn, A. O., Harlang, T., Chollet, M., Christensen, M., Gawelda, W., Henriksen, N. E., Haldrup, K., Kim, K. H., Ihee, H., Kim, J., Lemke, H. T., Sun, Z., Sundström, V., Zhang, W., Zhu, D., Møller, K. B., Nielsen, M. M. & Gaffney, K. J. (2016). *Nat. Commun.* **7**, 13678.
Enkovaara, J., Rostgaard, C., Mortensen, J. J., Chen, J., Dułak, M., Ferrighi, L., Gavnholt, J., Glinsvad, C., Haikola, V., Hansen, H. A., Kristoffersen, H. H., Kuisma, M., Larsen, A. H., Lehtovaara, L., Ljungberg, M., Lopez-Acevedo, O., Moses, P. G., Ojanen, J., Olsen, T., Petzold, V., Romero, N. A., Stausholm-Møller, J., Strange, M., Tritsaris, G. A., Vanin, M., Walter, M., Hammer, B., Häkkinen, H., Madsen, G. K. H., Nieminen, R. M., Nørskov, J. K., Puska, M., Rantala, T. T., Schiøtz, J., Thygesen, K. S. & Jacobsen, K. W. (2010). *J. Phys. Condens. Matter*, **22**, 253202.
Esswein, A. J. & Nocera, D. G. (2007). *Chem. Rev.* **107**, 4022–4047.
Glownia, J. M., Natan, A., Cryan, J. P., Hartsock, R., Kozina, M., Minitti, M. P., Nelson, S., Robinson, J., Sato, T., van Driel, T., Welch, G., Weninger, C., Zhu, D. & Bucksbaum, P. H. (2016). *Phys. Rev. Lett.* **117**, 153003.
Glownia, J. M., Natan, A., Cryan, J. P., Hartsock, R., Kozina, M., Minitti, M. P., Nelson, S., Robinson, J., Sato, T., van Driel, T., Welch, G., Weninger, C., Zhu, D. & Bucksbaum, P. H. (2017). *Phys. Rev. Lett.* **119**, 069302.
Gray, H. B., Zli, S. & Vlek, A. (2017). *Coord. Chem. Rev.* **345**(Suppl. C), 297–317.
Haldrup, K., Christensen, M. & Meedom Nielsen, M. (2010). *Acta Cryst.* A**66**, 261–269.
Haldrup, K., Vankó, G., Gawelda, W., Galler, A., Doumy, G., March, A. M., Kanter, E. P., Bordage, A., Dohn, A., van Driel, T. B., Kjaer, K. S., Lemke, H. T., Canton, S. E., Uhlig, J., Sundström, V., Young, L., Southworth, S. H., Nielsen, M. M. & Bressler, C. (2012). *J. Phys. Chem. A*, **116**, 9878–9887.
Hensley, C. J., Yang, J. & Centurion, M. (2012). *Phys. Rev. Lett.* **109**, 133202.
Himmetoglu, B., Marchenko, A., Dabo, I. & Cococcioni, M. (2012). *J. Chem. Phys.* **137**, 154309.
Horng, M., Gardecki, J. A. & Maroncelli, M. (1997). *J. Phys. Chem. A*, **101**, 1030–1047.
Ihee, H., Wulff, M., Kim, J. & Adachi, S. (2010). *Intl Rev. Phys. Chem.* **29**, 453–520.
Jonas, D. M., Bradforth, S. E., Passino, S. A. & Fleming, G. R. (1995). *J. Phys. Chem.* **99**, 2594–2608.
Jun, S., Lee, J. H., Kim, J., Kim, J., Kim, K. H., Kong, Q., Kim, T. K., Lo Russo, M., Wulff, M. & Ihee, H. (2010). *Phys. Chem. Chem. Phys.* **12**, 11536–11547.
Kim, J., Kim, K. H., Kim, J. G., Kim, T. W., Kim, Y. & Ihee, H. (2011). *J. Phys. Chem. Lett.* **2**, 350–356.
Kim, J. G., Kim, K. H., Oang, K. Y., Kim, T. W., Ki, H., Jo, J., Kim, J., Sato, T., Nozawa, S., Adachi, S. & Ihee, H. (2015*b*). *J. Phys. B*, **48**, 244005.
Kim, K. H., Kim, J. G., Nozawa, S., Sato, T., Oang, K. Y., Kim, T. W., Ki, H., Jo, J., Park, S., Song, C., Sato, T., Ogawa, K., Togashi, T., Tono, K., Yabashi, M., Ishikawa, T., Kim, J., Ryoo, R., Kim, J., Ihee, H. & Adachi, S. (2015*a*). *Nature (London)*, **518**, 385–389.
Kjaer, K. S., van Driel, T. B., Kehres, J., Haldrup, K., Khakhulin, D., Bechgaard, K., Cammarata, M., Wulff, M., Sørensen, T. J. & Nielsen, M. M. (2013). *Phys. Chem. Chem. Phys.* **15**, 15003–15016.
Kong, Q., Lee, J., Plech, A., Wulff, M., Ihee, H. & Koch, M. (2008). *Angew. Chem. Int. Ed.* **47**, 5550–5553.
Küpper, J., Stern, S., Holmegaard, L., Filsinger, F., Rouzée, A., Rudenko, A., Johnsson, P., Martin, A. V., Adolph, M., Aquila, A., Bajt, S., Barty, A., Bostedt, C., Bozek, J., Caleman, C., Coffee, R., Coppola, N., Delmas, T., Epp, S., Erk, B., Foucar, L., Gorkhover, T., Gumprecht, L., Hartmann, A., Hartmann, R., Hauser, G., Holl, P., Hömke, A., Kimmel, N., Krasniqi, F., Kühnel, K., Maurer, J., Messerschmidt, M., Moshammer, R., Reich, C., Rudek, B., Santra, R., Schlichting, I., Schmidt, C., Schorb, S., Schulz, J., Soltau, H., Spence, J. C. H., Starodub, D., Strüder, L., Thøgersen, J., Vrakking, M. J. J., Weidenspointner, G., White, T. A., Wunderer, C., Meijer, G., Ullrich, J., Stapelfeldt, H., Rolles, D. & Chapman, H. N. (2014). *Phys. Rev. Lett.* **112**, 083002.
Lakowicz, J. R. (2006). *Principle of Fluorescence Spectroscopy*. Berlin: Springer.
Larsen, A. H., Mortensen, J. J., Blomqvist, J., Castelli, I. E., Christensen, R., Duak, M., Friis, J., Groves, M. N., Hammer, B., Hargus, C., Hermes, E. D., Jennings, P. C., Jensen, P. B., Kermode, J., Kitchin, J. R., Kolsbjerg, E. L., Kubal, J., Kaasbjerg, K., Lysgaard, S., Maronsson, J. B., Maxson, T., Olsen, T., Pastewka, L., Peterson, A., Rostgaard, C., Schiøtz, J., Schütt, O., Strange, M., Thygesen, K. S., Vegge, T., Vilhelmsen, L., Walter, M., Zeng, Z. & Jacobsen, K. W. (2017). *J. Phys. Condens. Matter*, **29**, 273002.
Larsen, A. H., Vanin, M., Mortensen, J. J., Thygesen, K. S. & Jacobsen, K. W. (2009). *Phys. Rev. B*, **80**, 195112.
Lee, C., Yang, W. & Parr, R. G. (1988). *Phys. Rev. B*, **37**, 785–789.
Lemke, H. T., Kjaer, K. S., Hartsock, R., van Driel, T. B., Chollet, M., Glownia, J. M., Song, S., Zhu, D., Pace, E., Nielsen, M. M., Benfatto, M., Gaffney, K. J., Collet, E. & Cammarata, M. (2017). *Nat. Commun.* **8**, 15342.
Lorenz, U., Møller, K. B. & Henriksen, N. E. (2010). *New J. Phys.* **12**, 113022.
Maurer, R. J. & Reuter, K. (2011). *J. Chem. Phys.* **135**, 224303.
Minitti, M. P., Robinson, J. S., Coffee, R. N., Edstrom, S., Gilevich, S., Glownia, J. M., Granados, E., Hering, P., Hoffmann, M. C., Miahnahri, A., Milathianaki, D., Polzin, W., Ratner, D., Tavella, F., Vetter, S., Welch, M., White, W. E. & Fry, A. R. (2015). *J. Synchrotron Rad.* **22**, 526–531.
Møller, K. B. & Henriksen, N. E. (2012). *Struct. Bond.* **142**, 185–212.
Mortensen, J., Hansen, L. & Jacobsen, K. W. (2005). *Phys. Rev. B*, **71**, 035109.
Ozawa, Y., Terashima, M., Mitsumi, M., Toriumi, K., Yasuda, N., Uekusa, H. & Ohashi, Y. (2003). *Chem. Lett.* **32**, 62–63.
Palese, S., Schilling, L., Miller, R. J. D., Staver, P. R. & Lotshaw, W. T. (1994). *J. Phys. Chem.* **98**, 6308–6316.

Penfold, T. J., Tavernelli, I., Abela, R., Chergui, M. & Rothlisberger, U. (2012). *New J. Phys.* **14**, 113002.
Philipp, H. T., Hromalik, M., Tate, M., Koerner, L. & Gruner, S. M. (2011). *Nucl. Instrum. Methods Phys. Res. A*, **649**, 67–69.
Pinto, M. A. F. D. R., Sadler, P. J., Neidle, S., Sanderson, M. R., Subbiah, A. & Kuroda, R. (1980). *J. Chem. Soc. Chem. Commun.* pp. 13–15.
Roundhill, D. M., Gray, H. B. & Che, C. M. (1989). *Acc. Chem. Res.* **22**, 55–61.
Sørensen, T. J. & Kjaer, K. S., (2013). *Solvent response in TRWAXS*, https://sites.google.com/site/trwaxs/.
Stiegman, A. E., Rice, S. F., Gray, H. B. & Miskowski, V. M. (1987). *Inorg. Chem.* **26**, 1112–1116.
Takeda, H., Cometto, C., Ishitani, O. & Robert, M. (2017). *ACS Catal.* **7**, 70–88.
Van Kleef, E. H. & Powis, I. (1999). *Mol. Phys.* **96**, 757–774.
Veen, R. van der, Milne, C., El Nahhas, A., Lima, F., Pham, V., Best, J., Weinstein, J., Borca, C., Abela, R., Bressler, C. & Chergui, M. (2009). *Angew. Chem. Int. Ed.* **48**, 2711–2714.
White, C. (1982). *Organometallic Chemistry*, Vol. 10, edited by E. W. Abel & F. G. A. Stone, pp. 315–350. The Royal Society of Chemistry.
Yang, J., Guehr, M., Shen, X., Li, R., Vecchione, T., Coffee, R., Corbett, J., Fry, A., Hartmann, N., Hast, C., Hegazy, K., Jobe, K., Makasyuk, I., Robinson, J., Robinson, M. S., Vetter, S., Weathersby, S., Yoneda, C., Wang, X. & Centurion, M. (2016*b*). *Phys. Rev. Lett.* **117**, 153002.
Yang, J., Guehr, M., Vecchione, T., Robinson, M. S., Li, R., Hartmann, N., Shen, X., Coffee, R., Corbett, J., Fry, A., Gaffney, K., Gorkhover, T., Hast, C., Jobe, K., Makasyuk, I., Reid, A., Robinson, J., Vetter, S., Wang, F., Weathersby, S., Yoneda, C., Centurion, M. & Wang, X. (2016*a*). *Nat. Commun.* **7**, 11232.
Yasuda, N., Uekusa, H. & Ohashi, Y. (2004). *Bull. Chem. Soc. Jpn*, **77**, 933–944.
Zewail, A. H. (2000). *Pure Appl. Chem.* **72**, 2219–2231.
Ziegler, T., Rauk, A. & Baerends, E. J. (1977). *Theor. Chim. Acta*, **43**, 261–271.
Zipp, A. P. (1988). *Coord. Chem. Rev.* **84**(Suppl. C), 47–83.

Supporting online information for: Anisotropy enhanced X-ray scattering from solvated transition metal complexes

Elisa Biasin,[a,b]* Tim B. van Driel,[a,f] Gianluca Levi,[c] Mads G. Laursen,[a] Asmus O. Dohn,[d] Asbjørn Moltke,[a] Peter Vester,[a] Frederik B. K. Hansen,[a] Kasper S. Kjær,[a,b,e] Tobias Harlang,[a] Robert Hartsock,[b] Morten Christensen,[a] Kelly J. Gaffney,[b] Niels E. Henriksen,[c] Klaus B. Møller,[c] Kristoffer Haldrup[a] and Martin M. Nielsen[a]

[a]*Department of Physics, Technical University of Denmark, Fysikvej 307, DK-2800 Kongens Lyngby, Denmark,* [b]*PULSE Institute, SLAC National Accelerator Laboratory, Menlo Park, California 94025, USA,* [c]*Department of Chemistry, Technical University of Denmark, Kemitorvet 207, DK-2800 Kongens Lyngby, Denmark,* [d]*Faculty of Physical Sciences, University of Iceland,* [e]*Department of Chemical Physics, Lund University, Box 118, S-22100 Lund, Sweden, and* [f]*Linac Coherent Light Source, SLAC National Accelerator Laboratory, Menlo Park, California 94025, USA. E-mail: elbia@fysiks.dtu.dk*

1. Additional Figures

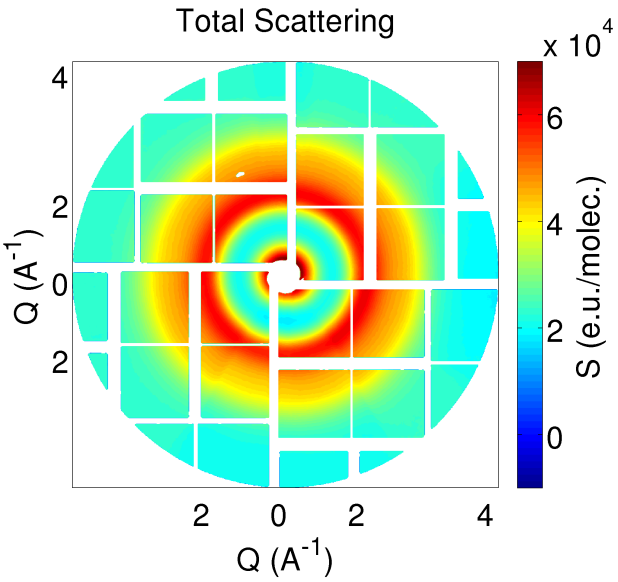

Fig. S1. Full X-ray scattering pattern arising from a 80 mM water solution of PtPOP, after corrections for X-ray polarization, solid angle coverage and masking. The magnitude of the difference scattering signal shown in the main article (Fig. 4b) is found $\sim$ 1 % of total scattering.

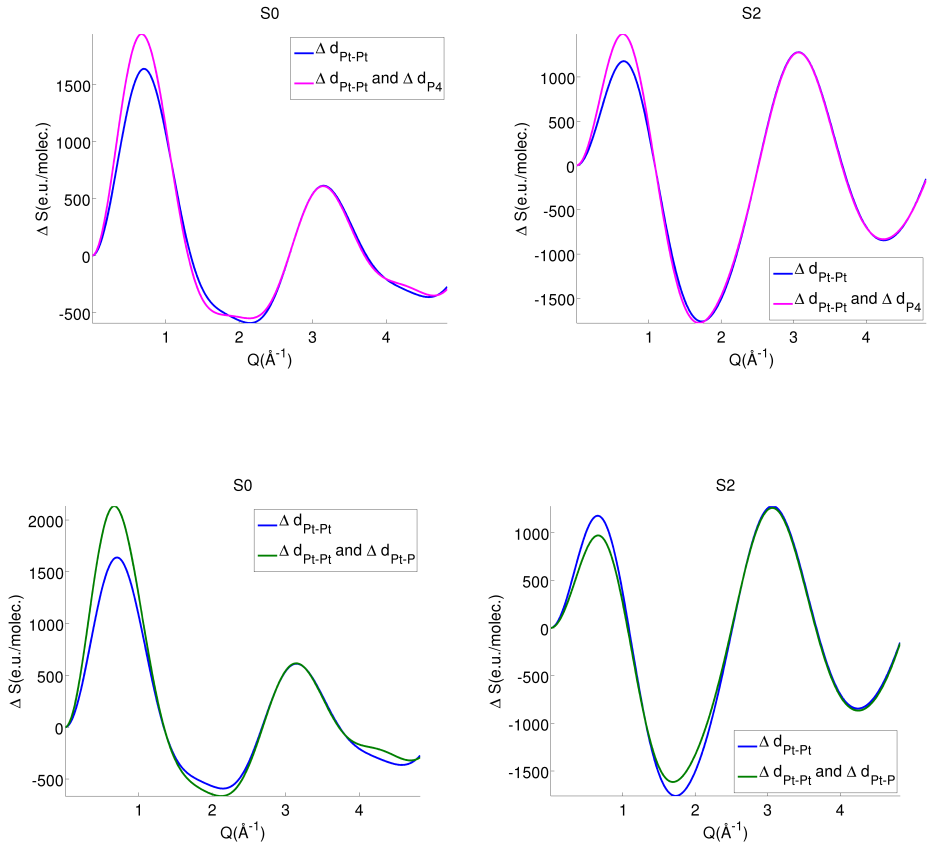

Fig. S2. **top)** Comparison between the isotropic (left) and anisotropic (right) difference scattering signals arising from a 0.25 Å contraction of the Pt-Pt bond (blue line) and from this contraction with an additional 0.04 Å contraction of the four-phosphorous planes (magenta line). This additional deformation involves mostly changes of intra-molecular distances that are parallel to the Pt-Pt axis and add a positive contribution to both the isotropic and anisotropic difference scattering signal. **bottom)** Comparison between the isotropic (left) and anisotropic (right) difference scattering signals arising from a 0.25 Å contraction of the Pt-Pt bond (blue line) and from this contraction with an additional 0.02 Å contraction of each Pt-ligand distance (green line). This additional deformation involves mostly changes of intra-molecular distances that are perpendicular to the Pt-Pt axis and add a positive contribution to the isotropic difference scattering signal and a negative contribution to the anisotropic signal, accordingly to Eq.10.

2. DFT calculations in vacuum

The set of molecular structures used to simulate the solute difference scattering signal (ΔS^{solute}) was obtained from a DFT-optimized geometry of ground state PtPOP by varying the Pt-Pt distance from 2.700 to 3.300 Å in steps of 0.001 Å while keeping all the other atoms fixed.

The geometry optimization was performed in the Atomic Simulation Environment (Bahn & Jacobsen, 2002; Larsen *et al.*, 2017) and employing the Grid-based Projector Augmented Wave (GPAW) DFT code (Mortensen *et al.*, 2005; Enkovaara *et al.*, 2010). The exchange-correlation functional was BLYP (Becke, 1988; Lee *et al.*, 1988), while a linear combination of atomic orbitals (LCAO) with tzp basis for Pt and dzp for the rest of the atoms was used to represent the Kohn-Sham wave functions (Larsen *et al.*, 2009). We employed a grid spacing of 0.18 Å. The geometry was optimized until the maximum force on all individual atoms was less than 0.02 eV/Å. A vibrational analysis using the finite difference method implemented in ASE was carried out on the optimized geometry to confirm that it is a true minimum of the potential energy surface. The resulting structure has approximate C_{4h} symmetry, and features a Pt-Pt distance of 3.005 Å. In comparison, the values found from X-ray crystallographic studies lie in the range 2.913-2.979 Å (Pinto *et al.*, 1980; Che *et al.*, 1983; Ozawa *et al.*, 2003; Yasuda *et al.*, 2004), while previous X-ray diffraction measurements in water solution delivered a Pt-Pt distance of 2.98 Å (Christensen *et al.*, 2008).

3. Simulation of ΔS^{cage} and $\Delta S^{solvent}$

ΔS^{cage} in Eq.15 is calculated from solute-solvent RDFs of QM/MM simulations performed in the ground and excited states, as detailed in the next section, and following the procedure described by Dohn *et al.* (Dohn *et al.*, 2015). $\Delta S^{solvent}$ in Eq.15 is

calculated as following:

$$\Delta S^{solvent}(Q) = \Delta T \frac{\partial S(Q)}{\partial T}\bigg|_{\rho}. \tag{S1}$$

where ΔT is the change in temperature and $\frac{\partial S(Q)}{\partial T}\Big|_{\rho}$ is the water solvent differential, that was measured in separate experiment and archived (Kjær *et al.*, 2013; Sørensen & Kjær, 2013). The fit of Eq.15 to the isotropic scattering signal in Fig.5(right) yields $\beta \sim 1.9$ % and $\Delta T \sim 0.28$ K.

4. QM/MM MD simulations

The solute-solvent RDFs for PtPOP in water were obtained from a previous QM/MM Born-Oppenheimer Molecular Dynamics (BOMD) investigation (Dohn *et al.*, 2017). The DFT level of theory and atomic orbital basis set used to the describe the complex were the same as those utilized here for the geometry optimization in vacuum. The ground state RDFs were calculated from 230000 MD frames spanning a total simulation time of around 460 ps. A detailed account of the QM/MM interfacing strategy, MM force field and MD protocol that were used in the QM/MM BOMD simulations is provided in (Dohn *et al.*, 2017). To compute the RDFs for PtPOP in the first singlet excited state, 99 excited-state QM/MM trajectories were started from uncorrelated frames of the equilibrium ground state trajectories collected in (Dohn *et al.*, 2017). In these simulations the excited state was described with a modified version of ΔSCF (Ziegler *et al.*, 1977) in the spin unpolarized formalism (Maurer & Reuter, 2011; Himmetoglu *et al.*, 2012). The method uses Gaussian smeared constraints of the orbitals occupation numbers (Maurer & Reuter, 2011) to achieve stable convergence of the density at each step of the dynamics and is implemented in a local version of GPAW. Time step and thermostatting scheme were the same as those used for the ground state equilibrium simulations in (Dohn *et al.*, 2017). Equilibrium excited-state RDFs were calculated from around 80000 MD snapshots, corresponding to 160 ps remaining

after having removed the non-equilibrated part of each trajectory.

References

Bahn, S. R. & Jacobsen, K. W. (2002). *Computing in Science & Engineering*, **4**, 55.

Becke, A. D. (1988). *Physical Review A*, **38**, 3098.

Che, C. M., Herbstein, F. H., Schaefer, W. P., Marsh, R. E. & Gray, H. B. (1983). *Journal of the American Chemical Society*, **105**(14), 4604–4607.

Christensen, M., Haldrup, K., Bechgaard, K., Feidenhans, R., Kong, Q., Cammarata, M., Russo, M. L., Wulff, M., Harrit, N., Nielsen, M. M., Kong, Q., Cammarata, M., Russo, M. L. & Wulff, M. (2008). *J. Am. Chem. Soc*, **131**(Ii), 502–508.

Dohn, A. O., Biasin, E., Haldrup, K., Nielsen, M. M., Henriksen, N. E. & Møller, K. B. (2015). *Journal of Physics B: Atomic, Molecular and Optical Physics*, **48**, 244010.

Dohn, A. O., Jonsson, E. Ö., Levi, G., Mortensen, J. J., Lopez-Acevedo, O., Thygesen, K. S., Jacobsen, K. W., Ulstrup, J., Henriksen, N. E., Møller, K. B. & Jonsson, H. (2017). *J. Chem. Theory Comput.* **JustAccepted**.

Enkovaara, J., Rostgaard, C., Mortensen, J. J., Chen, J., Dulak, M., Ferrighi, L., Gavnholt, J., Glinsvad, C., Haikola, V., Hansen, H. A., Kristoffersen, H. H., Kuisma, M., Larsen, A. H., Lehtovaara, L., Ljungberg, M., Lopez-Acevedo, O., Moses, P. G., Ojanen, J., Olsen, T., Petzold, V., Romero, N. A., Stausholm-Møller, J., Strange, M., Tritsaris, G. A., Vanin, M., Walter, M., Hammer, B., Häkkinen, H., Madsen, G. K. H., Nieminen, R. M., Nørskov, J. K., Puska, M., Rantala, T. T., Schiøtz, J., Thygesen, K. S. & Jacobsen, K. W. (2010). *Journal of Physics: Condensed matter*, **22**, 253202.

Himmetoglu, B., Marchenko, A., Dabo, I. & Cococcioni, M. (2012). *Journal of Chemical Physics*, **137**(15), 154309.

Kjær, K. S., van Driel, T. B., Kehres, J., Haldrup, K., Khakhulin, D., Bechgaard, K., Cammarata, M., Wulff, M., Sørensen, T. J. & Nielsen, M. M. (2013). *Physical Chemistry Chemical Physics*, **15**, 15003–15016.

Larsen, A. H., Mortensen, J. J., Blomqvist, J., Castelli, I. E., Christensen, R., Duak, M., Friis, J., Groves, M. N., Hammer, B., Hargus, C., Hermes, E. D., Jennings, P. C., Jensen, P. B., Kermode, J., Kitchin, J. R., Kolsbjerg, E. L., Kubal, J., Kaasbjerg, K., Lysgaard, S., Maronsson, J. B., Maxson, T., Olsen, T., Pastewka, L., Peterson, A., Rostgaard, C., Schitz, J., Schtt, O., Strange, M., Thygesen, K. S., Vegge, T., Vilhelmsen, L., Walter, M., Zeng, Z. & Jacobsen, K. W. (2017). *Journal of Physics: Condensed Matter*, **29**(27), 273002.

Larsen, A. H., Vanin, M., Mortensen, J. J., Thygesen, K. S. & Jacobsen, K. W. (2009). *Phys. Rev. B*, **80**, 195112.

Lee, C., Yang, W. & Parr, R. G. (1988). *Physical Review B*, **37**, 785–789.

Maurer, R. J. & Reuter, K. (2011). *Journal of Chemical Physics*, **135**(22), 224303.

Mortensen, J., Hansen, L. & Jacobsen, K. W. (2005). *Physical Review B*, **71**, 035109.

Ozawa, Y., Terashima, M., Mitsumi, M., Toriumi, K., Yasuda, N., Uekusa, H. & Ohashi, Y. (2003). *Chemistry Letters*, **32**(1), 62–63.

Pinto, M. A. F. D. R., Sadler, P. J., Neidle, S., Sanderson, M. R., Subbiah, A. & Kuroda, R. (1980). *J. Chem. Soc., Chem. Commun.* pp. 13–15.

Sørensen, T. J. & Kjær, K. S., (2013). Https://sites.google.com/site/trwaxs/.

Yasuda, N., Uekusa, H. & Ohashi, Y. (2004). *Bulletin of the Chemical Society of Japan*, **77**(5), 933–944.

Ziegler, T., Rauk, A. & Baerends, E. J. (1977). *Theoretica Chimica Acta*, **43**(3), 261–271.

Paper IV

PCCP

PAPER

Solvent control of charge transfer excited state relaxation pathways in [Fe(2,2′-bipyridine)(CN)$_4$]$^{2-}$†

Cite this: DOI: 10.1039/c7cp07838b

Kasper S. Kjær,*[abc] Kristjan Kunnus,[a] Tobias C. B. Harlang,[bc] Tim B. Van Driel,[d] Kathryn Ledbetter,[a] Robert W. Hartsock,[a] Marco E. Reinhard,[a] Sergey Koroidov,[a] Lin Li,[a] Mads G. Laursen,[b] Elisa Biasin,[b] Frederik B. Hansen,[b] Peter Vester,[b] Morten Christensen,[b] Kristoffer Haldrup,[b] Martin M. Nielsen,[b] Pavel Chabera,[c] Yizhu Liu,[ce] Hideyuki Tatsuno,[c] Cornelia Timm,[c] Jens Uhlig,[c] Villy Sundström,[c] Zoltán Németh,[f] Dorottya Sárosiné Szemes,[f] Éva Bajnóczi,[f] György Vankó,[f] Roberto Alonso-Mori,[d] James M. Glownia,[d] Silke Nelson,[d] Marcin Sikorski,[d] Dimosthenis Sokaras,[g] Henrik T. Lemke,[dh] Sophie Canton,[ij] Kenneth Wärnmark,[e] Petter Persson,[k] Amy A. Cordones[a] and Kelly J. Gaffney*[ag]

The excited state dynamics of solvated [Fe(bpy)(CN)$_4$]$^{2-}$, where bpy = 2,2′-bipyridine, show significant sensitivity to the solvent Lewis acidity. Using a combination of optical absorption and X-ray emission transient spectroscopies, we have previously shown that the metal to ligand charge transfer (MLCT) excited state of [Fe(bpy)(CN)$_4$]$^{2-}$ has a 19 picosecond lifetime and no discernable contribution from metal centered (MC) states in weak Lewis acid solvents, such as dimethyl sulfoxide and acetonitrile.[1,2] In the present work, we use the same combination of spectroscopic techniques to measure the MLCT excited state relaxation dynamics of [Fe(bpy)(CN)$_4$]$^{2-}$ in water, a strong Lewis acid solvent. The charge-transfer excited state is now found to decay in less than 100 femtoseconds, forming a quasi-stable metal centered excited state with a 13 picosecond lifetime. We find that this MC excited state has triplet (^{3}MC) character, unlike other reported six-coordinate Fe(II)-centered coordination compounds, which form MC quintet (^{5}MC) states. The solvent dependent changes in excited state non-radiative relaxation for [Fe(bpy)(CN)$_4$]$^{2-}$ allows us to infer the influence of the solvent on the electronic structure of the complex. Furthermore, the robust characterization of the dynamics and optical spectral signatures of the isolated ^{3}MC intermediate provides a strong foundation for identifying ^{3}MC intermediates in the electronic excited state relaxation mechanisms of similar Fe-centered systems being developed for solar applications.

Received 21st November 2017,
Accepted 15th January 2018

DOI: 10.1039/c7cp07838b

rsc.li/pccp

Introduction

Inorganic complexes are attractive candidates for solar energy applications due to their tunable electronic properties, which can be varied synthetically by changing the metal atom and ligand composition or structure. Molecular photosensitizers based on 4d and 5d transition metals, such as Ru and Ir, have been successfully implemented in photovoltaic applications due to their intense absorption, long-lived charge transfer excited states, and their ability to undergo reversible redox

[a] PULSE Institute, SLAC National Accelerator Laboratory, Stanford University, Menlo Park, California 94025, USA. E-mail: kaspersk@gmail.com, kgaffney@slac.stanford.edu
[b] Molecular Movies, Department of Physics, Technical University of Denmark, DK-2800, Lyngby, Denmark
[c] Department of Chemical Physics, Lund University, P.O. Box 12 4, 22100 Lund, Sweden
[d] LCLS, SLAC National Accelerator Laboratory, Menlo Park, California 94025, USA
[e] Centre for Analysis and Synthesis, Department of Chemistry, Lund University, P.O. Box 124, 22100 Lund, Sweden
[f] Wigner Research Centre for Physics, Hungarian Academy of Sciences, P.O. Box 49, H-1525 Budapest, Hungary
[g] SSRL, SLAC National Accelerator Laboratory, Menlo Park, California, 94025, USA
[h] SwissFEL, Paul Scherrer Institut, Villigen PSI 5232, Switzerland
[i] ELI-ALPS, ELI-HU Non-Profit Ltd., Dugonics ter 13, Szeged 6720, Hungary
[j] FS-ATTO, Deutsches Elektronen-Synchrotron (DESY), Notkestrasse 85, D-22607 Hamburg, Germany
[k] Theoretical Chemistry Division, Lund University, P.O. Box 124, 22100 Lund, Sweden

† Electronic supplementary information (ESI) available: A description of the sample preparation, the high fluence TA measurements, analysis of the slow time scale in the XES ground state recovery, timing diagnostics, data treatment and computational chemistry. See DOI: 10.1039/c7cp07838b

processes.[3] However, their cost and scarcity render them impractical for large-scale development.

Transferring the functionality of 4d and 5d transition metal complexes to the more abundant 3d transition metal centered systems motivates wide-ranging investigations targeting solar energy applications.[4] Solar energy applications benefit from long-lived metal-to-ligand charge-transfer (MLCT) excited states, but the majority of optically generated MLCT excited states in 3d transition metal complexes relax on the sub-ps timescale. A central challenge to extending the charge transfer excited state lifetimes in light harvesting complexes based on 3d transition metals is the weaker ligand field splitting of 3d complexes, relative to their 4d or 5d counterparts. The smaller ligand field splitting leads to ligand field excited states with lower energies than the optically bright charge transfer excited states that very efficiently quench the MLCT excited states. This deactivation reduces the MLCT lifetime of 3d transition metal complexes by orders of magnitude compared to their 4d and 5d analogs. For instance, ruthenium(II)-centered polypyridyl compounds are characterized by MLCT states with hundreds of nanoseconds to microseconds lifetimes,[5–9] the MLCT state of similar complexes with an isoelectronic iron(II) center undergoes spin crossover to a metal centered quintet (^{5}MC) state within hundreds of femtoseconds.[10–24]

Significant progress in the design of iron-centered molecular systems with extended MLCT lifetimes targeted at solar energy applications has been made recently and demonstrates the potential of suppressing internal conversion and intersystem crossing.[2,25–30] The synthetic strategy pursued with the most success for octahedral iron(II) complexes has been ligand selection for increased ligand-to-metal σ-donation, beyond that of typical polypyridyl ligands. Increased σ-donation leads to larger ligand field splitting and destabilization of the MC excited states relative to MLCT excited states. A range of strong σ donating N-heterocyclic carbene ligands have provided Fe-complexes with MLCT lifetimes ranging from ~300 fs to ~30 ps,[2,25,27,30,31] long enough to allow transfer of the ligand-localized electron for photovoltaic applications.[27,28]

The metal centered triplet (^{3}MC) excited state has recently been suggested to play a critical role in mediating the MLCT decay pathway in the cases of both Fe(II)-centered spin crossover complexes (short-lived, ~100 fs, MLCT states)[21,22] and MLCT complexes (long-lived, ~20 ps, MLCT states),[2,26,29,30] and has additionally been observed as a precursor for ligand dissociation following excitation of $[Fe(CN)_6]$.[4–32] Although still under debate,[18] much experimental and computational evidence supports the presence of a very short lived ^{3}MC transient state in the spin state transition dynamics to the relatively long lived ^{5}MC state.[20–22,33,34] In the cases where MLCT lifetimes are extended to the picosecond time scale, they decay without well characterized intermediates, thus preventing experimental identification of decay-mediating states. Quantum chemical and dynamics calculations for several such complexes do suggest that the MLCT lifetime is strongly influenced by the relative positions of the potential curves of the MLCT and ^{3}MC excited states.[2,26,29,35–38] Although the important role of the ^{3}MC state in facilitating the excited state decay of hexacoordinated Fe(II) complexes has been suggested, a metastable ^{3}MC state has yet to be cleanly isolated for these complexes. Therefore, it is difficult to assess the capacity of experimental methods to identify the role of ^{3}MC intermediates in the excited state dynamics of Fe-based systems.

A strong solvatochromic effect has been well-established for Fe- and Ru-centered cyano-polypyridyl complexes,[39–44] and has been ascribed to the interaction of high Lewis acidity solvents (such as water) with the N lone pair of the CN^- ligand. Here, we exploit the solvent-dependent electronic structure of $[Fe(bpy)(CN)_4]^{2-}$, illustrated in Fig. 1, to vary the relative energies of the MLCT and MC states with the intent of generating a metastable ^{3}MC. The choice of $[Fe(bpy)(CN)_4]^{2-}$ was motivated by previous transient optical measurements that demonstrate the loss of characteristic MLCT features from the excited state spectrum upon changing the solvent Lewis acidity.[45] This study clearly demonstrated the solvent dependence of the non-radiative relaxation in this complex, but did not have the time resolution to determine relaxation rates nor the ability to determine the MC excited state intermediate formed in water.[45] The use of such a chemically amenable system allows us to develop our current understanding of how metal–ligand bonding controls the internal conversion and intersystem crossing pathways in 3d transition metal complexes. In this regard, the solvatochromic $[Fe(bpy)(CN)_4]^{2-}$ mixed ligand complex provides an excellent model for addressing these fundamental questions in physical chemistry, as the degree of metal–ligand σ- and π-bonding interactions can be varied with the solvent. Steady-state measurements have shown this interaction to shift electron density on the cyanide ligand and increase the metal-to-ligand π back-donation for the water-solvated complex.[39,40,46] The highest occupied molecular

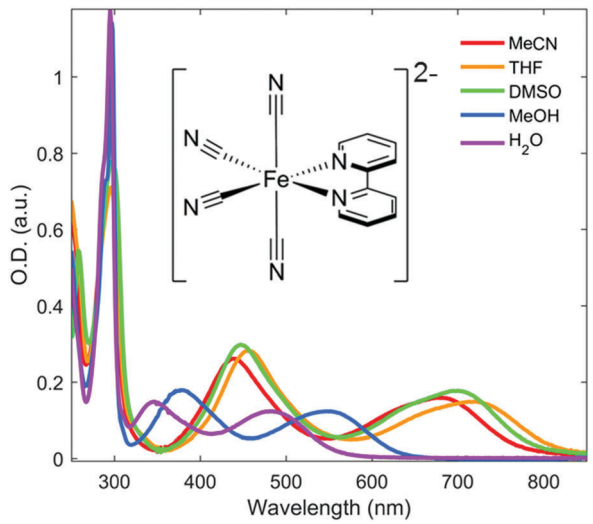

Fig. 1 Solvatochromism of $[Fe(bpy)(CN)_4]^{2-}$. The inset shows the $[Fe(bpy)(CN)_4]^{2-}$ system, and the rest of the panel shows its optical absorption spectrum in a series of solvents with varying Lewis acidity; acetonitrile (MeCN) tetrahydrofuran (THF), dimethyl sulfoxide (DMSO), methanol (MeOH), and water (H_2O).

orbitals (HOMO) of mixed Fe d (t_{2g}) and cyano π^* character are therefore stabilized relative to the lowest unoccupied molecular orbitals (LUMO) of bpy-ligand π^* character, resulting in a net destabilization of the respective MLCT excited state.[47] Experimental investigation of the solvent influence on the MC levels is significantly more scarce, but one study finds the trend of solvent-dependent excited state lifetimes for Ru cyano-polypyridyl complexes can be qualitatively reproduced under the assumption that the MC energy levels are unchanged relative to the ground state.[44]

To characterize the excited state dynamics of $[Fe(bpy)(CN)_4]^{2-}$ in water we have combined UV-visible pump–probe spectroscopy measuring the transient optical absorption (TA) with transient K-edge X-ray emission spectroscopy (XES), a combination which have delivered key insights in the dynamics of 3d transition metal centered systems before.[1,21,48–52] The signal recorded by TA arises from dipole-allowed transitions in the optical regime, rendering it sensitive to charge transfer excited states involving ligand-localized excited electrons. XES monitors the fluorescence emitted during the 2p-to-1s or 3p-to-1s decay following 1s core–hole ionization of the Fe metal center. The fluorescence intensity and spectral features are sensitive to the total spin moment on the iron center, and therefore, this method can distinguish MC excited states differing in Fe spin moments, such as ^{3}MC and ^{5}MC states. The combination of the two techniques enables full characterization of the excited state relaxation pathway of 3d transition metal complexes. The present study has unambiguously identified a metastable ^{3}MC excited state with the transient XES spectrum. This identification, in combination with the TA measurements enables the assignment of transient absorption features in the UV-visible spectrum to the ^{3}MC excited state that should prove valuable to the interpretation of electronic excited state relaxation dynamics in other Fe(II) systems.

We report the excited state dynamics of $[Fe(bpy)(CN)_4]^{2-}$ solvated in water and identify a temporally isolated ^{3}MC intermediate for the first time. In contrast, we have previously demonstrated a long lived MLCT excited state (19 ps) for $[Fe(bpy)(CN)_4]^{2-}$ in weak Lewis acidic solvents (dimethyl sulfoxide (DMSO) and acetonitrile (MeCN)), with no discernable contribution from metal centered states.[1] In the present work, we shift the bpy-localized MLCT state towards higher energy by using a high Lewis acidity solvent results in a faster MLCT-to-MC transition and slower MC-to-GS transition. The identification of a metastable ^{3}MC state provides further support for its role in deactivating MLCT excited states in Fe(II) complexes, and expands on the previously reported studies on Ru-centered systems which were unable to distinguish the influence of the solvent on the MC state energy levels.[44]

Experimental methods

X-ray emission

The time-resolved XES measurements were conducted at the X-ray Pump–Probe (XPP)[53] end station at the Linac Coherent Light Source (LCLS). An aqueous solution of 55 mM $[Fe(bpy)(CN)_4]^{2-}$ was pumped through a 50 μm diameter nozzle producing a cylindrical liquid jet. The sample was excited with 400 nm optical laser pulses of 45 fs duration, 120 μm focus diameter (FWHM), and 12.5 μJ per pulse, delivering a pulse fluence of 3×10^{12} W cm^{-2}. The sample was probed by 8.5 keV X-ray laser pulses of ~30 fs duration. The Fe 3p-1s (Kβ) fluorescence XES signal was detected on a 140k Cornell-SLAC Pixel Array Detector (CSPAD) area detector[54] located above the liquid jet using four dispersive Ge(620) crystal analyzers with a central Bragg angle of 79.1 degrees.[55] The Fe 2p-1s (Kα) fluorescence XES signal was detected on a second 140k CSPAD detector placed behind the sample, using a spherically bent Ge(440) crystal analyzer, set to a Bragg angle corresponding to the maximum signal of the iron Kα fluorescence of 6404 eV (75.4 degrees).

The full 2D images of the XES detectors were read out for each pump–probe event, normalized, and corrected as described in the ESI.† Difference images were constructed by subtracting a reference signal recorded from optical laser-off probe events for every seventh X-ray laser pulse event throughout the data collection. The difference images of each pump–probe event were then sorted into 250 individual time bins (400 shots per bin) according to their individually recorded time delay (see the ESI,† for a description of the timing tool diagnostic). The Kα difference images for each time bin were averaged and integrated, resulting in the kinetic trace presented in Fig. 5, while the Kβ difference images of each time bin were averaged and integrated along the nondispersive detector axis, resulting in the difference spectra presented in Fig. 6A.

The static Kα XES spectra of reference compounds were measured at the Stanford Synchrotron Radiation Lightsource (SSRL) beamline 6-2. Reference compounds were obtained from Sigma-Aldrich and used as-is. Samples were measured as powders (covered by Kapton tape) in a cryostat at 10 K. Samples were excited with monochromatic incident X-rays at 7300 eV (double-crystal Si(311) monochromator, 0.2 eV FWHM bandwidth) and Fe Kα fluorescence was detected with a Rowland geometry spectrometer utilizing (440) Bragg reflection from bent Ge crystals with a 1 m radius of curvature (energy resolution 0.6 eV FWHM).[56] X-rays were detected with a Si drift detector and a correction for detector nonlinearity was applied. The monochromator energy was calibrated with an Fe foil and the spectrometer calibration and transmission correction was done using elastic scattering. Each sample was checked for X-ray induced damage by measuring the Fe X-ray absorption near-edge structure (XANES) spectra at various incident fluxes using filters installed in the beamline. Each sample was measured multiple times at different positions to reduce exposure.

Optical transient absorption

Femtosecond time-resolved UV-visible transient absorption (TA) measurements were conducted on $[Fe(bpy)(CN)_4]^{2-}$ samples in H_2O (7 mM) and DMSO (2 mM), prepared directly before the experiments. Liquid sheet jets with 100 μm and 200 μm thicknesses were used to deliver the sample into the pump–probe overlap region, respectively. Continuous flow of the jet

ensured that any accumulation of photo-damaged sample was avoided.

Experiments were carried out using an amplified Ti:sapphire laser system (Coherent Mantis with Coherent Legend Elite Duo) with a 5 kHz repetition rate, 800 nm central wavelength, 2 mJ pulse energy and 40 fs FWHM pulse duration. A portion of the laser pumped an optical parametric amplifier (Spectra-Physics OPA-800C) to generate near IR signal and idler *via* difference frequency mixing. The output of the OPA was used to generate 500 nm pump pulses *via* sum-frequency generation of the signal with 800 nm light, and to generate 700 nm pump pulses *via* frequency doubling of the signal in a BBO crystal. The pump pulse was directed to the sample through a delay stage, a 2.5 kHz chopper, and a lens, resulting in pump pulses with 100 μm focus diameter (FWHM), 50 fs duration, and 1.6 μJ pulse energy providing a pump fluence of 4×10^{11} W cm^{-2}. The pump was overlapped with a white light probe pulse (*via* supercontinuum generation in 4 mm of CaF_2) at the sample position. The probe was transmitted through the sample and imaged on a spectrometer (Horiba Jobin Yvon iHR320, grating 150 grooves per mm). The probe spectrum was recorded at 5 kHz with a NMOS linear image sensor (Hamamatsu, S8380-512Q) simultaneously over the whole 300–700 nm spectral range. The differential absorbance (ΔA) was calculated as $\Delta A = \log(I_{off}/I_{on})$, where I_{on} and I_{off} are the pumped and unpumped intensity, respectively. Overall time-resolution of the experiment was approximately 100 fs.

Results and discussion

Steady-state and transient optical absorption spectroscopy

The steady-state optical absorption spectrum of $[Fe(bpy)(CN)_4]^{2-}$ in a series of solvents is presented in Fig. 1. In weak Lewis acid solvents (acetonitrile (MeCN, red), tetrahydrofuran (THF, orange), and dimethyl sulfoxide (DMSO, green)) the visible spectrum is characterized by two absorption features at roughly 450 nm and 700 nm assigned to MLCT excitations from orbitals of mixed Fe d and cyano π and π* character to π* orbitals of the bipyridine ligand.[57] For high Lewis acidity solvents, such as the hydrogen-bonding methanol (MeOH, blue) and H_2O (purple), these absorption features blue-shift. This solvatochromic effect has been extensively mapped for cyano-polypyridyl Fe and Ru complexes and shown to be linear, both with respect to the solvent acceptor number (a measure of the Lewis acidity) and the number of cyano ligands present.[39,40,42,57] This makes $[Fe(bpy)(CN)_4]^{2-}$ in solution an archetypical system to characterize the influence of the solvent Lewis acidity on the properties of these complexes.

The blue-shift of the MLCT absorption band clearly shows that increasing solvent Lewis acidity strongly destabilizes the MLCT state with respect to the ground state. To investigate how the solvent influences the energy levels of the MC states, and to determine how this modifies the MLCT deactivation pathways, we turn to the solvent dependence of the excited state relaxation dynamics.

Fig. 2 shows the solvent-dependent differential absorption spectra of $[Fe(bpy)(CN)_4]^{2-}$ obtained after excitation of the lowest energy MLCT transition (700 nm in DMSO, 500 nm in water). In DMSO (Fig. 2A), the differential spectra at all time delays are characterized by the ground state bleach (GSB), overlaid with a broad excited state absorption (ESA) feature everywhere below 600 nm, peaking at 370 nm and 525 nm. In bipyridine-containing complexes, the strong 370 nm ESA feature is typically associated with an excited electronic state having an electron localized on the pyridyl ligand.[1,2,23,58,59] In previous work, we have complemented such TA measurements by Kβ XES, determining that the excited state dynamics are well-described by a 19 ps single-exponential decay of a bipyridine-localized MLCT state.[1] In water (Fig. 2B), the difference spectra at very early time delays (~100 fs) can also be described by the GSB overlaid by a similar ESA feature

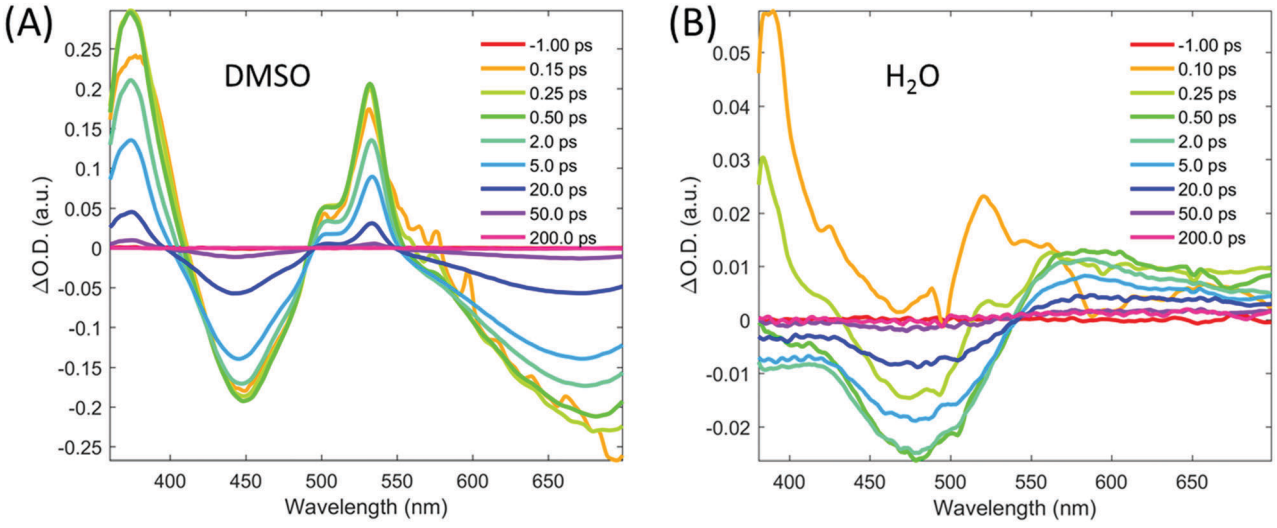

Fig. 2 Transient absorption spectra of $[Fe(bpy)(CN)_4]^{2-}$ at selected time delays in (A) DMSO with 700 nm excitation and (B) water with 500 nm excitation.

everywhere below 600 nm, peaking at 370 nm and 525 nm. However, within half a picosecond, the initial ESA features decay completely. Differential spectra at time delays longer than 0.5 ps are characterized by the GSB and a broad ESA feature above 600 nm. These features decay together over the following 50 ps as the ground state spectrum recovers. For $[Fe(bpy)(CN)_4]^{2-}$ in water, the ultrafast appearance and decay of the 370 nm ESA feature without the decay of the ground state bleach indicates that the excitation of the MLCT band initially populates a very short-lived bipyridine-localized MLCT state, which decays to a secondary electronic excited state before returning to the ground state on the tens of picosecond time scale. As described in the ESI,† high excitation fluencies lead to a longer lived absorption feature centered at 680 nm characteristic of the solvated electron[60] arising from multiphoton ionization.

From the optical data presented in Fig. 2B, the excited state cascade in aqueous solution can be formulated as an instantaneous generation of an MLCT state and a small fraction (<0.01) of photoionization products. The MLCT state undergoes ultrafast conversion to a second excited state which decays on the picosecond timescale, while the photoionization product remains. When this three-state model is implemented in a global analysis framework and applied to the data, the species associated spectra (SAS) shown in Fig. 3 are identified. SAS1, which we associate with the MLCT state, decays with a 0.17 ± 0.03 ps lifetime. SAS2, which we associate with the second excited electronic state, decays with a lifetime of 12.7 ± 0.4 ps. SAS3, which we associate with the solvated electrons remains within the 1 ns time window of these measurements.

To facilitate the direct comparison of the excited state dynamics measured with TA at low fluence to those measured by XES at higher fluence, we have applied the same analysis to additional TA measurements recorded at higher fluence, which exhibit a significant contribution from solvated electrons. The transient spectra and resulting SAS are shown in the ESI.† The spectral features of the photoexcited states (SAS1 and SAS2) are virtually identical between the high and the low fluence measurements, and the variation in the extracted relaxation dynamics lies within the uncertainties of the measurements. This demonstrates that the decay pathway of the single-photon MLCT non-radiative relaxation is independent of the excitation conditions over a large range of pump fluence.

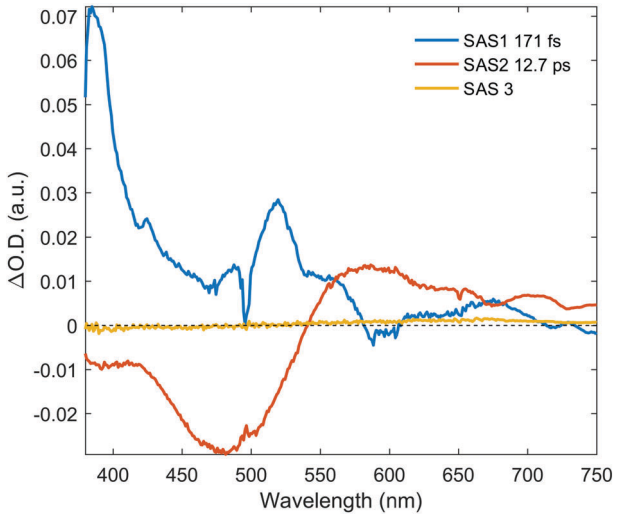

Fig. 3 Species associated spectra (SAS) from a global analysis of the transient absorption data for $[Fe(bpy)(CN)_4]^{2-}$ dissolved in water and shown in Fig. 2B.

Assigning the nature of the second electronic excited state associated with SAS2 in the global analysis is difficult based on optical TA data alone. The broad and relatively weak >600 nm ESA is the only significant spectral feature outside the ground state bleach. This ESA lacks significant or defining features that might otherwise allow assignment of the associated species. The short lifetime and complete ground state recovery rules out ionization and degradation products as candidates for SAS2. The lack of low-lying unoccupied ligand-centered electronic states (other than the bipyridine π^* states) suggests that SAS2 describes a secondary excited state with MC character. To unambiguously determine the nature of this intermediate, we turn to the transient Kα and Kβ XES measured at the LCLS X-ray free-electron laser.

Transient X-ray emission spectroscopy

Kα and Kβ XES monitors the 2p-to-1s and 3p-to-1s fluorescence, respectively, following 1s core–hole X-ray ionization. The strong influence of the exchange interaction between the *n*p and the 3d valence electrons make the XES spectra sensitive to the total spin multiplicity on the iron center.[56,61–64] The spin-sensitivity of the two techniques is illustrated by the reference spectra shown in Fig. 4A and B. The reference spectra are measured for a series of Fe-centered compounds with ground state electronic structure similar to those of the potential excited states of $[Fe(bpy)(CN)_4]^{2-}$. By selecting reference compounds with ligand bond covalency similar to $[Fe(bpy)(CN)_4]^{2-}$, good agreement between the reference spectra and the measured data is expected. By subtracting the reference signal of the ground state compound, from the references for the potential excited states, the reference difference spectra, illustrated in Fig. 4C and D can be constructed.

The Kβ spectra exhibit the clearest spectral shape variation between different electronic states, such that direct comparison between transient Kβ data and reference difference spectra allows for robust identification of the excited electronic states. Meanwhile, the Kα emission is roughly an order of magnitude more intense than the Kβ emission, which makes the Kα data well suited to derive the time scales of the underlying relaxation dynamics. Based on these considerations, we have measured Kα single-energy kinetics to determine the characteristic time scales of the experiment (time-zero, instrument-response function (IRF), and lifetimes), and measured full Kβ transient spectra for robust excited state identification. Since the Kα and Kβ data were recorded simultaneously, the time zero, temporal resolution, and quantum yields of the two datasets are identical. Therefore, the characteristic time constants of the experimental parameters, as well as the excited state lifetimes,

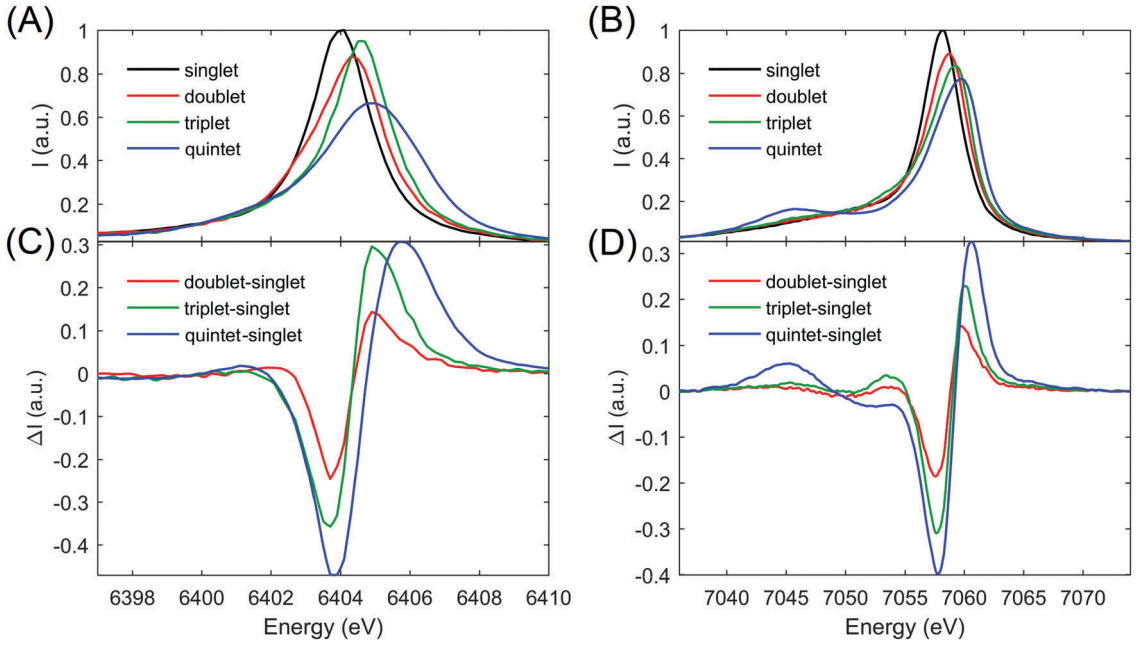

Fig. 4 $K\alpha_1$ (A) and Kβ (B) reference spectra measured for a series of Fe model complexes of similar spin state configuration as the potential excited states in this study. Kα references are $[Fe(bpy)(CN)_4]^{2-}$ (singlet), $[Fe(CN)_6]^{3-}$ (doublet), Fe(phthalocyanine) (triplet), and $[Fe(1,10\text{-phenanthroline})_2(NCS)_2]$ (quintet). Kβ references are taken from Zhang *et al.*[1] Reference difference spectra (C and D) constructed from the Kα and Kβ references generated by subtracting the ground state reference from each of the excited state references.

determined from the high signal-to-noise Kα kinetic data can be used in a global analysis framework for the Kβ spectral data.

The Kα kinetics shown in Fig. 5 were recorded at 6404 eV. As reported elsewhere,[62] and seen from the reference difference spectra (Fig. 4C), the Kα difference intensity at 6404 eV allow us to monitor the total spin increase on the Fe center. We observe

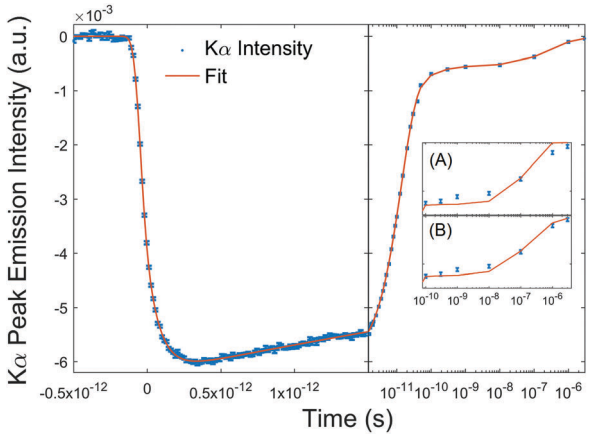

Fig. 5 Kinetics of the $K\alpha_1$ peak emission intensity measured at 6404 eV following MLCT excitation of $[Fe(bpy)(CN)_4]^{2-}$ in water. Blue data points are binned in 10 fs steps and supplied with error bars indicating the standard error. The red curve shows the fit of the data as described in the main text. Insets (A) and (B) show fits to the late data points using first and second order reaction kinetics, respectively. The second order reaction kinetics (B), capture the evolution of the data better, illustrating that the kinetics are due to charge-recombination of photoionized $[Fe(bpy)(CN)_4]^{-}$ with solvated electrons, as described in detail in the ESI.†

that the growth of the transient signal is delayed with respect to a broadened Heaviside step function. This delay arises from an excited state relaxation that results in a secondary increase in the Fe spin-moment, delayed with respect to excitation of the MLCT state. Overall, the growth is best described by the sum of a Heaviside step function and exponential grow-in broadened by a Gaussian representing the instrument-response function. The step function accounts for the instantaneously populated ^{1}MLCT and photoionization products.[65,66] These species each have a single unpaired electron on the Fe center, making them formal doublets with respect to the Fe center, and therefore they cannot be distinguished with the XES data. The exponential growth accounts for the transition from the MLCT to the secondary excited state of higher spin-moment. The fact that the Fe spin-moment increases for the secondary excited state confirms the assumption, based on the optical TA data, that the decay of the MLCT state leads to the population of an MC state with higher spin. The decay of the transient Kα signal is dominated by the single-exponential lifetime of the secondary MC excited state, but also includes a weaker long time-scale component for the recovery of the photoionization products.

In fitting the data to the kinetic model described above, a time-zero and IRF (rms) of -54 ± 4 fs and 34 ± 2 fs are recovered, with the uncertainty reflecting the standard deviation. The exponential component of the growth accounts for a $40 \pm 4\%$ increase of the total signal and has a time constant of 87 ± 5 fs, which we assign to the MLCT-to-MC transition. The decay is dominated by a component with a 13.1 ± 0.4 ps lifetime, readily assigned to the decay of the MC state and recovery of the ground state accounting for 84% of the decay.

The remaining decay of the transient signal occurs on the hundreds-of-nanoseconds to microsecond time scale. The MLCT-to-MC transition observed by the XES is faster than the lifetime associated with SAS1 in the TA analysis. This discrepancy likely reflects the challenge of differentiating intramolecular vibrational relaxation and population decay in TA, combined with the challenges of properly subtracting out cross-phase modulation artefacts.

The long time scale dynamics of the ground state recovery matches the expected second-order kinetics (as described in the ESI†) for the recovery from the photoionized $[Fe(bpy)(CN)_4]^-$.[60] Comparative fits to the long time delay data using first- and second order rate expressions for the decay are illustrated in Fig. 5 as insets (A) and (B), respectively. A detailed discussion of the mechanism and time scale of the recovery can be found in the ESI.† The increased ratio of photoionization product (16%) compared to the TA data is due to the increased laser power used for the XES experiments.

In summary, the Kα decay kinetics can be described by the same model used to interpret the TA data. Since the TA experiment shows that the dynamics of the single-photon excited state pathway is independent on the amount of two-photon excitation, the XES data can be used to identify the spin state of the 13 ps MC intermediate associated with SAS2 in the TA analysis. For this excited state identification, we rely on the Kβ data recorded simultaneously with the Kα data.

Transient Kβ differential spectra measured at multiple time delays are presented in Fig. 6A. Qualitative comparison of the data recorded at 0.5–5 ps (delays dominated by the MC intermediate) with the reference spectra in Fig. 4D reveals that the Kβ′ shoulder at 7045 eV is very weak. This allows the high spin ^{5}MC state to be eliminated as the dominant product of the MLCT decay and makes a ^{3}MC the most likely candidate for the MC excited state. To explicitly identify the nature of the MC state and derive excitation and speciation fractions, we have conducted a global analysis of the transient Kβ data using a three-state model that includes the MLCT state, the MC state, and the $[Fe(bpy)(CN)_4]^-$ photoproduct. Using the excited state cascade and time scales from the Kα analysis, the species associated spectra (SAS) for the excited states were extracted.

The extracted SAS are shown in Fig. 6B. SAS1 describes the signal that is lost with the 85 fs time constant after the excitation. SAS2 describes the signal that grows in as SAS1 decays, and has a lifetime of 13.1 ps. SAS1 was definitively identified as an MLCT state from the optical TA, and could therefore be used to establish a scaling factor between the SAS and reference difference spectra by minimizing the chi-squared between SAS1 and the MLCT (doublet–singlet) reference difference signal. Upon establishing this scaling factor, a quantitative comparison of SAS2 (representing the MC excited state) can be made against the triplet and quintet reference difference spectra (all plotted in Fig. 6B). It is immediately apparent that the signal shape, and in particular signal amplitude, of SAS2 matches the reference spectrum obtained for the ^{3}MC state. Taken together with the lack of additional fast time constants in the excited state cascade, the agreement between SAS2 and the ^{3}MC reference difference spectrum definitively assigns the ultrafast interconversion observed in the optical TA and Kα data to an MLCT-to-^{3}MC interconversion. Furthermore, the spectral features of SAS2 in the optical TA analysis can now be assigned as characteristic of the ^{3}MC state. The ultrafast XES measurements provide a robust assignment of the ^{3}MC state, which enables the interpretation of the ESA seen in the optical pump–probe measurement. The most significant feature of the spectrum is the excited state absorption feature at 570 nm, to the red side of the ground state bleach. Similar, but somewhat weaker, ESA features have been observed for ^{3}MC states assigned of Ru-centered polypyridyl complexes.[67]

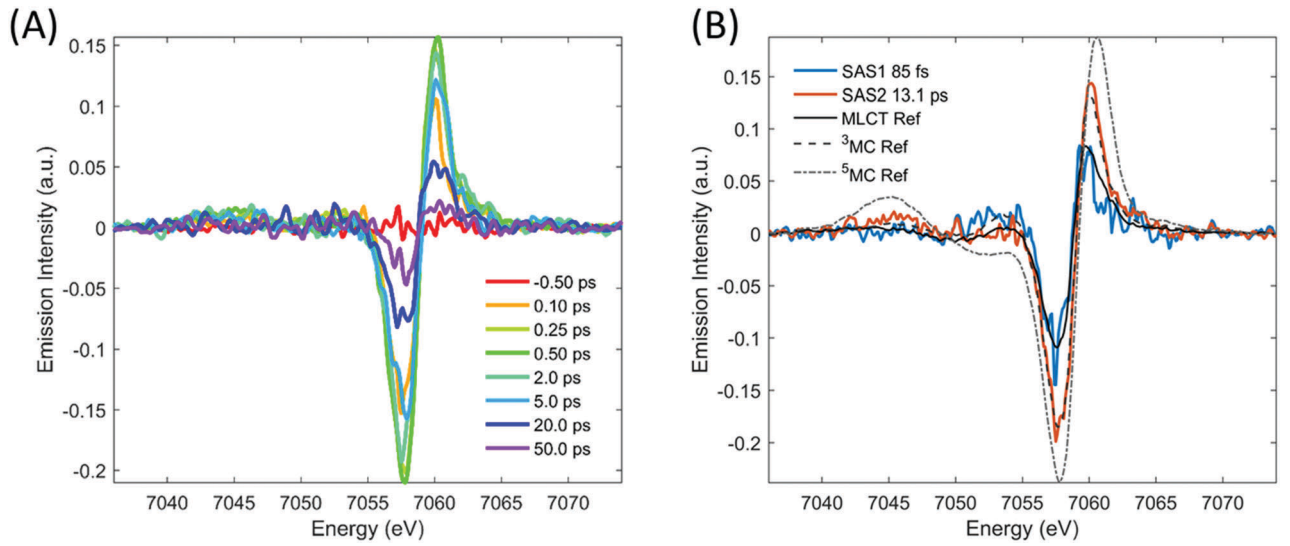

Fig. 6 Transient Kβ spectra and analysis. (A) Transient Kβ emission signal of $[Fe(bpy)(CN)_4]^{2-}$ in water. (B) Species associated spectra (SAS, red and blue) from a global analysis, invoking the model used for fitting the TA and Kα kinetics and the reference difference spectra of Fig. 2D scaled by mapping the MLCT reference to SAS1.

Solvent-dependent electronic structure

The solvent Lewis acidity strongly influences the excited state dynamics of $[Fe(bpy)(CN)_4]^{2-}$. Increasing solvent Lewis acidity leads to rapid excited state interconversion of the otherwise relatively long lived MLCT state. Furthermore, the ^{3}MC intermediate, which is expected to govern the MLCT decay, is stabilized to the point where it can be considered a well-isolated intermediate in the non-radiative relaxation. These changes in excited state dynamics reflect the solvent-dependent changes in the electronic structure of $[Fe(bpy)(CN)_4]^{2-}$. A qualitative molecular orbital (MO) diagram of $[Fe(bpy)(CN)_4]^{2-}$ in weak Lewis acid solvent is shown in Fig. 7A. Both t_{2g} and e_g levels of the cyano-pyridyl complex increase upon substitution of bpy with CN^- ligands, as demonstrated by the reduction in the metal oxidation potential, the reduction in the MLCT excitation energy, and the elimination of the quintet state from the excited state relaxation pathway.[1,2,39,44] These energetic changes in the redox potentials are readily explained by the σ and π* energy levels of the CN^- ligand being of higher than the σ and π* levels of bpy, as illustrated schematically in Fig. 7A. This MO picture is consistent with the projected potential energy surfaces (PES), calculated for $[Fe(bpy)(CN)_4]^{2-}$ in DMSO, which are illustrated in a schematic form in Fig. 7B, based on the calculations in Zhang *et al.*[1]

Increasing solvent Lewis acidity leads to a blue-shift of the MLCT absorption bands, as shown in Fig. 1. A similar solvation response has also been observed for Ru-centered cyano-pyridyls, where the solvent-dependent blue-shift has been shown to increase linearly with both the number of CN^- ligands and the Lewis acidity of the solvent.[39] The blue-shift is interpreted as a result of the high Lewis acidity solvent shifting electron density of the CN^- orbitals away from the metal center, decreasing the $\pi(CN^-) \rightarrow d(Fe)$ π-bonding and increasing the $d(Fe) \rightarrow \pi^*(CN^-)$ π-backbonding. Both of these changes stabilize the Fe t_{2g} levels relative to the (poly)pyridyl centered π* levels (which are relatively unaffected by solvation).

The influence of lowering the t_{2g} levels on the PES is illustrated in Fig. 7C. The GS having 6 t_{2g} electrons is stabilized more than the MLCT and the ^{3}MC states each having 5 t_{2g} electrons, which are in turn stabilized more than the ^{5}MC state having only 4 t_{2g} electrons. Since the GS is stabilized the most, all excited states undergo an apparent destabilization since the PES in Fig. 7C are normalized relative to the ground state energy. Since the ^{5}MC state has two less t_{2g} electrons than the GS, and the ^{3}MC and MLCT states have one less t_{2g} electron than the GS, the relative destabilization of the ^{5}MC state is twice that of the ^{3}MC and MLCT states.

While the changes in the t_{2g} energy levels can be addressed by steady state measurements, the changes in e_g levels are most clearly addressed with transient measurements since the e_g levels only influence the metal centered electronic excited states. To explain the significant shortening of the MLCT lifetime of $[Fe(bpy)(CN)_4]^{2-}$ in water relative to DMSO, the ^{3}MC state has to intersect the MLCT surface closer to its energy minimum. Therefore, the ^{3}MC state must be stabilized relative

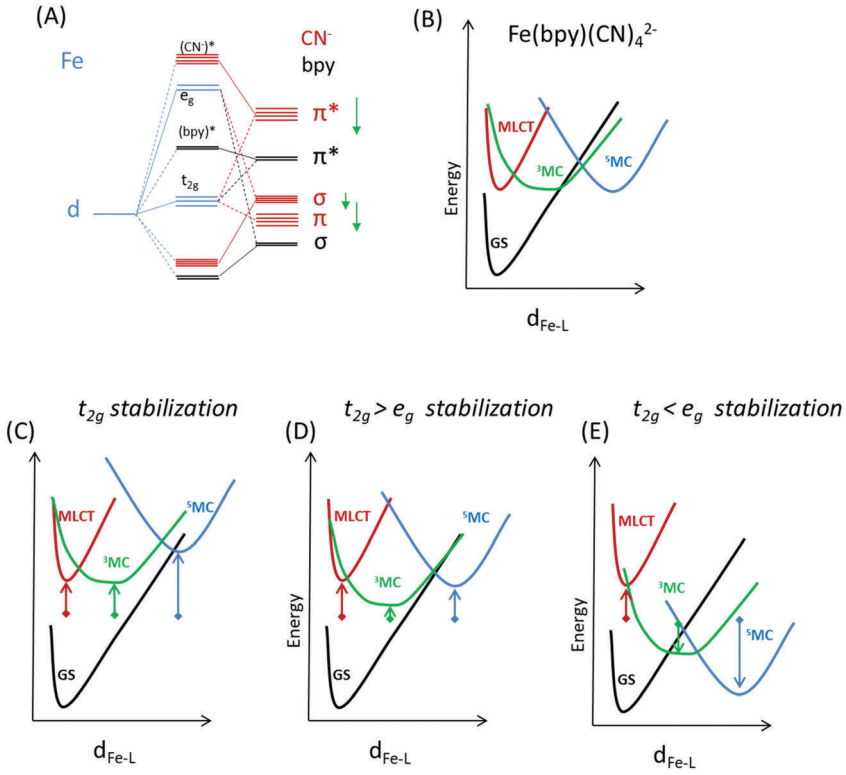

Fig. 7 (A) Schematic molecular orbital diagram for $[Fe(bpy)(CN)_4]^{2-}$. Green arrows indicate the shift in energy levels upon solvation in high Lewis acidity solvents. (B) Schematic of the potential energy surfaces of $[Fe(bpy)(CN)_4]^{2-}$ in low Lewis acidity solvents.[1] (C–E) Effect of variable t_{2g} and e_g orbital stabilization on the MLCT and MC excited state PES.

to the MLCT state, which indicates that the e_g levels also decrease in energy with increasing solvent Lewis acidity. This stabilization of the σ-bonded e_g orbitals is rationalized by the same argument for the π-bonded t_{2g} orbital stabilization discussed above. Stabilization of the e_g orbitals will shift down the ^{3}MC and ^{5}MC states relative to the illustration in Fig. 7C, which only accounts for the t_{2g} orbital stabilization. Two cases accounting for both t_{2g} and e_g stabilization are illustrated in Fig. 7D and E.

Stabilization of the e_g orbitals is consistent with the solvent dependence of the MLCT lifetimes in Ru-centered cyano-pyridyls.[44] For these Ru complexes, the relationship between MLCT lifetime and solvent acceptor number (a measure of the solvent Lewis acidity) could be described by assuming that the ^{3}MC energy was unchanged relative to the GS, requiring identical stabilization of the t_{2g} and the e_g levels. Interestingly, our experiments show that the ^{3}MC lifetime, which is too short to be clearly observed in low Lewis acidity solvents,[1] is significantly extended in high Lewis acidity solvents, meaning that a reaction barrier for the inter-system crossing and internal conversion back to the GS is required. This reaction barrier can only arise by stabilizing the e_g levels by a smaller amount than the t_{2g} levels, such that the MC states are destabilized relative to the GS (Fig. 7D). If the e_g levels are destabilized equal to or more than the t_{2g} levels, then the MC states are stabilized with respect to the GS, as illustrated in Fig. 7E. In this case, it becomes impossible to arrange the potential energy surfaces such that there is a reaction barrier to the ground state, while maintaining a significant reaction barrier to the ^{5}MC state consistent with the stabilization of the ^{3}MC and ^{5}MC states being proportionally with their number of e_g electrons. Since we observe no signature of the ^{5}MC state in the excited state cascade, we conclude the ordering of the potential energy surfaces of $[Fe(bpy)(CN)_4]^{2-}$ in high Lewis acidity solvents match the illustration in Fig. 7D. In summary, the observation that the MLCT lifetime decreases with increasing solvent Lewis acidity shows that the e_g levels are stabilized in strong Lewis acid solvents, but not as strongly as the t_{2g} levels.

To support our interpretation of the solvent influence on the excited state energy levels, we have performed preliminary DFT calculations with a polarizable continuum description of both water and DMSO, and by including explicit water molecules at the N lone-pair site of the CN^- groups. The effects of implicit and explicit solvent interactions on the excited state energy levels are summarized in Table S1 in the ESI.† It is observed that there is virtually no difference between the energy levels calculated for water and DMSO when representing the solvents with continuum models. However, upon inclusion of the explicit waters at the N lone pair sites of the CN^- groups, the DFT calculations shows a destabilization of ^{3}MLCT, ^{5}MC, and ^{3}MC states with respect to the ground state, in parallel to our experimental observations. In accordance with our interpretation of the experimental results, the calculations also show that the ^{3}MLCT state is destabilized the most, and the ^{3}MC state is destabilized the least. The minimum energy structures of our calculations (presented in Fig. S5, ESI†) shows that the water orients to form hydrogen bonds between to the cyanide N lone-pairs, supporting our interpretation of the experimental results that the reordering of the excited state level arises from explicit electronic interactions between solute and solvent.

Closing remarks

Combined ultrafast optical and XES measurements provide a clear picture for the MLCT excited state relaxation dynamics in $[Fe(bpy)(CN)_4]^{2-}$. In high Lewis acidity solvents, coordination of the CN^- ligands to the solvent significantly changes the lifetimes of the MLCT and the ^{3}MC excited states relative to their lifetimes in low Lewis acidity solvents. The influence of the solvent on the excited state relaxation dynamics arise from inequivalent solvent stabilization of the CN^- and bpy energy levels, shifting the CN^--influenced t_{2g} and e_g orbitals down relative to the bpy π* levels, which in turn modifies the relative energies of the MLCT, ^{3}MC, and ^{5}MC excited state potential energy surfaces. Our study presents a clear identification and characterization of a metastable Fe-centered ^{3}MC state in a hexacoordinated Fe centered complex.

Extracting this level of detail about the excited state relaxation mechanism has been made possible by the combined application of time resolved UV-visible TA and XES. Combining these techniques has allowed us to address not only the MLCT state dynamics, but also to identify the role of MC excited states in the electronic excited state relaxation, obtaining a more detailed picture of the excited state potential energy surfaces involved in the relaxation process. The increased robustness of the relaxation mechanisms extracted from the combined analysis of XES and TA measurements make them more amenable targets for computational quantum dynamics studies. Moreover, the relative simplicity of the Fe cyano-pyridyl compounds, and the fact that their potential energy landscape can be extensively modified by the choice of solvent, enabled a systematic exploration of the relationship between the potential energy landscape and the excited state lifetime and relaxation pathways.

These experiments also act as a stepping stone towards the investigation of Fe-centered photoactive molecular systems. With regards to future XES measurements, the good agreement with our reference spectra and the difference signal extracted from global analysis, provide further support for using the XES technique to identify the excited state species in 3d transition metal centered systems. With regards to future TA measurements, the clearly identified and isolated ^{3}MC state presented here exhibit significant excited state absorption features throughout the visible spectrum. This should significantly help the assignment of excited state absorptions in future TA measurements on chemically related Fe coordination complexes.

Conflicts of interest

Q5

Acknowledgements

Experiments were carried out at LCLS and SSRL, National User Facilities operated for DOE, OBES by Stanford University. K. K.,

A. A. C., and K. J. G. acknowledge support from the AMOS program within the Chemical Sciences, Geosciences and Biosciences Division of the Office of Basic Energy Sciences, Office of Science, US Department of Energy. KL acknowledges a Melvin and Joan Lane Stanford Graduate Fellowship. KSK, KH, MMN, MGL, PV, EB, FBH, MC gratefully acknowledge DANSCATT support for the beamtime efforts. TCBH, EB, MGL, and MMN gratefully acknowledge support by the Danish Council for independent Research under grant no. DFF-4002-00272B. KSK gratefully acknowledge the support of the Carlsberg Foundation and the Danish Council for Independent Research. This project was supported by the 'Lendület' (Momentum) Program of the Hungarian Academy of Sciences (LP2013-59), the European Research Council *via* contract ERC-StG-259709 (X-cited!), and the Hungarian Scientific Research Fund (OTKA) under contract K 109257. ZN acknowledges support from the Bolyai Fellowship of the Hungarian Academy of Sciences. The ELI-ALPS project (GINOP-2.3.6-15-2015-00001) is supported by the European Union and co-financed by the European Regional Development Fund. JU acknowledges support from the Knut and Alice Wallenberg Foundation (KAW). SK acknowledges the support from Knut & Alice Wallenberg foundation (KAW 2014.0370). MER acknowledges a Swiss National Science Foundation fellowship, project number 158890.

References

1 W. Zhang, *et al.*, Manipulating charge transfer excited state relaxation and spin crossover in iron coordination complexes with ligand substitution, *Chem. Sci.*, 2016, **8**, 515–523.
2 Y. Liu, *et al.*, A Heteroleptic Ferrous Complex with Mesoionic Bis(1,2,3-triazol-5-ylidene) Ligands: Taming the MLCT Excited State of Iron(II), *Chem. – Eur. J.*, 2015, **21**, 3628–3639.
3 J. He, B. Wang, S. Chang and T. Chen, Ruthenium-Based Photosensitizers for Dye-Sensitized Solar Cells, in *Organometallics and Related Molecules for Energy Conversion*, ed. W.-Y. Wong, Springer, Berlin Heidelberg, 2015, pp. 91–114, DOI: 10.1007/978-3-662-46054-2_4.
4 E. Baranoff, First-Row Transition Metal Complexes for the Conversion of Light into Electricity and Electricity into Light, in *Organometallics and Related Molecules for Energy Conversion*, ed. W.-Y. Wong, Springer, Berlin Heidelberg, 2015, pp. 61–90, DOI: 10.1007/978-3-662-46054-2_3.
5 J. V. Caspar and T. J. Meyer, Photochemistry of tris(2,2′-bipyridine)ruthenium(2+) ion (Ru(bpy)32+). Solvent effects, *J. Am. Chem. Soc.*, 1983, **105**, 5583–5590.
6 A. Juris, *et al.*, Ru(II) polypyridine complexes: photophysics, photochemistry, electrochemistry, and chemiluminescence, *Coord. Chem. Rev.*, 1988, **84**, 85–277.
7 N. H. Damrauer, *et al.*, Femtosecond Dynamics of Excited-State Evolution in $[Ru(bpy)3]^{2+}$, *Science*, 1997, **275**, 54–57.
8 M. Abrahamsson, *et al.*, A 3.0 μs Room Temperature Excited State Lifetime of a Bistridentate RuII−Polypyridine Complex for Rod-like Molecular Arrays, *J. Am. Chem. Soc.*, 2006, **128**, 12616–12617.
9 D. G. Brown, N. Sanguantrakun, B. Schulze, U. S. Schubert and C. P. Berlinguette, Bis(tridentate) Ruthenium–Terpyridine Complexes Featuring Microsecond Excited-State Lifetimes, *J. Am. Chem. Soc.*, 2012, **134**, 12354–12357.
10 S. Nozawa, *et al.*, Direct Probing of Spin State Dynamics Coupled with Electronic and Structural Modifications by Picosecond Time-Resolved XAFS, *J. Am. Chem. Soc.*, 2010, **132**, 61–63.
11 J. E. Monat and J. K. McCusker, Femtosecond Excited-State Dynamics of an Iron(II) Polypyridyl Solar Cell Sensitizer Model, *J. Am. Chem. Soc.*, 2000, **122**, 4092–4097.
12 H. T. Lemke, *et al.*, Femtosecond X-ray Absorption Spectroscopy at a Hard X-ray Free Electron Laser: Application to Spin Crossover Dynamics, *J. Phys. Chem. A*, 2013, **117**, 735–740.
13 N. Huse, *et al.*, Femtosecond Soft X-ray Spectroscopy of Solvated Transition-Metal Complexes: Deciphering the Interplay of Electronic and Structural Dynamics, *J. Phys. Chem. Lett.*, 2011, **2**, 880–884.
14 A. Cannizzo, *et al.*, Light-induced spin crossover in Fe(II)-based complexes: The full photocycle unraveled by ultrafast optical and X-ray spectroscopies, *Coord. Chem. Rev.*, 2010, **254**, 2677–2686.
15 K. Haldrup, *et al.*, Observing Solvation Dynamics with Simultaneous Femtosecond X-ray Emission Spectroscopy and X-ray Scattering, *J. Phys. Chem. B*, 2016, **120**, 1158–1168.
16 N. Huse, *et al.*, Photo-Induced Spin-State Conversion in Solvated Transition Metal Complexes Probed via Time-Resolved Soft X-ray Spectroscopy, *J. Am. Chem. Soc.*, 2010, **132**, 6809–6816.
17 M. Khalil, *et al.*, Picosecond X-ray Absorption Spectroscopy of a Photoinduced Iron(II) Spin Crossover Reaction in Solution, *J. Phys. Chem. A*, 2006, **110**, 38–44.
18 G. Auböck and M. Chergui, Sub-50 fs photoinduced spin crossover in $[Fe(bpy)3]2^{+}$, *Nat. Chem.*, 2015, **7**, 629–633.
19 J. K. McCusker, *et al.*, Subpicosecond 1MLCT.fwdarw. 5T2 intersystem crossing of low-spin polypyridyl ferrous complexes, *J. Am. Chem. Soc.*, 1993, **115**, 298–307.
20 A. Marino, *et al.*, The Role of Ligand-Field States in the Ultrafast Photophysical Cycle of the Prototypical Iron(II) Spin-Crossover Compound [Fe(ptz)6](BF4)2, *Angew. Chem., Int. Ed.*, 2014, **53**, 3863–3867.
21 W. Zhang, *et al.*, Tracking excited-state charge and spin dynamics in iron coordination complexes, *Nature*, 2014, **509**, 345–348.
22 C. Sousa, *et al.*, Ultrafast Deactivation Mechanism of the Excited Singlet in the Light-Induced Spin Crossover of $[Fe(2,2'-bipyridine)3]^{2+}$, *Chem. – Eur. J.*, 2013, **19**, 17541–17551.
23 W. Gawelda, *et al.*, Ultrafast Nonadiabatic Dynamics of [FeII(bpy)3]2+ in Solution, *J. Am. Chem. Soc.*, 2007, **129**, 8199–8206.
24 C. Consani, *et al.*, Vibrational Coherences and Relaxation in the High-Spin State of Aqueous [FeII(bpy)3]2+, *Angew. Chem., Int. Ed.*, 2009, **48**, 7184–7187.
25 Y. Liu, *et al.*, Towards longer-lived metal-to-ligand charge transfer states of iron(II) complexes: an N-heterocyclic carbene approach, *Chem. Commun.*, 2013, **49**, 6412–6414.

26 L. A. Fredin, *et al.*, Exceptional Excited-State Lifetime of an Iron(II)–N-Heterocyclic Carbene Complex Explained, *J. Phys. Chem. Lett.*, 2014, **5**, 2066–2071.
27 T. C. B. Harlang, *et al.*, Iron sensitizer converts light to electrons with 92% yield, *Nat. Chem.*, 2015, **7**, 883–889.
28 T. Duchanois, *et al.*, An Iron-Based Photosensitizer with Extended Excited-State Lifetime: Photophysical and Photovoltaic Properties, *Eur. J. Inorg. Chem.*, 2015, 2469–2477.
29 M. Pápai, G. Vankó, T. Rozgonyi and T. J. Penfold, High-Efficiency Iron Photosensitizer Explained with Quantum Wavepacket Dynamics, *J. Phys. Chem. Lett.*, 2016, **7**, 2009–2014.
30 Y. Liu, P. Persson, V. Sundström and K. Wärnmark, Fe N-Heterocyclic Carbene Complexes as Promising Photosensitizers, *Acc. Chem. Res.*, 2016, **49**, 1477–1485.
31 L. Liu, *et al.*, A new record excited state 3MLCT lifetime for metal organic iron(II) complexes, *Phys. Chem. Chem. Phys.*, 2016, **18**, 12550–12556.
32 M. Reinhard, *et al.*, Photoaquation Mechanism of Hexacyanoferrate(II) Ions: Ultrafast 2D UV and Transient Visible and IR Spectroscopies, *J. Am. Chem. Soc.*, 2017, **139**, 7335–7347.
33 C. D. Graaf and C. Sousa, On the role of the metal-to-ligand charge transfer states in the light-induced spin crossover in FeII (bpy)3, *Int. J. Quantum Chem.*, 2011, **111**, 3385–3393.
34 A. Moguilevski, *et al.*, Ultrafast Spin Crossover in $[FeII(bpy)_3]^{2+}$: Revealing Two Competing Mechanisms by Extreme Ultraviolet Photoemission Spectroscopy, *ChemPhysChem*, 2017, DOI: 10.1002/cphc.201601396. Q6
35 I. M. Dixon, F. Alary, M. Boggio-Pasqua and J.-L. Heully, Reversing the relative 3MLCT–3MC order in Fe(II) complexes using cyclometallating ligands: a computational study aiming at luminescent Fe(II) complexes, *Dalton Trans.*, 2015, **44**, 13498–13503.
36 L. L. Jamula, A. M. Brown, D. Guo and J. K. McCusker, Synthesis and Characterization of a High-Symmetry Ferrous Polypyridyl Complex: Approaching the 5T2/3T1 Crossing Point for FeII, *Inorg. Chem.*, 2014, **53**, 15–17.
37 I. M. Dixon, F. Alary, M. Boggio-Pasqua and J.-L. Heully, The (N4C2)2– Donor Set as Promising Motif for Bis(tridentate) Iron(II) Photoactive Compounds, *Inorg. Chem.*, 2013, **52**, 13369–13374.
38 M. Pápai, T. J. Penfold and K. B. Møller, Effect of *tert*-Butyl Functionalization on the Photoexcited Decay of a Fe(II)-N-Heterocyclic Carbene Complex, *J. Phys. Chem. C*, 2016, **120**, 17234–17241.
39 C. J. Timpson, C. A. Bignozzi, B. P. Sullivan, E. M. Kober and T. J. Meyer, Influence of Solvent on the Spectroscopic Properties of Cyano Complexes of Ruthenium(II), *J. Phys. Chem.*, 1996, **100**, 2915–2925.
40 I. Georgieva, A. J. A. Aquino, N. Trendafilova, P. S. Santos and H. Lischka, Solvatochromic and Ionochromic Effects of Iron(II)bis(1,10-phenanthroline)dicyano: a Theoretical Study, *Inorg. Chem.*, 2010, **49**, 1634–1646.
41 W. Linert and V. Gutmann, Structural and electronic responses of coordination compounds to changes in the molecule and molecular environment, *Coord. Chem. Rev.*, 1992, **117**, 159–183.
42 A. Al-alousy and J. Burgess, Bis(1,10-phenanthroline) dicyanoiron(II): an almost universal inorganic solvent polarity indicator, *Inorg. Chim. Acta*, 1990, **169**, 167–170.
43 L. Fodor, G. Lendvay and A. Horváth, Solvent Dependence of Absorption and Emission Spectra of Ru(bpy)2(CN)2: Experiment and Explanation Based on Electronic Structure Theory, *J. Phys. Chem. A*, 2007, **111**, 12891–12900.
44 M. T. Indelli, C. A. Bignozzi, F. Scandola and J.-P. Collin, Design of Long-Lived Ru(II) Terpyridine MLCT States. Tricyano Terpyridine Complexes, *Inorg. Chem.*, 1998, **37**, 6084–6089.
45 J. R. Winkler, C. Creutz and N. Sutin, Solvent tuning of the excited-state properties of (2,2'-bipyridine)tetracyanoferrate(II): direct observation of a metal-to-ligand charge-transfer excited state of iron(II), *J. Am. Chem. Soc.*, 1987, **109**, 3470–3471.
46 T. J. Penfold, *et al.*, X-ray Spectroscopic Study of Solvent Effects on the Ferrous and Ferric Hexacyanide Anions, *J. Phys. Chem. A*, 2014, **118**, 9411–9418.
47 Note that while the $[Fe(bpy)(CN)4]^{2-}$ is formally of C_{2v} symmetry we refer to the d-π and d-σ* orbitals with the octahedral eg and t2g notation to facilitate direct comparison between the different systems that are all near octahedral symmetry.
48 K. Haldrup, *et al.*, Guest–Host Interactions Investigated by Time-Resolved X-ray Spectroscopies and Scattering at MHz Rates: Solvation Dynamics and Photoinduced Spin Transition in Aqueous $Fe(bipy)_3^{2+}$, *J. Phys. Chem. A*, 2012, **116**, 9878–9887.
49 S. E. Canton, *et al.*, Visualizing the non-equilibrium dynamics of photoinduced intramolecular electron transfer with femtosecond X-ray pulses, *Nat. Commun.*, 2015, **6**, 6359.
50 G. Vankó, *et al.*, Detailed Characterization of a Nanosecond-Lived Excited State: X-ray and Theoretical Investigation of the Quintet State in Photoexcited $[Fe(terpy)2]2^+$, *J. Phys. Chem. C*, 2015, **119**, 5888–5902.
51 Z. Fox *et al.*, Monitoring Excited State Charge Transfer of Transition Metal Mixed-Valence Complexes with Femtosecond X-ray Absorption and Emission Spectroscopy, in International Conference on Ultrafast Phenomena (2016), paper UTh4A.2, UTh4A.2 (Optical Society of America, 2016), DOI: 10.1364/UP.2016.UTh4A.2. Q7
52 R. Alonso-Mori, *et al.*, Photon-in photon-out hard X-ray spectroscopy at the Linac Coherent Light Source, *J. Synchrotron Radiat.*, 2015, **22**, 612–620.
53 M. Chollet, *et al.*, The X-ray Pump–Probe instrument at the Linac Coherent Light Source, *J. Synchrotron Radiat.*, 2015, **22**, 503–507.
54 H. T. Philipp, M. W. Tate and S. M. Gruner, Low-flux measurements with Cornell's LCLS integrating pixel array detector, *J. Instrum.*, 2011, **6**, C11006.
55 R. Alonso-Mori, *et al.*, A multi-crystal wavelength dispersive x-ray spectrometer, *Rev. Sci. Instrum.*, 2012, **83**, 073114.
56 P. Glatzel and U. Bergmann, High resolution 1s core hole X-ray spectroscopy in 3d transition metal complexes –

electronic and structural information, *Coord. Chem. Rev.*, 2005, **249**, 65–95.
57 H. E. Toma and M. S. Takasugi, Spectroscopic studies of preferential and asymmetric solvation in substituted cyanoiron(II) complexes, *J. Solution Chem.*, 1983, **12**, 547–561.
58 A. M. Brown, C. E. McCusker and J. K. McCusker, Spectroelectrochemical identification of charge-transfer excited states in transition metal-based polypyridyl complexes, *Dalton Trans.*, 2014, **43**, 17635–17646.
59 K. S. Kjær, *et al.*, Ligand manipulation of charge transfer excited state relaxation and spin crossover in [Fe(2,2′-bipyridine)2(CN)2], *Struct. Dyn.*, 2017, **4**, 044030.
60 A. Horváth, J. Szõke and L. Wojnárovits, Mechanism of photoinduced redox reactions in aqueous solutions of $[Fe(bpy)(CN)4]2^{-}$, *Inorg. Chim. Acta*, 1991, **179**, 97–104.
61 F. de Groot, High-Resolution X-ray Emission and X-ray Absorption Spectroscopy, *Chem. Rev.*, 2001, **101**, 1779–1808.
62 G. Vankó, *et al.*, Probing the 3d Spin Momentum with X-ray Emission Spectroscopy: The Case of Molecular-Spin Transitions, *J. Phys. Chem. B*, 2006, **110**, 11647–11653.
63 N. Lee, T. Petrenko, U. Bergmann, F. Neese and S. DeBeer, Probing Valence Orbital Composition with Iron Kβ X-ray Emission Spectroscopy, *J. Am. Chem. Soc.*, 2010, **132**, 9715–9727.
64 G. Vankó, *et al.*, Spin-state studies with XES and RIXS: From static to ultrafast, *J. Electron Spectrosc. Relat. Phenom.*, 2013, **188**, 166–171.
65 N. A. Anderson, K. Hang, J. B. Asbury and T. Lian, Ultrafast mid-IR detection of the direct precursor to the presolvated electron following electron ejection from ferrocyanide, *Chem. Phys. Lett.*, 2000, **329**, 386–392.
66 M. Reinhard, *et al.*, Photooxidation and photoaquation of iron hexacyanide in aqueous solution: A picosecond X-ray absorption study, *Struct. Dyn.*, 2014, **1**, 024901.
67 Q. Sun, *et al.*, On the role of ligand-field states for the photophysical properties of ruthenium(II) polypyridyl complexes, *Coord. Chem. Rev.*, 2015, **282–283**, 87–99.

Sample preparation

Samples of $K_2[Fe(bpy)(CN)_4]$ (Schilt 1960) and $TBA_2[Fe(bpy)(CN)_4]$ (Toma 1983) were prepared according to literature procedures. $K_2[Fe(bpy)(CN)_4]$ was used for aqueous solution experiments, $TBA_2[Fe(bpy)(CN)_4]$ was used for experiments in DMSO.

High fluence TA measurements

TA measurements of 500 nm excitation in water were conducted at excitation pulse energies of 1.6 µJ and 6.4 µJ and fluences of approximately of $4x10^{11}$ W/cm^2 and $2x10^{12}$ W/cm^2, respectively. The recorded data is presented in the Figure S1A,B respectively. It is seen that the amplitude of all transient features below 550 nm increase by around a factor of four, while the long-lived positive feature at 680 nm becomes significantly more pronounced.

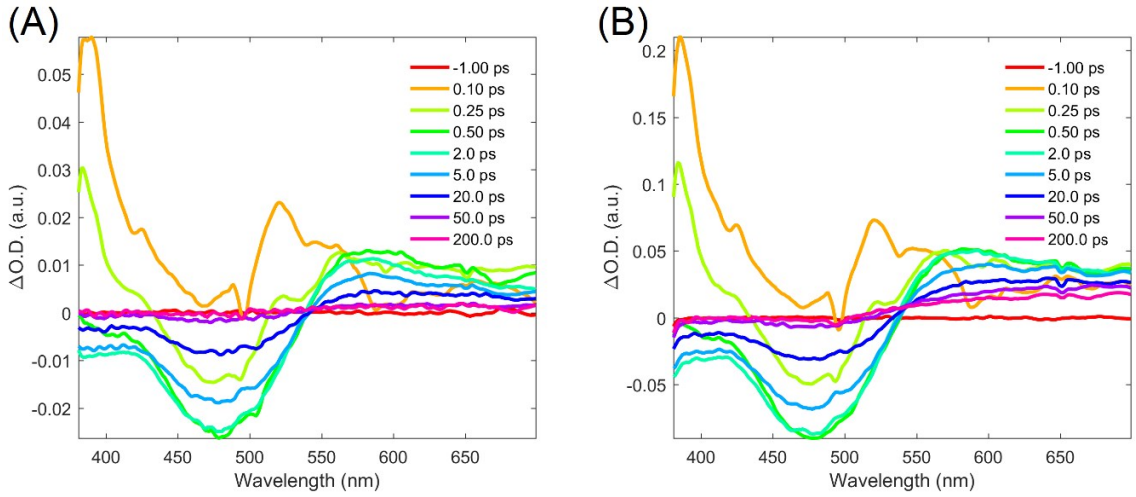

Figure S1. Transient absorption spectra of $[Fe(bpy)(CN)_4]^{2-}$ at selected time delays in H_2O excited at 500 nm with 1.6 µJ (A) and 6.4 µJ (B) pulse energy.

Global analysis of the data allows us to retrieve the amplitude and time scales of the dynamic processes observed in the data. We find that the positive feature of SAS1 and the negative feature of SAS2 both increase by a factor of 3.6, slightly below the factor of four excitation fluency increase. Meanwhile the positive feature of SAS3 increases by a factor of 15 (from a ΔO.D. of 0.0014 to 0.021), very close to the expected factor of 16 increase from a 2-photon process.

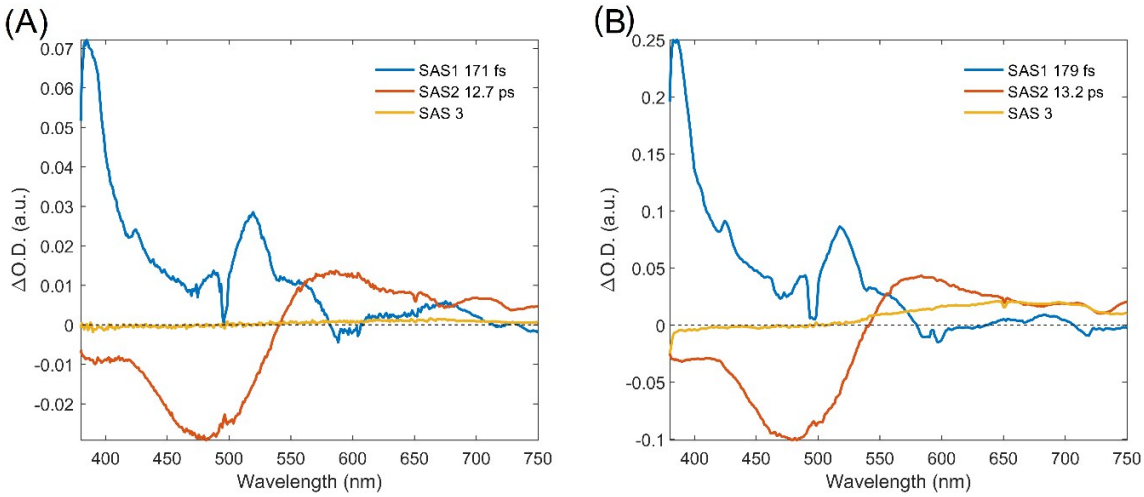

Figure S2. Species associated spectra returned from the global analysis of the $[Fe(bpy)(CN)_4]^{2-}$ transient absorption in H_2O, excited at 500 nm with 1.6 µJ (A) and 6.4 µJ (B) excitation pulse energy.

It is also seen that the shape of SAS1 and SAS2 from the two measurements are practically identical, and that the extracted time scales are well within the error of each other: $SAS1_{4mj}$ 171 ± 32 fs, $SAS2_{4mJ}$ 12.7 ± 0.4 ps $SAS1_{16mj}$ 179 ± 38 fs, $SAS2_{16mJ}$ 13.2 ± 0.3 ps

The yield of photoionization can be estimated by comparing the amplitude of the GSB and solvated electron absorption, to their molar extinction coefficients at their absorption maximum (2500 $M^{-1}cm^{-1}$ and 20000 $M^{-1}cm^{-1}$ (Lenchenkov 2001)), respectively). For the low fluence data in Figure S2A, the amplitude of these features (0.029 and 0.0014 O.D. respectively) shows that the photoionization quantum yield is 0.006 ± 0.001, well below 1%. The low quantum yield of photoionization for these low fluence measurements means that the influence of the photoionization on the excited state cascade is negligible.

Laser fluence measurements for XES experiments

For the XES measurements conducted at 400 nm excitation in water the laser flounce was scanned to ensure that experiments were conducted before the onset of higher order excitation events asides from the first order excitation and second order photoionization events observed by the TA experiments. The integrated XES difference signal intensity at 5 ps time delay as a function excitation fluence is presented in Figure S3. A linear

fit of the difference signal intensity as a function of fluence (red line) shows weak deviation above 8 μJ, and significant deviation above 15 μJ. The, transient experiments were conducted at 12.5μJ, before the onset of significant deviation from a linear relationship between excitation fluence and difference signal.

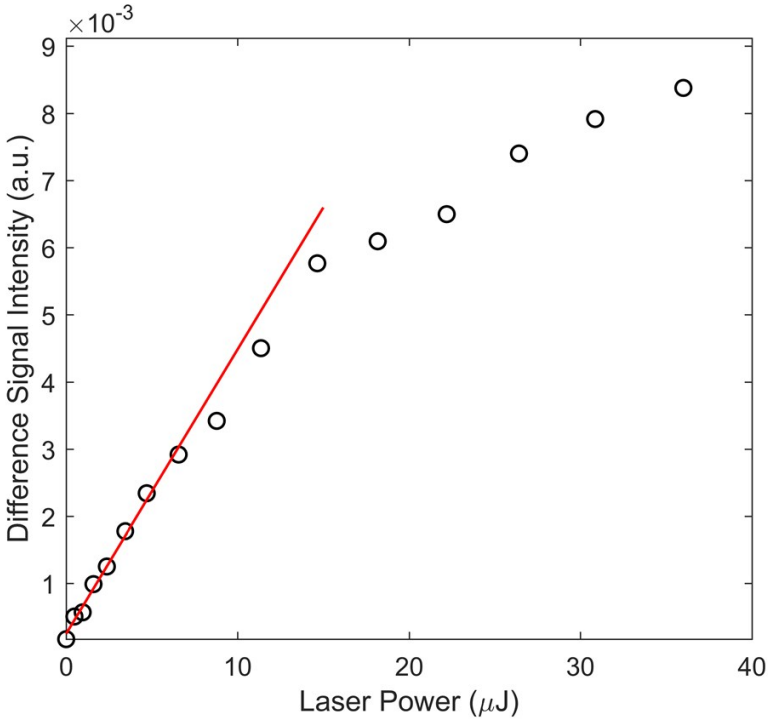

Figure S3, XES difference signal intensity at 5 ps time delay as a function excitation fluence is (black circles), and linear fit at low fluence (red line).

Identifying the slow time scale in the XES ground state recovery

Previous work that monitored signatures of the bipyridine radical anion demonstrated that solvated electrons are scavenged by ground state $[Fe(bpy)(CN)_4]^{2-}$ to form $[Fe(bpy)(CN)_4]^{3-}$, and that ground state recovery is a recombination of $[Fe(bpy)(CN)_4]^{3-}$ and $[Fe(bpy)(CN)_4]^{-}$ to from $[Fe(bpy)(CN)_4]^{2-}$ (Horváth 1991). Horváth et al. determined the rate constant of the scavenging of solvated electrons ($e^-(aq)$ + $[Fe(bpy)(CN)_4]^{2-} \rightarrow [Fe(bpy)(CN)_4]^{3-}$) is $k = 1.3 \times 10^{10}$ $M^{-1}s^{-1}$, while the rate constant of charge recombination ($[Fe(bpy)(CN)_4]^{-}$ + $[Fe(bpy)(CN)_4]^{3-} \rightarrow [Fe(bpy)(CN)_4]^{2-}$) is $k = 1.8 \times 10^{10}$ $M^{-1}s^{-1}$. (Horváth 1991) Given the concentrations used in the present study, this translates to a few nanosecond characteristic timescale for the formation of $[Fe(bpy)(CN)_4]^{3-}$ and a hundreds-of-nanosecond timescale for the secondary charge recombination. For the reduced species,

$[Fe(bpy)(CN)_4]^{3-}$, the electron resides on the bipyridine ligand, such that the iron center is a formal Fe(II) species and the XES signal is expected to be extremely similar to that of the ground state. Thus, both Kα and Kβ measurements are expected to be insensitive to the $[Fe(bpy)(CN)_4]^{3-}$, as indicated by the lack of dynamics on the few nanosecond time scale where the species is formed. Thus, the long time scale dynamics only tracks the loss of $[Fe(bpy)(CN)_4]^{-}$ upon reformation of ground state.

The time evolution of the decay kinetic describing recombination is a 2nd order reaction (involving $[Fe(bpy)(CN)_4]^{-}$ and $[Fe(bpy)(CN)_4]^{3-}$, formed in equal amounts after few nanoseconds), expressed as $[A] = \frac{1}{\frac{1}{[A]_0} + kt}$. Comparative fits to the long time delay data using first and second order rate expressions for the decay are illustrated in Figure 5 as inserts (A) and (B), respectively. Second order decay kinetics provide an overall better description of the data and captures the incomplete recovery observed within the 3 µs time window of the experiment. From the fit shown in Figure 5b we obtain a rate constant of 1.1 ± 0.8x10^{10} M^{-1}s^{-1} and an initial concentration of $[Fe(bpy)(CN)_4]^{-}$ of 1.8 ± 1 mM. The fitted rate constant matches the literature value of 1.8 ± 0.4x10^{10} M^{-1}s^{-1}, and the initial $[Fe(bpy)(CN)_4]^{-}$ concentration is in good agreement with the total excitation fraction, as we will be show in the following.

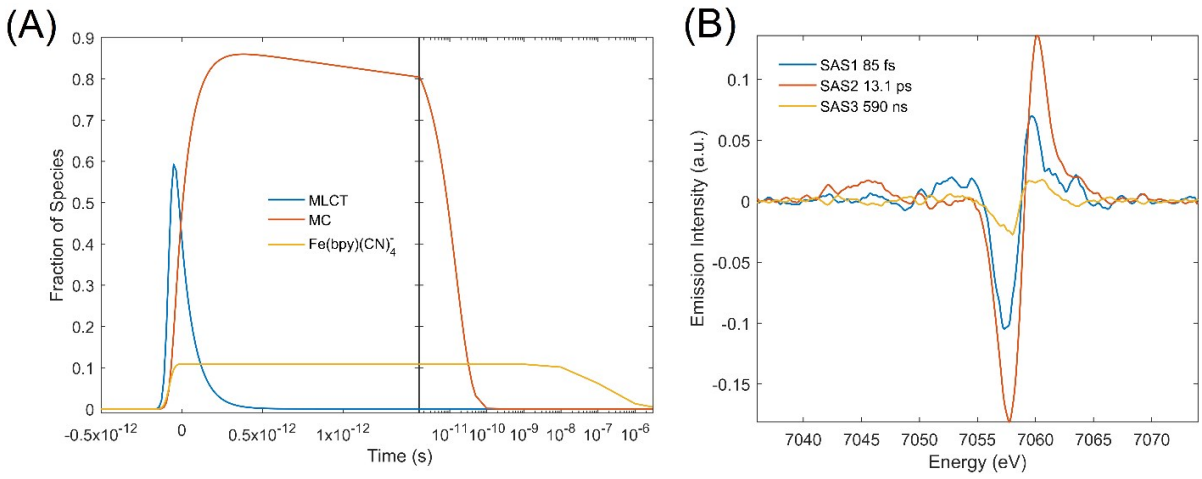

Figure S4 The time-evolution of the $[Fe(bpy)(CN)_4]^{2-}$ species in the excited state cascade as derived from the analysis of the Kα and optical TA data (A), and their respective SAS derived from global analysis of the Kβ data (B).

SAS3, associated with the long lived third species, is compared to SAS1 and SAS2 in Figure 7c. Since SAS1 and SAS3 describe a very similar species with respect to the Fe center, the scaling factor that yields the best

agreement between the two can be used to calculate the photoionization yield. The best-fit scaling factor is a multiplication of SAS3 by 6.3. This indicates that 84% of the photoinitiated cascade progresses through the MLCT and ^{3}MC state before returning to the ground state, and 16% undergoes photoionization and eventual recombination with $[Fe(bpy)(CN)_4]^{3-}$. Using this model for the excited state cascade, the excitation fraction can be retrieved as the scaling factor between the MLCT reference and the sum of SAS1 and SAS3. Alternatively, it can be retrieved as the sum of the scaling factor between the MLCT reference and SAS3 plus the scaling factor between the ^{3}MC reference and SAS2. Both estimates return an excitation faction of 33%. With an $[Fe(bpy)(CN)_4]^{2-}$ concentration of 50 mM, an excitation fraction of 33%, and a 16% photoionization fraction, the initial absolute concentration of $[Fe(bpy)(CN)_4]^{3-}$ is calculated to be 2.3 mM. This is in good agreement with the 1.8 ± 1 mM retrieved from the recombination time quantified in the Kα kinetics.

As a final note, we stress that, neither $e^-(aq)$ nor $[Fe(bpy)(CN)_4]^{3-}$ contribute to the total difference signal measured by (Kα and Kβ) XES. Therefore, only the oxidized $[Fe(bpy)(CN)_4]^-$ photoproduct is included in the analysis of the Kα and Kβ data.

Timing diagnostics

The shot-to-shot x-ray-optical relative time of arrival fluctuations were measured for every x-ray-optical pulse pair with a timing diagnostic tool based on optical detection of x-ray generated carriers in a Si3N4 thin film (Harmand). This experimental measure of the relative timing was used to sort each experimental shot by the relative time of arrival. Thus, the final time resolution of the experiment results from the convolution of the optical and x-ray pulse durations, the difference group velocity of the x-ray and optical pulses in the sample, and the error in the relative time of arrival measurement. These set the resolution to roughly 80 fs FWHM.

XES Data Treatment

The CSPAD detectors recording the Kα and Kβ fluorescence were calibrated through a pixel dependent dark current (pedestal) subtraction, a common mode off-set subtraction, and an experimentally determined gain map. The gain map was built from histograms of the response of each pixel in all datasets used in the analysis, after dark current and common mode subtraction. Gaussians were fit to the zeroth, first, second, and third photon peaks of the histograms, enabling fine-tuned dark and gain corrections directly from the data. The zero-

photon peaks were centered at zero analog-to-digital units (ADU) and the separation between photon peaks were scaled to unity for all pixels. To remove the zero-photon read-out noise, all ADU values below a threshold of 3σ of the zero-photon peak were set to zero.

At this stage in the data analysis, each pump-probe event is associated with a Kα and a Kβ detector image which reflects the number of photons seen by each pixel. For both the Kα and Kβ signal, difference images are constructed by scaling each image to the incident photon energy, and subtracting the average signal recorded for the optical laser-off x-ray exposures associated with the nominal time step from which each individual pump-probe event was recorded.

Average difference images are then constructed from all pump-probe events belonging to the same time-bin as sorted by the nominal time-delay and the timing tool correction value. The Kα difference signal of each time bin is then given by the integrated average difference image of that time bin. The Kβ difference signal of each time bin is obtained by integrating the difference image along the nondispersive axis of the detector.

Kβ XES data correction

Misalignment of one of the four analyzer crystals of the multicrystal spectrometer during the LCLS experiment resulted in distorted Kβ XES spectra. In order to remove this distortion the spectra were corrected with a following formula

$$S_{corr} = FT^{-1}\left\{\frac{FT\{D^*\}FT\{S_{uncorr}\}}{FT\{D^*\}FT\{D\}}\right\}$$

S_{corr} is the corrected spectrum, S_{uncorr} is uncorrected (measured) spectrum and D is the function describing the distortion defined by two delta peaks whose relative height and position correspond to misalignment of the fourth crystal. Note that direct application of the deconvolution theorem would result in singularities and therefor before the division is carried out both nominator and denominator are multiplied by $FT\{D^*\}$. The correction procedure includes finding the suitable relative height and shift of the two delta peaks in D.

Computational Chemistry

The ground state (S0), ^{3}MLCT, ^{3}MC, ^{5}MLCT, and ^{5}MC geometries of the complex were fully reoptimized from recently presented DFT structures (Zhang 2016) without symmetry constraints using the B3LYP* hybrid DFT functional (Reiher 2001) together with the standard triple-ζ 6-311G(d,p) basis set (Dunning 1977), and with a complete acetonitrile or water polarizable continuum model (PCM) (Tomasi 2005) in Gaussian G09. (Frish 2016) A secondary series of calculations estimating the effects of specific solvation interactions in water were conducted by also including four explicit water molecules, arranged with a hydrogen pointing towards each of the nitrogen lone-pairs of the CN^- ligands, and with the full system comprising the complex plus explicit water molecules immersed in a PCM water solvent model. The fully optimized excited state local minima of the respective state multiplicities were identified and could be clearly distinguished on the basis of the spin density on the Fe atom, and bpy ligand. The following table presents the energies of the different excited states with respect to the ground state energy for the three different solvent environments.

ESI Table 1. Calculated optimized state energies in different solvent environments.

State*	DMSO(s)	H_2O(s)	$(H_2O)_4$/H2O(s)	$\Delta E_{Sp.Solv}$**
S0	0.00	0.00	0.00	0
^{3}MLCT	1.04	1.07	1.32	+0.25
^{3}MC	1.03	1.03	1.16	+0.13
^{5}MC	1.41	1.41	1.58	+0.17

* State energies for different solvent environments are given (in eV) relative to the respective S0 energy for that solvent environment.

** Energy change arising from specific solvation interactions $\Delta E_{Sp.Solv}$ is defined as the energy difference between PCM water, and PCM water + 4 H_2O

The explicit energy change upon specific solvation ($\Delta E_{Sp.Solv}$) for the S0, ^{3}MLCT, ^{3}MC, and ^{5}MC states qualitatively reproduce the experimental assignment illustrated in Figure 7D: All states are destabilized relative to the ground state, the ^{3}MLCT is destabilized the most, and the ^{3}MC state is destabilized the least. The relaxed energy minimum structures shows that the explicit waters form hydrogen-like bonds to the cyanide nitrogen lone pairs. This is illustrated for the ground state structure in Figure S5.

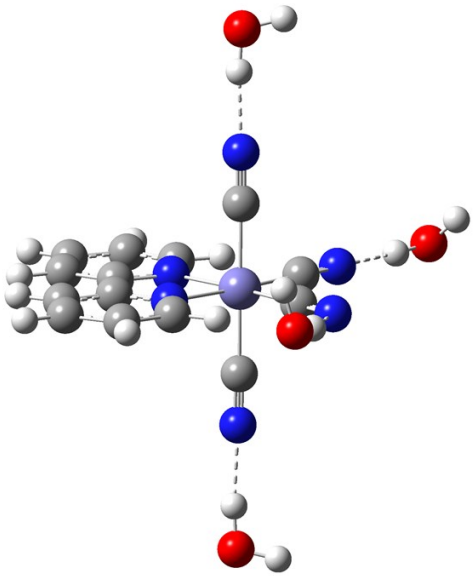

Figure S5 Relaxed ground state energy minimum structure of $[Fe(bpy)(CN)_4]^{2-}$ with 4 explicit water molecules resulting from the DFT calculations.

References

(Dunning 1977) T.H. Dunning, P.J. Hay, 1977, "Gaussian basis sets for molecular calculations," in: "Modern Theoretical Chemistry," vol. 3. Ed. H.F. Schaefer III, pp. 1-28, Plenum Press, New York.

(Frish 2016) Gaussian 09, Revision A.02, M. J. Frisch, G. W. Trucks, H. B. Schlegel, G. E. Scuseria, M. A. Robb, J. R. Cheeseman, G. Scalmani, V. Barone, G. A. Petersson, H. Nakatsuji, X. Li, M. Caricato, A. Marenich, J. Bloino, B. G. Janesko, R. Gomperts, B. Mennucci, H. P. Hratchian, J. V. Ortiz, A. F. Izmaylov, J. L. Sonnenberg, D. Williams-Young, F. Ding, F. Lipparini, F. Egidi, J. Goings, B. Peng, A. Petrone, T. Henderson, D. Ranasinghe, V. G. Zakrzewski, J. Gao, N. Rega, G. Zheng, W. Liang, M. Hada, M. Ehara, K. Toyota, R. Fukuda, J. Hasegawa, M. Ishida, T. Nakajima, Y. Honda, O. Kitao, H. Nakai, T. Vreven, K. Throssell, J. A. Montgomery, Jr., J. E. Peralta, F. Ogliaro, M. Bearpark, J. J. Heyd, E. Brothers, K. N. Kudin, V. N. Staroverov, T. Keith, R. Kobayashi, J. Normand, K. Raghavachari, A. Rendell, J. C. Burant, S. S. Iyengar, J. Tomasi, M. Cossi, J. M. Millam, M. Klene, C. Adamo, R. Cammi, J. W. Ochterski, R. L. Martin, K. Morokuma, O. Farkas, J. B. Foresman, and D. J. Fox, Gaussian, Inc., Wallingford CT, 2016.

(Horváth 1991) Horváth, A., Szõke, J. & Wojnárovits, L. Mechanism of photoinduced redox reactions in aqueous solutions of $[Fe(bpy)(CN)4]^{2-}$. *Inorganica Chim. Acta*, 1991, **179,** 97–104.

(Lenchenkov 2001) Lenchenkov et al. Chemical Physics Letters, 2001, **342**, 277-286

(Reiher 2001) Reiher, M.; Salomon, O.; Artur Hess, B. Theor. Chem. Acc. 2001, **107**, 48

(Schilt 1960) A. Schilt. Mixed Ligand Complexes of Iron(I1) and (111) with Cyanide and Aromatic Di-imines. J. Am. Chem. Soc. 1960, **82**, 3000-3005.

(Toma 1983) H. E. Toma, M. S. Takasugi. Spectroscopic Studies of Preferential and Asymmetric Solvation in Substituted Cyanoiron(ll) Complexes. *J. Sol. Chem.* 1983, **12,** 547-561.

(Tomasi 2005) J. Tomasi, B. Mennucci, and R. Cammi, "Quantum mechanical continuum solvation models," *Chem. Rev.*, 2005, **105**, 2999-3093. DOI: 10.1021/cr9904009

(Zhang 2016) W. Zhang, *et al.* Manipulating charge transfer excited state relaxation and spin crossover in iron coordination complexes with ligand substitution. *Chem. Sci.,* 2016, **8,** 515–523.

Proposal I

Proposal view

[2111] Revealing the Ultrafast Dynamics and Hidden Symmetries During Ion-Release from a Transition-Metal Complex

- Status: Submitted
- Last edited: 2017-11-16 12:08:35

General

Proposal

Title	Revealing the Ultrafast Dynamics and Hidden Symmetries During Ion-Release from a Transition-Metal Complex
Instrument	FXE SASE1
Scientific area	Femtochemistry, solid- and liquid-state chemistry
Innovative impact	Yes The system will be a prototype for a larger class of ion-release systems in e.g. biology, one example being the transport in ion channels. + Increase our understanding of the structure-function relationship in inorganic photo-catalysis As such, the innovative impact is medium- to long-term.
Horizon 2020 Challenges	Secure, clean and efficient energy

Beamtime required

Number of Shifts Required	5

Abstract, description and references

Abstract

A key goal of the experiment is to study the photo-induced Ag+ detachment of AgIr2(dim)4. As the detachment involves breaking of an Ir-Ag bond and subsequent formation of an Ir-Ir bond it represents an excellent opportunity to study dynamics related to breaking and formation of metal-metal bonds. Further we want to resolve the sub-ps coherent dynamics.

The system will also serve as a model system for method development of X-ray Cross Correlation Analysis, which uses Cross-Correlation Functions to analyze the non-isotropic part of the scattered intensity to extract fine-structure information

Description

View uploaded PDF (https://in.xfel.eu/upex/proposal/2111/description_pdf)

References

1. **DOI: 10.1038/ncomms13678**
   T. van Driel et al., Atomistic characterization of the active-site solvation dynamics of a model photocatalyst, Nature Communications, 2016
2. **DOI: 10.1021/acs.jpcb.5b12471**
   K. Haldrup et al., Observing Solvation Dynamics with Simultaneous Femtosecond X-ray Emission Spectroscopy and X-ray Scattering, Journal of Physical Chemistry B, 2016
3. **DOI: 10.1103/PhysRevLett.117.013002**
   E. Biasin et al., Femtosecond X-Ray Scattering Study of Ultrafast Photoinduced Structural Dynamics in Solvated Co[terpy]_2, Physical Review Letters, 2016
4. **DOI: 10.1103/PhysRevLett.119.158102**
   R. Kurta et al., Correlations in Scattered X-Ray Laser Pulses Reveal Nanoscale Structural Features of Viruses, Physical Review Letters, 2017
5. **DOI: 10.1002/9781119290971.ch1**
   R. Kurta et al., Structural Analysis by X-ray Intensity Angular Cross Correlations, Advances in Chemical Physics, 2016.
6. **DOI: 10.1038/ncomms7359**
   S. Canton et al., Visualizing the non-equilibrium dynamics of photoinduced intramolecular electron transfer with femtosecond X-ray pulses, Nature Communications, 2015.
7. **DOI: 10.1038/ncomms15342**
   H.T. Lemke et al., Coherent structural trapping through wave packet dispersion during photoinduced spin state switching, Nature Communications, 2017.
8. **DOI: 10.1063/1.4985017**
   K.S. Kjær et al., Ligand manipulation of charge transfer excited state relaxation and spin crossover in [Fe(2,2¿-bipyridine)2(CN)2], Structural Dynamics, 2017.
9. **DOI: 10.1039/c6sc03070j**
   W. Zhang et al., Manipulating Charge Transfer Excited State Relaxation and Spin Crossover in Iron Coordination Complexes with Ligand Substitution, Chemical Science, 2017.
10. **DOI: 10.1039/C4FD00203B**
    T. van Driel et al., Disentangling Detector Data in XFEL Studies of Temporally Resolved Solution State Chemistry, Faraday Discussions, 2017.
11. **DOI: 10.1107/S1600577515005536**
    T. van Driel et al., Correction of complex nonlinear signal response from a pixel array detector, Journal of Synchrotron Radiation, 2015.

Proposers

Main proposer

Mr. Peter Vester (Technical Univ. of Denmark, Denmark) Experiment role: main proposer, data collection, data analysis, sample preparation

Principal investigator

Prof. Dr. Martin Meedom Nielsen (Technical Univ. of Denmark, Denmark)

Co-proposers

- Miss Diana Bregenholt Zederkof (Technical University of Denmark, Denmark) Experiment role: data collection, data analysis, sample preparation
- Mr. Mads G Laursen (Technical Univ. of Denmark, Denmark) Experiment role: data collection, data analysis, sample preparation
- Dr. Kristoffer Haldrup (Technical Univ. of Denmark, Denmark) Experiment role: data collection, data analysis, sample preparation
- Dr. Kasper Skov Kjaer (Technical Univ. of Denmark, Denmark) Experiment role: data collection, data analysis, sample preparation
- Prof. Dr. Martin Meedom Nielsen (Technical Univ. of Denmark, Denmark) Experiment role: data collection, data analysis
- Prof. Dr. Ivan Vartaniants (DESY Deutsches Elektronen-Synchrotron, Germany) Experiment role: theory, data collection
- Dr. Ruslan Kurta (European XFEL GmbH, Germany) Experiment role: theory, data collection
- Dr. Ivan Zaluzhnyy (Moscow Engineering Physics Inst., Russia) Experiment role: theory, data collection

User consortium

No

Industrial partners

No

Revealing the Ultrafast Dynamics and Hidden Symmetries During Ion-Release from a Transition-Metal Complex

Studied with Time-Resolved X-ray Scattering and Cross-Correlation Analysis

1) Expected results and their impact in relevant scientific area(s)

The high X-ray flux and sub-100 femtosecond pulse duration at the European XFEL facility present a novel opportunity to study photo-excited molecular dynamics with X-ray scattering. Ultrafast X-ray scattering directly measures distance changes in between pairs of atoms, making the technique a direct structural probe of molecular dynamics, independent of the details of the vibrational structure as in optical studies. This has potential to change how we access structural dynamics.

This proposal is related to an earlier study of $Ir_2(dim)_4$ at LCLS in 2013 [1] (Figure 1) but with an Ag+-ion encapsulated between the two Ir atoms [8]. A key goal of the experiment is to study the influence on the dynamics by the addition of the Ag+-ion and resolve the ultrafast coherent excited state dynamics we were not able to confirm in our earlier study due to the limitations in time-resolution (Figure 2).

During an experiment at the ESRF synchrotron we confirmed the photo-induced Ag+ detachment of $AgIr_2(dim)_4$ from a substantial decrease in low-Q scattering at 100 ps. It is expected that the Ag+-ion is "squeezed" out of the molecule when the Ir-Ir distance contracts significantly in the excited state of $Ir_2(dim)_4$. We propose to measure the ultrafast dynamics during this process and map out the escape path of the Ag atom through the molecule. The system will be a prototype for a larger class of ion-release systems in e.g. biology, one example being the transport in ion channels.

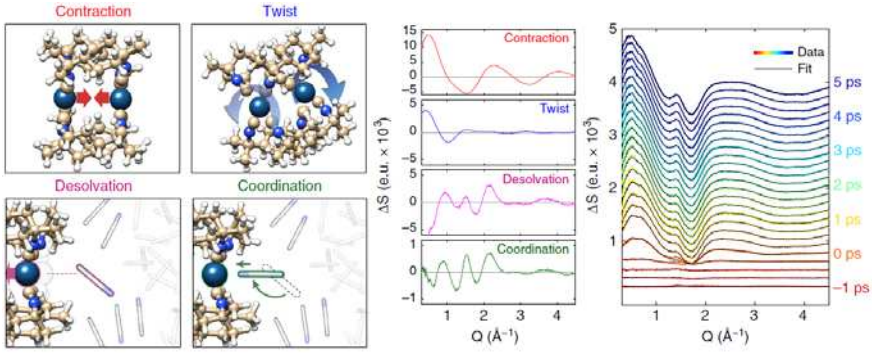

Figure 1: A sketch of four dynamics in $Ir_2(Dim)_4$ **(left)** and their difference scattering contributions **(middle)** giving rise to the previously measured difference scattering signals in a 2013 LCLS experiment **(right)**.

As the detachment involves breaking of an Ir-Ag bond and subsequent formation of an Ir-Ir bond it represents an excellent opportunity to study dynamics related to breaking and formation of metal-metal bonds. The system will also serve as a model system for method development of X-ray Cross Correlation Analysis (XCCA) [2].

The $Ir_2(dim)_4$ host molecule consists of two Ir[I] ions bridged by four diisocyanomenthane ligands. Each isocyano group ligates a different Ir[I], leading to a D_{4h} symmetry on each metal center [6]

When electronically excited an electron is promoted from an Ir-Ir antibonding orbital ($d\sigma_z^*$) to a bonding orbital ($p\sigma_z$), causing a significant reduction of the Ir-Ir bondlength of ~1 Å and twisting about the Ir-Ir bond by ~20 degrees in the otherwise weakly interacting Ir atoms [7]. The large structural change generates a photo-catalytically active complex and a very clear difference scattering signal. When analyzing the stimulated emission and comparing with QM/MM simulations [5], excitation leads to fundamental vibrational wave packets assigned predominantly to Ir-Ir bond stretching (~420 fs) and dihedral twisting (~280 fs).

Our earlier experiments at LCLS (Figure 1,2) confirmed this general picture, but lacked sufficient time-resolution to resolve the coherent oscillations. We did however provide evidence of the

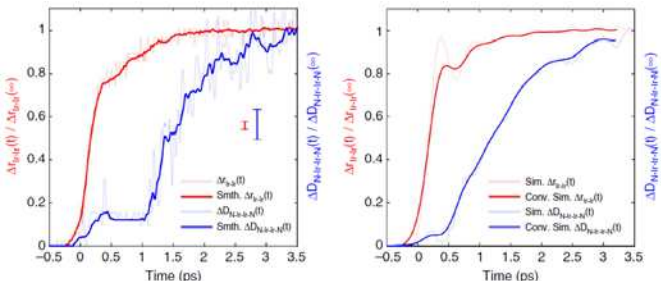

Figure 2: The measured Ir-Ir contraction (red) and the N-Ir-Ir-N dihedral twist (blue) determined from the XDS analysis **(left)** compared to QM/MM simulations **(right)**.

coordination of the Ir atoms by the acetonitrile solvent molecules upon photo-excitation and directly probed this solvation effect.

$AgIr_2(dim)_4$ is formed when Ag+ is added to solutions of $Ir_2(dim)_4$, and has been shown to be expelled upon photoexcitation with UV light [8]. This reaction thus offers an excellent opportunity to measure some fundamental processes in chemistry: i) the Ag+-ion dissociation pathway from the center of the molecule until $Ag/Ir_2(dim)_4$ separation and formation of a new solvent shell around Ag+, ii) The breaking and making of chemical bonds, through the subsequent change from two intermolecular Ir-Ag bonds to a single contracted Ir-Ir bond in the excited state. It is e.g. currently unknown whether both bonds are broken simultaneously.

With a tri-nuclear chain of strong scatterers, it is an ideal system for a direct structural study of this kind. It also gives a picture of the ultrafast excited state dynamics of the $Ir_2(dim)_4$ system to increase our understanding of the structure-function relationship in inorganic photo-catalysis and benchmarking of computer simulations.

The femtosecond laser/X-ray pump/probe pulses at XFEL are much shorter than the ~50 ps rotational times of solvated $Ir_2(dim)_4$, which ensures that the exact instantaneous orientation distribution is captured by the X-ray scattering. As these molecules have a transition dipole moment along the Ir-Ir axis, the molecules will predominantly be excited with an Ir-Ir bond orientation parallel to the polarization of the laser pulses. This creates non-isotropic detector scattering images. Such data are very suitable for XCCA, which uses Cross-Correlation Functions (CCFs) to analyze the non-isotropic part of the scattered intensities, and extract fine-structure information, going beyond radially integrated intensity analysis [2]. The Fourier analysis of the CCFs allows revealing hidden structural information about the system, particularly symmetries and their lifetimes. Therefore, we expect that XCCA will significantly improve the information content accessible in the experiment. At the same time, we also expect that by varying such parameters as sample concentration and laser power we will explore the capabilities of XCCA, which is crucial for method development.

We recently performed an experiment at LCLS on the structural related PtPOP system, which exhibits a similarly well-defined transition dipole moment along the Pt-Pt axis (connected by four ligand structures) and symmetric Pt-Pt bond contraction. The dominant n=2 Fourier component of the images were successfully compared to scattering simulations confirming the validity of our structural model (Figure 3). Two otherwise hidden timescales were revealed by model-independent XCCA, later associated to rotational dephasing and internal dynamics respectively. These studies illustrate the potential of XCCA as a tool to enhance the structural and temporal information from a scattering experiment. As the technique is still in its infancy it will benefit greatly from a dedicated study.

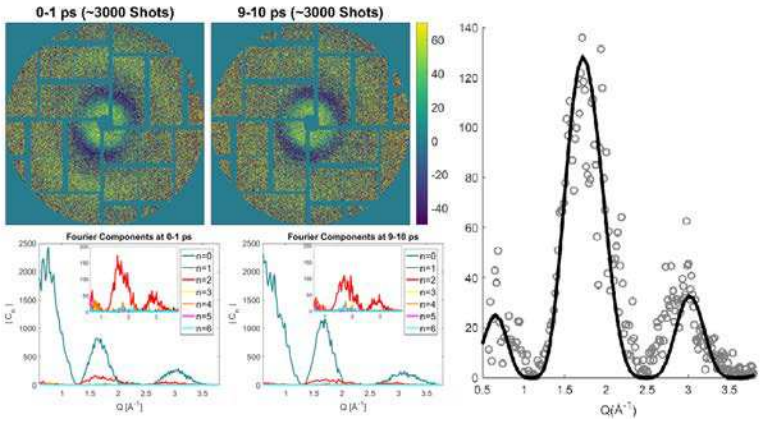

Figure 3: Top: Averaged difference scattering detector images at two time intervals from a previous LCLS experiment on PtPOP, **Bottom:** Fourier components of the CCFs. The insert highlights the dominant and temporally decreasing n = 2 contribution on top of the isotropic scattering signal. **Right:** Comparison of the n=2 component with our simulations.

$Ag/Ir_2(dim)_4$ represents an excellent model system to further develop the XCCA method and investigate fundamental chemical processes, due to several reasons: i) the significant structural changes in the Ir-Ir bondlength/ligand twisting, ii) the strong scatters (Ir-Ag-Ir) along the excitation axis of the molecules, iii) the destruction of 2-fold symmetry in $AgIr_2(dim)_4$ due to Ag+ dissociation, iv) solvent coordination in $Ir_2(dim)_4$

One question is e.g. if the solvation dynamics (desolvation/coordination) in the $Ir_2(dim)_4$ experiment, which were primarily visible at low-Q (Figure 1), can be more easily distinguished at higher Q-values by considering the higher order CCF components. Directly showing the additional 2-fold symmetry in solvent coordination by XCCA would significantly enhance the evidence for the effect compared to the previous experiments at LCLS, which only relied on comparison with 1D scattering curves calculated from QM/MM simulations. This could pave the way for future experiments. The data quality of the early versions of the CSPAD detector at LCLS in 2013, did not allow for XCCA.

2) Description of the planned experiment
The experiment will be carried out at the FXE instrument, designed to perform time-resolved femtosecond experiments. The setup will be conceptually identical to the previously performed experiment at LCLS on $Ir_2(dim)_4$ [1], where the collinear laser and X-ray beam intersect a thin fast flowing liquid film with the scattered X-rays collected on an area detector in a pump-probe scheme.

In order to probe the ultrafast coherent dynamics of the systems a sub-100 fs time revolution would be beneficial, but even the jitter-limited resolution of 500 fs will be sufficient for the method development of XCCA and probing of the structural transformations. The 9.00 keV photon energy provided in early user mode is well suited for the experiment and allows measurements of momentum transfers up to 4-5 $Å^{-1}$. This will allow for sufficiently accurate refinement of the key structural parameters in $Ag/Ir_2(dim)_4$. If possible, it could be interesting to additionally record a few data sets with the fundamental SASE radiation of 14 keV. This would allow us to determine the structures with even higher resolution and would demonstrate the state-of-the-art capability of the European XFEL.

Pump laser pulses at 400 nm will be used to trigger the dissociation process in $AgIr_2(dim)_4$, which is sufficient based on the previous experiment at ESRF. The laser will be focused collinearly with the X-rays on a 50 µm thickness flat jet. Using a jet with a thickness well below 0.1 mm will significantly reduce the group velocity mismatch between the optical laser and X-rays and will eliminate significant contributions to the overall time-resolution of the experiment.

The solution of $Ir_2(dim)_4$ will be made onsite by direct mixing of 1,8-diisocyano-paramenthane (dimen) and $Ir_2Cl_2(COD)_2$ (COD=1,5-cyclooctadiene) in a 4:1 ratio in degassed acetonitrile in a glovebox [3-4]. $AgIr_2(dim)_4$ will be made by slow infusion of $AgPF_6$. This reaction scheme and the purity of the resulting compounds have been tested in-house. A helium chamber is needed to protect from oxidation and reduce X-ray scattering by the air during the experiment.

[1] Driel et al. *Nature Communications* (2016) 7:13678
[2] Kurta et al. *Advances in Chemical Physics* (2016) 161.
[3] Mann et al. *Advances in Chemistry Series* (1979) 173, 225-235
[4] Rhodes et al. *Inorganic Chemistry* (1984) 23, 2053-2058
[5] Dohn et al. *J. Phys. Chem. Lett.* (2014) 5, 2414-2418.
[6] Coppens et al. *Chemical Communications* (2004) 2144-45.
[7] Haldrup et al. *Inorganic Chemistry* (2011) 50, 9329-9336
[8] Sykes et al. *Journal of American Chemical Society* (1988) 110, 8252-8253

3) Justification for the use of an X-ray free-electron laser facility and motivation for the selected instrument
To resolve structural changes in the molecule and surrounding solvent cage on sub-ps to ps timescale, we require a high-brilliance beamline equipped with optical lasers and capable of performing time-resolved pump-probe X-ray scattering measurements with sufficient time-resolution. The FXE beamline at the European XFEL offers all these conditions.

4) Justification for the number of shifts requested
We expect that each shift will need a significant number of hours for diagnostics and alignment prior to the measurements due to the start-up of XFEL/FXE. Based on experience with similar experiments at the XPP beamline of the LCLS, collection of high-quality data requires around 5 hours of beamtime (120 pulses/s and around 5*10^11 photons/pulse). We estimate that in terms of data collection, three-four 12-h shifts will be sufficient for measurements up to 5-10 ps (50 fs steps) and up to 50 ps (1 ps steps) with sufficient quality to analyze the non-isotropic part of the signal. Allowing for the early user start-up the likelihood of success is higher if five shifts are available with a tentative schedule as presented:

Shift 1: Setup of the detector, reference measurements and establishing temporal overlap. Measure the characteristic heating response of the solvent. Measure $Ir_2(dim)_4$ signal.
Shift 2+3: Setup and alignment, good quality data collection from $AgIr_2(dim)_4$ at 400 nm.
Shift 4+5: Measurements at different laser power and sample concentrations – in order to investigate the potential of XCCA. Supplementary measurements based on the analysis of the acquired data.